Variationally consistent discretization schemes and numerical algorithms for contact problems

Barbara Wohlmuth

Variationally consistent discretization schemes and numerical algorithms for contact problems

Barbara Wohlmuth
Technische Universität München
Fakultät für Mathematik M2,
Boltzmannstr. 3, 85748 Garching, Germany
E-mail: wohlmuth@ma.tum.de
URL: www-m2.ma.tum.de

We consider variationally consistent discretization schemes for mechanical contact problems. Most of the results can also be applied to other variational inequalities, such as those for phase transition problems in porous media, for plasticity or for option pricing applications from finance. The starting point is to weakly incorporate the constraint into the setting and to reformulate the inequality in the displacement in terms of a saddle-point problem. Here, the Lagrange multiplier represents the surface forces, and the constraints are restricted to the boundary of the simulation domain. Having a uniform inf-sup bound, one can then establish optimal low-order *a priori* convergence rates for the discretization error in the primal and dual variables. In addition to the abstract framework of linear saddle-point theory, complementarity terms have to be taken into account. The resulting inequality system is solved by rewriting it equivalently by means of the non-linear complementarity function as a system of equations. Although it is not differentiable in the classical sense, semi-smooth Newton methods, yielding super-linear convergence rates, can be applied and easily implemented in terms of a primal–dual active set strategy. Quite often the solution of contact problems has a low regularity, and the efficiency of the approach can be improved by using adaptive refinement techniques. Different standard types, such as residual- and equilibrated-based *a posteriori* error estimators, can be designed based on the interpretation of the dual variable as Neumann boundary condition. For the fully dynamic setting it is of interest to apply energy-preserving time-integration schemes. However, the differential algebraic character of the system can result in high oscillations if standard methods are applied. A possible remedy is to modify the fully discretized system by a local redistribution of the mass. Numerical results in two and three dimensions illustrate the wide range of possible applications and show the performance of the space discretization scheme, non-linear solver, adaptive refinement process and time integration.

1. Introduction

In many industrial applications or engineering problems, contact between deformable elastic bodies plays a crucial role. As examples we mention incremental forming processes, the simulation of rolling wheels, braking pads on tyres and roller bearings. Although early theoretical results go back to Hertz (1882), there are still many open problems, and the numerical simulation of dynamic contact problems remains challenging.

These problems are discussed in several monographs on contact mechanics such as Fischer-Cripps (2000), Johnson (1985) and Kikuchi and Oden (1988). More recent theoretical results on existence and uniqueness can be found in Eck, Jarušek and Krbec (2005) and Han and Sofonea (2000), and on mathematical models and numerical simulation techniques in Laursen (2002), Willner (2003), Wriggers (2006), Wriggers and Nackenhorst (2007) and the references therein. One of the main challenges relates to the fact that the actual contact zone is not known *a priori* and has to be identified by use of an iterative solver. Moreover, the transition between contact and non-contact is characterized by a change in the type of the boundary condition, and thus possibly results in a solution of reduced regularity. From the mathematical point of view, contact problems can be formulated as free boundary value problems and analysed within the abstract framework of variational inequalities (Facchinei and Pang 2003*a*, 2003*b*, Glowinski, Lions and Trémolières 1981, Harker and Pang 1990, Kinderlehrer and Stampacchia 2000).

This work is an overview of theoretical and numerical results obtained in recent years. Most of the numerical examples are therefore taken from the original papers which are cited in the reference list. The numerical implementation is based on different software codes. In particular, DUMUX (Flemisch, Fritz, Helmig, Niessner and Wohlmuth 2007), DUNE (Bastian, Blatt, Dedner, Engwer, Klöfkorn, Kornhuber, Ohlberger and Sander 2008), NETGEN (Schöberl 1997), PARAVIEW (Ahrens, Geveci and Law 2005),

PARDISO (Karypis and Kumar 1998, Schenk and Gärtner 2004, 2006), and UG (Bastian, Birken, Johannsen, Lang, Neuß, Rentz-Reichert and Wieners 1997) have been used.

The structure of this paper is as follows. In Section 2, the governing equations and corresponding inequality constraints for frictional contact problems are stated. Different equivalent formulations are discussed and a weak saddle-point formulation is presented. Section 3 is devoted to space discretization. Special emphasis is placed on uniformly inf-sup stable pairings and a suitable approximation of the dual cone. Optimal *a priori* estimates for the discretization error in the displacement and in the surface traction are given for low-order finite elements in Section 4. Here, we restrict ourselves to very simple contact settings with given friction bounds and do not take non-matching contact zones into account, but allow for non-matching meshes.

In Section 5, we survey different solver techniques for the non-linear inequality system. Of special interest are so-called semi-smooth Newton methods applied to an equivalent non-linear system of equations. We discuss in detail the structure of the systems to be solved after consistent linearization. In particular, in the case of no friction the Newton solver can easily be implemented as a standard primal–dual active set strategy, updating in each iteration step the type and the value of the boundary condition node-wise.

Section 6 is devoted to different aspects of adaptive refinement. Bearing in mind that the mechanical role of the discrete Lagrange multiplier is that of a surface traction, different error indicators can easily be designed. However, the analysis is quite challenging and only a few theoretical results exist, taking into account possibly non-matching meshes and the inequality character of the formulation. Here, we provide upper and lower bounds for a simplified setting and comment on possible generalizations.

Section 7 is devoted to aspects of time integration. For many applications structure-preserving time-integration schemes are of special interest. In this context, energy preservation is of crucial importance. Unfortunately most of the standard techniques result either in very high oscillations in the dual variable or in numerical dissipation. We apply a newly combined time and space integration scheme which is motivated by a reduction of the index of the differential algebraic system.

Finally, in Section 8 we illustrate the flexibility of the proposed approach by considering applications from different areas. In particular, an example from finance shows that the Lagrange multiplier approach based on a $(d-1)$-dimensional $H^{1/2}$-duality pairing can also be applied to obstacle-type inequalities reflecting a d-dimensional H^1-duality pairing. Of special interest are examples where d- and $(d-1)$-dimensional constraints are imposed, such as phase transition problems in heterogeneous porous media and elasto-plastic mechanical contact problems.

2. Problem setting for mechanical contact

In many applications involving several deformable bodies, frictional contact has to be considered in conjunction with inelastic material behaviour such as plasticity. A great deal of research has been done on both of these topics: see for example Boieri, Gastaldi and Kinderlehrer (1987), Eck *et al.* (2005), Johnson (1985), Laursen (2002), Willner (2003), Wriggers (2006) and the references therein for an overview of contact problems. Characteristically, this type of application leads to a constrained minimization problem or more generally to a variational inequality (Harker and Pang 1990, Haslinger, Hlaváček, Nečas and Lovíšek 1988, Kikuchi and Oden 1988, Kinderlehrer and Stampacchia 2000). Mathematical analyses of variational inequalities and constrained minimization problems can also be found in Facchinei and Pang (2003*a*, 2003*b*), Geiger and Kanzow (2002), Glowinski (1984), Glowinski, Lions and Trémolières (1981) and Haslinger, Hlaváček and Nečas (1996). We refer to the recent monographs by Han and Reddy (1999) and Han and Sofonea (2002) and the references therein for an overview of the mathematical theory and numerical analysis for inequality problems in continuum mechanics.

Our formulation will be based on a primal–dual pair of variables. In addition to the displacement which represents the primal variable, the surface traction on the possible contact zone is introduced as dual variable: see, *e.g.*, Christensen, Klarbring, Pang and Strömberg (1998). This new pair of variables has to be admissible, *i.e.*, satisfy the inequality constraints arising from the non-penetration condition and the friction law.

In this section, we provide the setting of a quasi-static frictional contact problem between elastic bodies. Figure 2.1 shows the stress components σ_{xx} and σ_{xy} for two different situations in the case of three elastic bodies in contact.

Here, the contact of a deformable body with a rigid obstacle has been taken into account as well as the contact between deformable bodies. A fully symmetric situation is shown in Figure 2.1(a,b), and no Dirichlet boundary condition is imposed. The rigid body motions are fixed by the non-penetration condition and a zero tangential displacement of the centre of the upper circle. In Figure 2.1(c,d), there is an additional rigid obstacle on the right of the three circles. Then all rigid body modes are automatically fixed by the contact conditions.

To simplify the notation, we restrict our attention to two bodies, linear elasticity in the compressible range and a given constant Coulomb friction coefficient. However, most of our algorithmic results can easily be extended to more complex situations. We refer to the early papers by Laursen and Simo (1993*a*), Oden, Becker, Lin and Demkowicz (1985), Puso and Laursen (2004*a*, 2004*b*), Puso, Laursen and Solberg (2008), Yang and

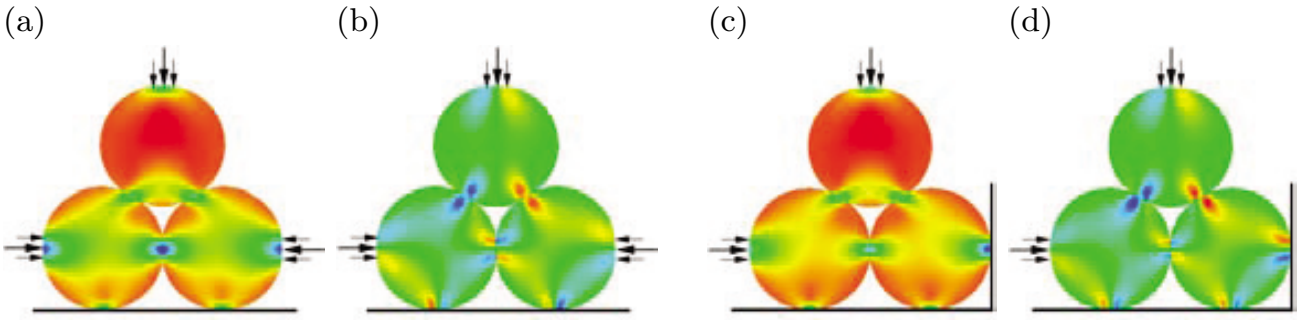

Figure 2.1. Stress component σ_{xx} and σ_{xy} for a symmetric (a,b) and a non-symmetric setting (c,d).

Laursen (2008*a*, 2008*b*) and Yang, Laursen and Meng (2005) for large deformation contact discretizations on non-matching meshes and to the recent contributions on solvers by Gitterle, Popp, Gee and Wall (2010), Popp, Gitterle, Gee and Wall (2010), Popp, Gee and Wall (2009) and Krause and Mohr (2011). Numerical examples also illustrate the performance of these approaches in more general formulations, *e.g.*, for nearly incompressible materials and the inclusion of thermal effects with a temperature-dependent friction coefficient.

The two bodies in the reference configuration are given by two open bounded domains Ω^{s} and $\Omega^{\mathrm{m}} \subset \mathbb{R}^d$, $d = 2, 3$, with Lipschitz boundary $\partial\Omega^{\mathrm{s}}$ and $\partial\Omega^{\mathrm{m}}$, respectively. The notation is adapted to the standard mortar framework, *i.e.*, the upper index s stands for the slave side, and the index m refers to the master side. The contact conditions will be imposed weakly in terms of Lagrange multipliers defined on the slave side. Thus the displacement on the slave side has to follow the displacement of the master side in the event that the constraints are active. This observation motivates the terminology. The boundary $\partial\Omega^k$ is partitioned into three open disjoint measurable parts $\Gamma^k_{\mathrm{D}}, \Gamma^k_{\mathrm{N}}$, and Γ^k_{C}, $k \in \{\mathrm{m}, \mathrm{s}\}$. Dirichlet conditions will be set on Γ^k_{D} and Neumann data on Γ^k_{N}. For simplicity of notation, we assume firstly that $\mathrm{meas}(\Gamma^k_{\mathrm{D}}) > 0$, $k \in \{\mathrm{s}, \mathrm{m}\}$, secondly that $\Gamma^{\mathrm{s}}_{\mathrm{D}}$ is compactly embedded in $\partial\Omega^{\mathrm{s}} \setminus \overline{\Gamma}^{\mathrm{s}}_{\mathrm{C}}$, and thirdly that the actual contact zone $B_n \subset \Gamma^{\mathrm{s}}_{\mathrm{C}}$ is compactly embedded in $\Gamma^{\mathrm{s}}_{\mathrm{C}}$. The first assumption on the Dirichlet boundary part means that Korn's inequality holds on each body, and thus that we do not have to deal with extra rigid body motions. The second assumption guarantees that the trace space restricted to $\Gamma^{\mathrm{s}}_{\mathrm{C}}$ does not see any boundary condition originating from $\Gamma^{\mathrm{s}}_{\mathrm{D}}$. As we will see later, the third assumption on the actual contact zone guarantees that the support of the surface traction on $\Gamma^{\mathrm{s}}_{\mathrm{C}}$ is compactly embedded in $\Gamma^{\mathrm{s}}_{\mathrm{C}}$.

Throughout this paper, we use the standard notation for the Sobolev space $H^s(\omega)$, $s \geq 1$, where ω is a suitable subdomain of Ω^k, $k \in \{\mathrm{s}, \mathrm{m}\}$, and denote the associated norm with $\|\cdot\|_{s;\omega}$. The broken H^s-norm on Ω is given by $\|v\|^2_{s;\Omega} := \|v^{\mathrm{s}}\|^2_{s;\Omega^{\mathrm{s}}} + \|v^{\mathrm{m}}\|^2_{s;\Omega^{\mathrm{m}}}$ for $v := (v^{\mathrm{s}}, v^{\mathrm{m}}) \in H^s(\Omega^{\mathrm{s}}) \times H^s(\Omega^{\mathrm{m}})$.

On $(d-1)$-dimensional manifolds γ such as $\Gamma_{\mathrm{C}}^{\mathrm{s}}$, we use the Sobolev space $H^s(\gamma)$, $s \geq 0$, and its dual space $H^{-s}(\gamma)$. We point out that in our notation $H^{-1/2}(\gamma)$ is not the dual space of $H_{00}^{1/2}(\gamma)$ but of $H^{1/2}(\gamma)$. The dual norm is defined in the standard way by

$$\|\mu\|_{-s;\gamma} := \sup_{v \in H^s(\gamma)} \frac{\langle \mu, v \rangle_{s;\gamma}}{\|v\|_{s;\gamma}}, \quad s \geq 0, \tag{2.1}$$

where $\langle \cdot, \cdot \rangle_{s;\gamma}$ denotes the duality pairing. We note that the second assumption on the Dirichlet boundary part allows one to work with $H^{1/2}(\Gamma_{\mathrm{C}}^{\mathrm{s}})$. Otherwise, we would have to consider the more complex $H_{00}^{1/2}(\Gamma_{\mathrm{C}}^{\mathrm{s}})$ space, as in the mortar framework with cross-points (Bernardi, Maday and Patera 1993, 1994). We refer to the recent monograph on the theory and implementation of mortar methods by Lacour and Ben Belgacem (2011)

In what follows, we shall frequently use the generic constants $0 < c, C < \infty$, which are independent of the mesh size but possibly depend on the regularity of the domain or the mesh. Vectorial quantities are written in bold, *e.g.*, $\mathbf{x}$, $\mathbf{y}$, and for simplicity of notation $\mathbf{xy}$ stands for the scalar product between $\mathbf{x}$ and $\mathbf{y}$. Tensorial quantities are represented by bold greek symbols.

2.1. Problem formulation in its strong form

For the moment we restrict ourselves on each body to a homogeneous isotropic linearized Saint Venant–Kirchhoff material and also to the small strain assumption. Then, the strain-displacement relation is defined by $\boldsymbol{\varepsilon}(\mathbf{v}) := 1/2(\nabla \mathbf{v} + (\nabla \mathbf{v})^\top)$ and the constitutive equation for the stress tensor is given in terms of the fourth-order Hooke tensor $\mathcal{C}$ by

$$\boldsymbol{\sigma}(\mathbf{v}) := \lambda \operatorname{tr}(\boldsymbol{\epsilon}(\mathbf{v}))\mathbf{Id} + 2\mu\boldsymbol{\epsilon}(\mathbf{v}) =: \mathcal{C}\boldsymbol{\epsilon}(\mathbf{v}). \tag{2.2}$$

Here tr denotes the trace operator and $\mathbf{Id}$ the identity in $\mathbb{R}^{d\times d}$. The positive coefficient λ and the shear modulus μ are the Lamé parameters, which are assumed to be constant in each subdomain Ω^k, $k \in \{\mathrm{s}, \mathrm{m}\}$, but have possibly quite different values on the slave and master side. We note that the Lamé parameters can be easily calculated from the Poisson ratio and Young's modulus.

Then, the linearized elastic equilibrium condition for the displacement $\mathbf{u} := (\mathbf{u}^{\mathrm{m}}, \mathbf{u}^{\mathrm{s}})$ can be written as

$$\begin{aligned} -\operatorname{div} \boldsymbol{\sigma}(\mathbf{u}) &= \mathbf{f} \quad && \text{in } \Omega, \\ \mathbf{u} &= \mathbf{u}_{\mathrm{D}} && \text{on } \Gamma_{\mathrm{D}} := \Gamma_{\mathrm{D}}^{\mathrm{m}} \cup \Gamma_{\mathrm{D}}^{\mathrm{s}}, \\ \boldsymbol{\sigma}(\mathbf{u})\mathbf{n} &= \mathbf{f}_{\mathrm{N}} && \text{on } \Gamma_{\mathrm{N}} := \Gamma_{\mathrm{N}}^{\mathrm{m}} \cup \Gamma_{\mathrm{N}}^{\mathrm{s}}, \end{aligned} \tag{2.3}$$

where $\mathbf{n}$ stands for the outer unit normal vector, which is almost everywhere well-defined. Here, the volume force $\mathbf{f}$, the Neumann data $\mathbf{f}_{\mathrm{N}}$, and

the Dirichlet condition $\mathbf{u}_{\mathrm{D}}$ are assumed to be in $(L^2(\Omega))^d$, $(L^2(\Gamma_{\mathrm{N}}))^d$ and $(C(\Gamma_{\mathrm{D}}^{\mathrm{s}}) \cap H^{1/2}(\Gamma_{\mathrm{D}}^{\mathrm{s}}))^d \times (C(\Gamma_{\mathrm{D}}^{\mathrm{m}}) \cap H^{1/2}(\Gamma_{\mathrm{D}}^{\mathrm{m}}))^d$, respectively. Moreover, we assume that $C_{\mathrm{reg}} < \infty$ exists such that

$$\sup_{\substack{\mathbf{v} \in (H^1(\Omega^{\mathrm{s}}))^d \\ \mathbf{v}|_{\Gamma_{\mathrm{D}}^{\mathrm{s}}} = \mathbf{0}}} \frac{\int_{\Omega^{\mathrm{s}}} \mathbf{f}\mathbf{v} \, \mathrm{d}x + \int_{\Gamma_{\mathrm{N}}^{\mathrm{s}}} \mathbf{f}_{\mathrm{N}}\mathbf{v} \, \mathrm{d}s}{\|\mathbf{v}\|_{1;\Omega^{\mathrm{s}}}} \leq C_{\mathrm{reg}} \sup_{\substack{\mathbf{v} \in (H^1(\Omega^{\mathrm{s}}))^d \\ \mathbf{v}|_{\Gamma_{\mathrm{D}}^{\mathrm{s}} \cup \Gamma_{\mathrm{C}}^{\mathrm{s}}} = \mathbf{0}}} \frac{\int_{\Omega^{\mathrm{s}}} \mathbf{f}\mathbf{v} \, \mathrm{d}x + \int_{\Gamma_{\mathrm{N}}^{\mathrm{s}}} \mathbf{f}_{\mathrm{N}}\mathbf{v} \, \mathrm{d}s}{\|\mathbf{v}\|_{1;\Omega^{\mathrm{s}}}}. \tag{2.4}$$

These regularity assumptions on the data can be considerably weakened but for most examples these hold.

In addition to (2.3), we have to satisfy the contact constraints on $\Gamma_{\mathrm{C}}^{\mathrm{s}}$: the linearized non-penetration condition in the normal direction and the friction law in the tangential direction. These constraints can be formulated by means of the displacement and the surface traction $\boldsymbol{\lambda} := -\boldsymbol{\sigma}(\mathbf{u}^{\mathrm{s}})\mathbf{n}^{\mathrm{s}}$. The linearized non-penetration condition reads as

$$[u_n] \leq g, \quad \lambda_n \geq 0, \quad \lambda_n([u_n] - g) = 0, \tag{2.5}$$

where $g \in H^{1/2}(\Gamma_{\mathrm{C}}^{\mathrm{s}})$ is the linearized gap function between the two deformable bodies. The linearized setting can be expressed in terms of the normal contributions with respect to the reference configuration. Here $\lambda_n := \boldsymbol{\lambda}\mathbf{n}^{\mathrm{s}}$ is the normal component of the boundary stress, and $[u_n] := (\mathbf{u}^{\mathrm{s}} - \mathbf{u}^{\mathrm{m}} \circ \chi)\mathbf{n}^{\mathrm{s}}$ is the jump of the mapped boundary displacements, where $\chi(\cdot)$ denotes a suitable mapping from $\Gamma_{\mathrm{C}}^{\mathrm{s}}$ onto $\Gamma_{\mathrm{C}}^{\mathrm{m}}$.

In addition to (2.5), we have to satisfy the quasi-static Coulomb law

$$\|\boldsymbol{\lambda}_t\| \leq \nu\lambda_n, \quad [\dot{\mathbf{u}}_t]\boldsymbol{\lambda}_t - \nu\lambda_n\|[\dot{\mathbf{u}}_t]\| = 0, \tag{2.6}$$

where the tangential components are defined by $\boldsymbol{\lambda}_t := \boldsymbol{\lambda} - \lambda_n\mathbf{n}^{\mathrm{s}}$ and $[\mathbf{u}_t] := [\mathbf{u}] - [u_n]\mathbf{n}^{\mathrm{s}}$, $[\mathbf{u}] := \mathbf{u}^{\mathrm{s}} - \mathbf{u}^{\mathrm{m}} \circ \chi$, $\nu \geq 0$ is the friction coefficient, and $\|\cdot\|$ stands for the Euclidean norm. We note that for the dynamic case, inertia terms have to be included, and the volume mass density of the two bodies has to be taken into account: see Section 7. For the moment we focus on the static Coulomb law, *i.e.*, we replace the tangential velocity by the tangential displacement in (2.6). This problem type has then to be solved in each time step if an implicit time-integration scheme is used.

Figure 2.2 illustrates the notation and the situation for finite deformations. In that case the Jacobian of the deformation mapping has to be taken into account and the non-penetration has to be formulated with respect to the actual configuration.

We recall that in the reference configuration $\Gamma_{\mathrm{C}}^{\mathrm{s}}$ and $\Gamma_{\mathrm{C}}^{\mathrm{m}}$ do not have to be matching, and thus the displacement from the master side has to be projected onto the slave side. Moreover, the contact surface tractions on the master and slave body have to be in equilibrium in the actual configuration. In the case of linear elasticity, reference and actual configuration can be

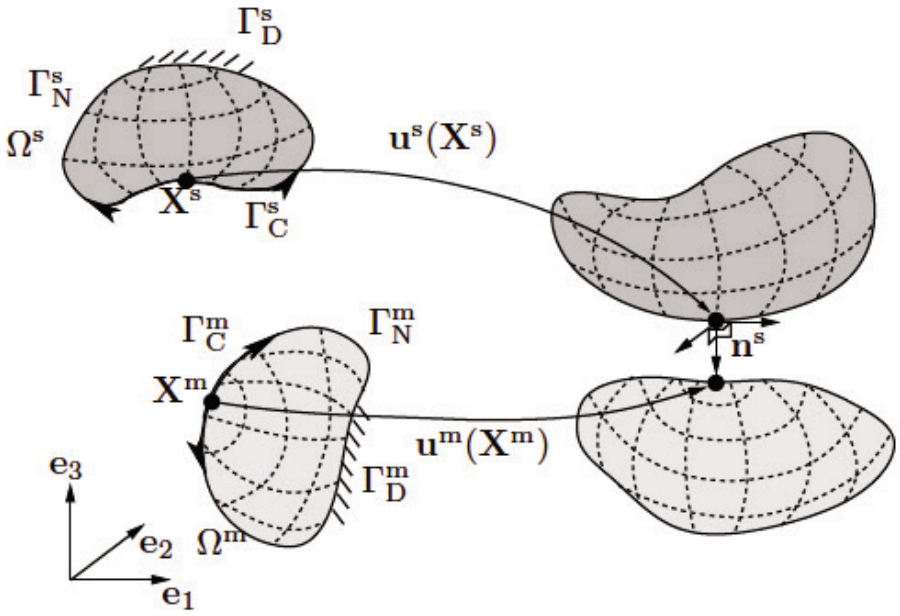

Figure 2.2. Illustration of the notation.

identified, and thus the approach is simplified considerably compared to the case of finite deformations.

We note that the Signorini problem with Coulomb friction was introduced by Duvaut and Lions (1976); see also Fichera (1964) and Lions and Stampacchia (1967). Although it is widely studied, not all aspects are yet fully understood and some open questions remain. It is well known that frictional contact problems do not necessarily have a unique weak solution. Many of the early results are designed for the case of one elastic body in contact with a rigid foundation. First existence results can be found in Demkowicz and Oden (1982), Jarušek (1983) and Nečas, Jarušek and Haslinger (1980). An alternative proof based on a penalization technique is given in Eck and Jarušek (1998). Examples for non-uniqueness are given in Ballard (1999) and Hild (2003, 2004), and uniqueness criteria are studied, *e.g.*, in Ballard and Basseville (2005), Hild and Renard (2006) and Renard (2006). We refer to the recent monograph by Eck *et al.* (2005) for an excellent overview of existence and uniqueness results for these contact problems. Roughly speaking, for $\nu \geq 0$ small enough, the existence and uniqueness of a weak solution is guaranteed.

Figure 2.3 shows the influence of the friction coefficient ν on the normal and tangential component of the surface traction for the classical Hertz problem (Hertz 1882). In between the maximal and minimal value of the tangential contact traction, the two bodies stick together. On the rest of the actual contact zone, a relative tangential displacement occurs. As can be seen directly from (2.6) for $\nu = 0$, we have $\boldsymbol{\lambda}_t = \mathbf{0}$, which is also obtained by the numerical scheme. We observe that the size of the slippy contact zone is largely influenced by ν. The smaller ν, the larger is the slippy contact zone, whereas the contact radius is not very sensitive with respect to ν.

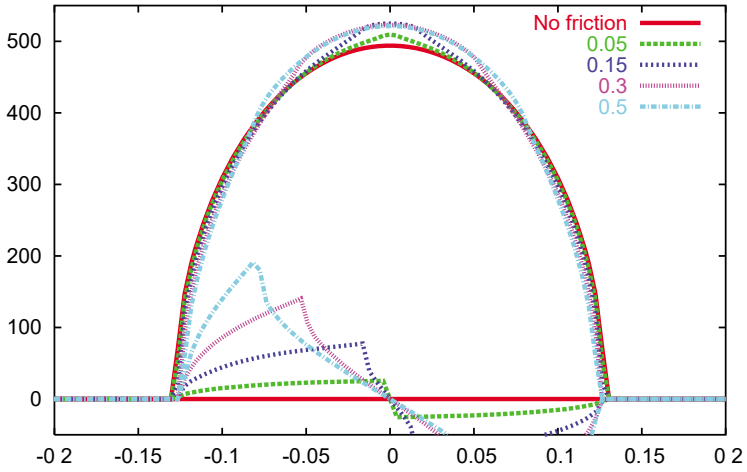

Figure 2.3. Surface traction of a Hertz contact problem with Coulomb friction for different values of the friction coefficient $\nu \in \{0, 0.05, 0.15, 0.3, 0.5\}$.

2.2. Formulation of the weak problem

We start with a detailed discussion of different but equivalent formulations of the contact problem with no friction, *i.e.*, $\nu = 0$. Then the problem is equivalent to a standard variational inequality of the first kind or to an energy-minimization problem on a convex set. The frictionless contact problem with a linearized non-penetration condition can be stated as follows. Find $\mathbf{u} \in \mathbf{K}$ such that

$$J(\mathbf{u}) = \inf_{\mathbf{v}\in\mathbf{K}} J(\mathbf{v}), \tag{2.7}$$

where the convex set $\mathbf{K}$ is given by all admissible solutions, and the energy is defined by $J(\mathbf{v}) := \frac{1}{2}a(\mathbf{v},\mathbf{v}) - f(\mathbf{v})$. Here, the bilinear form $a(\cdot,\cdot)$ is given, for $\mathbf{v},\mathbf{w} \in \mathbf{V} := \mathbf{V}^{\mathrm{m}} \times \mathbf{V}^{\mathrm{s}} := (H^1(\Omega^{\mathrm{m}}))^d \times (H^1(\Omega^{\mathrm{s}}))^d$, by

$$a(\mathbf{w},\mathbf{v}) := a_{\mathrm{m}}(\mathbf{w}^{\mathrm{m}},\mathbf{v}^{\mathrm{m}}) + a_{\mathrm{s}}(\mathbf{w}^{\mathrm{s}},\mathbf{v}^{\mathrm{s}}),$$
$$a_k(\mathbf{w}^k,\mathbf{v}^k) := \int_{\Omega^k} \boldsymbol{\sigma}(\mathbf{w}^k) : \boldsymbol{\epsilon}(\mathbf{v}^k)\,\mathrm{d}x, \quad k \in \{\mathrm{m},\mathrm{s}\},$$

and the linear form $f(\cdot)$ is defined for all $\mathbf{v} \in \mathbf{V}$ in terms of

$$f(\mathbf{v}) := f_{\mathrm{s}}(\mathbf{v}^{\mathrm{s}}) + f_{\mathrm{m}}(\mathbf{v}^{\mathrm{m}}), \quad f_k(\mathbf{v}^k) := \int_{\Omega^k} \mathbf{f}\mathbf{v}^k\,\mathrm{d}x + \int_{\Gamma_{\mathrm{N}}^k} \mathbf{f}_{\mathrm{N}}\mathbf{v}^k\,\mathrm{d}s.$$

In addition to the Hilbert space $\mathbf{V}$, we introduce the subset $\mathbf{K} \subset \mathbf{V}$:

$$\mathbf{K} := \{\mathbf{v} \in \mathbf{V} \mid \mathbf{v} = \mathbf{u}_{\mathrm{D}} \text{ on } \Gamma_{\mathrm{D}} \text{ and } [v_n] \le g \text{ on } \Gamma_{\mathrm{C}}^{\mathrm{s}}\}.$$

By definition $\mathbf{K}$ is a closed convex non-empty set, $f(\cdot)$ is a continuous linear functional on $\mathbf{V}$, and the bilinear form $a(\cdot,\cdot)$ is continuous on $\mathbf{V}\times\mathbf{V}$ and elliptic with respect to the Hilbert space $\mathbf{V}_0 := \{\mathbf{v} \in \mathbf{V}, \mathbf{v} = \mathbf{0} \text{ on } \Gamma_{\mathrm{D}}\}$.

Thus the constrained minimization problem (2.7) has a unique solution: see, *e.g.*, Glowinski (1984). Due to the symmetry of the bilinear form $a(\cdot,\cdot)$, (2.7) can be equivalently written as a variational inequality of the first kind, *i.e.*, find $\mathbf{u} \in \mathbf{K}$ such that

$$a(\mathbf{u}, \mathbf{v} - \mathbf{u}) \geq f(\mathbf{v} - \mathbf{u}), \quad \mathbf{v} \in \mathbf{K}, \tag{2.8}$$

or as a variational inequality of the second kind, *i.e.*, find $\mathbf{u} \in \mathbf{V}$ such that

$$a(\mathbf{u}, \mathbf{v} - \mathbf{u}) + \chi_{\mathbf{K}}(\mathbf{v}) - \chi_{\mathbf{K}}(\mathbf{u}) \geq f(\mathbf{v} - \mathbf{u}), \quad \mathbf{v} \in \mathbf{V}, \tag{2.9}$$

where $\chi_{\mathbf{K}}$ is the indicator functional of $\mathbf{K}$, *i.e.*, $\chi_{\mathbf{K}}(\mathbf{v}) := \infty$ if $\mathbf{v} \notin \mathbf{K}$ and zero otherwise. We refer to Brezis (1971), Duvaut and Lions (1976), Fichera (1964), Glowinski (1984), Glowinski *et al.* (1981), Kinderlehrer and Stampacchia (2000) and the references therein for an abstract mathematical framework on inequalities as well as for the so-called Signorini problem and its physical and mechanical interpretation. It is easy to see that in the special case of a variational inequality of the first kind with the convex set being a Hilbert space, existence and uniqueness of a solution follow directly from the Lax–Milgram theorem. Alternatively to the pure displacement-based formulation, the Signorini problem can be characterized in terms of the contact pressure as unknown variable; see, *e.g.*, Demkowicz (1982).

We note that the convex set $\mathbf{K}$ can be characterized in terms of a dual cone. To do so, we introduce the dual space $\mathbf{M} := (M)^d := (W')^d =: \mathbf{W}'$ of the trace space $\mathbf{W} := W^d := (H^{1/2}(\Gamma_{\mathrm{C}}^{\mathrm{s}}))^d$ and define the bilinear form $b(\cdot,\cdot)$ by

$$b(\boldsymbol{\mu}, \mathbf{v}) := \langle \boldsymbol{\mu}, [\mathbf{v}] \rangle_{\Gamma_{\mathrm{C}}^{\mathrm{s}}}, \quad \mathbf{v} \in \mathbf{V}, \boldsymbol{\mu} \in \mathbf{M},$$

where $\langle \cdot, \cdot \rangle_{\Gamma_{\mathrm{C}}^{\mathrm{s}}}$ stands for the $H^{1/2}$-duality pairing on $\Gamma_{\mathrm{C}}^{\mathrm{s}}$, and $[\mathbf{v}] := \mathbf{v}^{\mathrm{s}} - \mathbf{v}^{\mathrm{m}} \circ \chi$. It is assumed that χ is smooth enough such that for $\mathbf{v} \in \mathbf{V}$ we have $[\mathbf{v}] \in \mathbf{W}$. In terms of the bilinear form $b(\cdot,\cdot)$, the closed non-empty convex cone $\mathbf{M}^+$ is set to

$$\mathbf{M}^+ := \{\boldsymbol{\mu} \in \mathbf{M} \mid \langle \boldsymbol{\mu}, \mathbf{w} \rangle_{\Gamma_{\mathrm{C}}^{\mathrm{s}}} \geq 0, \mathbf{w} \in \mathbf{W}_n^+\}, \tag{2.10a}$$

$$\mathbf{W}_n^+ := \{\mathbf{w} \in \mathbf{W} \mid w_n \in W^+\}, \quad W^+ := \{w \in W \mid w \geq 0\}. \tag{2.10b}$$

Here, we assume that $\mathbf{n}^{\mathrm{s}}$ is smooth enough such that for $\mathbf{w} \in \mathbf{W}$ and $w \in W$ we also have $w_n \in W$ and $w\mathbf{n}^{\mathrm{s}} \in \mathbf{W}$, respectively. Then the definitions of $\mu_n \in M$ for $\boldsymbol{\mu} \in \mathbf{M}$ and of $\mu_n \mathbf{n}^{\mathrm{s}} \in \mathbf{M}$ for $\mu_n \in M$ given by

$$\langle \mu_n, w \rangle_{\Gamma_{\mathrm{C}}^{\mathrm{s}}} := \langle \boldsymbol{\mu}, w\mathbf{n}^{\mathrm{s}} \rangle_{\Gamma_{\mathrm{C}}^{\mathrm{s}}}, \quad w \in W,$$
$$\langle \mu_n \mathbf{n}^{\mathrm{s}}, \mathbf{w} \rangle_{\Gamma_{\mathrm{C}}^{\mathrm{s}}} := \langle \mu_n, w_n \rangle_{\Gamma_{\mathrm{C}}^{\mathrm{s}}}, \quad \mathbf{w} \in \mathbf{W},$$

respectively, are consistent in the sense that $\langle \mu_n, w_n \rangle_{\Gamma_{\mathrm{C}}^{\mathrm{s}}} = \langle \mu_n \mathbf{n}^{\mathrm{s}}, w_n \mathbf{n}^{\mathrm{s}} \rangle_{\Gamma_{\mathrm{C}}^{\mathrm{s}}}$ for all $\boldsymbol{\mu} \in \mathbf{M}$ and $\mathbf{w} \in \mathbf{W}$. As a result the bilinear form $b(\cdot,\cdot)$ can be split

in a well-defined normal and tangential part,

$$b(\boldsymbol{\mu}, \mathbf{v}) = b_n(\boldsymbol{\mu}, \mathbf{v}) + b_t(\boldsymbol{\mu}, \mathbf{v}) \tag{2.11}$$

with $b_n(\boldsymbol{\mu}, \mathbf{v}) := b(\mu_n \mathbf{n}^{\mathrm{s}}, \mathbf{v})$, $b_t(\boldsymbol{\mu}, \mathbf{v}) := b(\boldsymbol{\mu}_t, \mathbf{v})$, $\boldsymbol{\mu}_t := \boldsymbol{\mu} - \mu_n \mathbf{n}^{\mathrm{s}}$.

The situation that $\mathbf{n}^{\mathrm{s}}$ is only piecewise well-defined on $\Gamma_{\mathrm{C}}^{\mathrm{s}}$ can be handled by decomposing the contact zone into non-overlapping subparts $\gamma_j \subset \Gamma_{\mathrm{C}}^{\mathrm{s}}$, defining all quantities with respect to γ_j and using product spaces and broken duality pairings.

Now, observing that $\mathbf{K}$ can be written as

$$\mathbf{K} = \{\mathbf{v} \in \mathbf{V} \mid \mathbf{v} = \mathbf{u}_{\mathrm{D}} \text{ on } \Gamma_{\mathrm{D}} \text{ and } b(\boldsymbol{\mu}, \mathbf{v}) \leq g(\boldsymbol{\mu}), \boldsymbol{\mu} \in \mathbf{M}^+\},$$

where $g(\boldsymbol{\mu}) := \langle \mu_n, g \rangle_{\Gamma_{\mathrm{C}}^{\mathrm{s}}}$, $\boldsymbol{\mu} \in \mathbf{M}$, we obtain the saddle-point formulation of (2.8). Find $(\mathbf{u}, \boldsymbol{\lambda}) \in \mathbf{V}_{\mathrm{D}} \times \mathbf{M}^+$ such that

$$\begin{aligned} a(\mathbf{u}, \mathbf{v}) + b(\boldsymbol{\lambda}, \mathbf{v}) &= f(\mathbf{v}), & \mathbf{v} &\in \mathbf{V}_0, \\ b(\boldsymbol{\mu} - \boldsymbol{\lambda}, \mathbf{u}) &\leq g(\boldsymbol{\mu} - \boldsymbol{\lambda}), & \boldsymbol{\mu} &\in \mathbf{M}^+, \end{aligned} \tag{2.12}$$

with the convex set $\mathbf{V}_{\mathrm{D}} := \{\mathbf{v} \in \mathbf{V}, \mathbf{v} = \mathbf{u}_{\mathrm{D}} \text{ on } \Gamma_{\mathrm{D}}\}$.

Lemma 2.1. The three inequality formulations (2.8), (2.9) and (2.12) are equivalent in the sense that if $(\mathbf{u}, \boldsymbol{\lambda})$ solves (2.12), then $\mathbf{u}$ is the solution of (2.8) and (2.9), and if $\mathbf{u}$ solves (2.8) or (2.9), then $(\mathbf{u}, \boldsymbol{\lambda})$, with $\boldsymbol{\lambda} \in \mathbf{M}$,

$$\langle \boldsymbol{\lambda}, \mathbf{w} \rangle_{\Gamma_{\mathrm{C}}^{\mathrm{s}}} := f(\mathcal{H}\mathbf{w}) - a(\mathbf{u}, \mathcal{H}\mathbf{w}), \quad \mathbf{w} \in \mathbf{W} \tag{2.13}$$

satisfies (2.12). Here we have used $\mathcal{H}\mathbf{w} := (\mathbf{0}, \mathcal{H}_{\mathrm{s}}\mathbf{w})$, where $\mathcal{H}_{\mathrm{s}}$ is the harmonic extension onto $\mathbf{V}_0^{\mathrm{s}} := \{\mathbf{v} \in \mathbf{V}^{\mathrm{s}} \mid \mathbf{v} = \mathbf{0} \text{ on } \Gamma_{\mathrm{D}}^{\mathrm{s}}\}$ with respect to the bilinear form $a_{\mathrm{s}}(\cdot, \cdot)$.

Proof. For convenience of the reader we recall some of the basic steps and refer to the monographs by Glowinski (1984) and Glowinski *et al.* (1981) for further details. In particular, we comment on the formula (2.13) for the Lagrange multiplier. The equivalence between (2.8) and (2.9) is standard.

Let $(\mathbf{u}, \boldsymbol{\lambda})$ be a solution of (2.12); then for all $\boldsymbol{\mu} \in \mathbf{M}^+$ we have $\boldsymbol{\mu} + \boldsymbol{\lambda} \in \mathbf{M}^+$ and thus $\mathbf{u} \in \mathbf{K}$, and moreover $b(\boldsymbol{\lambda}, \mathbf{u}) = g(\boldsymbol{\lambda})$. For $\mathbf{v} \in \mathbf{K}$ we find $\mathbf{v} - \mathbf{u} \in \mathbf{V}_0$ and thus $a(\mathbf{u}, \mathbf{v} - \mathbf{u}) = f(\mathbf{v} - \mathbf{u}) - b(\boldsymbol{\lambda}, \mathbf{v} - \mathbf{u}) \geq f(\mathbf{v} - \mathbf{u}) + g(\boldsymbol{\lambda}) - g(\boldsymbol{\lambda})$.

Let $\mathbf{u}$ be the solution of (2.8). Then, for all $\mathbf{w} \in \mathbf{W}_n^+$, we have $\mathbf{v} := \mathbf{u} - \mathcal{H}\mathbf{w} \in \mathbf{K}$. Now the definition (2.13) of $\boldsymbol{\lambda}$ yields $\langle \boldsymbol{\lambda}, \mathbf{w} \rangle_{\Gamma_{\mathrm{C}}^{\mathrm{s}}} = a(\mathbf{u}, \mathbf{v} - \mathbf{u}) - f(\mathbf{v} - \mathbf{u}) \geq 0$ for all $\mathbf{w} \in \mathbf{W}_n^+$ and thus $\boldsymbol{\lambda} \in \mathbf{M}^+$. Moreover, observing that $\mathbf{v}_{\pm} := \mathbf{u} \pm \mathcal{H}((g - [u_n])\mathbf{n}^{\mathrm{s}})$ is in $\mathbf{K}$, we get $a(\mathbf{u}, \mathcal{H}((g - [u_n])\mathbf{n}^{\mathrm{s}})) = f(\mathcal{H}((g - [u_n])\mathbf{n}^{\mathrm{s}}))$, from which we conclude that

$$0 = \langle \boldsymbol{\lambda}, (g - [u_n])\mathbf{n}^{\mathrm{s}} \rangle_{\Gamma_{\mathrm{C}}^{\mathrm{s}}} = \langle \lambda_n, g \rangle_{\Gamma_{\mathrm{C}}^{\mathrm{s}}} - b_n(\boldsymbol{\lambda}, \mathbf{u}) = g(\boldsymbol{\lambda}) - b(\boldsymbol{\lambda}, \mathbf{u}).$$

Then the second line of (2.12) holds by the definition of $\mathbf{K}$. To see that (2.13) also satisfies the first line of (2.12), we set $\mathbf{w} := \mathbf{u} \pm (\mathbf{v} - \mathcal{H}[\mathbf{v}]) \in \mathbf{K}$

for $\mathbf{v} \in \mathbf{V}_0$ and use $\mathbf{w}$ as a test function in (2.8), resulting in

$$0 = a(\mathbf{u}, \mathbf{v} - \mathcal{H}[\mathbf{v}]) - f(\mathbf{v} - \mathcal{H}[\mathbf{v}]) = a(\mathbf{u}, \mathbf{v}) - f(\mathbf{v}) + \langle \boldsymbol{\lambda}, [\mathbf{v}] \rangle_{\Gamma_{\mathrm{C}}^{\mathrm{s}}}. \qquad \square$$

Remark 2.2. We note that the saddle-point formulation (2.12) also has a unique solution. The uniqueness of the displacement is already established by Lemma 2.1. For the uniqueness of the surface traction a suitable inf-sup condition has to be satisfied. By definition, $\mathbf{M}$ is the dual space of $\mathbf{W}$, which is the trace space of $\mathbf{V}_0^{\mathrm{s}} := \{\mathbf{v} \in \mathbf{V}^{\mathrm{s}} \mid \mathbf{v} = \mathbf{0} \text{ on } \Gamma_{\mathrm{D}}^{\mathrm{s}}\}$, and the extension theorem yields that

$$\begin{aligned} \inf_{\boldsymbol{\mu} \in \mathbf{M}} \sup_{\mathbf{v} \in \mathbf{V}_0} \frac{b(\boldsymbol{\mu}, \mathbf{v})}{\|\boldsymbol{\mu}\|_{-\frac{1}{2};\Gamma_{\mathrm{C}}^{\mathrm{s}}} \|\mathbf{v}\|_{1;\Omega}} &\geq \inf_{\boldsymbol{\mu} \in \mathbf{M}} \sup_{\mathbf{v} \in \mathbf{V}_0^{\mathrm{s}}} \frac{b(\boldsymbol{\mu}, \mathbf{v})}{\|\boldsymbol{\mu}\|_{-\frac{1}{2};\Gamma_{\mathrm{C}}^{\mathrm{s}}} \|\mathbf{v}\|_{1;\Omega^{\mathrm{s}}}} \\ &\geq C_{\mathrm{inf}} \inf_{\boldsymbol{\mu} \in \mathbf{M}} \sup_{\mathbf{w} \in \mathbf{W}} \frac{\langle \boldsymbol{\mu}, \mathbf{w} \rangle_{\Gamma_{\mathrm{C}}^{\mathrm{s}}}}{\|\boldsymbol{\mu}\|_{-\frac{1}{2};\Gamma_{\mathrm{C}}^{\mathrm{s}}} \|\mathbf{w}\|_{\frac{1}{2};\Gamma_{\mathrm{C}}^{\mathrm{s}}}} = C_{\mathrm{inf}}. \end{aligned}$$

The case of Coulomb friction is more involved; we refer to Eck *et al.* (2005) for existence and regularity results and only mention that, for ν small enough, a unique solution exists. For contact problems in viscoelasticity we refer to Eck and Jarušek (2003) and Han and Sofonea (2002). In particular, the admissible solution space depends on the solution itself and cannot be characterized without knowledge of the contact pressure.

After these preliminary remarks, we can now easily extend our saddle-point formulation (2.12) for $\nu = 0$ to $\nu \geq 0$. We observe that $\mathbf{M}^+$ defined by (2.10a) can also be written as

$$\mathbf{M}^+ = \{\boldsymbol{\mu} \in \mathbf{M} \mid \mu_n \in M^+, \boldsymbol{\mu}_t = \mathbf{0}\},$$

with $M^+ := \{\mu \in M \mid \langle \mu, w \rangle_{\Gamma_{\mathrm{C}}^{\mathrm{s}}} \geq 0, w \in W^+\}$. For $\nu > 0$ the tangential part of the surface traction, in general, does not vanish, and thus one has to work with a vectorial Lagrange multiplier, which is not necessary for a frictionless contact problem. Replacing the convex cone $\mathbf{M}^+$ in (2.12) by

$$\mathbf{M}(\lambda_n) := \{\boldsymbol{\mu} \in \mathbf{M} \mid \langle \boldsymbol{\mu}, \mathbf{v} \rangle_{\Gamma_{\mathrm{C}}^{\mathrm{s}}} \leq \langle \nu \lambda_n, \|\mathbf{v}_t\| \rangle_{\Gamma_{\mathrm{C}}^{\mathrm{s}}}, \mathbf{v} \in \mathbf{W} \text{ with } -v_n \in W^+\}, \tag{2.14}$$

we obtain the weak saddle-point formulation of a static Coulomb problem between two linearly elastic bodies as follows. Find $(\mathbf{u}, \boldsymbol{\lambda}) \in \mathbf{V}_{\mathrm{D}} \times \mathbf{M}(\lambda_n)$ such that

$$\begin{aligned} a(\mathbf{u}, \mathbf{v}) + b(\boldsymbol{\lambda}, \mathbf{v}) &= f(\mathbf{v}), & \mathbf{v} &\in \mathbf{V}_0, \\ b(\boldsymbol{\mu} - \boldsymbol{\lambda}, \mathbf{u}) &\leq g(\boldsymbol{\mu} - \boldsymbol{\lambda}), & \boldsymbol{\mu} &\in \mathbf{M}(\lambda_n). \end{aligned} \tag{2.15}$$

In the case of the quasi-static version, one has to replace $b(\boldsymbol{\mu} - \boldsymbol{\lambda}, \mathbf{u})$ in the second line of (2.15) by $b_n(\boldsymbol{\mu} - \boldsymbol{\lambda}, \mathbf{u}) + b_t(\boldsymbol{\mu} - \boldsymbol{\lambda}, \dot{\mathbf{u}})$. Comparing (2.12) and (2.15), we find that the only, but essential, difference is the solution cone for the Lagrange multiplier $\boldsymbol{\lambda}$. The key idea for the proof of existence is to

define a series of solutions $(\mathbf{u}^k, \boldsymbol{\lambda}^k) \in \mathbf{V}_{\mathrm{D}} \times \mathbf{M}(\lambda_n^{k-1})$ and apply Tikhonov's fixed-point theorem: see, *e.g.*, Eck *et al.* (2005).

In the following we will frequently make use of the Karush–Kuhn–Tucker (KKT) conditions.

Lemma 2.3. Let $(\mathbf{u}, \boldsymbol{\lambda}) \in \mathbf{V}_{\mathrm{D}} \times \mathbf{M}(\lambda_n)$ be the solution of (2.15); then the non-penetration KKT condition

$$\lambda_n \in M^+, \quad g - [u_n] \in W^+, \quad b_n(\boldsymbol{\lambda}, \mathbf{u}) = \langle \lambda_n, g \rangle_{\Gamma_{\mathrm{C}}^{\mathrm{s}}} \tag{2.16}$$

holds. Moreover, under suitable regularity, the Coulomb law in its weak form

$$\boldsymbol{\lambda} \in \mathbf{M}(\lambda_n), \quad b_t(\boldsymbol{\lambda}, \mathbf{u}) = \langle \nu\lambda_n, \|[\mathbf{u}_t]\| \rangle_{\Gamma_{\mathrm{C}}^{\mathrm{s}}} \tag{2.17}$$

is satisfied.

Proof. We observe that the constraint on λ_n in (2.16) follows directly from the definition of $\mathbf{M}(\lambda_n)$. Using the additive splitting (2.11) and setting as test function $\boldsymbol{\mu} := \boldsymbol{\lambda} \pm \lambda_n \mathbf{n}^{\mathrm{s}}$ in (2.15), we get the equality in (2.16). Observing that W^+, defined in (2.10b), can also be characterized by $W^+ = \{w \in W \mid \langle \mu, w \rangle_{\Gamma_{\mathrm{C}}^{\mathrm{s}}} \geq 0, \mu \in M^+\}$, it trivially holds that $g - [u_n] \in W^+$. For (2.17) we assume that there exists a $\boldsymbol{\chi}$ such that $\|\boldsymbol{\chi}\| \leq 1$, $\boldsymbol{\chi}[\mathbf{u}_t] = \|[\mathbf{u}_t]\|$, and we have $\boldsymbol{\chi}\mathbf{v} \in W$ for $\mathbf{v} \in \mathbf{W}$. Then, we get $\boldsymbol{\mu} := \lambda_n \mathbf{n}^{\mathrm{s}} + \nu\lambda_n \boldsymbol{\chi} \in \mathbf{M}(\lambda_n)$ and $b(\boldsymbol{\mu} - \boldsymbol{\lambda}, \mathbf{u}) = b(\nu\lambda_n\boldsymbol{\chi}, \mathbf{u}) - b(\boldsymbol{\lambda}_t, \mathbf{u}) = \langle \nu\lambda_n, \|[\mathbf{u}_t]\| \rangle_{\Gamma_{\mathrm{C}}^{\mathrm{s}}} - b_t(\boldsymbol{\lambda}, \mathbf{u}) \leq 0$, from which the equality in (2.17) follows from the definition (2.14). □

Remark 2.4. The special case of a contact problem between one elastic body and a rigid obstacle can be obtained from the two-body situation. A rigid body can be regarded as an infinitively stiff elastic body, and thus the limit case $\lambda^{\mathrm{m}}, \mu^{\mathrm{m}} \to \infty$ results in a one-body case where formally $\mathbf{u}^{\mathrm{m}} = \mathbf{0}$.

To conclude this section, we briefly comment on numerical stability issues in elasticity and on the extension to the case of a solution-dependent friction coefficient.

2.3. Nearly incompressible materials

In the nearly incompressible case, the Poisson ratio tends to 0.5 and thus the ratio between λ and μ tends to infinity. The definition of the bilinear form $a(\cdot, \cdot)$ in terms of the linearized stress (2.2) shows that the continuity constant depends on $\max(\lambda, \mu)$, while the coercivity constant depends on μ. As a consequence, *a priori* estimates for standard low-order finite elements involve large constants, and volumetric locking can be observed numerically. To handle such a case appropriately, special discretization techniques are required. Methods associated with the enrichment or enhancement of the strain or stress field by the addition of carefully chosen basis functions have proved to be highly effective and popular. The key work dealing with

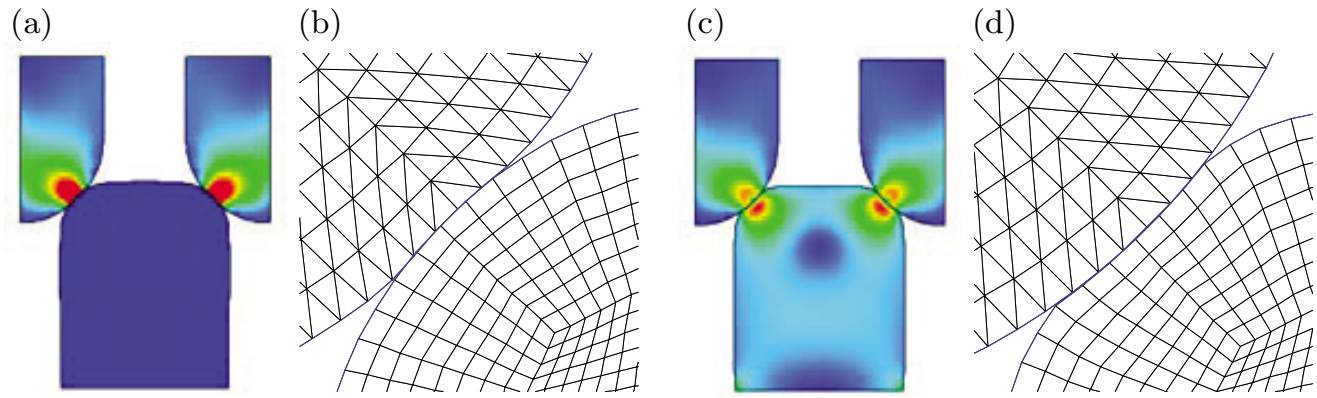

Figure 2.4. Von Mises stress and deformed mesh of a contact between a soft nearly incompressible material (lower body) and two hard compressible ones (upper bodies): standard low-order (a,b) and Hu–Washizu-based (c,d) discretization.

enhanced assumed strain formulations is Simo and Rifai (1990). Figure 2.4 shows the setting of a contact problem between a nearly incompressible soft rubber-like material and a compressible hard one. In Figure 2.4(a,b) standard conforming low-order finite elements are applied, whereas in (c,d) special low-order Hu–Washizu-based elements are used. Here the starting point is the Hu–Washizu formulation (Hu 1955, Washizu 1955), in which the unknown variables are displacement, strain, and stress. This formulation (see also Felippa (2000) for some historical comments) can serve as the point of departure for the development of enhanced strain formulations; see also, *e.g.*, Braess, Carstensen and Reddy (2004), Kasper and Taylor (2000*a*, 2000*b*), Simo and Armero (1992), Simo, Armero and Taylor (1993) and Simo and Rifai (1990).

For both discretization schemes the numerically obtained von Mises stress and a zoom of the deformed meshes are depicted in Figure 2.4. As can be clearly observed in the case of the standard scheme, volumetric locking occurs, resulting in a very stiff response of the soft material; only a modified scheme can provide a good approximation. In the numerical experiment, we use a pure displacement-based formulation obtained from local static condensation of a three-field formulation: see Lamichhane, Reddy and Wohlmuth (2006) for details.

To get a better feeling for the influence of Poisson's ratio on the quality of the discretization, we consider the classical Hertz contact problem between a circle and a half-plane, which is approximated by a rectangle. In that situation the maximum of the contact pressure as well as the contact radius can be computed analytically in terms of the material parameters (Johnson 1985)

$$p_{\max} = \frac{2f}{\pi r_{\text{cont}}}, \quad r_{\text{cont}} = 2\sqrt{\frac{fr(1-\nu^2_{\text{Poisson}})}{E\pi}},$$

Table 2.1. Comparison of standard scheme (Q1) with a displacement-based Hu–Washizu method (HW) for different values of the Poisson ratio.

Poisson ratio ν_{Poisson}	Contact pressure: $p_{\max}$			Contact radius: r_{cont}		
	Q1	HW	'Exact'	Q1	HW	'Exact'
0.1	16.7840	16.7708	17.1564	0.3437	0.3750	0.3709
0.45	19.0973	19.0460	18.9238	0.3125	0.3125	0.3363
0.49	19.9255	19.5690	19.3374	0.2812	0.3125	0.3291
0.499	21.5690	19.7007	19.4394	0.2500	0.3125	0.3274
0.4999	31.0458	19.7144	19.4497	0.1875	0.3125	0.3272
0.49999	52.2592	19.7158	19.4508	0.1250	0.3125	0.3272
0.499999	58.4622	19.7159	19.4509	0.0938	0.3125	0.3272

where r is the radius of the circle, f the applied point load, ν_{Poisson} the Poisson number and E Young's modulus.

A quantitative comparison of the two discretization schemes is given in Table 2.1. In the compressible range, both schemes provide quite good and accurate numerical approximations even for coarse meshes. However, the situation is drastically changed if Poisson's ratio tends to 0.5. From 0.49 on, from row to row, λ is increased by a factor of 10. In the case of standard conforming low-order elements, the contact radius tends to zero, and thus the maximal contact pressure tends to infinity. In contrast, the analytical solution as well as the Hu–Washizu-based formulation yield convergence to a non-zero contact radius, and the maximum of the contact pressure remains finite. The limit of the standard scheme is an unphysical point contact, with the surface traction being a delta distribution.

From now on, we assume that we are in the compressible range and that we do not have to face numerical problems due to the material parameters.

2.4. Thermo-mechanical contact problem

Coupled contact problems where the coefficient of friction depends on the solution itself are quite difficult to analyse. Although non-trivial from the theoretical point of view, these generalized settings do fit perfectly well into the computational framework. Figure 2.5 shows the temperature distribution of a sliding body undergoing thermo-mechanical contact. The discretization in space is based on non-matching meshes and no re-meshing has to be done. For the time integration we apply a simple mid-point rule in combination with standard mass lumping techniques; see Hüeber and Wohlmuth (2009) for details and further numerical results for this example.

In addition to the displacement, the temperature T is a primal variable, and a bi-directionally coupled thermo-mechanical system has to be con-

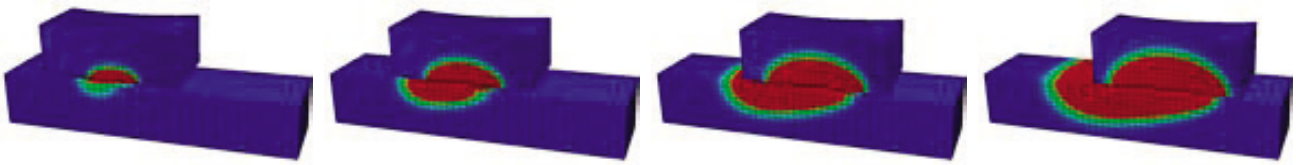

Figure 2.5. Temperature distribution at time $t^{k-1/2}$ for $k = 14, 26, 38, 50$.

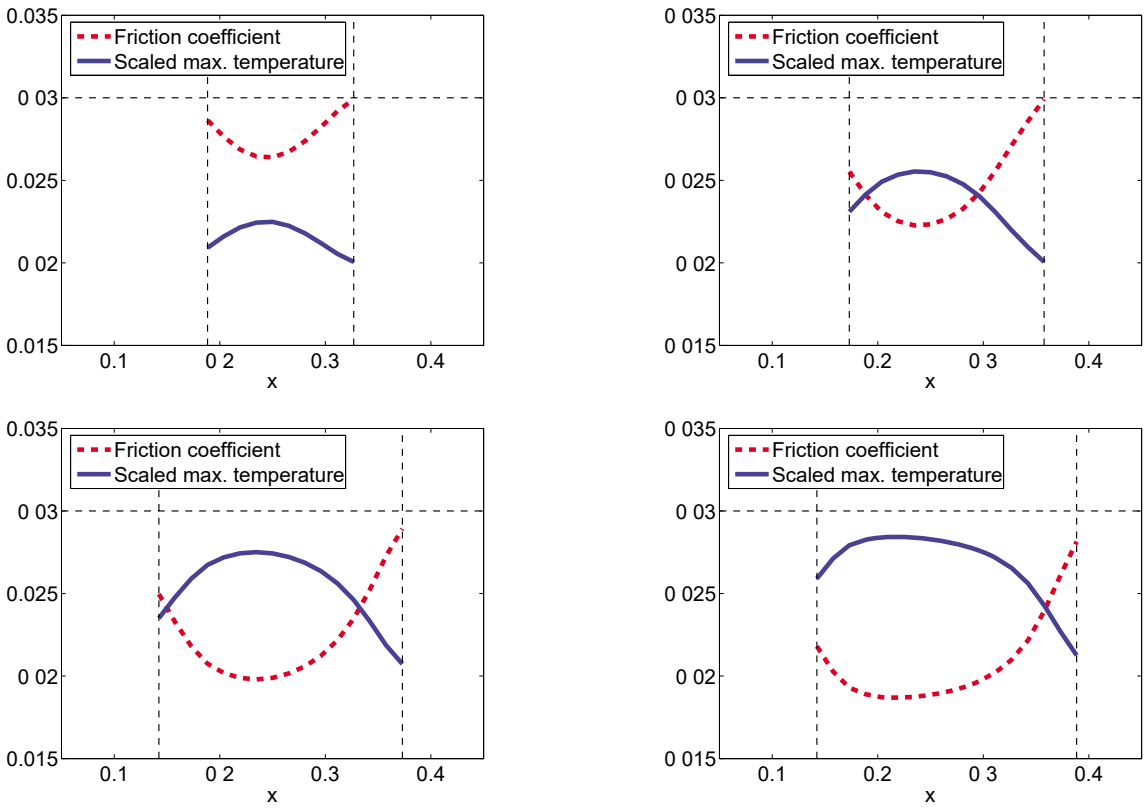

Figure 2.6. Friction coefficient and temperature at the contact nodes on the cutting line $y = 0$ for $k = 14, 26, 38, 50$.

sidered. More precisely, the relative temperature enters in terms of the thermal expansion coefficient in the definition of the mechanical stress. In addition, we have to consider the first and second law of thermodynamics. The heating from the Joule effect adds the source term $\operatorname{div} \dot{\mathbf{u}}$ to the heat equation, and thus a fully coupled system is obtained: see, *e.g.*, Fluegge (1972) and Willner (2003). From the theoretical point of view, thermo-mechanical contact problems have been analysed in Eck (2002) and Eck and Jarušek (2001)

Moreover a friction coefficient $\nu(T) \geq 0$, which is monotone decreasing in T, modelling a thermal softening effect, has been applied. It tends to zero in the critical case that the temperature tends to the damage temperature: see, *e.g.*, Laursen (2002).

Figure 2.6 shows the evolution of the temperature-dependent friction coefficient and the temperature at the nodes in contact for different time steps. The dashed horizontal line marks the static coefficient of friction, and the two vertical lines indicate the actual contact zone. Due to the heating of the two bodies, the temperature increases over time and thus $\nu(T)$ decreases.

3. Variationally consistent space discretization

In the past, penalty methods and simple node-to-node coupling concepts have been widely used and are quite often integrated in commercial software codes. The starting point of penalty techniques is the observation that contact without friction can easily be formulated as a minimization problem on a constrained space. This approach is closely related to (2.9) when replacing the proper convex and lower semi-continuous indicator functional by a regularized one with finite values. Working on the larger unconstrained space, but incorporating the restriction as an additional finite energy contribution, a non-linear variational system of equations is obtained. Although relatively easy to implement, oscillations possibly occur, and the numerical results are very sensitive to the choice of the penalty parameter. A too-small penalty parameter gives considerable penetration and a poor approximation of the contact forces. A too-large penalty parameter yields a badly conditioned system which has to be solved by a suitable non-linear scheme. Figure 3.1 illustrates the influence of the penalty parameter on the deformed geometry.

For a small penalty parameter (see Figure 3.1(a)), significant penetration of the rigid obstacle into the elastic material occurs, and the von Mises stress is highly underestimated. In Figure 3.1(b), a very large penalty parameter is applied which gives numerical results of high quality. However, the number of multigrid steps then required to solve the system is quite high compared to the case of a small penalty parameter.

Figure 3.2 illustrates the difference between a penalty and a Lagrange multiplier-based approach. Figures 3.2(a) and 3.2(d) show, respectively, the influence of the penalty parameter ϵ on the penetration and the contact stress. As can be seen, for small penalty parameters there is significant penetration and the approximation of the contact stress is rather poor. In the limit $\epsilon \to 0$, the solution tends to the unconstrained one and the

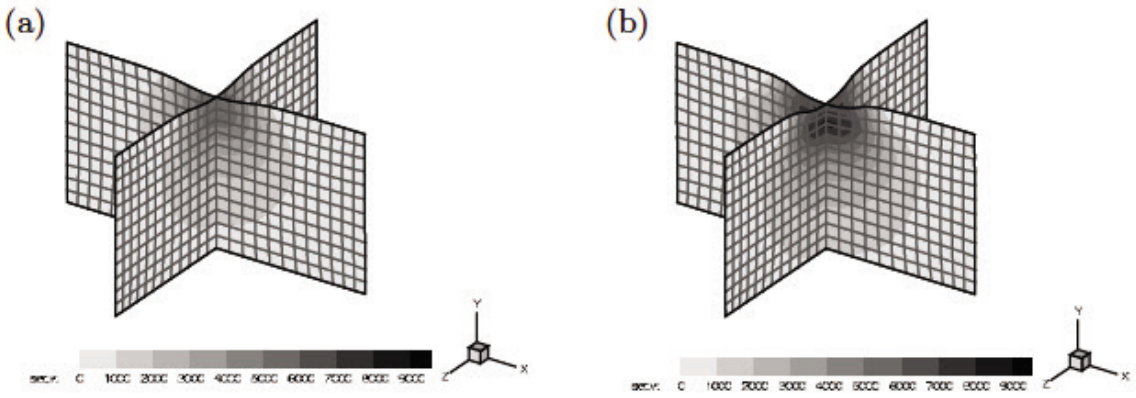

Figure 3.1. Comparison of the deformed geometry and the von Mises stress for a three-dimensional one-sided contact problem: small penalty parameter (a) and large penalty parameter (b).

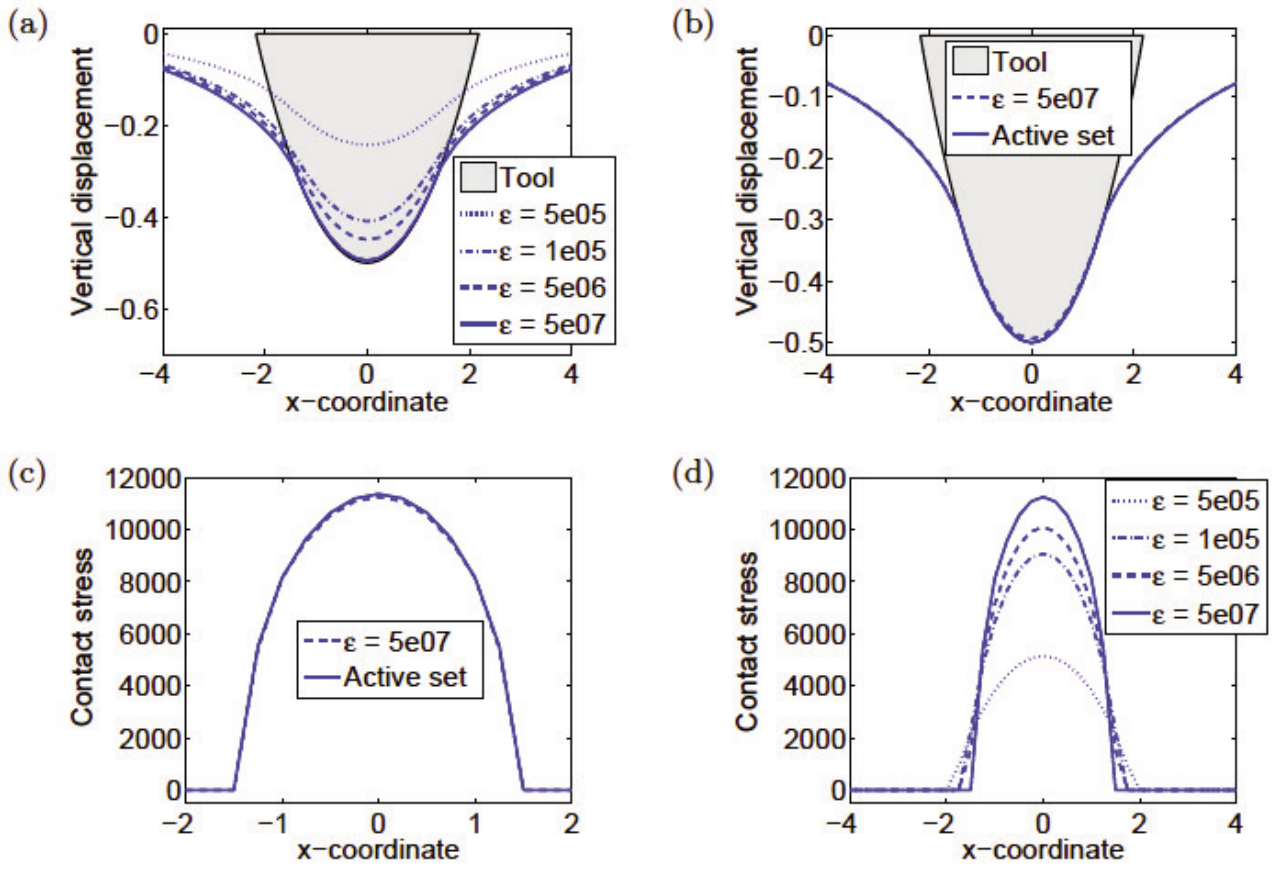

Figure 3.2. Penalty versus Lagrange multiplier approach.

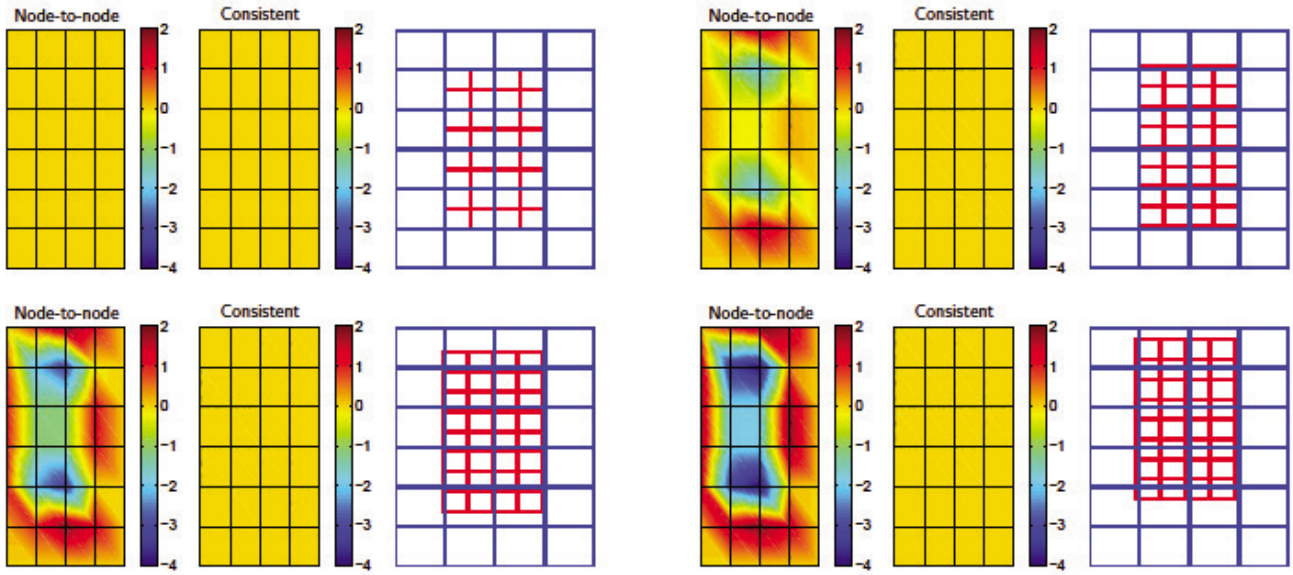

Figure 3.3. Node-to-node interpolation versus variationally consistent coupling.

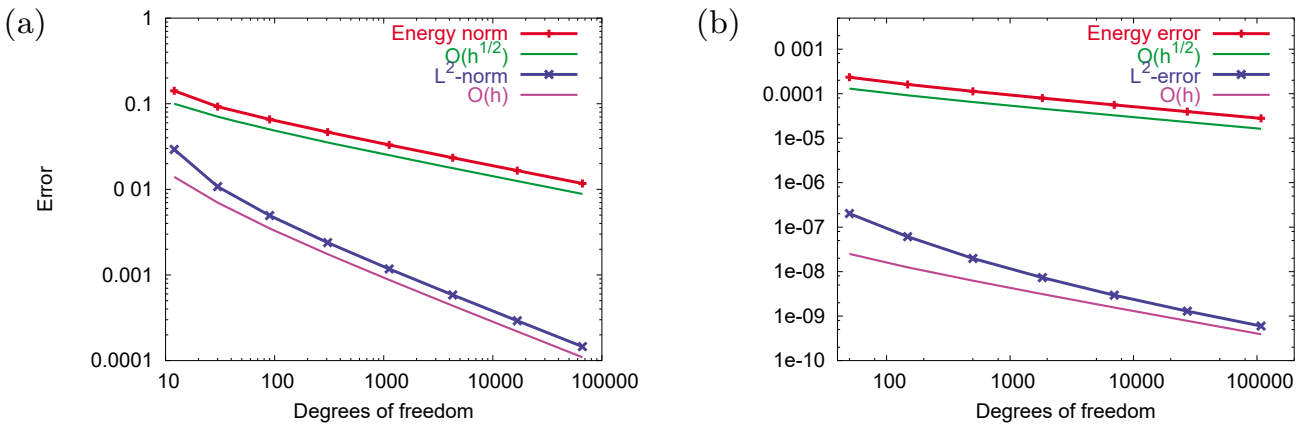

Figure 3.4. Non-optimal error decay for a node-to node coupling: scalar case (a) and linear elasticity (b).

contact stress vanishes. In the limit $\epsilon \to \infty$, the correct constrained solution is recovered but then the condition number of the system tends to be extremely large. Figures 3.2(b) and 3.2(c) compare the numerical results of a penalty approach with a large value for ϵ with a weakly consistent Lagrange multiplier-based formulation. Both results show the same good quality of approximation, but the latter approach has a much better condition number and thus is more suitable for fast iterative solvers such as multigrid or domain decomposition methods.

Nowadays penalty techniques and simple node-to-node coupling strategies are increasingly replaced by variationally consistent methods which pass suitable patch tests in the case of non-matching meshes. The admissibility of the discrete solution is then formulated in a weak variational framework. Displacement and surface traction form a primal–dual pair of unknown variables and have to be discretized.

Figure 3.3 illustrates the difference between a simple node-to-node coupling strategy and a variationally consistent approach. A constant force can only be mapped correctly from the slave to the master side if a weak coupling is applied. The simple node-to-node coupling yields poor numerical results if non-matching meshes are used, whereas a sliding of the mesh does not influence the approximation quality in the case of a variationally consistent scheme.

Figure 3.4 shows the quantitative error decay for a node-to-node coupling in the case of non-matching meshes. As a patch test, we select a linear solution which can be represented exactly by standard low-order finite elements. In Figure 3.4(a), the scalar-valued Laplace operator is considered, whereas in Figure 3.4(b) the results for the vector-valued system of linear elasticity are presented; see Dohrmann, Key and Heinstein (2000) for the parameter specifications. In both cases, the exact solution cannot be reproduced, and the error decay is sub-optimal. A first-order error decay can be only observed for the L^2-norm but not for the H^1-norm. However, in the

case of a variationally consistent weak formulation, the exact solution can be recovered and the error is equal to zero on all meshes. From the theoretical point of view, a node-to-node coupling is associated with a discrete Lagrange multiplier being represented by a linear combination of delta distributions, which is not compatible with the required $H^{1/2}$-duality pairing. In the following, we restrict ourselves to discrete Lagrange multiplier spaces being L^2-conforming.

To obtain a stable and well-posed discrete setting, a uniform inf-sup condition has to be satisfied. Roughly speaking this means that the trace space of the discrete displacement has to be well balanced with the finite-dimensional space for the surface traction, also called the Lagrange multiplier. A necessary condition is that the dimension of the Lagrange multiplier space is less than or equal to the dimension of the jump of the trace spaces. There exists a large variety of different construction principles, all leading to optimal *a priori* estimates in the case of standard variational equalities. Quite often such a condition is numerically verified by the Bathe–Chapelle inf-sup test (Chapelle and Bathe 1993). A mathematically rigorous analysis can be performed within the abstract framework of mortar settings on non-matching meshes; see, *e.g.*, Ben Belgacem and Maday (1997) and Bernardi, Maday and Patera (1993, 1994). Early theoretical results on uniform stable discretization schemes for contact problems without friction can be found in Ben Belgacem (2000) and Ben Belgacem, Hild and Laborde (1997, 1999). When a vector-valued Lagrange multiplier is used, there is no algebraic difference between a contact problem with Coulomb friction and one without. Thus, quite often solvers and error estimators designed for contact problems without friction naturally apply to contact problems with Coulomb friction. However, we recall that from the theoretical point of view there is a possibly considerable difference, as for existence and uniqueness results; see, *e.g.*, Eck *et al.* (2005) and Kikuchi and Oden (1988).

In this section, we illustrate the fact that a weakly consistent discretization based on a biorthogonal set of displacement traces and surface tractions is well suited to the numerical simulation of contact problems. While simple node-to-node coupling strategies are known to show locking effects as well as unphysical oscillations when applied to non-matching meshes, variationally consistent formulations based on uniform inf-sup stable pairings do not exhibit this behaviour. Moreover, the biorthogonality of the basis functions of such a pairing yields a stable node-to-segment coupling concept where the simple interpolation is replaced by a quasi-projection. This is quite attractive because of the locality of the coupling constraints.

The discretization of the system is based on the saddle-point formulation (2.15). Both cases, the frictionless case and that with Coulomb friction, can be handled within the same abstract framework. In the case $\nu = 0$, we do not work with the primal variational inequality (2.8) but also use

the primal–dual variational inequality setting. A low-order pair of primal–dual variables for the displacement $\mathbf{u}$ and the surface traction $\boldsymbol{\lambda}$ on the contact zone will be applied. As usual in the mortar context, the Lagrange multiplier space is associated with the $(d-1)$-dimensional surface mesh on $\Gamma_{\mathrm{C}}^{\mathrm{s}}$ inherited from the volume mesh on the slave side. In addition, the degrees of freedom from the master side will not be required for the inf-sup condition to hold. Thus the inf-sup constant is independent of the ratio between the mesh sizes of the master and slave sides and also independent of the non-matching character of the meshes, which is quite attractive in dynamic situations when sliding geometries occur.

In the linear saddle-point theory, it is well established (Brezzi and Fortin 1991, Nicolaides 1982) that *a priori* estimates in terms of the best approximation error of the primal and dual variables can be obtained if stability and continuity of the relevant bilinear forms are given. The norm for the displacement is the product H^1-norm, and for the surface traction, the $H^{-1/2}$-norm defined as the dual norm of the $H^{1/2}$-norm on $\Gamma_{\mathrm{C}}^{\mathrm{s}}$. Thus, to obtain first-order estimates for the best approximation error, the natural choice for the displacement is the lowest-order conforming finite element space on each of the two subdomains, whereas for the Lagrange multiplier several interesting choices exist. Basically all existing possibilities from the mortar literature can be used, *e.g.*, piecewise constants associated with the dual mesh or low-order conforming finite elements.

3.1. A pairing, not uniformly stable

Before going into the details of the discretization, we consider a counter-example. We note that element-wise constants for the Lagrange multiplier do not yield optimal estimates. Although the best approximation error of element-wise constants with respect to the L^2-norm is of order one, this combination of primal and dual variables is not uniformly inf-sup stable. A mesh-dependent inf-sup constant results in a reduced convergence rate. Figure 3.5 illustrates this non-uniformly stable pairing in a one-dimensional setting.

Let the unit interval $I := (0,1)$ be decomposed into $N_l := 2^l$, $l \in \mathbb{N}$, sub-intervals $I_i := (i-1, i)/N_l$, $i = 1, \ldots, N_l$, of equal length and

$$W_l := \{v \in C(I); v|_{I_i} \in P_1(I_i), i = 1, \ldots, N_l\},$$
$$M_l := \{v \in L^2(I); v|_{I_i} \in P_0(I_i), i = 1, \ldots, N_l\}.$$

Then each $\mu_l \in M_l$ can be written as $\mu_l = \sum_{i=1}^{N_l} \alpha_i \psi_i$, with $\alpha_i \in \mathbb{R}$, and where ψ_i stands for the characteristic function of the sub-interval I_i. Each $v_l \in W_l$ has the form $v_l = \sum_{i=0}^{N_l} b_i \phi_i$, with $b_i \in \mathbb{R}$, and where ϕ_i denotes the standard hat function associated with the node $x_i := i/N_l$, $i = 0, \ldots, N_l$.

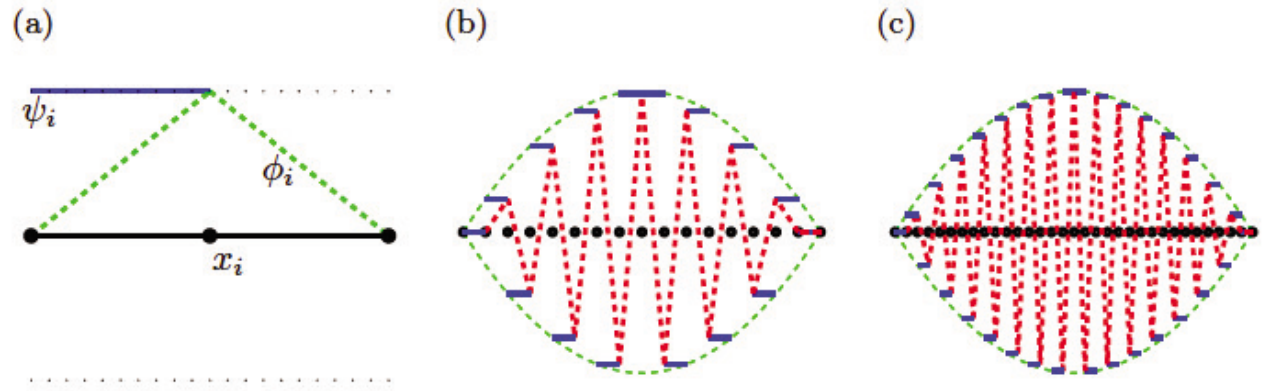

Figure 3.5. Nodal finite element ϕ_i and Lagrange multiplier basis function ψ_i (a), special choice of μ_l and v_l for $l = 4$ and $l = 5$ (b,c).

Lemma 3.1. The pairing (W_l, M_l) is not uniformly inf-sup stable with respect to the $H^{\frac{1}{2}}$-duality. Moreover there exists a $c_{\text{inf}} > 0$ independent of the number of sub-intervals N_l such that

$$\inf_{\mu_l \in M_l} \sup_{v_l \in W_l} \frac{\int_0^1 \mu_l v_l \, \mathrm{d}s}{\|\mu_l\|_{-\frac{1}{2};I} \, \|v_l\|_{\frac{1}{2};I}} \geq \frac{c_{\text{inf}}}{N_l}, \tag{3.1}$$

and the estimate in (3.1) is sharp.

Proof. To see that the non-uniform inf-sup condition given by (3.1) holds, it is sufficient to define a Fortin operator $F_l : H^{\frac{1}{2}}(I) \to W_l$ such that $\int_I \mu_l F_l v \, \mathrm{d}s = \int_I \mu_l v \, \mathrm{d}s$ for all $\mu_l \in M_l$ and $\|F_l v\|_{\frac{1}{2};I} \leq c N_l \|v\|_{\frac{1}{2};I}$ for all $v \in H^{\frac{1}{2}}(I)$: see, *e.g.*, Brezzi and Fortin (1991). Let $v \in H^{1/2}(I)$ be given. In a first step, we set $w_1 := \sum_{i=0}^{N_l} \gamma_i \phi_i$ with

$$\gamma_i := \frac{2 \int_{I_i \cup I_{i+1}} v(2\phi_i - \phi_{i-1} - \phi_{i+1}) \, \mathrm{d}s}{|I_i \cup I_{i+1}|}, \quad i = 0, \ldots N_l, I_0 := I_{N_l+1} := \emptyset.$$

In a second step, we define recursively $\Delta\gamma_i := 2N_l \int_{I_i} (v - w_1) \, \mathrm{d}s - \Delta\gamma_{i-1}$, $i = 1, \ldots, N_l$ and $\Delta\gamma_0 := 0$, $w_2 := \sum_{i=0}^{N_l} \Delta\gamma_i \phi_i$. We note from the definition of w_1 that it is $H^{\frac{1}{2}}$-stable and has L^2-approximation properties. In terms of w_1 and w_2, we set $F_l v := w_1 + w_2$. Then by construction, $F_l v$ and v have the same mean value on each sub-interval I_i, $i = 1, \ldots, N_l$. Introducing the matrix $B_l \in \mathbb{R}^{N_l \times N_l}$ as follows, we get for its inverse

$$B_l := \begin{pmatrix} 1 & & & & & \\ 1 & 1 & & & & \\ & 1 & 1 & & & \\ & & 1 & 1 & & \\ & & & 1 & 1 & \\ & & & & \ddots & \ddots \end{pmatrix}, \quad B_l^{-1} = \begin{pmatrix} 1 & & & & & \\ -1 & 1 & & & & \\ 1 & -1 & 1 & & & \\ -1 & 1 & -1 & 1 & & \\ 1 & -1 & 1 & -1 & 1 & \\ & & & & \ddots & \ddots \end{pmatrix}.$$

Moreover, a standard inverse estimate for finite elements and the fact that the Euclidean norm of B_l^{-1} is bounded in terms of N_l, *i.e.*, $\|B_l^{-1}\| \le CN_l$, gives

$$\begin{aligned}\|F_l v\|_{\frac{1}{2};I} &\le \|w_1\|_{\frac{1}{2};I} + \|w_2\|_{\frac{1}{2};I} \le C(\|v\|_{\frac{1}{2};I} + \sqrt{N_l}\|w_2\|_{0;I}) \\ &\le C(\|v\|_{\frac{1}{2};I} + \sqrt{N_l}\|B_l^{-1}\|\|\Pi_l(v-w_1)\|_{0;I}) \\ &\le C(\|v\|_{\frac{1}{2};I} + \sqrt{N_l}N_l\|v-w_1\|_{0;I}) \le CN_l\|v\|_{\frac{1}{2};I},\end{aligned}$$

where Π_l stands for the L^2-projection onto M_l.

To show that the estimate (3.1) is sharp, we have to specify a $\mu_l \in M_l$ such that no better bound can be obtained. Let us consider the choice $\alpha_i := (-1)^i(i-1)(N_l-i)$: see Figure 3.5(b,c). The definition of the dual norm (2.1) yields $\|\mu_l\|_{-\frac{1}{2};I} \ge c\sum_{i=1}^{N_l}|\alpha_i|/(N_l\sqrt{N_l}) \ge cN_l\sqrt{N_l}$. Then, for $l \ge 2$ a straightforward computation and a standard inverse estimate shows

$$\begin{aligned}\int_I \mu_l v_l \,\mathrm{d}s &= \sum_{i=1}^{N_l}(-1)^i(i-1)(N_l-i)(b_{i-1}+b_i)/(2N_l) \\ &= \sum_{i=1}^{N_l-1}(-1)^i(2i-N_l)b_i/(2N_l) \\ &= \frac{1}{2N_l}\sum_{i=1}^{N_l/4}(N_l+1-4i)\big((b_{2i-1}-b_{2i})+(b_{N_l-2i}-b_{N_l+1-2i})\big) \\ &\quad + \frac{1}{2N_l}\sum_{i=1}^{N_l/2-1}(b_i - b_{N_l/2+i}) \\ &\le C(|v_l|_{1;I} + \|v_l\|_{0;I}) \le C\sqrt{N_l}\|v_l\|_{\frac{1}{2};I} \le \frac{C}{N_l}\|v_l\|_{\frac{1}{2};I}\|\mu_l\|_{-\frac{1}{2};I}. \quad \square\end{aligned}$$

Remark 3.2. A possible remedy would be to use a coarser mesh for the Lagrange multiplier space. The pairing (W_l, M_{l-1}) is uniformly inf-sup stable. Alternatively, the space W_l can be enriched by locally supported bubble functions, as is done in Brezzi and Marini (2001) and Hauret and Le Tallec (2007). Here we do not follow these possibilities, but use only Lagrange multiplier spaces being defined on the same mesh as the trace space of the slave side and having the same nodal degrees of freedom.

3.2. Stable low-order discretization

On each subdomain Ω^k, $k \in \{\mathrm{m},\mathrm{s}\}$, independent families of shape-regular triangulations $\mathcal{T}_l^k$, $l \in \mathbb{N}_0$, will be used, and we set $\mathcal{T}_l := \mathcal{T}_l^{\mathrm{m}} \cup \mathcal{T}_l^{\mathrm{s}}$ and $\overline{\Omega}_l^k := \cup_{T\in\mathcal{T}_l^k}\overline{T}$. The maximum element diameter of the triangulation $\mathcal{T}_l$ is

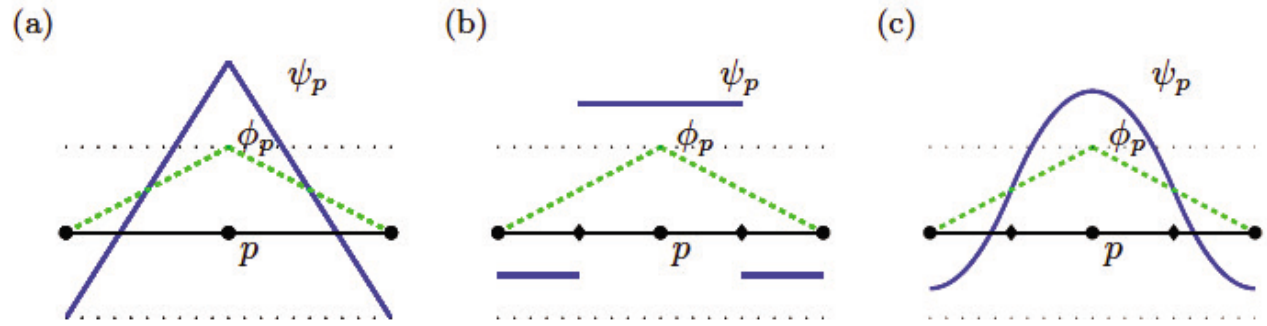

Figure 3.6. Discontinuous biorthogonal basis functions satisfying (3.2)–(3.5).

denoted by h_l. The restriction of $\mathcal{T}_l^k$ to $\Gamma_{\mathrm{C};l}^k := \cup_{F\in\mathcal{F}_l^k}\overline{F}$, where $\mathcal{F}_l^k$ stands for the set of all contact faces on the side k, defines a $(d-1)$-dimensional surface mesh. Moreover, the surface mesh on $\Gamma_{\mathrm{C};l}^{\mathrm{m}}$ will be mapped by χ_l^{-1} onto $\Gamma_{\mathrm{C};l}^{\mathrm{s}}$, resulting in possibly non-matching meshes on the contact zone.

For the displacement, we use standard low-order conforming finite elements and for the surface traction dual finite elements which reproduce constants

$$\begin{aligned} \mathbf{V}_l &:= \mathbf{V}_l^{\mathrm{m}} \times \mathbf{V}_l^{\mathrm{s}}, \quad & \mathbf{V}_l^k &:= (V_l^k)^d, \quad & V_l^k &:= \operatorname{span}_{p\in\mathcal{P}_l^k}\{\phi_p\}, \\ \mathbf{M}_l &:= \mathbf{M}_l^{\mathrm{s}}, & \mathbf{M}_l^k &:= (M_l^k)^d, & M_l^k &:= \operatorname{span}_{p\in\mathcal{P}_{\mathrm{C};l}^k}\{\psi_p\}, \end{aligned}$$

where $\mathcal{P}_l^k$ stands for all vertices of $\mathcal{T}_l^k$ not being on $\overline{\Gamma}_{\mathrm{D}}^k$, and $\mathcal{P}_{\mathrm{C};l}^k$ is the set of all vertices on $\overline{\Gamma}_{\mathrm{C}}^k$, $k \in \{\mathrm{m},\mathrm{s}\}$. Moreover ϕ_p denotes the standard conforming nodal basis function associated with the vertex p. The basis functions $\psi_p \in M_l^k$ are required to have the following properties.

- Locality of the support:

$$\operatorname{supp}\psi_p = \operatorname{supp}\phi_p|_{\Gamma_{\mathrm{C};l}^k}, \quad p \in \mathcal{P}_{\mathrm{C};l}^k, \tag{3.2}$$

- Local biorthogonality relation:

$$\int_F \psi_p\phi_q \,\mathrm{d}s = \delta_{pq}\int_F \phi_q \,\mathrm{d}s \geq 0, \quad p,q \in \mathcal{P}_{\mathrm{C};l}^k, F \in \mathcal{F}_l^k, \tag{3.3}$$

- Best approximation property:

$$\inf_{\mu_l\in M_l^k} \|\mu-\mu_l\|_{-\frac{1}{2};\Gamma_{\mathrm{C};l}^k} \leq C_{\mathrm{best}} h_l |\mu|_{\frac{1}{2};\Gamma_{\mathrm{C};l}^k}, \quad \mu \in H^{\frac{1}{2}}(\Gamma_{\mathrm{C};l}^k), \tag{3.4}$$

  where $C_{\mathrm{best}} < \infty$ does not depend on the mesh size.

- Uniform inf-sup condition:

$$\sup_{v_l\in W_l^k} \frac{\int_{\Gamma_{\mathrm{C};l}^k} \mu_l v_l \,\mathrm{d}s}{\|v_l\|_{\frac{1}{2};\Gamma_{\mathrm{C};l}^k}} \geq c_{\mathrm{inf}} \|\mu_l\|_{-\frac{1}{2};\Gamma_{\mathrm{C};l}^k}, \quad \mu_l \in M_l^k, \tag{3.5}$$

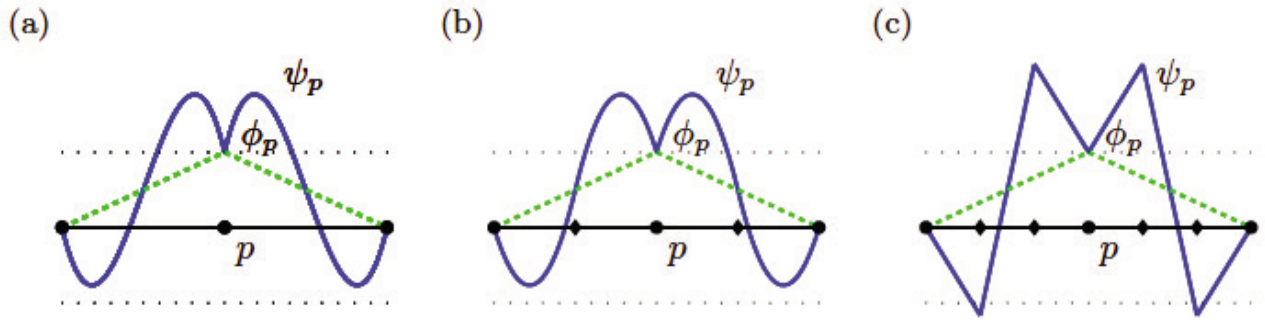

Figure 3.7. Continuous biorthogonal basis functions satisfying (3.2)–(3.5).

where $c_{\text{inf}} > 0$ does not depend on the mesh size and the discrete trace space W_l^k is given by $W_l^k := \text{span}_{p \in \mathcal{P}_{\text{C};l}^k} \{\phi_p|_{\Gamma_{\text{C};l}^k}\}$.

From the local relation (3.3) follows directly a global one, *i.e.*,

$$\int_{\Gamma_{\text{C};l}^k} \psi_p \phi_q \, \mathrm{d}s = \delta_{pq} m_p := \delta_{pq} \int_{\Gamma_{\text{C};l}^k} \phi_q \, \mathrm{d}s \geq 0, \quad p, q \in \mathcal{P}_{\text{C};l}^k, \tag{3.6}$$

with $m_p > 0$. We note that there exists no set of non-negative basis functions satisfying (3.6). Moreover (3.3) in combination with (3.4) automatically yields $\sum_{p \in \mathcal{P}_{\text{C};l}^k} \psi_p = 1$ and

$$\int_F \psi_p \, \mathrm{d}s = \int_F \phi_p \, \mathrm{d}s, \quad p \in \mathcal{P}_{\text{C};l}^k, F \in \mathcal{F}_l^k. \tag{3.7}$$

The most popular choice of a dual Lagrange multiplier (Wohlmuth 2000, 2001) is obtained by an element-wise biorthogonalization process of the local nodal finite elements followed by a node-wise glueing step to reduce the number of degrees of freedom. As a result piecewise-linear but discontinuous basis functions are created for a one-dimensional contact zone. This technique works for the lowest-order finite elements on all types of surface meshes. In the case of higher-order elements, we have to use Gauss–Lobatto nodes. This approach is restricted to tensorial meshes where the element mapping is affine: see Lamichhane and Wohlmuth (2007). Alternatively, for low-order elements, as in the present discussion, we can apply piecewise-constant or -quadratic basis functions on a sub-mesh: see Figure 3.6(b,c), respectively.

In some applications it is of interest to work with continuous basis functions. Although the local construction of biorthogonal basis functions, node-wise defined, quite often results in a set of discontinuous basis functions, continuous ones do exist. Figure 3.7 shows basis functions which satisfy (3.2)–(3.5) and which in addition are continuous. In Figure 3.7(a), the basis function is cubic on each element. For the construction of the basis function shown in Figure 3.7(b,c), we use sub-elements and a piecewise quadratic and

linear approach, respectively. As will be seen, the cubic dual Lagrange multiplier goes hand in hand with the definition of $H(\mathrm{div})$-conforming mixed finite elements for linear elasticity and fits well into the construction of *a posteriori* error estimators based on element-wise lifting techniques: see Section 6.

The following two remarks briefly comment on more general formulations. In particular, the construction of a dual Lagrange multiplier basis possibly depends on the geometry in the case of cylinder coordinates or of sliding meshes.

Remark 3.3. If a three-dimensional situation is reduced to a two-dimensional setting by introducing cylinder coordinates and exploiting symmetry arguments, then duality has to be formulated with respect to a weighted scalar product. The distance to the symmetry axis enters as weight in the local biorthogonality relation (3.3). As example, we consider the piecewise affine case. Let r_1 and r_2 be the distances of the two face nodes to the symmetry axis. Then the dual Lagrange multiplier restricted to a face can be written as

$$\psi_1 = \frac{2r_1 + r_2}{r_1^2 + 4r_1r_2 + r_2^2}\big((r_1 + 3r_2)\phi_1 - (r_1 + r_2)\phi_2\big),$$
$$\psi_2 = \frac{r_1 + 2r_2}{r_1^2 + 4r_1r_2 + r_2^2}\big((3r_1 + r_2)\phi_2 - (r_1 + r_2)\phi_1\big),$$

where ϕ_1 and ϕ_2 are the two nodal basis function associated with the face. We note that $\psi_1 + \psi_2 = 1$, and for $r_1 = r_2$ we fall back to the piecewise affine dual Lagrange multiplier depicted in Figure 3.6(a).

Remark 3.4. A typical benchmark problem for large deformation contact is a small cube sliding over a larger block. If the large block is defined as slave side, then the integral over the face $F \in \mathcal{F}_l^{\mathrm{s}}$ in the local biorthogonality relation (3.3) has to be replaced by the integral over $F \cap \Gamma_{\mathrm{C};l}^{\mathrm{m}}$. Let us consider the 2D reference case $F = (0, 1)$ and $(s, 1) \subset \Gamma_{\mathrm{C};l}^{\mathrm{m}}$ with $s \in (0, 1)$. Then a straightforward calculation shows

$$\psi_1 = \frac{2(1 + s + s^2)}{1 - s}\phi_1 - (1 + 2s)\phi_2,$$
$$\psi_2 = -\frac{(1 + 2s)(1 + s)}{1 - s}\phi_1 + 2(1 + s)\phi_2,$$

where ϕ_1 is the nodal basis function associated with the endpoint $p = 0$ and ϕ_2 is associated with $p = 1$.

The weak problem formulation will be based on suitable subsets of $\mathbf{V}_l$ and $\mathbf{M}_l$. For the displacement, we only impose the Dirichlet condition on the space and use no constraint related to the non-penetration condition.

The convex set $\mathbf{V}_{l;\mathrm{D}}$ is given by

$$\mathbf{V}_{l;\mathrm{D}} := \mathbf{V}^{\mathrm{m}}_{l;D} \times \mathbf{V}^{\mathrm{s}}_{l;D}, \quad \mathbf{V}^{k}_{l;D} := \sum_{p \in \mathcal{P}^{k}_{\mathrm{D};l}} \mathbf{u}_{\mathrm{D}}(p)\phi_p + \mathbf{V}^{k}_{l},$$

where $\mathcal{P}^{k}_{\mathrm{D};l}$ stands for the set of all vertices of the actual mesh $\mathcal{T}^{k}_{l}$ on $\overline{\Gamma}^{k}_{\mathrm{D}}$. To handle the contact conditions (2.5) and (2.6) in a weakly consistent form, we have to impose constraints on the Lagrange multiplier space. The non-penetration condition restricts the normal part of $\mathbf{M}_l$, and the Coulomb law requires a solution-dependent inequality bound for the tangential part.

Let the discrete solution $\boldsymbol{\lambda}_l \in \mathbf{M}_l$ be given by

$$\boldsymbol{\lambda}_l = \sum_{p \in \mathcal{P}^{\mathrm{s}}_{\mathrm{C};l}} \boldsymbol{\gamma}_p \psi_p, \quad \boldsymbol{\gamma}_p \in \mathbb{R}^d,$$

and denote the discrete normal component by

$$\lambda^n_l := \sum_{p \in \mathcal{P}^{\mathrm{s}}_{\mathrm{C};l}} \gamma^n_p \psi_p, \quad \gamma^n_p := \boldsymbol{\gamma}_p \mathbf{n}^{\mathrm{s}}_p.$$

Here $\mathbf{n}^{\mathrm{s}}_p$ stands for a discrete normal vector associated with the node p. In the case of a non-planar contact surface, it can be obtained as a weighted combination of the adjacent element centre normals. We observe that $\lambda^n_l \in M^{\mathrm{s}}_l$ but, in general, it is not equal to $\boldsymbol{\lambda}_l \mathbf{n}^{\mathrm{s}}$. Based on the discrete normal surface traction λ^n_l, we then define the convex set

$$\mathbf{M}_l(\lambda^n_l) := \left\{ \boldsymbol{\mu}_l = \sum_{p \in \mathcal{P}^{\mathrm{s}}_{\mathrm{C};l}} \boldsymbol{\beta}_p \psi_p,\, \boldsymbol{\beta}_p \in \mathbb{R}^d,\, \beta^n_p \geq 0,\, \|\boldsymbol{\beta}^t_p\| \leq \nu \gamma^n_p \right\}, \tag{3.8}$$

as an approximation for the solution-dependent cone $\mathbf{M}(\lambda^n)$ defined in (2.14). Here $\beta^n_p := \boldsymbol{\beta}_p \mathbf{n}^{\mathrm{s}}_p$, $\boldsymbol{\beta}^t_p := \boldsymbol{\beta}_p - \beta^n_p \mathbf{n}^{\mathrm{s}}_p$. We assume that $\Gamma^{\mathrm{s}}_{\mathrm{C};l}$ is large enough such that $\boldsymbol{\gamma}_p = \mathbf{0}$ for $p \in \partial\Gamma^{\mathrm{s}}_{\mathrm{C};l}$.

Remark 3.5. If $\nu = 0$, the convex set $\mathbf{M}_l(\lambda^n_l)$ is solution-independent, and its definition reduces to

$$\mathbf{M}^{+}_l := \left\{ \boldsymbol{\mu}_l = \sum_{p \in \mathcal{P}^{\mathrm{s}}_{\mathrm{C};l}} \boldsymbol{\beta}_p \psi_p,\, \boldsymbol{\beta}_p \in \mathbb{R}^d,\, \beta^n_p \geq 0,\, \boldsymbol{\beta}^t_p = \mathbf{0} \right\}.$$

In this case it is sufficient to work with a scalar-valued Lagrange multiplier space as is often done in the literature. Here, we use a vector-valued Lagrange multiplier to be in the same abstract framework for all $\nu \geq 0$.

If the standard nodal Lagrange multiplier basis is used to define M_l, there are then two natural but different ways to discretize M^{+}; see also, *e.g.*, Hild

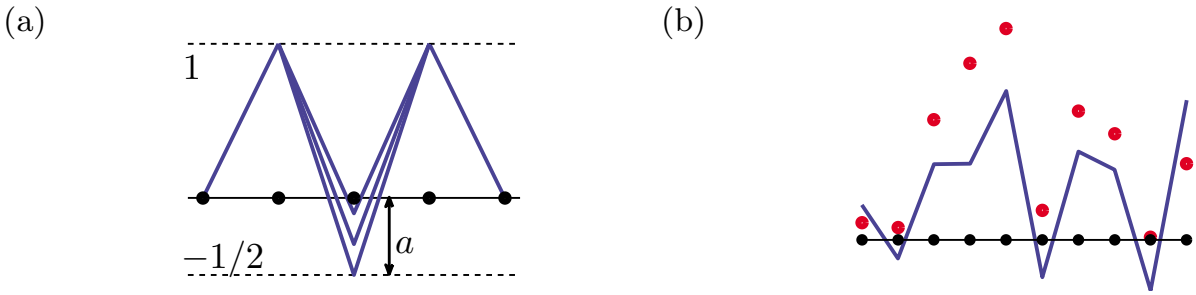

Figure 3.8. Two elements of $M^+_{l;2} \setminus M^+_{l;1}$: local support (a) and global support (b).

and Renard (2010). The first yields $M^+_{l;1} \subset M^+$, whereas the second choice is based on the definition of M^+ as a dual cone:

$$M^+_{l;1} := \left\{ \mu_l \in M_l \mid \mu_l = \sum_{p \in \mathcal{P}^{\mathrm{s}}_{\mathrm{C};l}} \beta_p \psi_p, \beta_p \geq 0,\ p \in \mathcal{P}^{\mathrm{s}}_{\mathrm{C};l} \right\},$$

$$M^+_{l;2} := \left\{ \mu_l \in M_l \mid \int_{\Gamma^{\mathrm{s}}_{\mathrm{C};l}} \mu_l \phi_p \, \mathrm{d}s \geq 0,\ p \in \mathcal{P}^{\mathrm{s}}_{\mathrm{C};l} \right\}.$$

We note that these two definitions yield two different spaces, with $M^+_{l;1}$ being a proper subspace of $M^+_{l;2}$. Figure 3.8 shows elements of $M^+_{l;2}$ which are clearly not in $M^+_{l;1}$. In Figure 3.8(a), the element $\mu_l \in M_l$ depends on the parameter value a and, as a straightforward computation shows, $\mu_l \in M^+_{l;2} \setminus M^+_{l;1}$ if and only if $a \in [-0.5; 0)$. The function in Figure 3.8(b) is obviously not in $M^+_{l;1}$. Testing it with all nodal basis functions ϕ_p, $p \in \mathcal{P}^{\mathrm{s}}_{\mathrm{C};l}$, yields the non-negative values (marked with bullets) and thus $\mu_l \in M^+_{l;2}$.

Both choices of $M^+_{l;i}$, $i = 1, 2$, can be applied in the discrete setting. The first one yields a conforming approach, whereas in the second one the non-conformity of M^+_l has to be taken into account in the *a priori* estimates. The difference in the spaces stems from the fact that the matrix given by $\int_{\Gamma^{\mathrm{s}}_{\mathrm{C};l}} \psi_q \phi_p \, \mathrm{d}s$ is then the standard mass matrix, which is not an M-matrix. The situation is different if our Lagrange multiplier basis, satisfying (3.6), is applied. Then the mass matrix is diagonal and positive definite and both definitions yield the same space M^+_l. However, using a biorthogonal basis automatically results in a non-conforming approach, *i.e.*, $M^+_l \not\subset M^+$. To enforce conformity in that situation is not a good idea, since then the locality of the elements in $M^+_l \cap M^+$ is lost; see also Figure 3.9.

Having the conforming finite element space $\mathbf{V}_l \subset \mathbf{V}_0$ and the non-conforming closed convex cone $\mathbf{M}_l(\lambda^n_l)$, we can formulate the discrete weak version of (2.15) as follows. Find $\mathbf{u}_l := (\mathbf{u}^{\mathrm{m}}_l, \mathbf{u}^{\mathrm{s}}_l) \in \mathbf{V}_{l;\mathrm{D}}$, $\boldsymbol{\lambda}_l \in \mathbf{M}_l(\lambda^n_l)$ such that

$$\begin{aligned} a_l(\mathbf{u}_l, \mathbf{v}_l) + b_l(\boldsymbol{\lambda}_l, \mathbf{v}_l) &= f_l(\mathbf{v}_l), & \mathbf{v}_l &\in \mathbf{V}_l, \\ b_l(\boldsymbol{\mu}_l - \boldsymbol{\lambda}_l, \mathbf{u}_l) &\leq g_l(\boldsymbol{\mu}_l - \boldsymbol{\lambda}_l), & \boldsymbol{\mu}_l &\in \mathbf{M}_l(\lambda^n_l). \end{aligned} \tag{3.9}$$

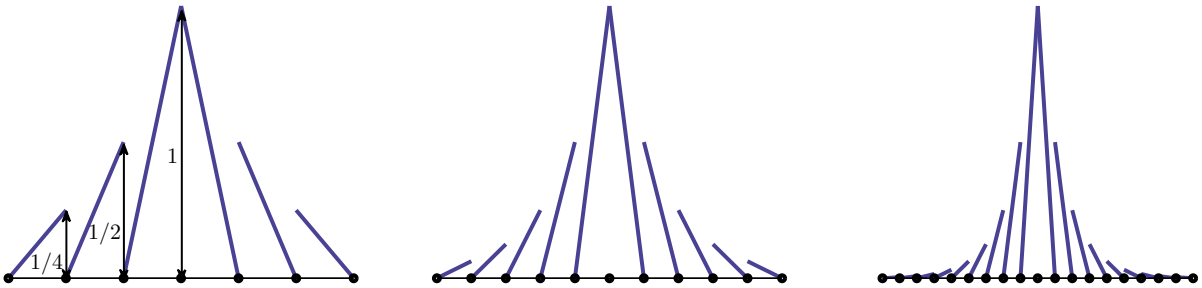

Figure 3.9. Elements in $M_l^+ \cap M^+$ for different refinement levels.

The mesh-dependent bilinear and linear forms are obtained from the associated continuous ones in a natural way by replacing the volume and surface terms by the corresponding discrete analogue, *i.e.*, summing over the volume and surface elements of the mesh.

3.3. Coupling in terms of the mortar projection

Although the given variational setting is a two-body formulation with possibly non-matching meshes, we can reformulate the contact conditions in a way similar to a one-body system. To do so, we introduce the mortar projection $\mathbf{\Pi}_l := (\Pi_l)^d$ onto $\mathbf{W}_l^{\mathrm{s}}$ and the dual mortar projection $\mathbf{\Pi}_l^* := (\Pi_l^*)^d$ onto $\mathbf{M}_l^{\mathrm{s}}$; see, *e.g.*, Bernardi, Maday and Patera (1993, 1994). We recall that due to the assumption on the Dirichlet boundary part, no modification at the endpoints is required. For $w \in H^{1/2}(\Gamma_{\mathrm{C};l}^{\mathrm{s}})$ and $\mu \in H^{-1/2}(\Gamma_{\mathrm{C};l}^{\mathrm{s}})$ we set

$$\int_{\Gamma_{\mathrm{C};l}^{\mathrm{s}}} \Pi_l w \mu_l \,\mathrm{d}s := \langle \mu_l, w \rangle_{\Gamma_{\mathrm{C};l}^{\mathrm{s}}}, \quad \mu_l \in M_l^{\mathrm{s}}, \tag{3.10a}$$

$$\int_{\Gamma_{\mathrm{C};l}^{\mathrm{s}}} \Pi_l^* \mu w_l \,\mathrm{d}s := \langle \mu, w_l \rangle_{\Gamma_{\mathrm{C};l}^{\mathrm{s}}}, \quad w_l \in W_l^{\mathrm{s}}. \tag{3.10b}$$

We note that $\mathbf{\Pi}_l$ and $\mathbf{\Pi}_l^*$ restricted to $\mathbf{W}_l^{\mathrm{s}}$ and $\mathbf{M}_l^{\mathrm{s}}$ is the identity, respectively. In terms of $\mathbf{\Pi}_l$, we can write $\mathbf{\Pi}_l[\mathbf{u}_l] = \sum_{p \in \mathcal{P}_{\mathrm{C};l}^{\mathrm{s}}} \boldsymbol{\alpha}_p \phi_p$. Moreover, we define $g_p := \int_{\Gamma_{\mathrm{C};l}^{\mathrm{s}}} g_l \psi_p \,\mathrm{d}s / m_p$ with a suitable approximation g_l for the linearized gap, where m_p is specified in (3.6). The following lemma shows that Lemma 2.3 has a node-wise discrete analogue.

Lemma 3.6. For each node $p \in \mathcal{P}_{\mathrm{C};l}^{\mathrm{s}}$ the following discrete node-wise KKT conditions hold for non-penetration:

$$0 \le \gamma_p^n, \quad \alpha_p^n \le g_p, \quad \gamma_p^n (\alpha_p^n - g_p) = 0. \tag{3.11}$$

Moreover, a discrete static Coulomb law holds for each node:

$$\|\boldsymbol{\gamma}_p^t\| \le \nu \gamma_p^n, \quad \boldsymbol{\alpha}_p^t \, \boldsymbol{\gamma}_p^t - \nu \gamma_p^n \|\boldsymbol{\alpha}_p^t\| = 0. \tag{3.12}$$

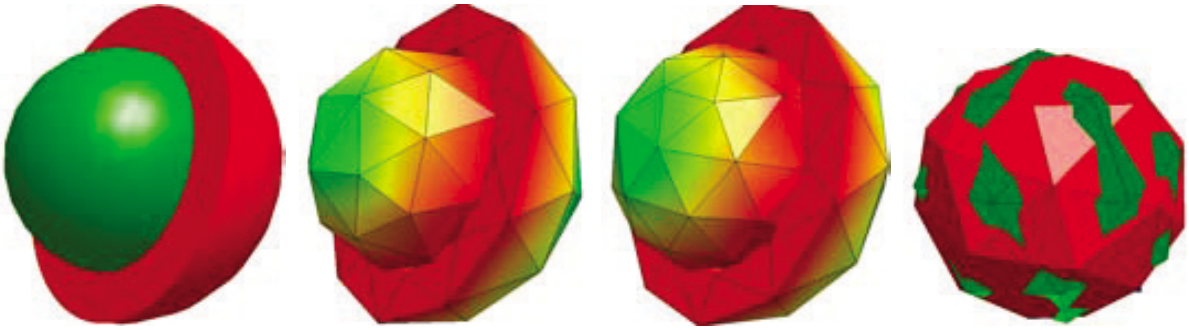

Figure 3.10. Discrete approximations Ω_l of the domain Ω.

Proof. We observe that the constraints on γ_p^n in (3.11) and on $\boldsymbol{\gamma}_p^t$ in (3.12) follow directly from the definition of $\mathbf{M}_l(\lambda_l^n)$. The biorthogonality (3.6) plays an essential role in the proof. Using $\boldsymbol{\mu}_l = \boldsymbol{\lambda}_l \pm \gamma_p^n \mathbf{n}_p^{\mathrm{s}} \psi_p \in \mathbf{M}_l(\lambda_l^n)$ as test function in (3.9), we find $\pm\gamma_p^n b(\mathbf{n}_p^{\mathrm{s}}\psi_p, \mathbf{u}_l) = \pm\gamma_p^n \alpha_p^n m_p \leq g_p \gamma_p^n m_p$ and thus the complementarity condition in (3.11). (3.12) obviously holds for $\boldsymbol{\alpha}_p^t = \mathbf{0}$. For $\boldsymbol{\alpha}_p^t \neq \mathbf{0}$, we set $\boldsymbol{\mu}_l = \boldsymbol{\lambda}_l - \boldsymbol{\gamma}_p^t \psi_p + \nu \gamma_p^n \mathbf{e}_t \psi_p \in \mathbf{M}_l(\lambda_l^n)$ with $\mathbf{e}_t := \boldsymbol{\alpha}_p^t / \|\boldsymbol{\alpha}_p^t\|$ as the test function in (3.9) and get (3.12). □

The discrete contact conditions (3.11) and (3.12) only involve quantities associated with the slave nodes and thus have the same structure as a one-body system. However, to compute $\boldsymbol{\alpha}_p$, we do have to evaluate the mortar projection $\boldsymbol{\Pi}_l$ applied on $[\mathbf{u}_l]$. Its algebraic representation can be obtained from the entries of the mass matrix associated with $b_l(\cdot,\cdot)$. For its implementation, we not only have to map the mesh elements on the possible contact zone but also the basis functions.

In Figure 3.10, we show different possible matching and non-matching situations in the case of a non-planar contact surface. We note that in this situation standard triangulations do not resolve the domain exactly. In contrast to the continuous setting where $\Gamma_{\mathrm{C}}^{\mathrm{s}} = \Gamma_{\mathrm{C}}^{\mathrm{m}}$, we find, in the discrete setting, that the possible contact zones on the master and the slave sides are not the same, *i.e.*, $\Gamma_{\mathrm{C};l}^{\mathrm{s}} \neq \Gamma_{\mathrm{C};l}^{\mathrm{m}}$.

Using hierarchical tree structures or front tracking techniques, the assembly of the surface-based coupling matrices between master and slave side can be realized quite efficiently and is of lower complexity, whereas in 3D a naive approach results in a higher complexity compared to the assembling process of the volume contributions. For the integration in 3D we use quadrature formulas on surface sub-triangles. Figure 3.11 illustrates different steps of the projection and partitioning procedure. This algorithm goes back to Puso (2004) (see also Puso *et al.* (2008)) and, alternatively, the recent papers by Dickopf and Krause (2009*a*, 2009*b*).

An analysis and a numerical study of the influence of curvilinear interfaces in the mortar situation can be found in Flemisch, Melenk and Wohlmuth (2005*a*). The abstract setting of blending elements (Gordon and Hall 1973*a*, 1973*b*) plays a key role in establishing optimal upper bounds

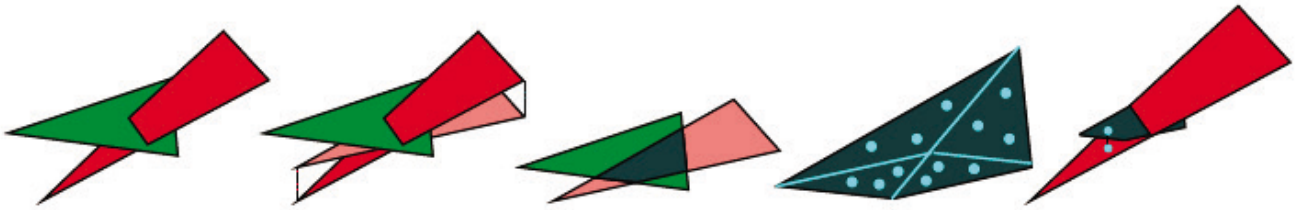

Figure 3.11. Element-wise mapping from the master to the slave side.

of the consistency error. From the theoretical point of view, the mapping between $\Gamma^{\mathrm{s}}_{\mathrm{C};l}$ and $\Gamma^{\mathrm{m}}_{\mathrm{C};l}$ has to be globally smooth. From the computational point of view, an element-wise smooth but possibly discontinuous mapping is more attractive and works well in practice. Replacing the $H^{1/2}$-norm on the contact interface by a weighted mesh-dependent L^2-norm, this simplification can also be theoretically justified. A 3D analysis, in the case of planar interfaces and mesh-dependent norms, can be found in Braess and Dahmen (1998).

We note that for non-planar interfaces, a slave side associated with the coarser mesh and a vectorial partial differential equation, *e.g.*, linear elasticity, possibly poor numerical results can be observed in the pre-asymptotic range, if the Lagrange multiplier with respect to its Cartesian coordinates is discretized by dual or piecewise constant basis functions: see, *e.g.*, Flemisch, Puso and Wohlmuth (2005*b*). This effect can be explained by the observation that a constant normal surface and a zero tangential force cannot very well be approximated in terms of the Lagrange multiplier space. Firstly decomposing the Lagrange multiplier into its normal and tangential parts, and secondly discretizing yield much better results. However, in that case we have to be quite careful to handle rigid body motions correctly. These oscillations do not occur for the Laplace operator, with a finer slave mesh side, standard linear Lagrange multipliers, or quadratic dual Lagrange multipliers. For contact problems, non-penetration and the friction law are directly expressed in terms of the normal and tangential component of the surface traction. Thus a discretization of the traction in its locally rotated coordinate system seems to be quite attractive, in particular for finite deformations, and has already been used to define $\mathbf{M}_l(\lambda_l^n)$. For small deformations and a constant contact normal, both approaches give the same results.

4. Optimal *a priori* error estimates

Abstract error estimates for variational inequalities can be found, *e.g.*, in Brezzi, Hager and Raviart (1977), Falk (1974), Glowinski (1984) and Glowinski *et al.* (1981) and *a priori* bounds for the discretization error of unilateral contact problems are given, *e.g.*, in Haslinger and Hlaváček (1981) and Haslinger *et al.* (1996). It is well known that the finite element solution of a variational inequality may have a reduced convergence order, compared to that of the best approximation. This holds true for higher-order finite

elements but may also be true for low-order approaches. A proof purely based on standard techniques will generally yield only $\mathcal{O}(\sqrt{h_l})$ *a priori* bounds. We refer to the monograph by Han and Reddy (1999) for an introduction into this area for applications in plasticity.

Mortar techniques for contact problems without friction have been introduced in Ben Belgacem, Hild and Laborde (1998), Ben Belgacem (2000) and Lhalouani and Sassi (1999). We also refer to Ben Belgacem and Renard (2003), Coorevits, Hild, Lhalouani and Sassi (2001), Hild (2000) and Hild and Laborde (2002), where standard Lagrange multiplier spaces have been considered and analysed. In early papers on mortar, unilateral contact problems have quite often been considered, taking no friction into account, and using a scalar-valued Lagrange multiplier. The choice of the contact pressure as Lagrange multiplier is motivated by the fact that in that case the tangential component of the surface traction is zero. There is a series of papers on *a priori* estimates for two-body contact problems with no friction on non-matching meshes starting with order 1/4 bounds for the discretization error (Ben Belgacem *et al.* 1998). *A priori* error estimates for the displacements in the H^1-norm and for the Lagrange multiplier in the $H^{-1/2}$-norm of order 3/4 have been established; see, *e.g.*, Ben Belgacem, Hild and Laborde (1999), Ben Belgacem and Renard (2003), Coorevits *et al.* (2001) and Lhalouani and Sassi (1999), under an H^2-regularity assumption. Using additional quite strong and restrictive regularity assumptions on the Lagrange multiplier, order one has been shown; see, *e.g.*, Coorevits *et al.* (2001) and Hild (2000). These first *a priori* results have been considerably improved over the last decade. Under suitable assumptions on the actual contact zone and a H^2-regular solution quasi-optimal, *i.e.*, $h_l\sqrt{|\log h_l|}$ and $h_l\sqrt[4]{|\log h_l|}$ *a priori* estimates can be found in Ben Belgacem (2000) and Ben Belgacem and Renard (2003). Most of the theoretical results are obtained for standard Lagrange multipliers, no friction and in the two-dimensional setting. Here, we apply these techniques to vector-valued dual Lagrange multiplier spaces and provide *a priori* error estimates for the displacement in the H^1-norm and for the surface traction in the $H^{-1/2}$-norm. In 3D, only sub-optimal bounds can be obtained for a problem with non-trivial friction. In 2D, we follow the lines of Hüeber, Matei and Wohlmuth (2005*b*) and Hüeber and Wohlmuth (2005*a*) and establish in a simplified problem setting optimal *a priori* bounds under some regularity assumption on the actual contact part and on the sticky zone.

We assume that no variational crimes are committed, *i.e.*, the discrete bilinear and linear forms are exact. In particular, this implies that no quadrature error occurs and that $\Omega_l^k = \Omega^k$; we refer to Ciarlet (1991, 1998) for a rigorous mathematical analysis of the influence of quadrature formulas. Moreover, we assume a zero gap, *i.e.*,

$$g = 0,\ \Gamma_{\mathrm{C}} := \Gamma_{\mathrm{C}}^{\mathrm{s}} = \Gamma_{\mathrm{C};l}^{\mathrm{s}} \subset \Gamma_{\mathrm{C}}^{\mathrm{m}} = \Gamma_{\mathrm{C};l}^{\mathrm{m}}$$

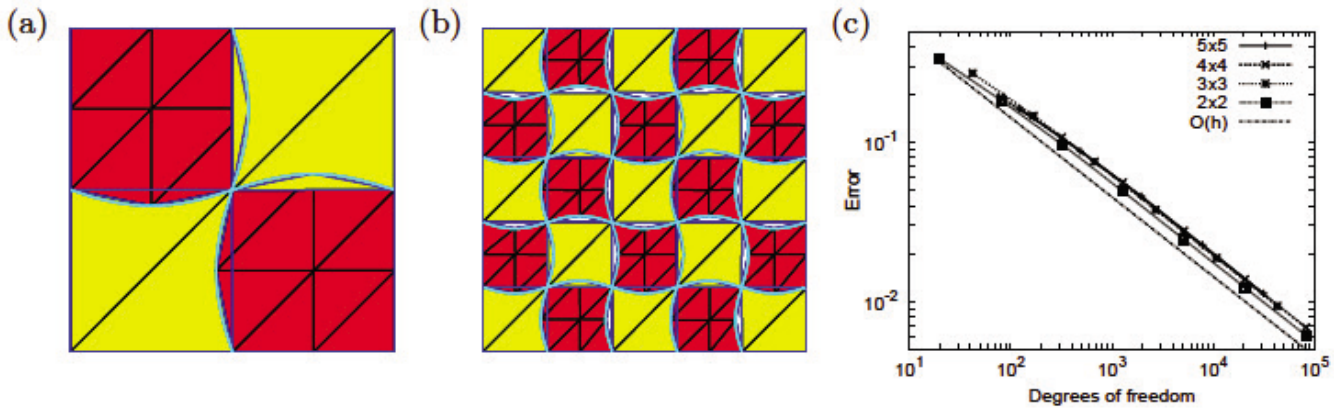

Figure 4.1. Decomposition into 4 and 25 subdomains (a,b) and error decay in the H^1-norm (c).

and a constant unit vector $\mathbf{n} := \mathbf{n}^s$ on the possible contact zone. The *a priori* analysis of a curvilinear interface for the classical linear- and scalar-valued mortar case can be found in Flemisch *et al.* (2005*a*). Figure 4.1 shows that the number of subdomains in the linear mortar setting does not influence the constants in the *a priori* bound. The unit square is decomposed into l^2, $l = 2, 3, 4, 5$ subdomains; the interface is given by a sinus wave function. Due to the curvilinear character of the interface, a mesh-dependent mapping between the discrete master and slave interface is required.

In the case of a non-linear contact problem, the same approach can be applied. For simplicity of notation, we do not provide any technical detail here and restrict ourselves to simple geometrical settings such as, *e.g.*, a square on a rectangle. Moreover, we will work with globally quasi-uniform meshes, such that there exists a regularity constant $c_{\text{reg}} > 0$ so that, for all nodes p on Γ_C, we have $B_p(c_{\text{reg}} h_l) \subset \operatorname{supp} \phi_p|_{\Gamma_C}$, where $B_p(c_{\text{reg}} h_l)$ is the $(d-1)$-dimensional ball with centre p and radius $c_{\text{reg}} h_l$.

Most importantly, we replace for the rest of this section the Coulomb friction law (2.6) by the more simple Tresca law with a constant friction bound $\mathcal{F}$, *i.e.*,

$$\|\boldsymbol{\lambda}_t\| \leq \mathcal{F}, \quad [\dot{\mathbf{u}}_t]\boldsymbol{\lambda}_t - \mathcal{F}\|[\dot{\mathbf{u}}_t]\| = 0. \tag{4.1}$$

In the following, we will frequently make use of the Tresca version of Lemmas 2.3 and 3.6. Following the lines of the proof, we find for the normal components the complementarity conditions

$$b_n(\boldsymbol{\lambda}, \mathbf{u}) = 0 = b_n(\boldsymbol{\lambda}_l, \mathbf{u}_l), \tag{4.2}$$

in addition to $\lambda_n \in M^+$, $\lambda_l^n \in M_l^+$ and $-[u_n], -\Pi_l[u_l^n] \in W^+$. We note that due to the possibly non-matching meshes, $-[u_l^n]$ is, in general, not in W^+. The friction law (4.1) guarantees that the tangential components satisfy

$$b_t(\boldsymbol{\lambda}, \mathbf{u}) = \int_{\Gamma_C} \mathcal{F}\|[\mathbf{u}_t]\| \, \mathrm{d}s, \quad b_t(\boldsymbol{\lambda}_l, \mathbf{u}_l) = \int_{\Gamma_C} \mathcal{F}\|\boldsymbol{\Pi}_l[\mathbf{u}_l^t]\|_l \, \mathrm{d}s, \tag{4.3}$$

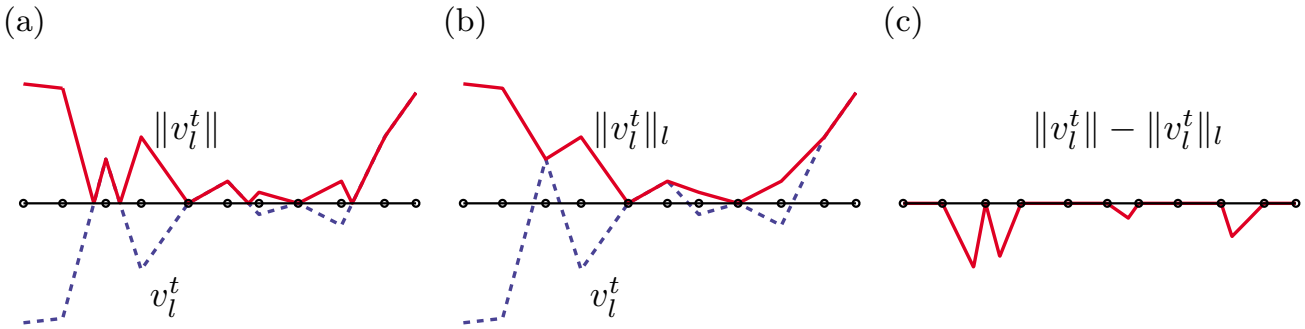

Figure 4.2. Absolute value in 2D $\|\cdot\|$ (a), discrete absolute value $\|\cdot\|_l$ (b) and the difference $\|\cdot\| - \|\cdot\|_l$ (c).

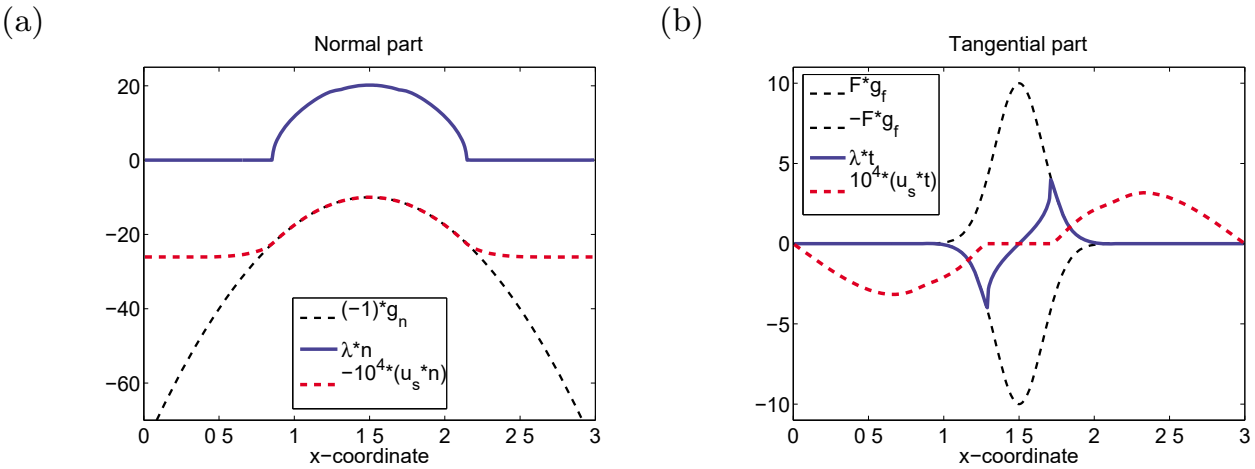

Figure 4.3. Numerical results for a contact problem with Tresca friction: normal displacement and contact pressure (a) and surface traction in normal and tangential direction (b).

where the mesh-dependent Euclidean norm $\|\cdot\|_l$ is defined by

$$\|\mathbf{\Pi}_l[\mathbf{u}_l^t]\|_l := \sum_{p \in \mathcal{P}^{\mathrm{s}}_{\mathrm{C};l}} \|\boldsymbol{\alpha}_p^t\| \phi_p \in W_l^+.$$

Figure 4.2 illustrates the difference between $\|\cdot\|$ and $\|\cdot\|_l$. The dashed line shows an element in W_l if Γ_{C} is a straight line. It is easy to verify that $\|\mathbf{\Pi}_l[\mathbf{u}_l^t]\| - \|\mathbf{\Pi}_l[\mathbf{u}_l^t]\|_l$ is equal to zero at all vertices of the slave-side mesh and that, in general, we do not have $\|\mathbf{\Pi}_l[\mathbf{u}_t]\| \in W_l$. Moreover, we find that $\|\mathbf{\Pi}_l[\mathbf{u}_l^t]\| - \|\mathbf{\Pi}_l[\mathbf{u}_l^t]\|_l \leq 0$.

Figure 4.3 shows a simple numerical example for a contact problem with a non-constant Tresca friction bound and a non-zero gap. Further, we observe that for such examples the discrete complementarity conditions hold true. Figure 4.3(a) shows that the coefficients γ_p^n are non-zero only on the actual discrete contact zone and thus (4.2) is satisfied. In Figure 4.3(b), the tangential displacement vanishes if the tangential stress component is strictly below its given bound, and thus (4.3) holds.

In addition to the best approximation properties of the discrete Lagrange multiplier space (3.4), our proof relies on the properties of Π_l and Π_l^*: see

Wohlmuth (2001). For $1 \leq s \leq 2$, we have

$$\|\mu - \Pi_l^* \mu\|_{-\frac{1}{2};\Gamma_C} \leq C h_l^{s-1} |\mu|_{s-\frac{3}{2};\Gamma_C}, \quad \mu \in H^{s-\frac{3}{2}}(\Gamma_C), \tag{4.4a}$$

$$\|w - \Pi_l w\|_{\frac{1}{2};\Gamma_C} \leq C h_l^{s-1} |w|_{s-\frac{1}{2};\Gamma_C}, \quad w \in H^{s-\frac{1}{2}}(\Gamma_C). \tag{4.4b}$$

Remark 4.1. We note that our regularity assumptions on the data and geometry guarantee that for $\mathbf{u} \in (H^s(\Omega))^d$, $1 \leq s \leq 2$, we automatically have $\boldsymbol{\lambda} = -\boldsymbol{\sigma}(\mathbf{u}^s)\mathbf{n} \in (H^{s-3/2}(\Gamma_C))^d$, and moreover $|\boldsymbol{\lambda}|_{s-3/2;\Gamma_C} \leq C|\mathbf{u}|_{s;\Omega}$. For $s = 2$ this is obvious; for $s = 1$ this does not hold for all $\mathbf{f} \in \mathbf{V}_0'$ and $\mathbf{f}_N \in \{w = v|_{\Gamma_N}, v \in V_0\}$. However, by increasing the regularity of the data, as we do here, this holds true with a constant depending on C_{reg} (see (2.4)), and then a standard interpolation argument yields the result for all $s \in [1, 2]$.

4.1. Upper bound for the discretization error

The starting point is the following abstract lemma. A similar lemma can be found in Hild and Laborde (2002) without friction and with quadratic finite elements associated with standard Lagrange multipliers. Here, we also have to consider the friction part and take into account the tangential component of the bilinear form $b(\cdot,\cdot)$. Introducing the error $\mathbf{E}_l := (\mathbf{u} - \mathbf{u}_l, \boldsymbol{\lambda} - \boldsymbol{\lambda}_l)$ and its associated norm $\|\mathbf{E}_l\|^2_{\mathbf{V}\times\mathbf{M}} := \|\mathbf{u}-\mathbf{u}_l\|^2_{1;\Omega} + \|\boldsymbol{\lambda}-\boldsymbol{\lambda}_l\|^2_{-1/2;\Gamma_C}$, the standard saddle-point theory and the complementarity conditions (4.2) provide a first *a priori* result.

Lemma 4.2. Let $(\mathbf{u}, \boldsymbol{\lambda}) \in \mathbf{V}\times\mathbf{M}(\mathcal{F})$ be the solution of (2.15) with $\mathbf{M}(\lambda_n)$ replaced by $\mathbf{M}(\mathcal{F})$ and let $(\mathbf{u}_l, \boldsymbol{\lambda}_l) \in \mathbf{V}_l \times \mathbf{M}_l(\mathcal{F})$ be the solution of the discrete formulation (3.9) with $\mathbf{M}_l(\lambda_l^n)$ replaced by $\mathbf{M}_l(\mathcal{F})$. Then, we have

$$\begin{aligned}\|\mathbf{E}_l\|_{\mathbf{V}\times\mathbf{M}} \leq C\Big\{ &\inf_{\mathbf{v}_l\in\mathbf{V}_l} \|\mathbf{u} - \mathbf{v}_l\|_{1;\Omega} + \inf_{\boldsymbol{\mu}_l\in\mathbf{M}_l} \|\boldsymbol{\lambda} - \boldsymbol{\mu}_l\|_{-\frac{1}{2};\Gamma_C} \\ &+ \max\big(b_n(\boldsymbol{\lambda}_l, \mathbf{u}),\, 0\big)^{\frac{1}{2}} + \max\big(b_n(\boldsymbol{\lambda}, \mathbf{u}_l),\, 0\big)^{\frac{1}{2}} \\ &+ \max\big(b_t(\boldsymbol{\lambda}_l - \boldsymbol{\lambda}, \mathbf{u}), 0\big)^{\frac{1}{2}} + \inf_{\mathbf{w}_l\in\mathbf{W}_l^s} \|[\mathbf{u}^t] - \mathbf{w}_l\|_{\frac{1}{2};\Gamma_C} \Big\}.\end{aligned}$$

Proof. Introducing $\mathbf{e}_l := \mathbf{u} - \mathbf{u}_l$, we find for the error $\mathbf{e}_l$ in the energy norm, and for $\mathbf{v}_l \in \mathbf{V}_l$

$$\begin{aligned}a(\mathbf{e}_l, \mathbf{e}_l) &= a(\mathbf{e}_l, \mathbf{u} - \mathbf{v}_l) - b(\boldsymbol{\lambda}, \mathbf{v}_l - \mathbf{u}_l) + b(\boldsymbol{\lambda}_l, \mathbf{v}_l - \mathbf{u}_l) \\ &= a(\mathbf{e}_l, \mathbf{u} - \mathbf{v}_l) - b(\boldsymbol{\lambda} - \boldsymbol{\lambda}_l, \mathbf{v}_l - \mathbf{u}) - b(\boldsymbol{\lambda} - \boldsymbol{\lambda}_l, \mathbf{e}_l).\end{aligned}$$

Then Korn's inequality, which holds on both subdomains by assumption, and the continuity of the bilinear forms $a(\cdot,\cdot)$ and $b(\cdot,\cdot)$ yield an upper bound for the H^1-error of the displacement:

$$\|\mathbf{e}_l\|^2_{1;\Omega} \leq C\big((\|\mathbf{e}_l\|_{1;\Omega} + \|\boldsymbol{\lambda} - \boldsymbol{\lambda}_l\|_{-\frac{1}{2};\Gamma_C})\big)\|\mathbf{u} - \mathbf{v}_l\|_{1;\Omega} - b(\boldsymbol{\lambda} - \boldsymbol{\lambda}_l, \mathbf{e}_l). \tag{4.5}$$

Using standard techniques from the saddle-point framework and applying the discrete inf-sup condition (3.5), we get

$$\begin{aligned}\|\boldsymbol{\mu}_l - \boldsymbol{\lambda}_l\|_{-\frac{1}{2};\Gamma_{\mathrm{C}}} &\leq C \sup_{\mathbf{w}_l \in \mathbf{V}_l} \frac{b(\boldsymbol{\mu}_l - \boldsymbol{\lambda}_l, \mathbf{w}_l)}{\|\mathbf{w}_l\|_{1;\Omega}} \\ &= C \sup_{\mathbf{w}_l \in \mathbf{V}_l} \frac{b(\boldsymbol{\mu}_l - \boldsymbol{\lambda}, \mathbf{w}_l) + a(\mathbf{u}_l - \mathbf{u}, \mathbf{w}_l)}{\|\mathbf{w}_l\|_{1;\Omega}} \\ &\leq C\big(\|\boldsymbol{\mu}_l - \boldsymbol{\lambda}\|_{-\frac{1}{2};\Gamma_{\mathrm{C}}} + \|\mathbf{u}_l - \mathbf{u}\|_{1;\Omega}\big).\end{aligned}$$

Then the triangle inequality and Young's inequality applied on $\|\boldsymbol{\lambda}-\boldsymbol{\lambda}_l\|_{-\frac{1}{2};\Gamma_{\mathrm{C}}}$ and (4.5), respectively, give

$$\|\mathbf{E}_l\|^2_{\mathbf{V}\times\mathbf{M}} \leq C\Big(\inf_{\mathbf{v}_l \in \mathbf{V}_l} \|\mathbf{u} - \mathbf{v}_l\|^2_{1;\Omega} + \inf_{\boldsymbol{\mu}_l \in \mathbf{M}_l} \|\boldsymbol{\lambda} - \boldsymbol{\mu}_l\|^2_{-\frac{1}{2};\Gamma_{\mathrm{C}}} - b(\boldsymbol{\lambda} - \boldsymbol{\lambda}_l, \mathbf{e}_l)\Big).$$

We use the additive decomposition of $b(\cdot,\cdot)$ into $b_n(\cdot,\cdot) + b_t(\cdot,\cdot)$ and recall (4.2)

$$b(\boldsymbol{\lambda}_l - \boldsymbol{\lambda}, \mathbf{e}_l) = b_n(\boldsymbol{\lambda}_l, \mathbf{u}) + b_n(\boldsymbol{\lambda}, \mathbf{u}_l) + b_t(\boldsymbol{\lambda}_l - \boldsymbol{\lambda}, \mathbf{u}) - b_t(\boldsymbol{\lambda}_l - \boldsymbol{\lambda}, \mathbf{u}_l).$$

Each of the first three terms on the right can be bounded by the maximum of zero and the term itself. To bound the last term, we use (4.3) and the $H^{1/2}$-stability (see (4.4b)) of the mortar projection $\boldsymbol{\Pi}_l$ defined by (3.10a). For all $\boldsymbol{\mu}_l \in \mathbf{M}_l$ and $\mathbf{w}_l \in \mathbf{W}^{\mathrm{s}}_l$, we have

$$\begin{aligned}b_t(\boldsymbol{\lambda} - \boldsymbol{\lambda}_l, \mathbf{u}_l) &= \langle \boldsymbol{\lambda}^t - \boldsymbol{\lambda}^t_l, [\mathbf{u}^t_l] - \boldsymbol{\Pi}_l[\mathbf{u}^t_l]\rangle_{\Gamma_{\mathrm{C}}} + \langle \boldsymbol{\lambda}^t - \boldsymbol{\lambda}^t_l, \boldsymbol{\Pi}_l[\mathbf{u}^t_l]\rangle_{\Gamma_{\mathrm{C}}} \\ &\leq \langle \boldsymbol{\lambda}^t - \boldsymbol{\mu}_l, [\mathbf{u}^t_l] - \boldsymbol{\Pi}_l[\mathbf{u}^t_l]\rangle_{\Gamma_{\mathrm{C}}} + \langle \mathcal{F}, \|\boldsymbol{\Pi}_l[\mathbf{u}^t_l]\| - \|\boldsymbol{\Pi}_l[\mathbf{u}^t_l]\|_l\rangle_{\Gamma_{\mathrm{C}}} \\ &\leq \langle \boldsymbol{\lambda}^t - \boldsymbol{\mu}_l, [\mathbf{u}^t_l] - \boldsymbol{\Pi}_l[\mathbf{u}^t_l]\rangle_{\Gamma_{\mathrm{C}}} \\ &\leq C\|\boldsymbol{\lambda} - \boldsymbol{\mu}_l\|_{-\frac{1}{2};\Gamma_{\mathrm{C}}}(\|\mathbf{u} - \mathbf{u}_l\|_{1;\Omega} + \|[\mathbf{u}^t] - \mathbf{w}_l\|_{\frac{1}{2};\Gamma_{\mathrm{C}}}).\end{aligned}$$

Now Young's inequality gives the required bound. □

The first two terms in the upper bound of Lemma 4.2 are the best approximation errors. They reflect the quality of the approximation of the spaces $\mathbf{V}_l$ and $\mathbf{M}_l$. The third, fourth and fifth term are consistency errors of the approach. We remark that the term $\max(b_n(\boldsymbol{\lambda}, \mathbf{u}_l), 0)$ takes into account the discrete penetration of the two bodies on the actual contact set. The term $\max(b_n(\boldsymbol{\lambda}_l, \mathbf{u}), 0)$ can be greater than zero if the discrete Lagrange multiplier λ^n_l is negative on a part of the actual contact set. We recall that M^+_l is not a subspace of M^+, and thus λ^n_l does not have to be non-negative. To some extent this term measures the non-conformity of λ^n_l with respect to the physical requirement of a positive contact pressure. The fifth term satisfies $\max(b_t(\boldsymbol{\lambda}_l - \boldsymbol{\lambda}, \mathbf{u}), 0) \leq \max(\int_{\Gamma_{\mathrm{C}}} (\|\boldsymbol{\lambda}^t_l\| - \mathcal{F})\|\mathbf{u}_t\| \,\mathrm{d}s, 0)$. Using that the maximum of a nodal dual Lagrange multiplier is larger than one, $\|\boldsymbol{\gamma}^t_p\| \leq \mathcal{F}$ does not necessarily give $\|\boldsymbol{\lambda}^t_l\| \leq \mathcal{F}$, and thus this term is in general non-

zero and measures the violation of the friction law. Finally, the last term does not appear for contact problems without friction. A closer look into the proof reveals that the $H^{1/2}$-norm estimate on Γ_{C} is too pessimistic for Coulomb problems, and it would be sufficient to consider the $H^{1/2}$-norm on the actual contact zone. Moreover, this term does not occur if we work with matching meshes.

4.2. Optimal a priori estimates

To prove optimal *a priori* error estimates under the H^s-regularity assumption for the displacements $\mathbf{u}$ with $1 \leq s \leq 2$, we have to consider in more detail the three terms in the upper bound of Lemma 4.2 which involve the bilinear form $b(\cdot,\cdot)$. We now give three lemmas providing upper bounds for these consistency errors.

Lemma 4.3. Let $(\mathbf{u},\boldsymbol{\lambda}) \in \mathbf{V}\times\mathbf{M}(\mathcal{F})$ be the solution of (2.15) with $\mathbf{M}(\lambda_n)$ replaced by $\mathbf{M}(\mathcal{F})$ and let $(\mathbf{u}_l,\boldsymbol{\lambda}_l) \in \mathbf{V}_l \times \mathbf{M}_l(\mathcal{F})$ be the solution of the discrete formulation (3.9) with $\mathbf{M}_l(\lambda_l^n)$ replaced by $\mathbf{M}_l(\mathcal{F})$. Under the regularity assumption $\mathbf{u} \in (H^s(\Omega))^d$, $1 \leq s \leq 2$, we then have the *a priori* error estimate

$$b_n(\boldsymbol{\lambda},\mathbf{u}_l) \leq C\big(h_l^{2(s-1)}|\mathbf{u}|_{s;\Omega}^2 + h_l^{(s-1)}|\mathbf{u}|_{s;\Omega}\|\mathbf{u}-\mathbf{u}_l\|_{1;\Omega}\big).$$

Proof. For standard Lagrange multipliers, we refer to Hild and Laborde (2002). Although our dual basis functions of $\mathbf{M}_l$ are not positive, we can apply the same techniques. Using the discrete saddle-point formulation (3.9) and the definition of the mortar projection, we find, in terms of the approximation properties (4.4) and Remark 4.1, the upper bound

$$\begin{aligned}
b_n(\boldsymbol{\lambda},\mathbf{u}_l) &= \langle\lambda_n,[u_l^n]-\Pi_l[u_l^n]+\Pi_l[u_l^n]\rangle_{\Gamma_{\mathrm{C}}} \leq \langle\lambda_n,[u_l^n]-\Pi_l[u_l^n]\rangle_{\Gamma_{\mathrm{C}}}\\
&\leq \langle\lambda_n-\Pi_l^*\lambda_n,[u_l^n]-\Pi_l[u_l^n]\rangle_{\Gamma_{\mathrm{C}}}\\
&\leq \|\lambda_n-\Pi_l^*\lambda_n\|_{-\frac{1}{2};\Gamma_{\mathrm{C}}}\|[u_l^n]-\Pi_l[u_l^n]\|_{\frac{1}{2};\Gamma_{\mathrm{C}}}\\
&\leq Ch_l^{s-1}|\lambda_n|_{s-\frac{3}{2};\Gamma_{\mathrm{C}}}\big(\|[u_l^n]-[u_n]\|_{\frac{1}{2};\Gamma_{\mathrm{C}}}+\|[u_n]-\Pi_l[u_n]\|_{\frac{1}{2};\Gamma_{\mathrm{C}}}\big)\\
&\leq C\big(h_l^{s-1}|\mathbf{u}|_{s;\Omega}\|\mathbf{u}-\mathbf{u}_l\|_{1;\Omega}+h_l^{2(s-1)}|\mathbf{u}|_{s;\Omega}^2\big). \qquad \square
\end{aligned}$$

Before we focus on the terms $b_n(\boldsymbol{\lambda}_l,\mathbf{u})$ and $b_t(\boldsymbol{\lambda}_l-\boldsymbol{\lambda},\mathbf{u})$, we consider a non-linear quasi-projection operator which preserves sign. This type of operator was originally introduced in Chen and Nochetto (2000). We also refer to Nochetto and Wahlbin (2002) for a negative result on the existence of higher-order sign-preserving operators and for a detailed discussion of the special role of extreme points. Let $\widehat{S}_l : W \longrightarrow W_l^{\mathrm{s}}$ be a Clément-type operator which is defined node-wise by

$$\widehat{S}_l w(p) := \frac{1}{|B_p(c_{\mathrm{reg}}h_l)|}\int_{B_p(c_{\mathrm{reg}}h_l)} w\,\mathrm{d}s, \quad p \in \mathcal{P}_{\mathrm{C};l}^{\mathrm{int}}.$$

Here $\mathcal{P}^{\mathrm{int}}_{\mathrm{C};l} := \{p \in \mathcal{P}^{\mathrm{s}}_{\mathrm{C};l}\,,\, p \notin \partial\Gamma_{\mathrm{C}}\}$, and for all nodes $p \in \partial\Gamma_{\mathrm{C}}$, we use a locally defined value depending only on the values of w restricted to $B_p(c_{\mathrm{reg}}h_l) \cap \Gamma_{\mathrm{C}}$ such that $\widehat{S}_l$ is L^2-stable and reproduces polynomials of degree one. Standard arguments show that for $1 \leq s \leq 2$ we get

$$\|\widehat{S}_l w - w\|_{\frac{1}{2};\Gamma_{\mathrm{C}}} \leq C h_l^{s-1} |w|_{s-\frac{1}{2};\Gamma_{\mathrm{C}}}.$$

More importantly, $\widehat{S}_l w$ preserves the sign of $w \in W^+$ in the mesh-dependent interior $\Gamma^{\mathrm{int}}_{\mathrm{C};l} := \Gamma_{\mathrm{C}} \setminus (\cup_{p \in \mathcal{P}^{\mathrm{s}}_{\mathrm{C};l} \setminus \mathcal{P}^{\mathrm{int}}_{\mathrm{C};l}} \operatorname{supp} \phi_p)$, *i.e.*, we have for $w \in W^+$ that $\widehat{S}_l w(p) \geq 0$ for $p \in \mathcal{P}^{\mathrm{int}}_{\mathrm{C};l}$.

In terms of the linear operator $\widehat{S}_l$, we define the non-linear operator S_l:

$$S_l w(p) := \begin{cases} \widehat{S}_l w(p) & \operatorname{supp} \phi_p \subset \operatorname{supp} w \text{ or } p \in \partial\Gamma_{\mathrm{C}}, \\ 0 & \text{otherwise,} \end{cases} \qquad p \in \mathcal{P}^{\mathrm{s}}_{\mathrm{C};l}, \tag{4.6}$$

the definition of which guarantees that $\operatorname{supp} S_l w \cap \Gamma^{\mathrm{int}}_{\mathrm{C};l} \subset \operatorname{supp} w$. Moreover, for $w \in W^+$ we have $S_l w(p) \geq 0$ for $p \notin \partial\Gamma_{\mathrm{C}}$.

Assumption 4.4. Let us define $\Sigma^n_l := \{x \in \Gamma_{\mathrm{C}} \mid \operatorname{dist}(x, \partial B_n) \leq 2h_l\}$, where B_n is the actual contact zone, *i.e.*, $B_n := \operatorname{supp} \lambda_n$. Then, we assume that Σ^n_l and B_n are compactly embedded in Γ_{C} and $\Gamma^{\mathrm{int}}_{\mathrm{C};l}$, respectively, and moreover that

$$\|[u_n]\|_{0;\Sigma^n_l} \leq C h_l^{s-\frac{1}{2}} |[u_n]|_{s-\frac{1}{2};\Gamma_{\mathrm{C}}}.$$

Let us briefly comment on different aspects of this assumption. We note that for h_l small enough, Σ^n_l and B_n are compactly embedded in Γ_{C} and $\Gamma^{\mathrm{int}}_{\mathrm{C};l}$, respectively, due to the assumption that B_n is compactly embedded in Γ_{C}. This assumption can be weakened, but then the notation would become more technical. Setting $B^{\mathrm{c}}_n := \Gamma_{\mathrm{C}} \setminus B_n$ and defining $H^{s-1/2}_{00}(B^{\mathrm{c}}_n) := \{w \in L^2(B^{\mathrm{c}}_n) \mid w = v|_{B^{\mathrm{c}}_n} \text{ for } v \in H^{s-1/2}(\Gamma_{\mathrm{C}}) \text{ and } \operatorname{supp} v \subset \overline{B^{\mathrm{c}}_n}\}$, we get $[u_n] \in H^{s-1/2}_{00}(B^{\mathrm{c}}_n)$ if $\mathbf{u} \in (H^s(\Omega))^d$. Now, if B^{c}_n is regular enough, the assumption is followed by a Poincaré–Friedrichs-type argument, together with suitable interpolation and a scaling. We refer to Li, Melenk, Wohlmuth and Zou (2010), where similar estimates for interfaces have been used, and to Melenk and Wohlmuth (2011), where these types of estimates are used to obtain quasi-optimal *a priori* L^2-norm estimates for the Lagrange multiplier in a linear mortar setting. In particular, an order-h_l estimate is given for H^1-functions with vanishing trace. The assumption is naturally satisfied if B_n is regular enough. If the boundary ∂B_n is smooth enough, we can locally flatten ∂B_n, use the fact that Sobolev spaces are invariant under smooth changes of variables and apply the 1D Sobolev embedding result $\|v\|_{L^\infty(I)} \lesssim \|v\|_{H^s(I)}$, $s > \frac{1}{2}$ recursively, where I is a fixed interval and $v \in H^s(I)$ (see, *e.g.*, Adams (1975)).

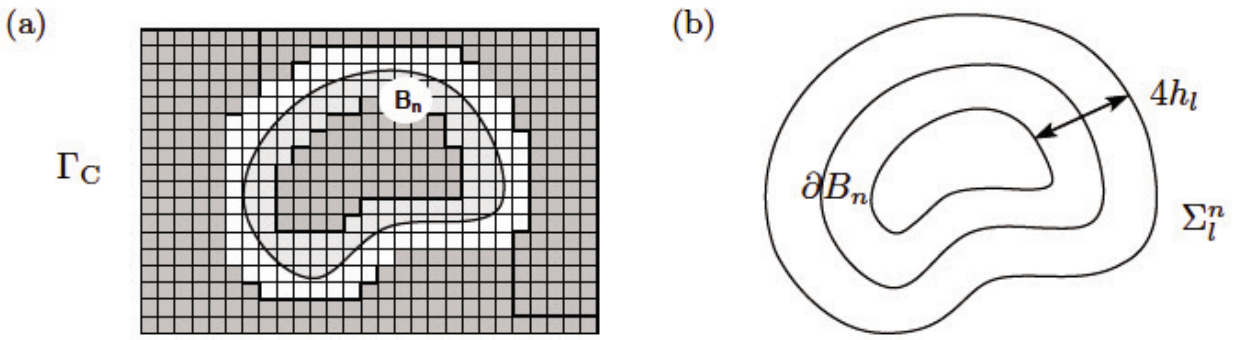

Figure 4.4. Actual contact zone B_n (a) and boundary strip Σ_l^n(b).

Figure 4.4 illustrates the definition of the strip Σ_l^n which has a diameter of $4h_l$ perpendicular to ∂B_n.

In terms of these preliminary considerations, we can show the following bound for the consistency error of λ_l^n.

Lemma 4.5. Let $(\mathbf{u}, \boldsymbol{\lambda}) \in \mathbf{V} \times \mathbf{M}(\mathcal{F})$ be the solution of (2.15) with $\mathbf{M}(\lambda_n)$ replaced by $\mathbf{M}(\mathcal{F})$ and let $(\mathbf{u}_l, \boldsymbol{\lambda}_l) \in \mathbf{V}_l \times \mathbf{M}_l(\mathcal{F})$ be the solution of the discrete formulation (3.9) with $\mathbf{M}_l(\lambda_l^n)$ replaced by $\mathbf{M}_l(\mathcal{F})$. Under Assumption 4.4 and the regularity assumption $\mathbf{u} \in (H^s(\Omega))^d$, $1 \le s \le 2$, we then have the *a priori* error estimate

$$b_n(\boldsymbol{\lambda}_l, \mathbf{u}) \le C h_l^{s-1} |\mathbf{u}|_{s;\Omega} \|\boldsymbol{\lambda} - \boldsymbol{\lambda}_l\|_{-\frac{1}{2};\Gamma_C}.$$

Proof. The operator $\widehat{S}_l$ yields $\|\widehat{S}_l[u_n] - [u_n]\|_{\frac{1}{2};\Gamma_C} \le C h_l^{s-1} |[u_n]|_{s-\frac{1}{2};\Gamma_C} \le C h_l^{s-1} |\mathbf{u}|_{s;\Omega}$ for $1 \le s \le 2$. Due to the fact that $\lambda_l^n \in M^+$ with $\gamma_p^n = 0$ for $p \in \partial\Gamma_C$, we find

$$\int_{\Gamma_C} \lambda_l^n S_l[u_n] \, ds = \sum_{p \in \mathcal{P}_{C;l}^{\text{int}}} \gamma_p^n S_l[u_n](p) m_p \le 0.$$

Then, (4.2), the construction of S_l and the assumption $B_n \subset \Gamma_{C;l}^{\text{int}}$ yield

$$\begin{aligned} b_n(\boldsymbol{\lambda}_l, \mathbf{u}) &= \int_{\Gamma_C} \lambda_l^n [u_n] \, ds \le \int_{\Gamma_C} \lambda_l^n ([u_n] - S_l[u_n]) \, ds \\ &= \langle \lambda_l^n - \lambda_n, [u_n] - S_l[u_n] \rangle_{\Gamma_C} \le \|\lambda_l^n - \lambda_n\|_{-\frac{1}{2};\Gamma_C} \|[u_n] - S_l[u_n]\|_{\frac{1}{2};\Gamma_C} \\ &\le \|\lambda_l^n - \lambda_n\|_{-\frac{1}{2};\Gamma_C} (\|[u_n] - \widehat{S}_l[u_n]\|_{\frac{1}{2};\Gamma_C} + \|S_l[u_n] - \widehat{S}_l[u_n]\|_{\frac{1}{2};\Gamma_C}). \end{aligned}$$

As already noted the linear operator $\widehat{S}_l$ has best approximation properties and thus it is sufficient to consider the second term on the right in more detail. The properties of the non-linear operator S_l defined by (4.6) play a crucial role.

We observe that $S_l[u_n]$ and $\widehat{S}_l[u_n]$ coincide in the two dark grey-shaded regions of Figure 4.4(a) and note that $S_l[u_n] - \widehat{S}_l[u_n] = 0$ on $\Gamma_C \setminus \Sigma_l^n$. For the

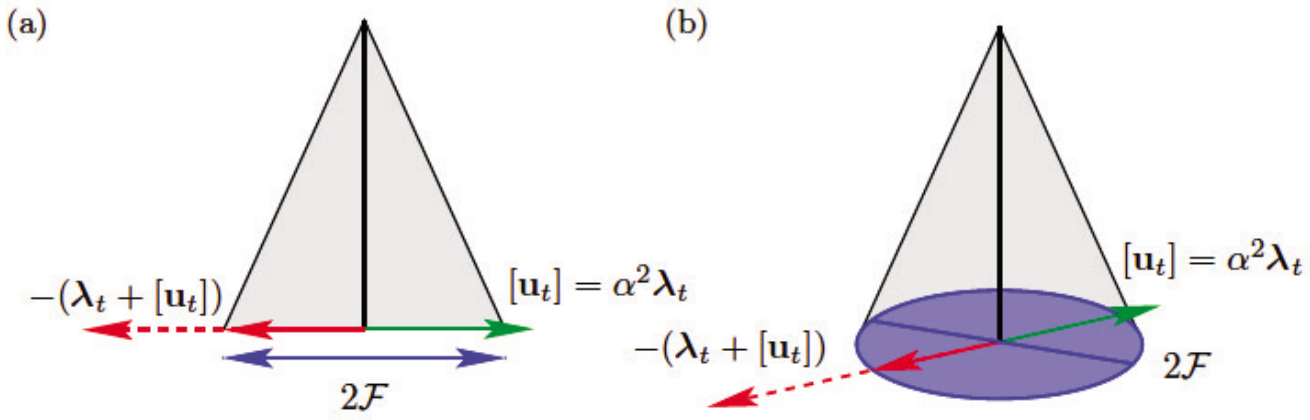

Figure 4.5. Friction cone for $d = 2$ (a) and $d = 3$ (b).

term $\|S_l[u_n] - \widehat{S}_l[u_n]\|_{\frac{1}{2};\Gamma_C}$, we can now apply a standard inverse inequality and get

$$\begin{aligned}\|S_l[u_n] - \widehat{S}_l[u_n]\|^2_{\frac{1}{2};\Gamma_C} &\leq \frac{C}{h_l}\|S_l[u_n] - \widehat{S}_l[u_n]\|^2_{0;\Gamma_C} \\ &\leq C \sum_{p \in \mathcal{P}_{\Sigma_l^n}} h_l^{d-2} (\widehat{S}_l[u_n](p))^2 \leq \frac{C}{h_l}\|[u_n]\|^2_{0;\Sigma_l^n},\end{aligned}$$

where $\mathcal{P}_{\Sigma_l^n} := \{p \in \mathcal{P}^s_{C;l}$ such that supp $\phi \subset \Sigma_l^n\}$. Now Assumption 4.4 can be applied and yields the required bound. □

Now we combine the previous results and formulate a first optimal *a priori* error estimate for a two-body contact problem with no friction.

Theorem 4.6. Let $(\mathbf{u}, \boldsymbol{\lambda}) \in \mathbf{V} \times \mathbf{M}^+$ be the solution of (2.15) and let $(\mathbf{u}_l, \boldsymbol{\lambda}_l) \in \mathbf{V}_l \times \mathbf{M}_l^+$ be the solution of the discrete formulation (3.9) with $\nu = 0$. Under the Assumption 4.4 and the regularity assumption $\mathbf{u} \in (H^s(\Omega))^d$, $1 \leq s \leq 2$, we then have the *a priori* error estimate

$$\|\mathbf{u} - \mathbf{u}_l\|_{1;\Omega} + \|\boldsymbol{\lambda} - \boldsymbol{\lambda}_l\|_{-\frac{1}{2};\Gamma_C} \leq C h_l^{s-1} |\mathbf{u}|_{s;\Omega}.$$

Proof. Using the well-known approximation property for the spaces $\mathbf{V}_l$ and $\mathbf{M}_l$, the proof is a direct consequence of Lemmas 4.2–4.5 by applying Young's inequality and noting that $\boldsymbol{\lambda}_t = \boldsymbol{\lambda}_l^t = \mathbf{0}$. □

For a non-trivial given friction bound $\mathcal{F}$, the situation is more complex, and moreover there is a substantial difference between the two- and three-dimensional setting. In 2D, the tangential stress component can be identified with a scalar-valued functional, and we can follow the proof of Lemma 4.5. Figure 4.5 illustrates the difference. In 2D, the tangential surface traction $\boldsymbol{\lambda}_t = \lambda_t \mathbf{t}$ of a regular solution is either $\lambda_t = \mathcal{F}$ or $\lambda_t = -\mathcal{F}$ for sliding nodes. Moreover, the tangential displacement $[\mathbf{u}_t] = [u_t]\mathbf{t}$ can be separated into two parts $[u_t] = \max(0, [u_t]) + \min(0, [u_t]) =: u_t^+ - u_t^-$, u_t^+,

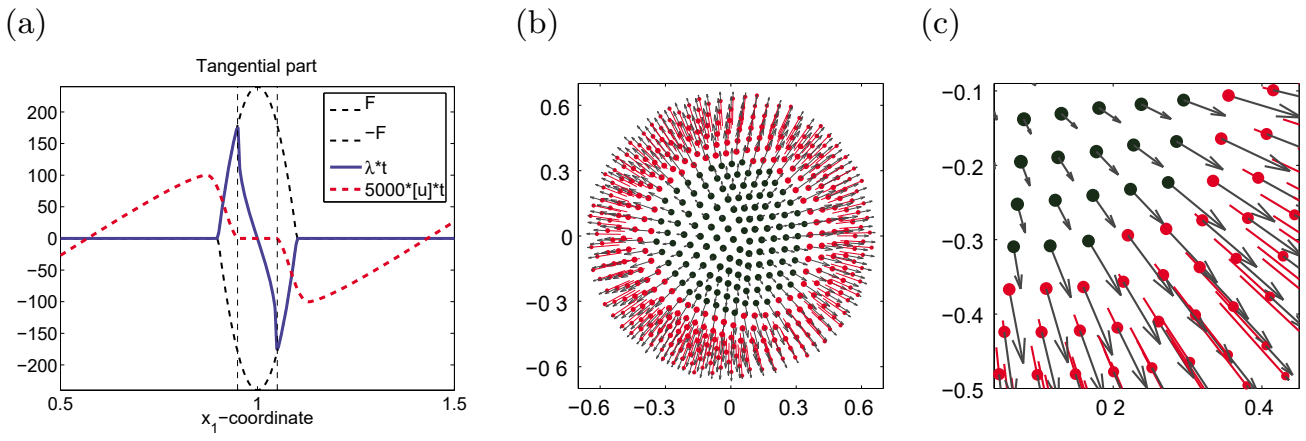

Figure 4.6. Tangential displacement for contact problems with friction: $d = 2$ (a) and $d = 3$ (b,c).

$u_t^- \in W^+$: see Figure 4.6(a). In 3D, the tangential part $[\mathbf{u}_t]$ is a vector-valued function, for which we cannot apply the friction law component-wise.

In Figure 4.6, we show typical numerical results for a contact problem with friction. We note that for these considerations there is no difference between a Tresca and a Coulomb problem. In Figure 4.6(a) a Hertz contact problem with a given but non-constant friction bound is simulated in 2D. In Figure 4.6(b), we show a visualization of the tangential displacement for $d = 3$ and Coulomb friction. The nodes in the centre marked with black bullets are sticky and do not carry a relative tangential displacement. For these nodes the tangential component of the stress satisfies the inequality of the Coulomb law strictly. The nodes situated in the outer ring do slide, and the sliding direction is possibly changing from node to node. As can be seen in the zoom in Figure 4.6(c), the sliding direction is, as required by the friction law, opposite to the tangential stress.

Assumption 4.7. (2D setting) Let us define

$$\Sigma_l^{\pm;t} := \{x \in \Gamma_C \mid \operatorname{dist}(x, \partial B_t^{\pm}) \leq 2h_l\},$$

where $\partial B_t^+ \cup \partial B_t^-$ is the boundary of the actual sticky zone. More precisely, we set $\partial B_t^{\pm} := \partial \operatorname{supp} u_t^{\pm} \cap \Gamma_C$. Then, we assume that $\Sigma_l^{\pm;t}$ and $B_t^{\pm}$ are compactly embedded in Γ_C, and moreover that for $p \in \partial\Gamma_C \cap \operatorname{supp} u_t^{\pm}$ we have $\gamma_p^t = \pm\mathcal{F}$,

$$\|u_t^{\pm}\|_{0;\Sigma_l^{\pm;t}} \leq C h_l^{s-\frac{1}{2}} |[u_t]|_{s-\frac{1}{2};\Gamma_C}.$$

We note that for a Coulomb problem, we have $B_t \subset B_n$, and thus B_t is automatically compactly embedded Γ_C if B_n is so. This is not necessarily the case for a Tresca friction problem. We point out that this assumption rules out the case $s = 2$ and $\boldsymbol{\lambda}_t = \lambda_t \mathbf{t}$ with λ_t being a function which jumps from plus to minus of the friction bound. In that case u_t^+ and u_t^- have a lower regularity than u_t. To be more precise $u_t \in H^{3/2}(\Gamma_C)$, whereas

$u_t^{\pm} \in H^{3/2-\epsilon}(\Gamma_C)$ for all $\epsilon > 0$, and thus only an order $h_l^{3/2-\epsilon}$ can be expected to hold true. Figure 4.7 shows the numerical solution for a Coulomb problem in 2D with two different friction coefficients. In Figure 4.7(a) the case $\nu = 0.8$ is shown whereas in Figure 4.7(b,c) the case $\nu = 0.3$ is presented. The close-up in Figure 4.7(c) reveals that u_t is zero not only in the centre point but also in a non-trivial sub-interval, and thus Assumption 4.7 is satisfied for both cases.

The following lemma is the counterpart of Lemma 4.5 for the tangential component. Due to the partition $u_t = u_t^+ - u_t^-$ it only holds true for $d = 2$.

Lemma 4.8. Let $(\mathbf{u}, \boldsymbol{\lambda}) \in \mathbf{V} \times \mathbf{M}(\mathcal{F})$ be the solution of (2.15) with $\mathbf{M}(\lambda_n)$ replaced by $\mathbf{M}(\mathcal{F})$ and let $(\mathbf{u}_l, \boldsymbol{\lambda}_l) \in \mathbf{V}_l \times \mathbf{M}_l(\mathcal{F})$ be the solution of the discrete formulation (3.9) with $\mathbf{M}_l(\lambda_l^n)$ replaced by $\mathbf{M}_l(\mathcal{F})$. Under Assumption 4.7 and the regularity assumption $\mathbf{u} \in (H^s(\Omega))^2$, $1 \leq s \leq 2$, we then have the *a priori* error estimate for $d = 2$:

$$b_t(\boldsymbol{\lambda}_l - \boldsymbol{\lambda}, \mathbf{u}) \leq C h_l^{s-1} |\mathbf{u}|_{s;\Omega} \|\boldsymbol{\lambda} - \boldsymbol{\lambda}_l\|_{-\frac{1}{2};\Gamma_C}.$$

Proof. The proof follows the lines of the proof of Lemma 4.5. We start with the observation that $b_t(\boldsymbol{\lambda}_l - \boldsymbol{\lambda}, \mathbf{u}) = \int_{\Gamma_C} (\lambda_l^t - \mathcal{F}) u_t^+ \, \mathrm{d}s - \int_{\Gamma_C} (\lambda_l^t + \mathcal{F}) u_t^- \, \mathrm{d}s$, where $\boldsymbol{\lambda}_l^t := \lambda_l^t \mathbf{t}$. Now we apply the operator S_l to u_l^+ and u_l^-. Then, under Assumption 4.7 we get

$$\|u_t^+ - S_l u_t^+\|_{\frac{1}{2};\Gamma_C} + \|u_t^- - S_l u_t^-\|_{\frac{1}{2};\Gamma_C} \leq C h_l^{s-1} \|[u_n]\|_{s-\frac{1}{2};\Gamma_C}.$$

The construction of S_l yields that

$$\begin{aligned}
b_t(\boldsymbol{\lambda}_l - \boldsymbol{\lambda}, \mathbf{u}) &= \langle \lambda_l^t - \lambda_t, u_t^+ - S_l u_t^+ \rangle + \langle \lambda_l^t - \lambda_t, S_l u_t^- - u_t^- \rangle \\
&\quad + \langle \lambda_l^t - \lambda_t, S_l u_t^+ \rangle - \langle \lambda_l^t - \lambda_t, S_l u_t^- \rangle \\
&\leq C h_l^{s-1} \|[u_n]\|_{s-\frac{1}{2};\Gamma_C} \|\lambda_l^t - \lambda_t\|_{-\frac{1}{2};\Gamma_C} \\
&\quad + \langle \lambda_l^t - \mathcal{F}, S_l u_t^+ \rangle - \langle \lambda_l^t + \mathcal{F}, S_l u_t^- \rangle \\
&= C h_l^{s-1} \|[u_n]\|_{s-\frac{1}{2};\Gamma_C} \|\lambda_l^t - \lambda_t\|_{-\frac{1}{2};\Gamma_C} \\
&\quad + \sum_{p \in \mathcal{P}_{C;l}^s} (\gamma_p^t - \mathcal{F}) S_l u_t^+(p) m_p \\
&\quad - \sum_{p \in \mathcal{P}_{C;l}^s} (\gamma_p^t + \mathcal{F}) S_l u_t^-(p) m_p.
\end{aligned}$$

Moreover, by definition of $M_l(\mathcal{F})$, it is easy to see that $\gamma_p^t - \mathcal{F} \leq 0$ and

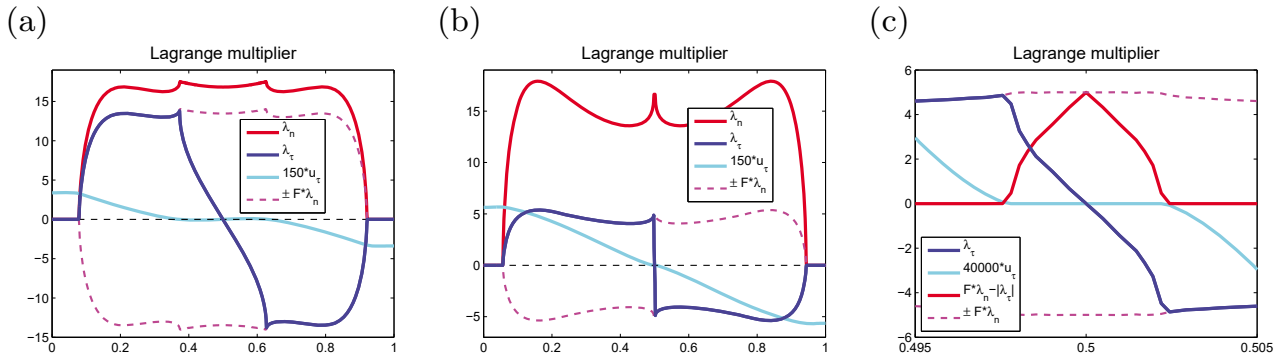

Figure 4.7. Tangential displacement for different friction coefficients.

$\gamma_p^t + \mathcal{F} \geq 0$, and thus we get

$$\sum_{p \in \mathcal{P}^{\text{int}}_{\text{C};l}} \left[(\gamma_p^t - \mathcal{F}) S_l u_t^+(p) - (\gamma_p^t + \mathcal{F}) S_l u_t^-(p) \right] m_p \leq 0.$$

For $p \in \mathcal{P}^{\text{s}}_{\text{C};l} \setminus \mathcal{P}^{\text{int}}_{\text{C};l}$, we have that $(\gamma_p^t - \mathcal{F}) S_l u_t^+(p) = 0 = (\gamma_p^t + \mathcal{F}) S_l u_t^-(p)$. We note that these last arguments are typical for $d = 2$ but cannot be applied in 3D. □

We now combine the previous results and formulate an optimal *a priori* error estimate for a two-body contact problem with Tresca friction in 2D.

Theorem 4.9. Let $(\mathbf{u}, \boldsymbol{\lambda}) \in \mathbf{V} \times \mathbf{M}(\mathcal{F})$ be the solution of (2.15), with $\mathbf{M}(\lambda_n)$ replaced by $\mathbf{M}(\mathcal{F})$, and let $(\mathbf{u}_l, \boldsymbol{\lambda}_l) \in \mathbf{V}_l \times \mathbf{M}_l(\mathcal{F})$ be the solution of the discrete formulation (3.9), with $\mathbf{M}_l(\lambda_l^n)$ replaced by $\mathbf{M}_l(\mathcal{F})$. Under Assumptions 4.4, 4.7 and the regularity assumption $\mathbf{u} \in (H^s(\Omega))^2$, $1 \leq s \leq 2$, we then have the *a priori* error estimate for $d = 2$:

$$\|\mathbf{u} - \mathbf{u}_l\|_{1;\Omega} + \|\boldsymbol{\lambda} - \boldsymbol{\lambda}_l\|_{-\frac{1}{2};\Gamma_{\text{C}}} \leq C h_l^{s-1} |\mathbf{u}|_{s;\Omega}.$$

Proof. Using the well-known approximation property for the spaces $\mathbf{V}_l$, $\mathbf{M}_l$ and $\mathbf{W}_l^{\text{s}}$, the proof is a direct consequence of Lemmas 4.2–4.8 by applying Young's inequality. □

Let us briefly comment on the three-dimensional case. Lemma 4.8 is the only one where we have explicitly used a 2D construction. All the other results hold true for $d = 2$ and $d = 3$. In 3D, we do still get *a priori* bounds for the discretization error, although the optimal order is lost if $\mathbf{u} \in (H^s(\Omega))^d$, $3/2 < s \leq 2$. We introduce the operators $\mathbf{Z}_l^* : \mathbf{M} \to \mathbf{W}_l^{\text{s}}$ and $\mathbf{Z}_l : \mathbf{W} \to \mathbf{W}_l^{\text{s}}$ by $\mathbf{Z}_l^* := (Z_l^*)^d$ and $\mathbf{Z}_l := (Z_l)^d$, $Z_l^* : M \to W_l^{\text{s}}$ and $Z_l : W \to W_l^{\text{s}}$:

$$Z_l^* \mu := \sum_{p \in \mathcal{P}^{\text{s}}_{\text{C};l}} \frac{\langle \mu, \phi_p \rangle_{\Gamma_{\text{C}}}}{m_p} \phi_p, \quad Z_l w := \sum_{p \in \mathcal{P}^{\text{s}}_{\text{C};l}} \frac{\langle \phi_p, w \rangle_{\Gamma_{\text{C}}}}{m_p} \phi_p. \tag{4.7}$$

Obviously, both Z_l and Z_l^* are locally defined and reproduce constants. Moreover, Z_l is L^2- and H^1-stable. From the $H^{1/2}$-stability we get the $H^{-1/2}$-stability of Z_l^* with the same stability constant

$$\|Z_l^*\mu\|_{-\frac{1}{2};\Gamma_C} = \sup_{w\in W} \frac{\langle Z_l^*\mu, w\rangle_{\Gamma_C}}{\|w\|_{\frac{1}{2};\Gamma_C}} = \sup_{w\in W} \frac{\langle \mu, Z_l w\rangle_{\Gamma_C}}{\|w\|_{\frac{1}{2};\Gamma_C}}.$$

In terms of these operators, we obtain the following non-optimal *a priori* bound for a Tresca friction problem in 3D with non-trivial but constant friction coefficient.

Theorem 4.10. Let $(\mathbf{u},\boldsymbol{\lambda}) \in \mathbf{V}\times\mathbf{M}(\mathcal{F})$ be the solution of (2.15), with $\mathbf{M}(\lambda_n)$ replaced by $\mathbf{M}(\mathcal{F})$, and let $(\mathbf{u}_l,\boldsymbol{\lambda}_l) \in \mathbf{V}_l\times\mathbf{M}_l(\mathcal{F})$ be the solution of the discrete formulation (3.9), with $\mathbf{M}_l(\lambda_l^n)$ replaced by $\mathbf{M}_l(\mathcal{F})$. If $\mathbf{u} \in (H^s(\Omega))^d$, $1\le s\le 3/2$, we then have the *a priori* error estimate

$$\|\mathbf{u}-\mathbf{u}_l\|_{1;\Omega} + \|\boldsymbol{\lambda}-\boldsymbol{\lambda}_l\|_{-\frac{1}{2};\Gamma_C} \le C h_l^{s-1}|\mathbf{u}|_{s;\Omega}.$$

Proof. We have to re-examine the two terms $b_n(\boldsymbol{\lambda}_l,\mathbf{u})$ and $b_t(\boldsymbol{\lambda}_l-\boldsymbol{\lambda},\mathbf{u})$ in the upper bound of Lemma 4.2. To do so, we apply the operators Z_l^* and $\mathbf{Z}_l^*$ and remark that $Z_l^*\lambda_l^n = \sum_{p\in\mathcal{P}^s_{C;l}} \gamma_p^n\phi_p \in W^+$ and

$$\|\mathbf{Z}_l^*\boldsymbol{\lambda}_l^t\| - \mathcal{F} = \left\|\sum_{p\in\mathcal{P}^s_{C;l}} \boldsymbol{\gamma}_p^t\phi_p\right\| - \mathcal{F} \le \sum_{p\in\mathcal{P}^s_{C;l}} \|\boldsymbol{\gamma}_p^t\|\phi_p - \mathcal{F} \le \sum_{p\in\mathcal{P}^s_{C;l}} \mathcal{F}\phi_p - \mathcal{F} = 0.$$

These preliminary observations in combination with (3.7) yield for the normal part

$$\begin{aligned} b_n(\boldsymbol{\lambda}_l,\mathbf{u}) &= \langle \lambda_l^n - Z_l^*\lambda_l^n, [u_n]\rangle_{\Gamma_C} + \langle Z_l^*\lambda_l^n, [u_n]\rangle_{\Gamma_C} \\ &\le \langle \lambda_l^n - Z_l^*\lambda_l^n, [u_n]\rangle_{\Gamma_C} = \langle \lambda_l^n - Z_l^*\lambda_l^n, [u_n] - \Pi_{0;l}[u_n]\rangle_{\Gamma_C} \\ &\le C h_l^{s-\frac{1}{2}} \|\lambda_l^n - Z_l^*\lambda_l^n\|_{0;\Gamma_C} |[u_n]|_{s-\frac{1}{2};\Gamma_C} \\ &\le C h_l^{s-1} \|\lambda_l^n - Z_l^*\lambda_l^n\|_{-\frac{1}{2};\Gamma_C} |\mathbf{u}|_{s;\Omega}, \end{aligned}$$

where $\Pi_{0;l}$ is the L^2-projection onto element-wise constants. Here we have also used additionally the inverse estimate for $\|\lambda_l^n - Z_l^*\lambda_l^n\|_{0;\Gamma_C}$, which results from standard inverse estimates for finite elements and the fact that $Z_l^*\lambda_l^n \ge 0$.

Keeping in mind that $b_t(\boldsymbol{\lambda},\mathbf{u}) = \int_{\Gamma_C} \mathcal{F}\|[\mathbf{u}]_t\|\,\mathrm{d}s$, the tangential part can be estimated in the same way:

$$\begin{aligned} b_t(\boldsymbol{\lambda}_l-\boldsymbol{\lambda},\mathbf{u}) &= b_t(\boldsymbol{\lambda}_l - \mathbf{Z}_l^*\boldsymbol{\lambda}_l,\mathbf{u}) + b_t(\mathbf{Z}_l^*\boldsymbol{\lambda}_l - \boldsymbol{\lambda},\mathbf{u}) \\ &\le b_t(\boldsymbol{\lambda}_l - \mathbf{Z}_l^*\boldsymbol{\lambda}_l,\mathbf{u}) \le C h_l^{s-1} \|\boldsymbol{\lambda}_l^t - \mathbf{Z}_l^*\boldsymbol{\lambda}_l^t\|_{-\frac{1}{2};\Gamma_C} |\mathbf{u}|_{s;\Omega}. \end{aligned}$$

In a last step, we have to consider $\|\boldsymbol{\lambda}_l - \mathbf{Z}_l^*\boldsymbol{\lambda}_l\|_{-\frac{1}{2};\Gamma_C}$ in more detail and

bound it. The stability of $\mathbf{Z}_l^*$ in the $H^{-1/2}$-norm gives

$$\begin{aligned}\|\boldsymbol{\lambda}_l - \mathbf{Z}_l^*\boldsymbol{\lambda}_l\|_{-\frac{1}{2};\Gamma_C} &\leq C\|\boldsymbol{\lambda}_l - \boldsymbol{\lambda}\|_{-\frac{1}{2};\Gamma_C} + \|\boldsymbol{\lambda} - \mathbf{Z}_l^*\boldsymbol{\lambda}\|_{-\frac{1}{2};\Gamma_C} \\ &\leq C(\|\boldsymbol{\lambda}_l - \boldsymbol{\lambda}\|_{-\frac{1}{2};\Gamma_C} + h_l^{s-1}|\mathbf{u}|_{s;\Omega}).\end{aligned}$$

Now, Lemma 4.3 in combination with Young's inequality yields the required *a priori* bound. □

Remark 4.11. We note that in contrast to Theorem 4.9 no additional assumptions on the actual contact zones are made in Theorem 4.10.

The main advantage of the dual Lagrange multiplier space is the possibility of computing $\boldsymbol{\lambda}_l$ by a local post-process from the discrete displacement. Taking the local residual and using a simple scaling directly yield the coefficients. However, for the visualization in general $\mathbf{Z}_l^*\boldsymbol{\lambda}_l$ is plotted and not $\boldsymbol{\lambda}_l$. However, both quantities have the same order of convergence. For $1 \leq s \leq 2$ and $\mathbf{u} \in (H^s(\Omega))^d$ we obtain in terms of the $H^{-1/2}$-stability of $\mathbf{Z}_l^*$ and its approximation property

$$\begin{aligned}\|\boldsymbol{\lambda} - \mathbf{Z}_l^*\boldsymbol{\lambda}_l\|_{-\frac{1}{2};\Gamma_C} &\leq \|\boldsymbol{\lambda} - \mathbf{Z}_l^*\boldsymbol{\lambda}\|_{-\frac{1}{2};\Gamma_C} + \|\mathbf{Z}_l^*(\boldsymbol{\lambda} - \boldsymbol{\lambda}_l)\|_{-\frac{1}{2};\Gamma_C} \\ &\leq C(\|\boldsymbol{\lambda} - \boldsymbol{\lambda}_l\|_{-\frac{1}{2};\Gamma_C} + h_l^{s-1}|\mathbf{u}|_{s;\Omega}).\end{aligned}$$

Remark 4.12. Quite often in the context of mortar methods (see, *e.g.*, Braess and Dahmen (2002)), one prefers to work with a norm that is easier to handle than the $H^{-1/2}$-norm. Thus this is replaced by a weighted mesh-dependent L^2-norm,

$$\|\mu\|_{M_l}^2 := \sum_{F \in \mathcal{F}_{C;l}^s} h_F \|\mu\|_{0;F}^2 \quad \mu \in L^2(\Gamma_C^s) \text{ or } \mu \in (L^2(\Gamma_C^s))^d. \tag{4.8}$$

Then all our theoretical results also cover $\|\boldsymbol{\lambda} - \boldsymbol{\lambda}_l\|_{M_l}$ if the regularity of the solution is good enough. The proof follows exactly the same lines as for the $H^{-1/2}$-norm and uses an inverse estimate. It is known from the linear mortar setting that in the case of weighted L^2-norms, a uniform inf-sup condition also holds. Moreover, one can replace, in the proof of the best approximation properties of the constrained space, the discrete harmonic extension by a discrete zero extension to the interior nodes.

4.3. Numerical results

We note that in all our numerical results the mesh-dependent norm (4.8) has been used to measure the discretization error in the Lagrange multiplier and $\mathbf{Z}_l^*\boldsymbol{\lambda}_l$ has been used to make the plots. To illustrate the convergence rates of low-order finite elements numerically, we consider two simple two-dimensional test settings. As a reference solution, we use the numerical solution on $\mathcal{T}_{l_{\max}+2}$.

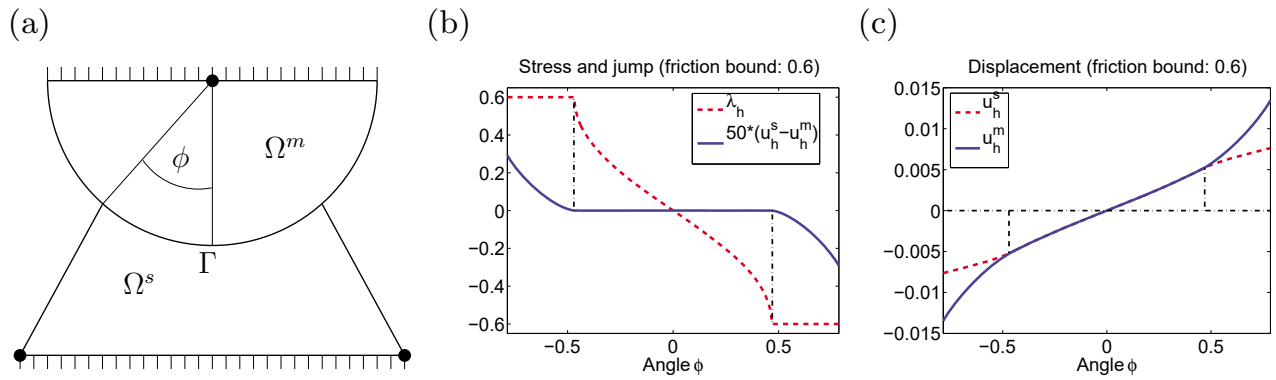

Figure 4.8. Problem setting (a), tangential Lagrange multiplier (b) and tangential displacement (c) on $\Gamma^s_{C;l}$.

Our first example is a scalar-valued model problem for anti-plane friction; we refer to Hüeber *et al.* (2005*b*) for details regarding the problem formulation. The friction bound is set to $\mathcal{F} = 0.6$. Figure 4.8 shows the geometry as well as the tangential Lagrange multiplier and the displacement on master and slave sides. In Figure 4.8(b), we can clearly observe the discrete complementarity (3.12) with $\nu\gamma_p^n$ being replaced by the given bound $\mathcal{F}$. In Figure 4.8(c) the tangential displacements are shown. For $\|\boldsymbol{\gamma}_p^t\|$ strictly smaller than $\mathcal{F}$, the two bodies have to stick together. Sliding is possible only on a part of the contact zone where $\|\boldsymbol{\gamma}_p^t\| = \mathcal{F}$.

Table 4.1 shows the convergence rates for this simplified frictional contact problem. We show the L^2-norm and the H^1-norm of the displacement error and the mesh-dependent norm of the error in the Lagrange multiplier. Our numerical results confirm the theoretical ones, and the computed rates are fairly close to the optimal order of convergence. Although we do not have a theoretical result for the L^2-norm, the numerical results also show a significantly better rate compared to the H^1-norm. Standard duality techniques such as the Aubin–Nitsche approach are tricky to apply in the setting of variational inequalities since they depend on regularity assumptions of the dual problem.

Our second test example is the classical Hertz problem (Hertz 1882, Johnson 1985, Kikuchi and Oden 1988) with Coulomb friction. Although our theoretical results do not cover the case of a Coulomb contact problem, Table 4.2 shows that also for this case we obtain almost optimal convergence rates. In that case, the convergence order for the error in the Lagrange multiplier in the weighted L^2-norm is close to the best approximation order of 3/2.

Remark 4.13. This effect is also numerically well observed for mortar problems in the linear setting (Wohlmuth 2001). A theoretical analysis can be found in the recent contribution by Melenk and Wohlmuth (2011), where it is shown that quasi-optimal L^2-norm estimates for the Lagrange multiplier hold in the linear mortar setting under suitable regularity assumptions.

Table 4.1. Convergence rates for a contact problem with given friction bound.

Level	$\frac{\|\mathbf{u}_l-\mathbf{u}_{\mathrm{ref}}\|_{0;\Omega}}{\|\mathbf{u}_{\mathrm{ref}}\|_{0;\Omega}}$		$\frac{\|\mathbf{u}_l-\mathbf{u}_{\mathrm{ref}}\|_{1;\Omega}}{\|\mathbf{u}_{\mathrm{ref}}\|_{1;\Omega}}$		$\|\boldsymbol{\lambda}_l-\boldsymbol{\lambda}_{\mathrm{ref}}\|_*$	
0	8.9343e−02	–	3.2317e−01	–	7.7185e−02	–
1	3.0960e−02	1.53	1.8933e−01	0.77	2.2162e−02	1.80
2	8.6519e−03	1.84	1.0343e−01	0.87	8.1336e−03	1.45
3	2.4272e−03	1.83	5.6431e−02	0.87	3.7816e−03	1.10
4	6.6657e−04	1.86	3.0414e−02	0.89	1.3031e−03	1.54
5	1.7918e−04	1.90	1.6132e−02	0.91	3.5214e−04	1.89
6	4.6522e−05	1.95	8.3113e−03	0.96	1.6712e−04	1.08

Table 4.2. Convergence rates for a Hertz contact problem with Coulomb friction, $\nu = 0.5$.

Level	$\frac{\|\mathbf{u}_l-\mathbf{u}_{\mathrm{ref}}\|_{1;\Omega}}{\|\mathbf{u}_{\mathrm{ref}}\|_{1;\Omega}}$		$\|\boldsymbol{\lambda}_l-\boldsymbol{\lambda}_{\mathrm{ref}}\|_*$	
1	4.465867e−01	–	5.065628	–
2	3.056095e−01	0.55	2.381819e+01	1.09
3	1.693210e−01	0.85	1.037995e+01	1.20
4	9.155008e−02	0.89	3.909448e+00	1.41
5	4.857727e−02	0.91	1.493191e+00	1.39
6	2.450933e−02	0.99	0.523946e+00	1.51

Finally, we briefly comment on higher-order elements; see also Belhachmi and Ben Belgacem (2000) for an analysis and Fischer and Wriggers (2006) and Puso *et al.* (2008) for simulation results in applications, and the influence of the choice of the Lagrange multiplier space. Recently, hp-techniques have also been applied for contact problems in combination with boundary elements (Chernov, Maischak and Stephan 2008). The p-version in the boundary element method for contact is discussed in Gwinner (2009). From the algorithmic point of view, higher-order elements can be easily applied. As we will see, quadratic elements do yield higher-order *a priori* estimates, but optimal quadratic order cannot be achieved. This results from the fact that there exists no monotonicity-preserving operator of higher order; see also Nochetto and Wahlbin (2002). In addition, the solution of a contact problem is, in general, not in $H^3(\Omega)$, and thus also, from the point of view of best approximation, no second-order error decay can be expected. Nevertheless, a higher-order *a priori* estimate can be obtained by replacing $\mathbf{V}_l$ by quadratic finite elements. Quadratic finite elements and linear dual

Table 4.3. Relative error for the displacement in the H^1-norm for linear and quadratic finite elements.

Level	$(i,j)=(1,1)$		$(i,j)=(2,1)$		$(i,j)=(2,2)$	
0	4.663632e−01	–	3.159307e−01	–	3.903263e−01	–
1	3.214737e−01	0.54	1.592747e−01	0.99	1.376072e−01	1.50
2	1.807130e−01	0.83	6.777325e−02	1.23	5.656398e−02	1.28
3	9.735853e−02	0.89	2.992646e−02	1.18	2.422295e−02	1.22
4	5.111965e−02	0.93	1.340727e−02	1.16	1.028243e−02	1.23
5	2.584391e−02	0.98	–	–	–	–

Table 4.4. Mesh-dependent L^2-error for the Lagrange multiplier in the linear and quadratic approach.

Level	$(i,j)=(1,1)$		$(i,j)=(2,1)$		$(i,j)=(2,2)$	
0	5.845412e+01	–	5.849757e+01	–	1.323412e+02	–
1	4.999477e+01	0.23	4.129640e+01	0.50	3.621992e+01	1.87
2	2.121223e+01	1.24	1.814467e+01	1.19	1.389391e+01	1.38
3	8.378905e+00	1.34	7.316218e+00	1.31	5.230080e+00	1.41
4	3.269796e+00	1.36	2.813967e+00	1.38	2.015976e+00	1.38
5	1.168347e+00	1.48	–	–	–	–

Lagrange multipliers yield an order h^{s-1}, $1 \leq s < \frac{5}{2}$, upper bound for the discretization error if the solution is H^s-regular. Replacing the linear Lagrange multiplier space by quadratic Lagrange multipliers does not give a higher order: see, *e.g.*, Hild and Laborde (2002). Revising the proof of Theorem 4.9 shows that the crucial steps are Lemma 4.5 and Lemma 4.8. These parts do not yield estimates of order two even if the spaces used have higher-order best approximation properties. For a proof and more detailed numerical results, comparing quadratic finite elements with linear Lagrange multipliers and with quadratic Lagrange multipliers, we refer to Hüeber, Mair and Wohlmuth (2005*a*). As a test example, we choose the simple Hertz contact problem without friction.

Table 4.3 shows the convergence rates for the relative H^1-norm of the error in the displacement, whereas Table 4.4 refers to the error of the Lagrange multiplier in the mesh-dependent L^2-norm. Here, we illustrate the influence of linear and quadratic finite elements. The indices $i = 1$ and $i = 2$ stand for the use of standard conforming linear and quadratic finite elements for the displacement, respectively. The indices $j = 1$ and $j = 2$ indicate the

use of biorthogonal basis function of lowest and second order, respectively. We note that the pairing $(i, j) = (1, 2)$ is not uniformly inf-sup stable with respect to the slave side and thus is not considered. Moreover $j = 1$ already gives a best approximation property of the Lagrange multiplier space of order 3/2, and thus we do not expect a qualitative increase in the case $j = 2$ compared to $j = 1$ for the Lagrange multiplier. Although the convergence order in the H^1-norm for $i = 2$ is not equal to two, it is much higher than compared to $i = 1$. A more efficient strategy, however, is to combine higher-order elements in the interior with adaptive refinement techniques on the contact part. We refer to the recent hp-strategy for a simplified Tresca problem in 2D (Dörsek and Melenk 2010).

The last test shows that the numerical solution is quite insensitive to the choice of the dual Lagrange multiplier basis. We test the discontinuous piecewise constant and linear one (see Figure 3.6(a,b)) and the continuous piecewise cubic one (see Figure 3.7(a)). Table 4.5 shows a comparison of the maximum contact pressure for different Lagrange multipliers. From the very first levels, the maximal value for all the three tested Lagrange multipliers is in very good agreement. Thus the choice of the Lagrange multiplier basis is not relevant as long as the conditions (3.2)–(3.5) are satisfied.

Table 4.5. Maximum contact pressure for different low-order dual Lagrange multipliers.

Level	Linear	Constant	Cubic
1	382.057	382.057	382.057
2	514.166	514.172	514.172
3	504.190	504.229	504.229
4	496.765	496.755	496.755
5	494.805	494.809	494.809
6	494.264	494.266	494.266
7	494.174	494.175	494.175
8	494.202	494.202	494.202

5. Semi-smooth Newton solver in space

Early numerical approaches for two-body contact problems on non-matching meshes and for contact problems with Coulomb friction often tried to weaken the non-linearity by suitable fixed-point or decoupling strategies. Following the proof of existence, a Coulomb friction problem can be reduced to a sequence of simplified problems with given bound for the tangential traction,

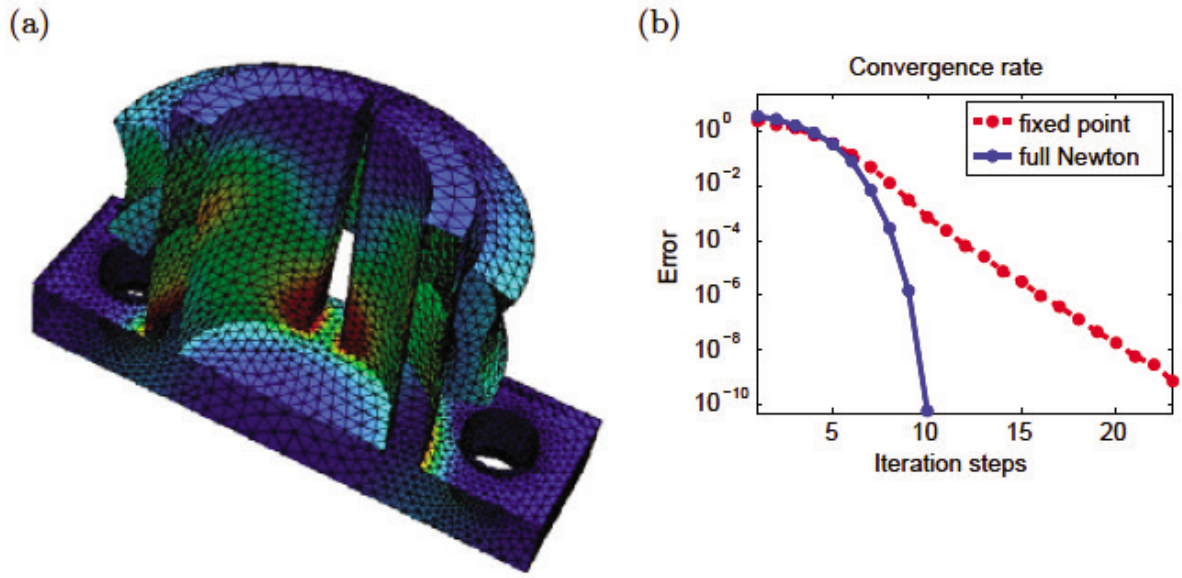

Figure 5.1. Section view of the problem geometry (a) and convergence rate (b).

and thus fixed-point strategies naturally apply, where in each step a contact problem with given friction bound has to be solved numerically. Figure 5.1 shows the convergence rates of two different solvers for a Coulomb contact problem with a complex geometry in 3D. As expected, the simple fixed-point approach has a linear convergence rate, whereas an alternative solver exhibits a super-linear rate.

Using the concept of domain decomposition, a two-sided contact problem can be rewritten as a one-sided contact problem in addition to the equilibrium of contact forces. Thus Dirichlet–Neumann-type algorithms are suitable; see, *e.g.*, Bayada, Sabil and Sassi (2002), Chernov, Geyn, Maischak and Stephan (2006), Chernov *et al.* (2008) and Krause and Wohlmuth (2002). More precisely, in each iteration step we solve on the master side a linear elasticity problem with given surface traction, and on the slave side we consider numerically a non-linear contact problem where the displacement of the master side acts as a rigid obstacle. The update of the interface data is realized globally after each cycle. From a theoretical point of view convergence can only be proved for a sufficiently small damping parameter (see Bayada, Sabil and Sassi (2008) and Eck and Wohlmuth (2003)), and in practice these methods require sophisticated damping strategies and are barely competitive. Figure 5.2 shows the undamped version applied to a long hexahedral bar between two cylinders. The length of the bar highly influences the convergence behaviour. If it is small, then the undamped algorithm shows fast convergence, whereas if the bar is long, no convergence at all is obtained unless a suitable damping parameter is applied.

Although simple to apply, these coupling strategies give rise to inner and outer iteration schemes and are therefore quite expensive. Thus there is a strong need for efficient solvers which focus on all non-linearities at the same time and tackle the fully coupled system.

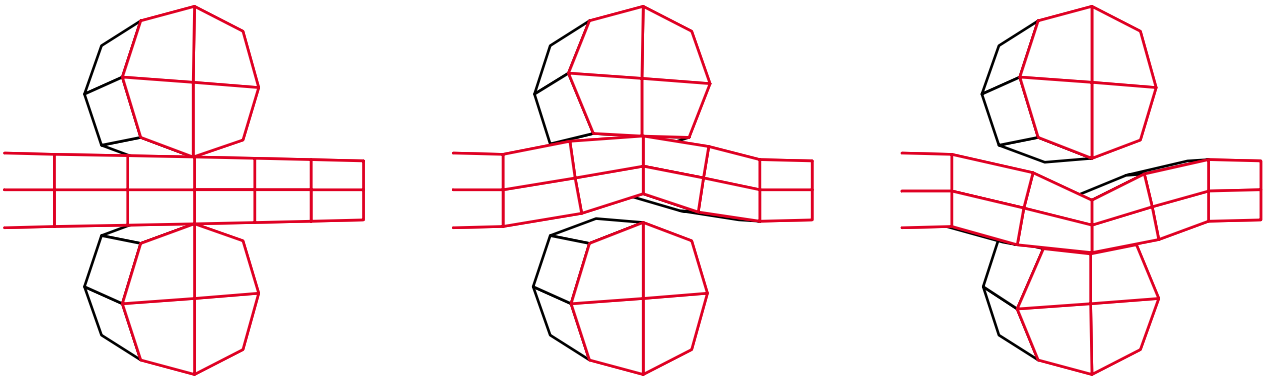

Figure 5.2. Oscillation of an undamped Dirichlet–Neumann contact solver.

Monotone multigrid methods have been shown to be very attractive due to guaranteed convergence, if the underlying system is equivalent to a constrained minimization problem. Early references on multigrid methods for variational inequalities or free boundary problems such as the obstacle problem are given by Brandt and Cryer (1983), Hackbusch and Mittelmann (1983), Hoppe (1987), Hoppe and Kornhuber (1994), Kornhuber (1994, 1996), Kornhuber and Krause (2001) and the monograph by Kornhuber (1997). Nowadays these techniques have been applied very successfully to more challenging contact problems including two bodies with non-matching meshes, finite deformations and complex geometries in 3D (Dickopf and Krause 2009*a*, Krause 2008, 2009, Krause and Mohr 2011, Wohlmuth and Krause 2003).

Domain decomposition-based solvers such as FETI techniques are also widely applied. An excellent overview of these techniques applied to variational inequalities can be found in the recent monograph by Dostál (2009); see also the original research papers of Dostál, Friedlander and Santos (1998), Dostál, Gomes Neto and Santos (2000), Dostál and Horák (2003), Dostál, Horák, Kučera, Vondrák, Haslinger, Dobiaš and Pták (2005), Dostál, Horák and Stefanica (2007, 2009) and Schöberl (1998). Different alternatives exist, *e.g.*, interior point methods (Wright 1997), SQP algorithms (Pang and Gabriel 1993), the radial return mapping or the catching-up algorithm (Moreau 1977, Simo and Hughes 1998), as well as penalty or augmented Lagrangian approaches (Glowinski and Le Tallec 1989, Laursen 2002, Simo and Laursen 1992). We refer to the recent monograph by Ito and Kunisch (2008*a*) for an overview of Lagrange multiplier-based methods for variational problems.

Here we choose an abstract and very flexible framework within which many different applications can be handled. The starting point is the observation that most inequality constraints can be equivalently stated in terms of a non-linear system. This holds true not only for contact problems but also

for other problems involving variational inequalities. The weak form of the underlying partial differential equation and the non-linear complementarity (NCP) function then form a coupled non-linear system on which a Newton scheme can be applied and easily combined with fast iterative solvers, such as multigrid (Hackbusch 1985) or domain decomposition techniques (Toselli and Widlund 2005), for the consistent linearized system. Due to the characteristic lack of classical differentiability of the NCP function, the assumptions for standard Newton methods (Deuflhard 2004) are not satisfied, but the so-called semi-smooth Newton methods (Facchinei and Pang 2003*a*, Ito and Kunisch 2003, Hintermüller, Kovtunenko and Kunisch 2004) can be applied; see also Pang (1990) and Pang and Qi (1993). Early applications of this type of method can be found in the engineering literature. The classical radial return mapping in plasticity (see Moreau (1977) for an early variant of it) can be handled within this abstract framework, but it has also been successfully applied to contact problems for roughly two decades (Alart and Curnier 1991, Christensen 2002*a*, 2002*b*, Christensen and Pang 1999, De Saxcé and Feng 1991, Simo and Laursen 1992). It is well established that the semi-smooth Newton method converges locally super-linearly: see, *e.g.*, the monograph by Facchinei and Pang (2003*b*). Global convergence can be shown for some special cases, *e.g.*, the Laplace operator-based obstacle problem: see Ito and Kunisch (2008*a*). A simplified Signorini problem has been analysed in Ito and Kunisch (2008*b*). For contact problems no global convergence holds, but the pre-asymptotic robustness can, in particular in 3D, be widely improved by a suitable local rescaling of an NCP function and a local node-wise regularization of the Jacobian. In each Newton step, the contact condition and its boundary type have to be updated locally, *e.g.*, a Robin-type condition applies in the case of a sliding node. As a consequence, the semi-smooth Newton method can be implemented as a primal–dual active set strategy (Hintermüller, Ito and Kunisch 2002, Hüeber, Stadler and Wohlmuth 2008, Ito and Kunisch 2004). The use of active sets allows for local static condensation of either the dual variable or the corresponding primal degrees of freedom, such that only a system of the size of the displacement has to be solved in each Newton step. One of the attractive features of this class of algorithms is that it can be easily combined with other types of non-linearities, such as non-linear material laws, for example. No inner and outer iteration loop is required even in the presence of the different types of non-linearities.

5.1. Equivalent formulation as a non-linear equation system

In a first step, we rewrite the inequality constraints associated with the discrete static Coulomb friction problem as a non-linear system. For simplicity of notation, we present the algebraic form only for homogeneous

Dirichlet boundary conditions. Thus, after discretization the weak formulation (3.9) has the following algebraic structure. Find $(\widetilde{\mathbf{u}}_l, \boldsymbol{\lambda}_l) \in \mathbb{R}^{N_l^V} \times \mathbb{R}^{N_l^M}$, $N_l^V := \dim \mathbf{V}_l$, $N_l^M := \dim \mathbf{M}_l$, such that

$$\begin{aligned} \widetilde{A}_l \widetilde{\mathbf{u}}_l + \widetilde{B}_l \boldsymbol{\lambda}_l &= \widetilde{\mathbf{f}}_l, \\ \widetilde{C}_l(\boldsymbol{\lambda}_l, \widetilde{\mathbf{u}}_l) &= \mathbf{0}. \end{aligned} \tag{5.1}$$

Here we use the same symbol for $\boldsymbol{\lambda}_l \in \mathbf{M}_l$ and its vector representation $\boldsymbol{\lambda}_l \in \mathbb{R}^{N_l^M}$. The matrices $\widetilde{A}_l \in \mathbb{R}^{N_l^V \times N_l^V}$, $\widetilde{B}_l \in \mathbb{R}^{N_l^V \times N_l^M}$ and the right-hand side $\widetilde{\mathbf{f}}_l \in \mathbb{R}^{N_l^V}$ result from the bilinear forms $a_l(\cdot,\cdot)$, $b_l(\cdot,\cdot)$ and the linear form $f_l(\cdot)$, respectively, and are assembled with respect to the nodal basis functions ϕ_p, ψ_p. We note that $d\#\mathcal{P}^{\mathrm{s}}_{\mathrm{C};l} =: N_l^{\mathrm{s}} = N_l^M$. The NCP function $\widetilde{C}_l(\cdot,\cdot) \in \mathbb{R}^{N_l^M}$ reflects the non-penetration condition (3.11) and the static Coulomb law (3.12). It has a node-wise form and can be written as $(\widetilde{C}_l(\boldsymbol{\lambda}_l, \widetilde{\mathbf{u}}_l))_p = \widetilde{C}_p(\boldsymbol{\gamma}_p, \widetilde{\mathbf{u}}_l) \in \mathbb{R}^d$, $p \in \mathcal{P}^{\mathrm{s}}_{\mathrm{C};l}$.

There exist many different choices for NCP functions in the literature. Quite often generalizations of the Fischer–Burmeister approach (Fischer 1992) are used. We refer to Chen, Chen and Kanzow (2000) for a penalized version and to Chen (2007), Hu, Huang and Chen (2009), Kanzow, Yamashita and Fukushima (1997) and Sun and Qi (1999) for the introduction and analysis of a family of NCP functions. An excellent overview can be found in the monograph by Facchinei and Pang (2003*a*). Here we use a different type of NCP function, which is based not on the root function but on the max function: see Alart and Curnier (1991). The main advantage of this type of NCP function is that the generalized derivatives are extremely easy to compute. This is quite important if not only the simple non-penetration law is considered but also more complex situations such as Coulomb friction or finite deformations. We refer to the series of recent papers by Gitterle *et al.* (2010) and Popp *et al.* (2009, 2010), where the concept of dual Lagrange multipliers and semi-smooth Newton schemes have been applied to finite deformation problems. Moreover, it can be implemented easily in terms of an active set strategy which switches off and on different types of non-linear boundary conditions on the possible contact zone.

As is standard in the case of radial return mappings, we introduce trial test vectors. Here we need two of them, one in the normal and one in the tangential direction, that is,

$$\gamma^n_{p;\mathrm{tr}} := \gamma^n_p + \frac{2\mu c_n}{m_p}(\alpha^n_p - g_p), \quad \boldsymbol{\gamma}^t_{p;\mathrm{tr}} := \boldsymbol{\gamma}^t_p + \frac{2\mu c_t}{m_p}\boldsymbol{\alpha}^t_p, \tag{5.2}$$

where c_n and c_t are two positive mesh-independent constants. Keeping in mind that $\boldsymbol{\alpha}_p$, $p \in \mathcal{P}^{\mathrm{s}}_{\mathrm{C};l}$, are the coefficients with respect to the nodal basis functions on the slave side of $\boldsymbol{\Pi}_l[\mathbf{u}_l]$, we find that $\boldsymbol{\alpha}_p$ is a function

of $\widetilde{\mathbf{u}}_l$. In terms of these trial vectors, which depend on $\boldsymbol{\gamma}_p$ and $\widetilde{\mathbf{u}}_l$, one can easily reformulate the inequality constraints (3.11) and (3.12) as equality conditions.

Lemma 5.1. The inequality constraints (3.11) and (3.12) for each node $p \in \mathcal{P}^{\mathrm{s}}_{\mathrm{C};l}$ are equivalent to $\widetilde{C}_p(\boldsymbol{\gamma}_p, \widetilde{\mathbf{u}}_l) := C_p(\boldsymbol{\gamma}_p, \boldsymbol{\alpha}_p(\widetilde{\mathbf{u}}_l)) = \mathbf{0}$, where the normal component $C^n_p(\gamma^n_p, \alpha^n_p)$ of $C_p(\boldsymbol{\gamma}_p, \boldsymbol{\alpha}_p)$ is given by

$$C^n_p(\gamma^n_p, \alpha^n_p) := \gamma^n_p - \max(0, \gamma^n_{p;\mathrm{tr}}), \tag{5.3}$$

and the tangential component of $C_p(\boldsymbol{\gamma}_p, \boldsymbol{\alpha}_p)$ is defined by $C^t_p(\boldsymbol{\gamma}_p, \boldsymbol{\alpha}_p) :=$

$$\begin{cases} \boldsymbol{\gamma}^t_p & \mathcal{F}_{p;\mathrm{tr}} = 0, \\ \max\bigl(\|\boldsymbol{\gamma}^t_{p;\mathrm{tr}}\|, \mathcal{F}_{p;\mathrm{tr}}\bigr)^s \left(\boldsymbol{\gamma}^t_p - \min\left(1, \dfrac{\mathcal{F}_{p;\mathrm{tr}}}{\|\boldsymbol{\gamma}^t_{p;\mathrm{tr}}\|}\right)\boldsymbol{\gamma}^t_{p;\mathrm{tr}}\right) & \text{otherwise}, \end{cases} \tag{5.4}$$

where $s \geq 0$ stands for a scaling parameter and $\mathcal{F}_{p;\mathrm{tr}} := \nu \max(0, \gamma^n_{p;\mathrm{tr}})$.

Proof. The proof is a rather straightforward calculation, but for convenience of the reader it is given. If $C^n_p(\gamma^n_p, \alpha^n_p) = 0$, then obviously $\gamma^n_p \geq 0$. If $\gamma^n_p = 0$, we get $\alpha^n_p - g_p \leq 0$, and for $\gamma^n_p > 0$, we have $\alpha^n_p = g_p$, and thus (3.11) is satisfied. Let $C^n_p(\gamma^n_p, \alpha^n_p) = 0$ and $C^t_p(\boldsymbol{\gamma}_p, \boldsymbol{\alpha}_p) = \mathbf{0}$; then $\mathcal{F}_{p;\mathrm{tr}} = \nu\gamma^n_p$. In the case $\mathcal{F}_{p;\mathrm{tr}} = 0$, (3.12) trivially holds. For $\mathcal{F}_{p;\mathrm{tr}} > 0$, the scaling factor $\max\bigl(\|\boldsymbol{\gamma}^t_{p;\mathrm{tr}}\|, \mathcal{F}_{p;\mathrm{tr}}\bigr)^s$ is non-zero, and thus from $C^t_p(\boldsymbol{\gamma}_p, \boldsymbol{\alpha}_p) = \mathbf{0}$ it follows that

$$\boldsymbol{\gamma}^t_p = \min\left(1, \frac{\mathcal{F}_{p;\mathrm{tr}}}{\|\boldsymbol{\gamma}^t_{p;\mathrm{tr}}\|}\right)\boldsymbol{\gamma}^t_{p;\mathrm{tr}}.$$

If $\|\boldsymbol{\gamma}^t_{p;\mathrm{tr}}\| \leq \nu\gamma^n_p$, then $\boldsymbol{\gamma}^t_p - \boldsymbol{\gamma}^t_{p;\mathrm{tr}} = \mathbf{0}$, and thus $\boldsymbol{\alpha}^t_p = \mathbf{0}$ and $\|\boldsymbol{\gamma}^t_p\| \leq \nu\gamma^n_p$. For $\|\boldsymbol{\gamma}^t_{p;\mathrm{tr}}\| > \nu\gamma^n_p$, we get $\|\boldsymbol{\gamma}^t_p\| = \nu\gamma^n_p$. Moreover, $\boldsymbol{\gamma}^t_{p;\mathrm{tr}} = (1+\beta)\boldsymbol{\gamma}^t_p$ with some positive value for β. Using the definition (5.2) of $\boldsymbol{\gamma}^t_{p;\mathrm{tr}}$, we find that $\boldsymbol{\alpha}^t_p$ points in the same direction as $\boldsymbol{\gamma}^t_p$ and thus (3.12) is satisfied.

Let (3.11) be true; then a straightforward computation shows that we have $C^n_p(\gamma^n_p, \alpha^n_p) = 0$. The situation is more complex for the discrete Coulomb law. If (3.11) and (3.12) hold, then either $\boldsymbol{\alpha}^t_p = \mathbf{0}$ or it points in the same direction as $\boldsymbol{\gamma}^t_p$ or $\gamma^n_p = 0$. In the first two cases, we can thus write $\boldsymbol{\gamma}^t_{p;\mathrm{tr}} = (1+\beta)\boldsymbol{\gamma}^t_p$ with some non-negative β. For $\beta = 0$, we trivially find that $\boldsymbol{\gamma}^t_{p;\mathrm{tr}} = \boldsymbol{\gamma}^t_p$ and thus $C^t_p(\boldsymbol{\gamma}_p, \boldsymbol{\alpha}_p) = \mathbf{0}$. For $\beta > 0$, we have $\|\boldsymbol{\gamma}^t_p\| = \nu\gamma^n_p$ and moreover $\|\boldsymbol{\gamma}^t_{p;\mathrm{tr}}\| > \nu\gamma^n_p$, yielding

$$\boldsymbol{\gamma}^t_p - \min\left(1, \frac{\mathcal{F}_{p;\mathrm{tr}}}{\|\boldsymbol{\gamma}^t_{p;\mathrm{tr}}\|}\right)\boldsymbol{\gamma}^t_{p;\mathrm{tr}} = \boldsymbol{\gamma}^t_p - \frac{1}{1+\beta}\boldsymbol{\gamma}^t_{p;\mathrm{tr}} = \boldsymbol{\gamma}^t_p - \frac{1+\beta}{1+\beta}\boldsymbol{\gamma}^t_p = \mathbf{0}.$$

The case that $\gamma^n_p = 0$ yields $\mathcal{F}_{p;\mathrm{tr}} = 0$ and $\boldsymbol{\gamma}^t_p = \mathbf{0}$ and thus $C^t_p(\boldsymbol{\gamma}_p, \boldsymbol{\alpha}_p) = \mathbf{0}$. □

Remark 5.2. We note that (3.11) and (5.3) are equivalent but (3.12) and (5.4) are not. In particular, the trial vector in the normal direction enters into the definition of $C_p^t(\boldsymbol{\gamma}_p, \boldsymbol{\alpha}_p)$.

5.2. Basis transformation: from nodal to constrained

As already mentioned, from the algebraic point of view each two-body problem can be rewritten formally as a one-body problem by introducing a new basis. The weak inequalities then result in node-wise inequalities for the slave side, even in the case of non-matching meshes. One of the main advantages of the choice of a dual Lagrange multiplier space is that the basis transformation is a local operator with a sparse matrix representation. This is not the case for standard Lagrange multipliers.

Although $\widetilde{C}_p(\boldsymbol{\gamma}_p, \widetilde{\mathbf{u}}_l)$ only depends on the nodal coefficient of $\boldsymbol{\lambda}_l$ at p, it does not have this simple structure with respect to $\widetilde{\mathbf{u}}_l$. A more local and thus implementationally attractive representation can be obtained by a suitable basis transformation. This transformation was introduced in Wohlmuth and Krause (2001) to construct a multigrid scheme for mortar finite element discretizations. The $\mathcal{V}$-cycle analysis of a level-independent convergence rate can be found in Wohlmuth (2005).

Introducing the nodal block structure for the displacement

$$\widetilde{\mathbf{u}}_l = (\widetilde{\mathbf{u}}_l^{\mathrm{i}}, \widetilde{\mathbf{u}}_l^{\mathrm{m}}, \widetilde{\mathbf{u}}_l^{\mathrm{s}})^\top, \quad \widetilde{\mathbf{u}}_l^{\mathrm{i}} \in \mathbb{R}^{N_l^{\mathrm{i}}}, \quad \widetilde{\mathbf{u}}_l^{\mathrm{m}} \in \mathbb{R}^{N_l^{\mathrm{m}}}, \quad \widetilde{\mathbf{u}}_l^{\mathrm{s}} \in \mathbb{R}^{N_l^{\mathrm{s}}},$$

where $N_l^{\mathrm{m}} := d\#\mathcal{P}_{\mathrm{C};l}^{\mathrm{m}}$ and $N_l^{\mathrm{i}} := N_l^V - N_l^{\mathrm{m}} - N_l^{\mathrm{s}}$ (see also Figure 5.3), we obtain the following structure for $\widetilde{A}_l$ and $\widetilde{B}_l$:

$$\widetilde{A}_l = \begin{pmatrix} \widetilde{A}_l^{\mathrm{i,i}} & \widetilde{A}_l^{\mathrm{i,m}} & \widetilde{A}_l^{\mathrm{i,s}} \\ \widetilde{A}_l^{\mathrm{m,i}} & \widetilde{A}_l^{\mathrm{m,m}} & 0 \\ \widetilde{A}_l^{\mathrm{s,i}} & 0 & \widetilde{A}_l^{\mathrm{s,s}} \end{pmatrix}, \quad \widetilde{B}_l = \begin{pmatrix} 0 \\ -M_l^\top \\ D_l \end{pmatrix},$$

where the entries of the coupling matrices D_l and M_l are defined by

$$d_{pp} := m_p \mathrm{Id}_{d\times d}, \quad m_{pq} := \int_{\Gamma_{\mathrm{C};l}^{\mathrm{s}}} \psi_p \phi_q \circ \chi_l \, \mathrm{d}s \, \mathrm{Id}_{d\times d}, \quad p \in \mathcal{P}_{\mathrm{C};l}^{\mathrm{s}}, q \in \mathcal{P}_{\mathrm{C};l}^{\mathrm{m}}.$$

The diagonal structure of D_l is a consequence of (3.6). In the case of standard Lagrange multipliers D_l has the band-structure of a $(d-1)$-dimensional mass matrix, and thus D_l^{-1} is dense.

We recall that, with respect to the nodal basis functions, the coefficient $\boldsymbol{\alpha}_p$ in (3.11) and (3.12) does depend on the coefficients of the master and the slave nodes. The definition (3.10) of the mortar projection yields that

$$(\boldsymbol{\alpha}_p)_{p\in\mathcal{P}_{\mathrm{C};l}^{\mathrm{s}}} =: \boldsymbol{\alpha} = \widetilde{\mathbf{u}}_l^{\mathrm{s}} - D_l^{-1} M_l \widetilde{\mathbf{u}}_l^{\mathrm{m}}.$$

To eliminate the dependence of the coefficient vector on the master side, we

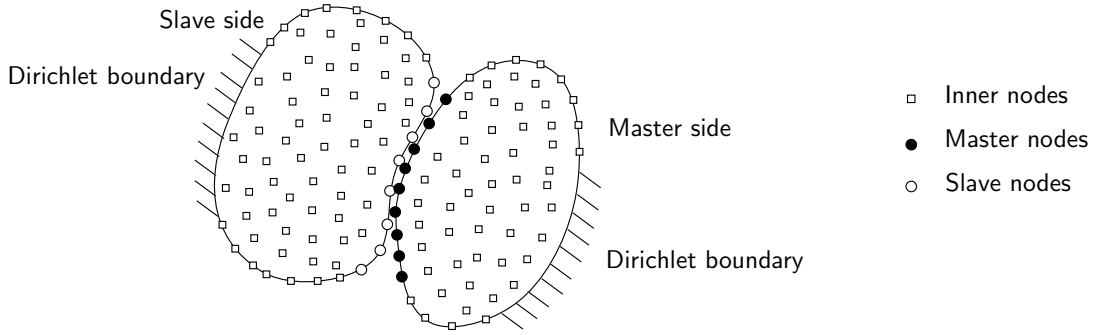

Figure 5.3. Partitioning of the nodes into the three blocks.

use a basis transformation. The nodal basis function ϕ_p, $p \in \mathcal{P}^{\mathrm{m}}_{\mathrm{C};l}$, will be replaced by a constrained basis function

$$\tilde{\phi}_p := \phi_p + \sum_{q \in \mathcal{P}^{\mathrm{s}}_{\mathrm{C};l}} r_{pq} \phi_q, \tag{5.5}$$

while all other basis functions remain unchanged, *i.e.*, $\tilde{\phi}_p := \phi_p$, $p \in \mathcal{P}_l \backslash \mathcal{P}^{\mathrm{m}}_{\mathrm{C};l}$.

Lemma 5.3. Setting $r_{pq} := ((D_l^{-1} M_l)_{qp})_{11}$, $q \in \mathcal{P}^{\mathrm{s}}_{\mathrm{C};l}$, $p \in \mathcal{P}^{\mathrm{m}}_{\mathrm{C};l}$ in (5.5) gives

$$\Pi_l[\tilde{\phi}_p] = 0, \quad p \in \mathcal{P}^{\mathrm{m}}_{\mathrm{C};l}.$$

Proof. The definition of the mortar projection (3.10a) shows that Π_l, restricted to W_l^{s}, is the identity and that

$$\Pi_l(\phi_p \circ \chi_l) = \sum_{q \in \mathcal{P}^{\mathrm{s}}_{\mathrm{C};l}} r_{pq} \phi_q, \quad p \in \mathcal{P}^{\mathrm{m}}_{\mathrm{C};l}$$

and thus

$$\Pi_l[\tilde{\phi}_p] = \sum_{q \in \mathcal{P}^{\mathrm{s}}_{\mathrm{C};l}} r_{pq} \phi_q - \Pi_l(\phi_p \circ \chi_l) = 0. \qquad \square$$

Algebraically this basis transformation can be realized very efficiently in a local pre-process. The coefficients with respect to the constrained basis multiplied by the matrix

$$Q_l = \begin{pmatrix} \mathrm{Id} & 0 & 0 \\ 0 & \mathrm{Id} & 0 \\ 0 & D_l^{-1} M_l & \mathrm{Id} \end{pmatrix} \tag{5.6}$$

yield the coefficients with respect to the nodal basis. If $\mathbf{v}_l = \sum_{p \in \mathcal{P}_l} \tilde{\boldsymbol{\beta}}_p \phi_p$, then $\mathbf{v}_l = \sum_{p \in \mathcal{P}_l} \boldsymbol{\beta}_p \tilde{\phi}_p$ with $(\tilde{\boldsymbol{\beta}}_p)_{p \in \mathcal{P}_l} = Q_l (\boldsymbol{\beta}_p)_{p \in \mathcal{P}_l}$. To obtain the stiffness matrices A_l, B_l and the right-hand side $\mathbf{f}_l$ with respect to the new constrained basis, we have to apply Q_l in a suitable way on $\widetilde{A}_l$, $\widetilde{B}_l$ and $\widetilde{\mathbf{f}}_l$:

$$A_l = Q_l^\top \widetilde{A}_l Q_l, \quad B_l = Q_l^\top \widetilde{B}_l, \quad \mathbf{f}_l = Q_l^\top \widetilde{\mathbf{f}}_l.$$

Due to the definition (5.6) of Q_l, it is easy to verify that the block structure of the matrix B_l, with respect to this new basis, has the form $B_l = (0,\, 0,\, D_l)^\top$. The non-linear system to be solved is equivalent to (5.1), and can be written as

$$\begin{aligned} A_l \mathbf{u}_l + B_l \boldsymbol{\lambda}_l &= \mathbf{f}_l, \\ C_p(\boldsymbol{\gamma}_p, \mathbf{u}_p) &= \mathbf{0}, \quad p \in \mathcal{P}^{\mathrm{s}}_{\mathrm{C};l}. \end{aligned} \tag{5.7}$$

Here we have used that, with respect to the new basis, $\boldsymbol{\alpha}_p = \mathbf{u}_p$, $p \in \mathcal{P}^{\mathrm{s}}_{\mathrm{C};l}$. We point out that the same notation for $\mathbf{u}_l \in \mathbf{V}_l$ is applied as for its coefficient vector $\mathbf{u}_l \in \mathbb{R}^{N_l^V}$ with respect to the new constrained basis. Finally, we mention that, with respect to this new basis, the p-component of the NCP function only depends on the p-component of $\boldsymbol{\lambda}_l$ and $\mathbf{u}_l$. The coefficients in the new basis with respect to the slave nodes no longer specify the total nodal displacement but now describe the movement of the underlying finite element node relative to the master side. Having $\mathbf{u}_l$, the Lagrange multiplier can easily be obtained, from the node-wise residual, by a diagonal scaling

$$\boldsymbol{\lambda}_l = D_l^{-1}(\mathbf{f}_l^s - A_l^{\mathrm{si}}\mathbf{u}_l^{\mathrm{i}} - A_l^{\mathrm{sm}}\mathbf{u}_l^{\mathrm{m}} - A_l^{\mathrm{ss}}\mathbf{u}_l^{\mathrm{s}}). \tag{5.8}$$

Remark 5.4. Such a basis transformation can be carried out for all types of Lagrange multiplier spaces as long as a discrete inf-sup condition holds. In most cases, it will result in a dense block corresponding to the possibly global character of the mortar projection. However, in our situation the basis transformation is a local operator for all space dimensions and thus inexpensive. Moreover, for uniformly stable pairs $(\mathbf{V}_l, \mathbf{M}_l)$, the basis transformation does not influence the order of the condition number of A_l, which is then comparable to that of $\widetilde{A}_l$.

5.3. Semi-smooth Newton solver

As can be easily seen from (5.3) and (5.4), the NCP function $C_p(\boldsymbol{\gamma}_p, \mathbf{u}_p)$ is not globally but only piecewise smooth. Thus, to solve (5.7), a Newton-type solver can be implemented in terms of an active set strategy. The active and inactive sets are defined by the different cases of $C_p(\cdot,\cdot)$ and can be selected node-wise.

Let $(\boldsymbol{\lambda}_l^{k-1}, \mathbf{u}_l^{k-1})$ be the previous iterate. We then obtain the new iterate

$$(\boldsymbol{\lambda}_l^{k}, \mathbf{u}_l^{k}) = (\boldsymbol{\lambda}_l^{k-1}, \mathbf{u}_l^{k-1}) + (\delta\boldsymbol{\lambda}_l^{k-1}, \delta\mathbf{u}_l^{k-1})$$

of the semi-smooth Newton step by solving a linear system for the update $(\delta\boldsymbol{\lambda}_l^{k-1}, \delta\mathbf{u}_l^{k-1})$. For each node $p \in \mathcal{P}^{\mathrm{s}}_{\mathrm{C};l}$, the local system

$$DC_p\big(\boldsymbol{\gamma}_p^{k-1}, \mathbf{u}_p^{k-1}\big)\big(\delta\boldsymbol{\gamma}_p^{k-1}, \delta\mathbf{u}_p^{k-1}\big)^\top = -C_p\big(\boldsymbol{\gamma}_p^{k-1}, \mathbf{u}_p^{k-1}\big) \tag{5.9}$$

has to be satisfied. Here, DC_p denotes the Jacobian of the local NCP function $C_p(\cdot,\cdot)$. We note that due to our basis transformation, DC_p can

be regarded as a $d \times 2d$ matrix. Defining the trial vectors of the increment $(\delta\boldsymbol{\gamma}_p, \delta\mathbf{u}_p)$, in a way similar to (5.2), by

$$\delta\gamma_{p;\mathrm{tr}}^n := \delta\gamma_p^n + \frac{2\mu c_n}{m_p}\delta u_p^n, \quad \delta\boldsymbol{\gamma}_{p;\mathrm{tr}}^t := \delta\boldsymbol{\gamma}_p^t + \frac{2\mu c_t}{m_p}\delta\mathbf{u}_p^t,$$

we introduce three sets in terms of $S_n(\boldsymbol{\gamma}_p, \mathbf{u}_p) := S_n := \max(0, \gamma_{p;\mathrm{tr}}^n)$:

$$\begin{aligned}
\mathcal{I}_n &:= \mathcal{I}_n(\boldsymbol{\gamma}_p, \mathbf{u}_p) := \big\{p \in \mathcal{P}_{\mathrm{C};l}^{\mathrm{s}} \,:\, S_n = 0\big\},\\
\mathcal{I}_t &:= \mathcal{I}_t(\boldsymbol{\gamma}_p, \mathbf{u}_p) := \big\{p \in \mathcal{P}_{\mathrm{C};l}^{\mathrm{s}} \,:\, \|\boldsymbol{\gamma}_{p;\mathrm{tr}}^t\| < \nu S_n\big\},\\
\mathcal{A} &:= \mathcal{A}(\boldsymbol{\gamma}_p, \mathbf{u}_p) := \big\{p \in \mathcal{P}_{\mathrm{C};l}^{\mathrm{s}} \,:\, \|\boldsymbol{\gamma}_{p;\mathrm{tr}}^t\| \geq \nu S_n, S_n > 0\big\}.
\end{aligned} \tag{5.10}$$

Now, we can easily define the generalized derivative $DC_p(\cdot,\cdot)$ for each $p \in \mathcal{P}_{\mathrm{C};l}^{\mathrm{s}}$ in the direction of the update $\big(\delta\boldsymbol{\gamma}_p, \delta\mathbf{u}_p\big)$. We observe that $\mathcal{I}_n$, $\mathcal{I}_t$ and $\mathcal{A}$ form a non-overlapping partition of $\mathcal{P}_{\mathrm{C};l}^{\mathrm{s}}$. On $\mathcal{I}_n$ the nodes are free and not in contact and no boundary forces apply. On $\mathcal{I}_t \cup \mathcal{A}$ the nodes are actually in contact and sliding on $\mathcal{A}$.

Before we discuss the general case, we focus on $\nu = 0$. Here $\mathcal{I}_t = \emptyset$, and the Newton algorithm simplifies considerably. Observing that the tangential component of $C_p(\cdot,\cdot)$ is then linear, we get

$$DC_p(\boldsymbol{\gamma}_p, \mathbf{u}_p)(\delta\boldsymbol{\gamma}_p, \delta\mathbf{u}_p) = \begin{cases} (\delta\gamma_p^n, \delta\boldsymbol{\gamma}_p^t)^\top & p \in \mathcal{I}_n,\\ (\delta\gamma_p^n - \delta\gamma_{p;\mathrm{tr}}^n, \delta\boldsymbol{\gamma}_p^t)^\top & p \in \mathcal{A}. \end{cases}$$

The Newton update (5.9) then gives $(\boldsymbol{\gamma}_p)^k = \mathbf{0}$ for $p \in \mathcal{I}_n^k := \mathcal{I}_n(\gamma_p^{k-1}, \mathbf{u}_p^{k-1})$ and $(\boldsymbol{\gamma}_p^t)^k = \mathbf{0}$, $(u_p^n)^k = g_p$ for $p \in \mathcal{A}^k := \mathcal{A}(\gamma_p^{k-1}, \mathbf{u}_p^{k-1})$. For all possible contact nodes, we have a homogeneous Neumann boundary condition in the tangential direction, whereas in the normal direction we have a Dirichlet or Neumann condition. Thus, the implementation can be easily realized as a primal–dual active set strategy.

The situation is more involved for $\nu > 0$. For a Coulomb problem with a non-trivial friction coefficient, we obtain three different situations for $C_p := C_p(\boldsymbol{\gamma}_p, \mathbf{u}_p)$ and $DC_p := DC_p(\boldsymbol{\gamma}_p, \mathbf{u}_p)(\delta\boldsymbol{\gamma}_p, \delta\mathbf{u}_p)$. Using the differential

$$\partial\frac{\mathbf{x}}{\|\mathbf{x}\|} = \frac{1}{\|x\|}\left(\mathrm{Id} \;- \frac{\mathbf{x}\otimes\mathbf{x}}{\|\mathbf{x}\|^2}\right), \quad \mathbf{x} \neq \mathbf{0},$$

a straightforward computation shows the following.

- If $p \in \mathcal{I}_n$, then $C_p = (\gamma_p^n, \boldsymbol{\gamma}_p^t)^\top$ and

$$DC_p = \begin{pmatrix} \delta\gamma_p^n \\ \delta\boldsymbol{\gamma}_p^t \end{pmatrix}.$$

- If $p \in \mathcal{I}_t$, then $C_p = (\gamma_p^n - \gamma_{p;\mathrm{tr}}^n, (\nu\gamma_{p;\mathrm{tr}}^n)^s(\boldsymbol{\gamma}_p^t - \boldsymbol{\gamma}_{p;\mathrm{tr}}^t))^\top$,

$$DC_p = \begin{pmatrix} \delta\gamma_p^n - \delta\gamma_{p;\mathrm{tr}}^n \\ (\nu\gamma_{p;\mathrm{tr}}^n)^s\big(\delta\boldsymbol{\gamma}_p^t - \delta\boldsymbol{\gamma}_{p;\mathrm{tr}}^t + \frac{s}{\gamma_{p;\mathrm{tr}}^n}\delta\gamma_{p;\mathrm{tr}}^n(\boldsymbol{\gamma}_p^t - \boldsymbol{\gamma}_{p;\mathrm{tr}}^t)\big) \end{pmatrix}.$$

- If $p \in \mathcal{A}$, then $C_p = (\gamma_p^n - \gamma_{p;\mathrm{tr}}^n, \|\boldsymbol{\gamma}_{p;\mathrm{tr}}^t\|^s(\boldsymbol{\gamma}_p^t + \alpha_2\boldsymbol{\gamma}_{p;\mathrm{tr}}^t))^\top$,

$$DC_p = \begin{pmatrix} \delta\gamma_p^n - \delta\gamma_{p;\mathrm{tr}}^n \\ \|\boldsymbol{\gamma}_{p;\mathrm{tr}}^t\|^s\big(\delta\boldsymbol{\gamma}_p^t + \alpha_1\boldsymbol{\gamma}_p^t + \alpha_2\delta\boldsymbol{\gamma}_{p;\mathrm{tr}}^t + \alpha_3\boldsymbol{\gamma}_{p;\mathrm{tr}}^t\big) \end{pmatrix},$$

  where the factors α_1, α_2 and α_3 are given by

$$\begin{aligned} \alpha_1 :=& s\frac{\boldsymbol{\gamma}_{p;\mathrm{tr}}^t\delta\boldsymbol{\gamma}_{p;\mathrm{tr}}^t}{\|\boldsymbol{\gamma}_{p;\mathrm{tr}}^t\|^2}, \quad \alpha_2 := -\frac{\nu\gamma_{p;\mathrm{tr}}^n}{\|\boldsymbol{\gamma}_{p;\mathrm{tr}}^t\|}, \\ \alpha_3 :=& (1-s)\frac{\nu\gamma_{p;\mathrm{tr}}^n}{\|\boldsymbol{\gamma}_{p;\mathrm{tr}}^t\|^3}(\delta\boldsymbol{\gamma}_{p;\mathrm{tr}}^t\boldsymbol{\gamma}_{p;\mathrm{tr}}^t) - \frac{\nu\delta\gamma_{p;\mathrm{tr}}^n}{\|\boldsymbol{\gamma}_{p;\mathrm{tr}}^t\|}. \end{aligned}$$

For all cases, the normal component of the NCP function is linear; this is not the case for the tangential component. Only for $p \in \mathcal{I}_n$ do we have a linear tangential component. Here, we restrict ourselves to $s \in [0,1]$ and note that for $s = 0$ or $s = 1$ some of the terms cancel.

Lemma 5.5. The semi-smooth Newton solver applied to (5.7) can be implemented as a primal–dual active set strategy, where in each Newton step we have to update for each node $p \in \mathcal{P}_{\mathrm{C};l}^{\mathrm{s}}$ the type and the value of the boundary condition. Moreover, for $\nu > 0$ we have the following.

- Homogeneous Neumann conditions for $p \in \mathcal{I}_n^k := \mathcal{I}_n(\boldsymbol{\gamma}_p^{k-1}, \mathbf{u}_p^{k-1})$:

$$(\boldsymbol{\gamma}_p)^k = \mathbf{0} \tag{5.11}$$

- Inhomogeneous Dirichlet conditions for $p \in \mathcal{I}_t^k := \mathcal{I}_t(\boldsymbol{\gamma}_p^{k-1}, \mathbf{u}_p^{k-1})$:

$$(u_p^n)^k = g_p \quad \text{and} \quad (\mathbf{u}_p^t)^k = \frac{-s(\delta\gamma_{p;\mathrm{tr}}^n)^{k-1}}{(\gamma_{p;\mathrm{tr}}^n)^{k-1}}(\mathbf{u}_p^t)^{k-1}, \tag{5.12}$$

  where the condition in the tangential direction also depends on the update of the normal surface traction.

- Dirichlet conditions in the normal and Robin conditions in the tangential direction for $p \in \mathcal{A}^k := \mathcal{A}(\boldsymbol{\gamma}_p^{k-1}, \mathbf{u}_p^{k-1})$:

$$(u_p^n)^k = g_p \quad \text{and} \tag{5.13a}$$

$$(\mathrm{Id} + L_{p;s}^{k-1})(\boldsymbol{\gamma}_p^t)^k + \hat{c}_t L_{p;s}^{k-1}(\mathbf{u}_p^t)^k - \frac{\nu(\gamma_p^n)^k(\boldsymbol{\gamma}_{p;\mathrm{tr}}^t)^{k-1}}{\|(\boldsymbol{\gamma}_{p;\mathrm{tr}}^t)^{k-1}\|} = \mathbf{g}_p^{k-1}, \tag{5.13b}$$

  where $\mathbf{g}_p^{k-1} := L_{p;s}^{k-1}(\boldsymbol{\gamma}_{p;\mathrm{tr}}^t)^{k-1}$, the mesh-dependent scaling factor $\hat{c}_t$ is

given by $\hat{c}_t := \frac{2\mu c_t}{m_p}$ and the matrix $L_{p;s}^{k-1}$ by

$$L_{p;s}^{k-1} := \beta_p^{k-1}\left(\alpha_2^{k-1}\mathrm{Id} + \frac{sL_1^{k-1} + (s-1)\alpha_2^{k-1}L_2^{k-1}}{\|(\boldsymbol{\gamma}_{p;\mathrm{tr}}^t)^{k-1}\|^2}\right),$$

$$\alpha_2^{k-1} := -\frac{\nu(\gamma_{p;\mathrm{tr}}^n)^{k-1}}{\|(\boldsymbol{\gamma}_{p;\mathrm{tr}}^t)^{k-1}\|}, \quad \beta_p^{k-1} := 1, \quad \omega_p^{k-1} := 1,$$

$$L_1^{k-1} := \omega_p^{k-1}(\boldsymbol{\gamma}_p^t)^{k-1} \otimes (\boldsymbol{\gamma}_{p;\mathrm{tr}}^t)^{k-1}, \quad L_2^{k-1} := (\boldsymbol{\gamma}_{p;\mathrm{tr}}^t)^{k-1} \otimes (\boldsymbol{\gamma}_{p;\mathrm{tr}}^t)^{k-1}.$$

Proof. The proof is based on (5.9) and the partitioning (5.10). For each node $p \in \mathcal{I}_n^k$, we get

$$\begin{pmatrix}(\delta\gamma_p^n)^{k-1}\\(\delta\boldsymbol{\gamma}_p^t)^{k-1}\end{pmatrix} = -\begin{pmatrix}(\gamma_p^n)^{k-1}\\(\boldsymbol{\gamma}_p^t)^{k-1}\end{pmatrix}$$

and thus (5.11). From now on, to simplify the notation we suppress the upper index $k-1$ of the Newton iteration.

If $p \in \mathcal{I}_t^k$, then

$$\begin{pmatrix}\delta\gamma_p^n - \delta\gamma_{p;\mathrm{tr}}^n\\\left(\delta\boldsymbol{\gamma}_p^t - \delta\boldsymbol{\gamma}_{p;\mathrm{tr}}^t + \frac{s}{\gamma_{p;\mathrm{tr}}^n}\delta\gamma_{p;\mathrm{tr}}^n(\boldsymbol{\gamma}_p^t - \boldsymbol{\gamma}_{p;\mathrm{tr}}^t)\right)\end{pmatrix} = -\begin{pmatrix}\gamma_p^n - \gamma_{p;\mathrm{tr}}^n\\(\boldsymbol{\gamma}_p^t - \boldsymbol{\gamma}_{p;\mathrm{tr}}^t)\end{pmatrix}.$$

Observing that

$$\gamma_p^n - \gamma_{p;\mathrm{tr}}^n = \frac{2\mu c_n}{m_p}(g_p - u_p^n) \quad \text{and} \quad \delta\gamma_p^n - \delta\gamma_{p;\mathrm{tr}}^n = -\frac{2\mu c_n}{m_p}\delta u_p^n,$$

we get the normal part of (5.12). For the tangential part, we use

$$\boldsymbol{\gamma}_p^t - \boldsymbol{\gamma}_{p;\mathrm{tr}}^t = -\frac{2\mu c_n}{m_p}\mathbf{u}_p^t \quad \text{and} \quad \delta\boldsymbol{\gamma}_p^t - \delta\boldsymbol{\gamma}_{p;\mathrm{tr}}^t = -\frac{2\mu c_n}{m_p}\delta\mathbf{u}_p^t.$$

For $p \in \mathcal{A}^k$, we find the same condition as in (5.12) for the normal part and thus (5.13a). Using the tangential component of the system (5.9), we find

$$\partial\boldsymbol{\gamma}_p^t + \alpha_1\boldsymbol{\gamma}_p^t + \alpha_2\delta\boldsymbol{\gamma}_{p;\mathrm{tr}}^t + \alpha_3\boldsymbol{\gamma}_{p;\mathrm{tr}}^t = -\boldsymbol{\gamma}_p^t - \alpha_2\boldsymbol{\gamma}_{p;\mathrm{tr}}^t. \tag{5.14}$$

Unfortunately, the new unknown updates are hidden in the coefficients α_1 and α_3. Using the definition of the matrix $L_{p;s}$ and applying the formula $(\mathbf{x}\otimes\mathbf{y})\mathbf{z} = (\mathbf{y}\mathbf{z})\mathbf{x}$, we get

$$\begin{aligned}\alpha_1\boldsymbol{\gamma}_p^t + \alpha_3\boldsymbol{\gamma}_{p;\mathrm{tr}}^t &= (L_{p;s} - \alpha_2\mathrm{Id})\delta\boldsymbol{\gamma}_{p;\mathrm{tr}}^t - \frac{\nu\delta\gamma_{p;\mathrm{tr}}^n}{\|\boldsymbol{\gamma}_{p;\mathrm{tr}}^t\|}\boldsymbol{\gamma}_{p;\mathrm{tr}}^t\\ &= (L_{p;s} - \alpha_2\mathrm{Id})\delta\boldsymbol{\gamma}_{p;\mathrm{tr}}^t - \frac{\nu(\gamma_{p;\mathrm{tr}}^n)^k}{\|\boldsymbol{\gamma}_{p;\mathrm{tr}}^t\|}\boldsymbol{\gamma}_{p;\mathrm{tr}}^t - \alpha_2\boldsymbol{\gamma}_{p;\mathrm{tr}}^t.\end{aligned}$$

Using (5.13a), which guarantees that $(\gamma_{p;\mathrm{tr}}^n)^k = (\gamma_p^n)^k$, and inserting the equality for $\alpha_1\boldsymbol{\gamma}_p^t + \alpha_3\boldsymbol{\gamma}_{p;\mathrm{tr}}^t$ in (5.14), we get (5.13b). □

Remark 5.6. If a non-local friction law or a simple combination of Coulomb friction and Tresca friction is applied, possibly more cases have to be considered, we refer to Hager and Wohlmuth (2009*b*) for an abstract framework. If the friction bound depends not only on the contact pressure, then nodes which are not in contact are not automatically surface traction-free nodes.

Table 5.1 shows the convergence rate of the semi-smooth Newton scheme with $s = 1$ applied to the 2D contact problem with given friction bound depicted in Figure 4.3. Here we have used a discrete mesh-dependent norm for the Lagrange multiplier. The third column shows the ratio of the error in step k and $k-1$. As expected, from the theoretical point of view, this ratio tends to zero.

Table 5.1. Super-linear convergence for the semi-smooth Newton scheme applied to a contact problem with given friction bound.

k	$e^k := \|\boldsymbol{\lambda}_l^k - \boldsymbol{\lambda}_l\|$	e^k/e^{k-1}
1	5.622e+02	–
2	2.553e+02	4.541e−01
3	1.087e+02	4.257e−01
4	3.515e+01	3.233e−01
5	5.761e+00	1.638e−01
6	2.362e−01	4.100e−02
7	3.360e−03	1.422e−02
8	1.760e−07	5.239e−05
9	1.004e−12	5.707e−06

For now, we do not comment on the solvability of the global system. However, we note that if convergence can be achieved, then the Newton update will converge to zero and thus (5.12) yields that the physical condition of a sticky node is satisfied, *i.e.*, the relative tangential displacement is equal to zero. However, in contrast to the physical non-penetration condition, it is not directly imposed as one might expect from a primal–dual active set strategy. A value for s strictly smaller than one provides an additional damping. Moreover, (5.12) and (5.13b) show that the Newton solver couples the tangential and normal parts in the boundary conditions.

Figure 5.4 shows the influence of the friction coefficient ν on the convergence rate of the semi-smooth Newton scheme applied to a 3D contact problem. A comparison between a fixed-point approach and the Newton solver is given. For all three cases, super-linear rates are obtained for the

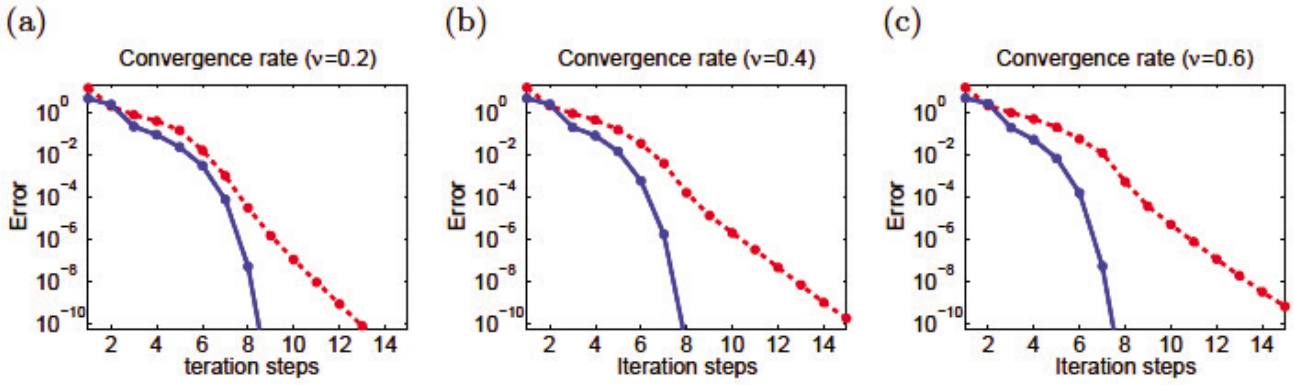

Figure 5.4. (a) $\nu = 0.2$, (b) $\nu = 0.4$, (c) $\nu = 0.6$.

semi-smooth Newton algorithm. The number of Newton steps required is quite insensitive to the friction coefficient, whereas for the simple fixed-point approach more iteration steps are required for a larger ν.

5.4. Influence of the scaling parameter

It is well known, *e.g.*, in plasticity, that the classical radial return algorithm, which is equivalent to setting $s = 0$, does not converge for large load steps. A similar observation can be made for contact problems with Coulomb or Tresca friction if $s = 0$. To get a better feeling for the scaling parameter s, we consider a simplified one-dimensional model $h(r,u) := \frac{5}{3}\max(|r+100u|,100)^s(r-100(r+100u)/\max(100,|r+100u|))$. Figure 5.5 shows the NCP function $h(\cdot,\cdot)$ for $s = 0$ and $s = 1$. A cut through $u = \text{const.}$ shows that for $s = 0$ the function is almost constant and thus a Newton linearization involves a badly conditioned Jacobian. The situation is improved for $s = 1$. This observation motivates the use of the scaling parameter s. The value $s = 1$ is already introduced in Hüeber *et al.* (2008) and also successfully applied in Koziara and Bicanic (2008).

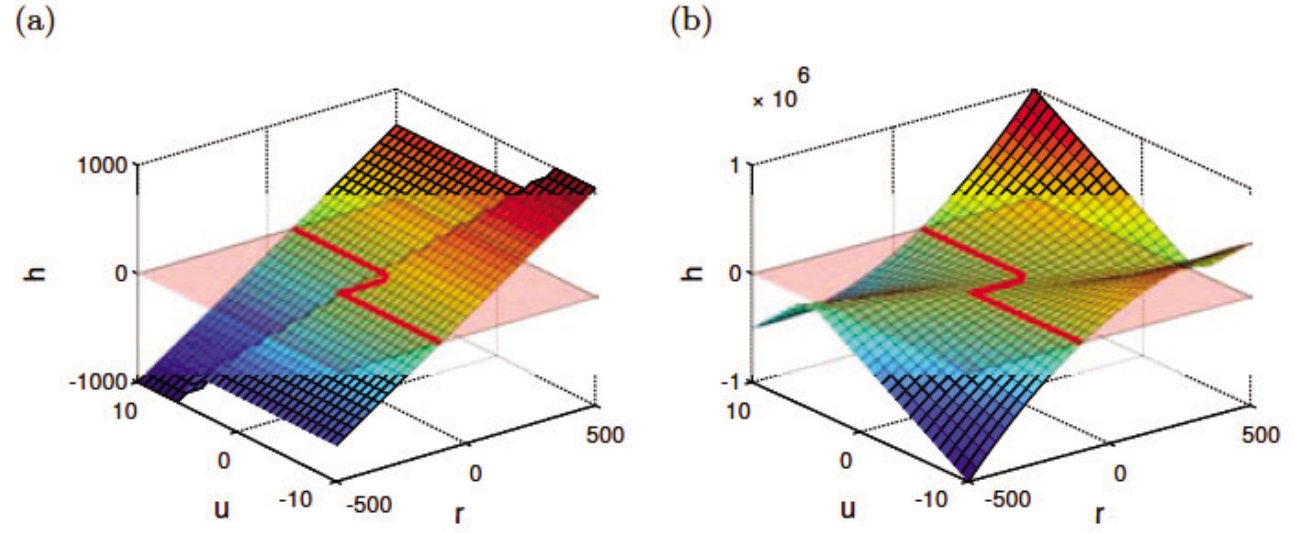

Figure 5.5. NCP function for $s = 0$ (a) and $s = 1$ (b).

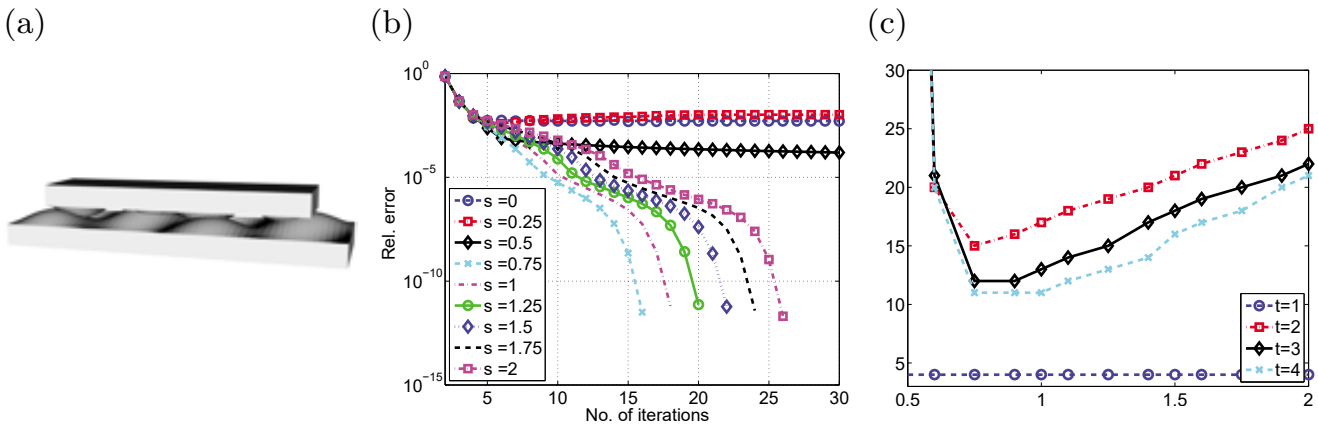

Figure 5.6. Geometry (a), error decay of the semi-smooth Newton iteration for different values of s (b) and total number of iterations for t_1 to t_4 with respect to s (c).

Figure 5.6(a) illustrates the geometry of a dynamic two-body contact problem in 3D with Coulomb friction. In Figure 5.6(b) we show the convergence of the semi-smooth Newton method for different scaling parameters. As can be clearly seen for small s, we do not have convergence. Numerically optimal convergence can be observed for $s = 0.75$. The convergence is also more robust for $s = 1$ than for smaller values of s. Figure 5.6(c) shows that for $s \in [0.75, 1]$, the global number of iterations required is almost constant. For $s > 1$, we observe a linear increase in the number of iteration steps, whereas for $s \leq 0.5$ we see divergence. From now on we will restrict ourselves to the case $s \in [0, 1]$.

5.5. Stabilization in the pre-asymptotic range

Numerical experience shows that the use of the Robin boundary condition in the form of (5.13b) does not necessarily yield a robust and stable algorithm. Similar observations have been made in totally different fields of applications. We refer to Chan, Golub and Mulet (1999) and Hintermüller and Stadler (2006) for the use of primal–dual active set strategies in the field of image restoration and to the early work by Andersen, Christiansen, Conn and Overton (2000).

To get a better feeling, we consider the definition of $L_{p;s}^{k-1}$ in more detail. Let us assume that the Newton iterates converge towards a solution satisfying (3.11) and (3.12). Then, for a sliding node, we find that L_1^{k-1} and $-\alpha_2^{k-1} L_2^{k-1}$ tend to the same limit and thus $L_{p;s}^{k-1}$ tends to the limit L_p^∞ independently of s:

$$L_p^\infty := \frac{1}{\|\boldsymbol{\gamma}_{p;\mathrm{tr}}^t\| \|\boldsymbol{\gamma}_p^t\|} \boldsymbol{\gamma}_p^t \otimes \boldsymbol{\gamma}_p^t - \frac{\|\boldsymbol{\gamma}_p^t\|}{\|\boldsymbol{\gamma}_{p;\mathrm{tr}}^t\|} \mathrm{Id}.$$

Noting that a rank-one matrix of the form $\mathbf{x} \otimes \mathbf{x}$ has exactly one non-trivial eigenvalue, namely $\|\mathbf{x}\|^2$, we find that $\mathrm{Id} + L_{p;s}^{k-1}$ tends to a symmetric matrix

with eigenvalues 1 and $1 - \|\boldsymbol{\gamma}_p^t\|/\|\boldsymbol{\gamma}_{p;\mathrm{tr}}^t\|$, which are strictly larger than zero for a physically correct sliding node. If no sliding occurs then $\|\boldsymbol{\gamma}_p^t\| = \|\boldsymbol{\gamma}_{p;\mathrm{tr}}^t\|$, and the matrix is singular. In that situation, we face a standard Dirichlet boundary condition for $\mathbf{u}_p^t$. Recalling that $\boldsymbol{\gamma}_p^t$ stands for the negative surface traction in the tangential direction acting on node p, we find in the limit of a non-degenerate Robin boundary condition that

$$-(\boldsymbol{\gamma}_p^t)^k + L_{p;\mathrm{R}}(\mathbf{u}_p^t)^k = \mathbf{g}_{\mathrm{R}}^k, \quad L_{p;\mathrm{R}} := \frac{2\mu c_t}{m_p}(-L_p^\infty)^{\frac{1}{2}}(\mathrm{Id} + L_p^\infty)^{-1}(-L_p^\infty)^{\frac{1}{2}}.$$

Here the Robin boundary data vector $\mathbf{g}_{\mathrm{R}}^k$ itself depends on the solution $(\gamma_p^n)^k$ and the previous iterate. The matrix $L_{p;\mathrm{R}}$ is symmetric and positive definite, and thus yields a well-posed Robin condition for elliptic systems, and unique solvability for the linearized system is established. Unfortunately, these observations do not necessarily hold true in the pre-asymptotic range. Then it might occur that $\mathrm{Id} + L_{p;s}^{k-1}$ is non-singular but that $-(\mathrm{Id} + L_{p;s}^{k-1})^{-1}L_{p;s}^{k-1}$ is not positive semi-definite. This may result in no convergence.

To stabilize our approach, we introduce two modifications such that in each Newton step we obtain a well-defined system. This will be done by modifying ω_p^{k-1} and β_p^{k-1}, introduced in Lemma 5.5, so that

$$\omega_p^{k-1} := \frac{\nu(\gamma_{p;\mathrm{tr}}^n)^{k-1}}{\max\big(\nu(\gamma_{p;\mathrm{tr}}^n)^{k-1}, \|(\boldsymbol{\gamma}_p^t)^{k-1}\|\big)}, \tag{5.15}$$

$$\beta_p^{k-1} := \min\left(1, \frac{1}{s(1 - \chi_p^{k-1}\zeta_p^{k-1})}\right), \tag{5.16}$$

where χ_p^{k-1} and ζ_p^{k-1} are defined by

$$\chi_p^{k-1} := \frac{(\boldsymbol{\gamma}_p^t)^{k-1}(\boldsymbol{\gamma}_{p;\mathrm{tr}}^t)^{k-1}}{\|(\boldsymbol{\gamma}_p^t)^{k-1}\|\|(\boldsymbol{\gamma}_{p;\mathrm{tr}}^t)^{k-1}\|}, \qquad \zeta_p^{k-1} := \min\left(\frac{\|(\boldsymbol{\gamma}_p^t)^{k-1}\|}{\nu(\gamma_{p;\mathrm{tr}}^n)^{k-1}}, 1\right).$$

Let us briefly comment on the definition of the two parameters ω_p^{k-1} and β_p^{k-1}. As we will see by our numerical results, both parameters play important roles in the pre-asymptotic range but do tend to 1 within the first few iterates if the algorithm converges. Thus asymptotically the exact Newton method is recovered. The damping parameter ω_p^{k-1} can be regarded as a penalty term and only differs from 1 if the friction bound is violated. It is obvious that $\zeta_p^{k-1} \in [0, 1]$ and that χ_p^{k-1}, being the cosine of the angle between $(\boldsymbol{\gamma}_p^t)^{k-1}$ and $(\boldsymbol{\gamma}_{p;\mathrm{tr}}^t)^{k-1}$, is in $[-1, 1]$.

It is now easy to see that β_p^{k-1} is equal to 1 if $s \in [0, 0.5]$ or if $\chi_p^{k-1} \geq 0$. The last condition is equivalent to the fact that the angle between the actual and the trial tangential stress is bounded by $\pi/2$. Figure 5.7 shows β_p^{k-1} as a function of $\chi_p^{k-1} \in [-1, 1]$ and $\zeta_p^{k-1} \in [0, 1]$ for $s \in \{0.5, 0.75, 1\}$. For

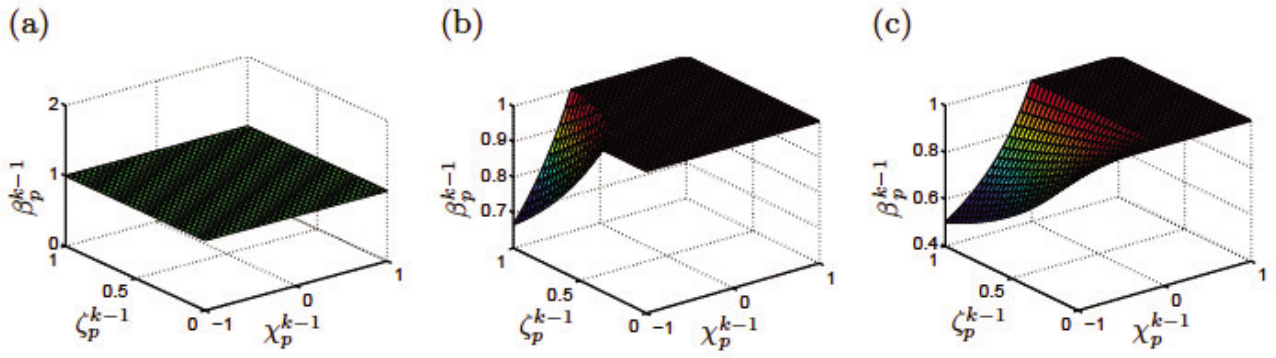

Figure 5.7. The damping term β_p^{k-1}: (a) $s = 0.5$, (b) $s = 0.75$, (c) $s = 1$.

the physically correct solution, the angle between the actual and the trial tangential stress is zero. As our numerical results show, β_p^{k-1} is mostly equal to one, reflecting the fact that within the first few iterations the orientation of the actual and trial tangential stress is adapted in the physically correct direction.

Lemma 5.7. Let ω_p^{k-1} and β_p^{k-1} be defined by (5.15) and (5.16), respectively. Then the boundary condition (5.13) is well-posed.

Proof. In the case that $\mathrm{Id} + L_{p;s}^{k-1}$ is singular, the Robin condition reduces to a Dirichlet condition for the component of $(\mathbf{u}_p^t)^k$ in the direction of the kernel K_1 of $\mathrm{Id} + L_{p;s}^{k-1}$. Moreover, if $L_{p;s}^{k-1}$ is singular, then the Robin condition reduces to a Neumann condition for the component of $(\boldsymbol{\gamma}_p^t)^k$ in the direction of the kernel K_2 of $L_{p;s}^{k-1}$. Since $K_1 \cap K_2 = \emptyset$, the Robin condition degenerates, in the direction of an element of the kernel K_1 or K_2, to either a well-defined Dirichlet or Neumann condition.

We have now to consider the non-degenerate case in more detail. Recalling that $L_{p;s}^{k-1} = \beta_p^{k-1}(\alpha_2^{k-1}\mathrm{Id} + \mathbf{x} \otimes \mathbf{y})$, we find for a non-singular $\mathrm{Id} + L_{p;s}^{k-1}$ and a non-singular $L_{p;s}^{k-1}$,

$$
\begin{aligned}
(\mathrm{Id} + L_{p;s}^{k-1})^{-1} L_{p;s}^{k-1} &= \mathrm{Id} - (\mathrm{Id} + L_{p;s}^{k-1})^{-1} \\
&= \frac{\beta_p^{k-1}}{1 + \beta_p^{k-1}\alpha_2^{k-1}} \left(\alpha_2^{k-1}\mathrm{Id} + \frac{\mathbf{x} \otimes \mathbf{y}}{1 + \beta_p^{k-1}\alpha_2^{k-1} + \beta_p^{k-1}\mathbf{xy}} \right) =: aZ.
\end{aligned}
$$

We note that $0 < \beta_p^{k-1} \leq 1$ and $\alpha_2^{k-1} \geq -1$ and thus the factor a in front of the matrix Z is positive. It is easy to verify that we obtain the two eigenvalues of the matrix Z by

$$
\alpha_2^{k-1} < 0, \quad \frac{(1 + \beta_p^{k-1}\alpha_2^{k-1})(\alpha_2^{k-1} + \mathbf{xy})}{1 + \beta_p^{k-1}(\alpha_2^{k-1} + \mathbf{xy})}.
$$

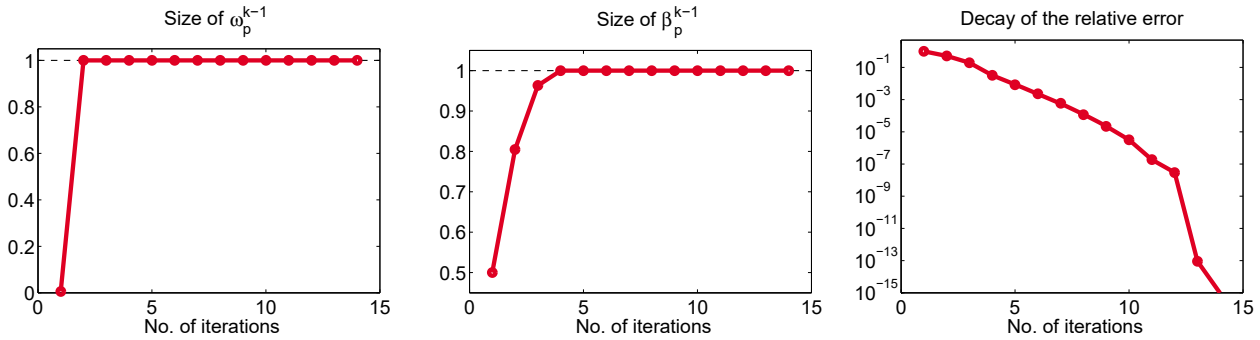

Figure 5.8. Scaling factors ω_p^{k-1} and β_p^{k-1} at iteration step k and global convergence rate for $s = 1$.

If $-1 < e_Z := \beta_p^{k-1}(\alpha_2^{k-1} + \mathbf{xy}) < 0$, then Z is negative definite. The definition of $L_{p;s}^{k-1}$ in Lemma 5.5 shows that we can set

$$\mathbf{x} := s\omega_p^{k-1}(\boldsymbol{\gamma}_p)^{k-1} + (s-1)\alpha_2^{k-1}(\boldsymbol{\gamma}_{p;\mathrm{tr}})^{k-1}, \quad \mathbf{y} := \frac{(\boldsymbol{\gamma}_{p;\mathrm{tr}})^{k-1}}{\|(\boldsymbol{\gamma}_{p;\mathrm{tr}})^{k-1}\|^2}.$$

Then, the value e_Z can be rewritten as

$$\begin{aligned} e_Z &= \beta_p^{k-1}\left(\alpha_2^{k-1} + s\omega_p^{k-1}\chi_p^{k-1}\frac{\|(\boldsymbol{\gamma}_p)^{k-1}\|}{\|(\boldsymbol{\gamma}_{p;\mathrm{tr}})^{k-1}\|} + (s-1)\alpha_2^{k-1}\right) \\ &= s\beta_p^{k-1}\left(\omega_p^{k-1}\chi_p^{k-1}\frac{\|(\boldsymbol{\gamma}_p)^{k-1}\|}{\|(\boldsymbol{\gamma}_{p;\mathrm{tr}})^{k-1}\|} + \alpha_2^{k-1}\right) \\ &= s\beta_p^{k-1}\alpha_2^{k-1}\left(1 - \omega_p^{k-1}\chi_p^{k-1}\frac{\|(\boldsymbol{\gamma}_p)^{k-1}\|}{\nu(\gamma_{p;\mathrm{tr}}^n)^{k-1}}\right) = s\beta_p^{k-1}\alpha_2^{k-1}(1 - \chi_p^{k-1}\zeta_p^{k-1}) \\ &\geq \alpha_2^{k-1} \geq -1. \end{aligned}$$

The case $e_Z = -1$ is ruled out by the assumption that $\mathrm{Id} + L_{p;s}^{k-1}$ is non-singular, since $e_Z + 1$ is an eigenvalue of this matrix.

These considerations show that the Robin boundary condition, given by (5.13b), reduces to a Neumann or Dirichlet condition in the direction of the kernel of $L_{p;s}^{k-1}$ or $\mathrm{Id} + L_{p;s}^{k-1}$, respectively. For all other cases it forms a well-defined Robin condition. □

Remark 5.8. We note that the proposed modifications are just one possibility. An alternative choice is to symmetrize and rescale $L_{p;s}^{k-1}$. All these modifications work well as long as they correctly normalize and, in the limit, tend to the original version; see also Hüeber *et al.* (2008) and Hüeber (2008).

To illustrate the effect of the modification, we consider different test examples in 3D. Figure 5.8 shows the case of a Tresca friction problem. We select a representative node and depict the value for ω_p^{k-1} and β_p^{k-1}. As can be seen, the modification actually applies only in the first few iteration steps.

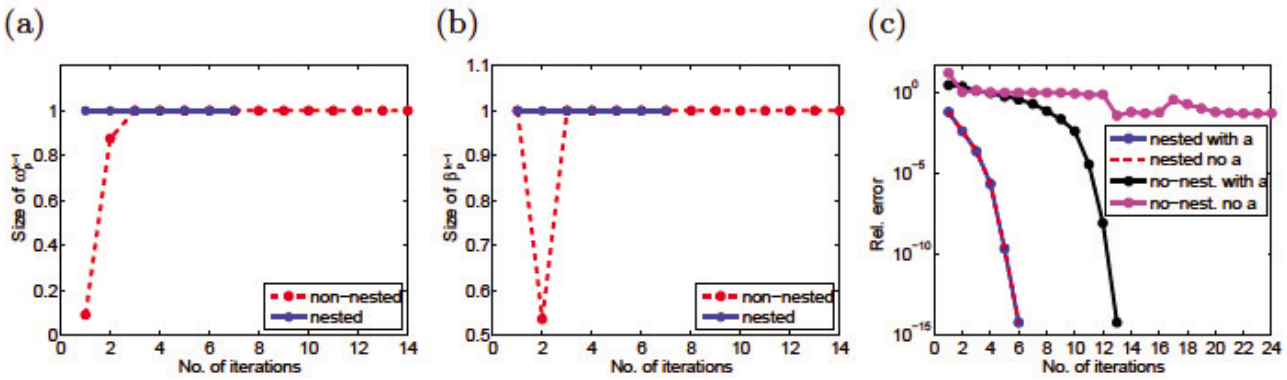

Figure 5.9. Scaling factors ω_p^{k-1}, β_p^{k-1} at iteration step k (a,b) and convergence rates for different strategies (c).

In Figure 5.9, we apply the modifications to a Coulomb problem and consider the influence of the modification on the local and global convergence. To do so, we select the initial guess in two different ways. In the first case, it is chosen randomly on a fine mesh, whereas in the second situation it is interpolated from the solution of the previous coarser level and thus can be expected to be good. For this nested approach the modification does not affect the iteration scheme and thus the same rates of convergence can be observed. This is in good agreement with the observation that asymptotically ω_p^{k-1} and β_p^{k-1} tend to 1 in the case of convergence. The situation is considerably different if we apply a bad initial guess. Here, without the modification, no convergence at all can be observed, whereas the modified version still shows a reasonable rate. These two test examples show that the effect of the modification can be neglected if the start iteration is already good enough. However in the pre-asymptotic range, it is of great significance and highly enlarges the domain of convergence.

Our last test combines the scaling $s \in [0, 1]$ with the modification for the nodes $p \in \mathcal{A}^k$. Here, we consider a dynamic Coulomb problem in 3D on non-matching meshes where the actual contact zone is not simply connected. Figure 5.10 shows the influence of the convergence rate as a function of s. As can be clearly seen in Figure 5.10(a), the number of Newton iterations required is quite insensitive provided that s is large enough. For small s, no convergence at all can be obtained. Therefore, at time t_2, only the results for $s = 0.5$, $s = 0.75$ and $s = 1$ are plotted. The choices $s = 0$ and $s = 0.25$ do not yield a convergent scheme.

Finally Figure 5.11 shows that for a selected node both parameters ω_p^{k-1} and β_p^{k-1} tend to 1 very fast in the case of $s > 0.5$. Moreover, the cosine of the angle between the tangential stress and the trial tangential stress tends to 1. This indicates that our algorithm is able to adjust the correct sliding direction within the first few iterates. The situation is changed drastically

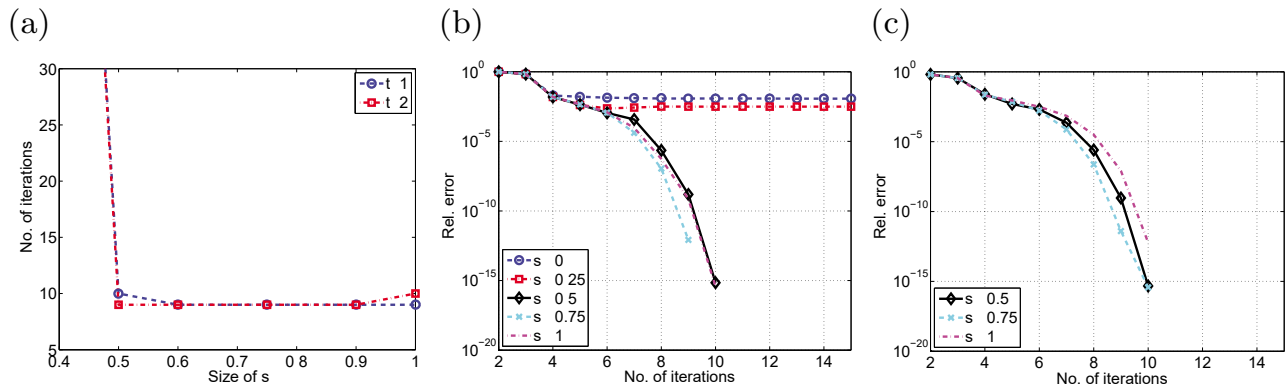

Figure 5.10. Number of required iterations (a) and convergence rates for two different time steps (b,c).

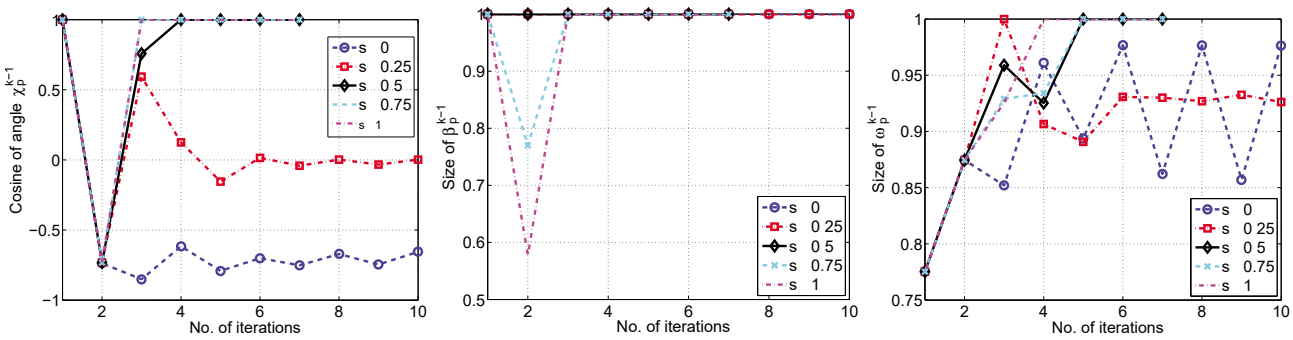

Figure 5.11. Scaling factors χ_p^{k-1}, β_p^{k-1} and ω_p^{k-1} at iteration step k.

if $s \leq 0.5$. Then the correct sliding direction cannot be identified and ω_p^{k-1} and χ_p^{k-1} do not tend to 1, reflecting the fact that no convergence is obtained.

5.6. Mesh-dependent convergence rates

Although the abstract framework of semi-smooth Newton methods is very flexible and quite attractive for a large class of problems, there is one bottleneck. The convergence rate is, in general, mesh-dependent. Numerical results show that the number of Newton steps increases linearly with the refinement level. Several strategies exist to overcome this problem, depending on the type of application. One of the most efficient ones is to embed the solver in a nested iteration. This is extremely easy to realize with time-dependent problems or with adaptive refinement techniques. In both situations the initial guess can be interpolated from the previous time step or mesh. This simple pre-processing is quite often sufficient to obtain a level-independent number of non-linear solver steps. Alternatively, or additionally, we can combine the Newton approach with an inexact solution strategy. Quite often the arising linear system is not solved by a fast direct solver but by preconditioned Krylov or subspace correction methods such as multigrid or FETI techniques. Then it is only natural to make the Newton update after a small number of steps of the linear solver. To avoid

over-solving, during the first non-linear iteration steps, the number of inner iterations should be set dynamically.

We consider the same example as shown in Figure 4.3 to illustrate the effect of the mesh-dependent convergence rates. We use a hierarchy of uniformly refined meshes and compare three different strategies. The 'exact' one starts with a randomly chosen initial guess on each level and solves the resulting linearized system in each Newton step by a multigrid method with fixed small tolerance. By K_l, we denote the number of Newton steps required. As can be seen in Table 5.2, K_l depends linearly on l, and thus the total number N_l^{MG} of multigrid steps on level l increases linearly with l. The situation is different if we apply an inexact strategy, using the same bad initial guess, but do a Newton update after each multigrid step. This results in an 'inexact' strategy where the correct Jacobian of the NCP function is used but the system stiffness matrix is replaced by its multigrid approximation. Here, M_l stands for the number of iterations required to identify the correct active sets. As before, this number increases linearly, but the total number of multigrid steps is significantly reduced. Finally we combine this inexact strategy with a good initial guess obtained by interpolation from the solution on the previous level. We call this the 'nested' approach. Then the total number of multigrid steps is bounded independently of the refinement level and is comparable to the number required to solve one linearized problem.

Table 5.2. Number of total multigrid steps for different strategies.

Strategy		Exact		Inexact		Nested	
Level l	DOF	K_l	MG	M_l	N_l^{MG}	M_l	N_l^{MG}
1	27	3	46	3	12	3	12
2	125	3	62	3	16	3	16
3	729	4	72	4	17	4	15
4	4913	6	86	6	17	6	14
5	35937	7	106	9	19	6	16

In more complex 3D situations, or for non-linear material laws, more than one multigrid step is required before an update can be performed. In a last test, we combine semi-smooth Newton techniques and inexact solvers for the linearized system with an overlapping two-scale domain decomposition method in 3D. We refer to Brunßen, Hager, Wohlmuth and Schmid (2008) and Brunßen and Wohlmuth (2009) for details of the model and the specification of the data. In addition to the contact formulation, plasticity effects are taken into account. The approach is motivated by possible

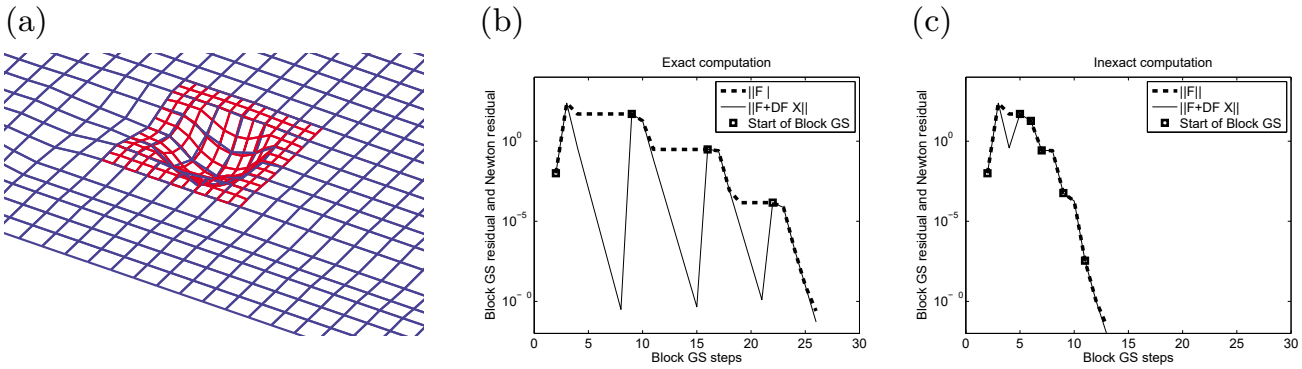

Figure 5.12. Surface mesh of the two-scale domain decomposition approach (a), convergence rates for the non-linear Newton solver (b,c).

applications to incremental metal cold forming processes. Here, the forming zone is small, but very mobile, and the work tool is contacting almost every point of the workpiece at some time in the process. To avoid expensive re-meshing and to reduce the complexity of the elasto-plastic constitutive equations, an operator splitting technique in space can be introduced. A small local but mobile subdomain, with a fine mesh and the fully non-linear contact and plasticity model, will interact with the global coarse mesh associated with a simplified model. To solve the fully coupled non-linear system, semi-smooth Newton techniques in combination with a block Gauss–Seidel solver are quite efficient. This is in particular true if inexact strategies are applied. To avoid over-solving during the first non-linear iteration steps, the number of inner iteration should be set dynamically. Here, the stopping criterion is based on Dembo, Eisenstat and Steinhaug (1982) and Eisenstat and Walker (1996).

Figure 5.12 shows the increase in efficiency of the non-linear solver if, within each Newton step, the linearized coupled domain decomposition system is not solved exactly but by a few block Gauss–Seidel steps. The number of inner iteration steps is set dynamically depending on the non-linear residual. As can be seen from Figure 5.12(c), during the first few Newton iterations, there is no need to solve the linearized system up to very high accuracy. To obtain the full efficiency of the approach, the accuracy of the linear solver has to be gradually improved during the non-linear solution process.

6. *A posteriori* error estimates and adaptivity

Adaptive techniques based on *a posteriori* error estimators play an important role in enhancing the performance of the numerical simulation algorithm and are well established for finite element methods: see the monographs by Ainsworth and Oden (2000), Babuška and Strouboulis (2001), Han (2005), Repin (2008), Verfürth (1996) and the references therein. For abstract variational inequalities we refer to Ainsworth, Oden and Lee (1993),

Bostan, Han and Reddy (2005), Erdmann, Frei, Hoppe, Kornhuber and Wiest (1993), Fuchs and Repin (2010), Liu and Yan (2000), Nochetto, von Petersdorff and Zhang (2010), Moon, Nochetto, von Petersdorff and Zhang (2007) and Suttmeier (2005), whereas obstacle-type problems are considered in Bildhauer, Fuchs and Repin (2008), Braess (2005), Chen and Nochetto (2000), French, Larsson and Nochetto (2001), Hoppe and Kornhuber (1994), Johnson (1992), Kornhuber and Zou (2011), Nochetto, Siebert and Veeser (2003, 2005) and Veeser (2001), and early approaches for contact problems can be found in Blum and Suttmeier (2000), Buscaglia, Duran, Fancello, Feijoo and Padra (2001), Carstensen, Scherf and Wriggers (1999), Lee and Oden (1994) and Wriggers and Scherf (1998). A residual-type error estimator is introduced and analysed in Hild and Nicaise (2005, 2007) and in Bostan and Han (2006) and Hild and Lleras (2009) for a one-sided contact problem without friction and with Coulomb friction, respectively. In addition to standard face and volume residual terms, extra terms reflecting the non-conformity of the approach are taken into account. For boundary element discretizations, we refer to Eck and Wendland (2003) and Maischak and Stephan (2005, 2007). Although the error estimator in Hild and Lleras (2009) provides a mesh-independent upper bound for the discretization error, not all terms result in optimal lower bounds. Thus the efficiency of the error estimator cannot be guaranteed from the theoretical point of view. Early results on hp-techniques for frictional contact problems can be found in Lee and Oden (1994), whereas in the recent contribution of Dörsek and Melenk (2010) a simplified Tresca problem with a given surface normal traction equal to zero has been studied.

As it turns out, the saddle-point approach (2.15) and its discrete version (3.9) provide an excellent starting point for the construction of an error indicator. In Wohlmuth (2007) an estimator was introduced for the case of no friction and non-matching meshes. A theoretical analysis shows that a constant-free global upper bound and local lower bounds for the error can be established. However, in contrast to the standard linear conforming setting, the additional higher-order term is solution-dependent and cannot be controlled within the adaptive refinement process.

These first results can be improved considerably by following a more general construction principle. Firstly, we use the equilibrium of the saddle-point approach to construct our indicator. Secondly, we consider the influence of the discretization (3.8) of (2.14). For the special case of a one-sided contact problem without friction, it is shown in Weiss and Wohlmuth (2009) that an indicator, constructed in this way, provides upper and local lower bounds for the discretization error and is thus an efficient error estimator. Moreover, the higher-order terms are standard data oscillation terms and can be controlled within the adaptive refinement strategy. The results are shown for a flux-based approach but can easily be generalized to cover the

case of a residual-based error estimator: see Hüeber and Wohlmuth (2010) for numerical results. Here, we follow these lines and extend the approach and the analysis to contact problems with friction.

In this section, we discuss different element-oriented error indicators, *i.e.*, $\eta^2 := \sum_{T\in\mathcal{T}_l} \eta_T^2$, and analyse the influence of the variational inequality. We focus both on the theoretical bounds and on computational aspects. Due to the variational inequality character of the given problem, we have to include a term which measures the non-conformity of the Lagrange multiplier. This contribution can be decomposed into a contact and friction term. For ease of presentation and analysis, we restrict ourselves to the two-dimensional setting, polygonal domains, a zero gap and a constant contact normal. Moreover, we do not analyse the influence of non-matching meshes but do provide the construction of the error indicator.

As is standard, we use a data oscillation term,

$$\xi_i^2 := \sum_{T\in\mathcal{T}_l} \frac{h_T^2}{2\mu} \|\mathbf{f} - \mathbf{\Pi}_i \mathbf{f}\|_{0;T}^2, \quad i = 0, 1. \tag{6.1}$$

To keep the notation simple, we further assume that we are working with simplicial meshes and that the given boundary data is compatible with the discretization, *i.e.*, $\mathbf{u}_l|_{\Gamma_\mathrm{D}} = \mathbf{u}_\mathrm{D}$ and $\mathbf{f}_\mathrm{N}$ is piecewise cubic and continuous on each straight segment γ_i of Γ_N. Moreover, we assume that $\mathbf{n}_j \mathbf{f}_\mathrm{N}|_{\gamma_i}(p) = \mathbf{n}_i \mathbf{f}_\mathrm{N}|_{\gamma_j}(p)$ with $\partial\gamma_i \cap \partial\gamma_j = p$ and that $\mathbf{n}\mathbf{f}_\mathrm{N}|_{\Gamma_\mathrm{N}}(p) = 0$ where $p = \partial\Gamma_\mathrm{C} \cap \partial\Gamma_\mathrm{N}$, and $\mathbf{n}$ is the outer unit normal on Γ_C. Otherwise, as is standard, additional boundary face terms have to be included, measuring the weighted L^2-norms of the boundary error: see, *e.g.*, Repin, Sauter and Smolianski (2003). The weight $\sqrt{h_f/(2\mu)}$ for the Neumann term is the inverse of the weight for the Dirichlet term, reflecting the $H^{1/2}$-duality between displacement trace and surface tractions. Here h_f stands for the diameter of the boundary face f. In the following, we use the piecewise cubic biorthogonal basis function shown in Figure 3.7(a).

As a first preliminary step, we reformulate the coupled problem (3.9) by introducing a weakly consistent Neumann force in $\mathbf{M}_l^\mathrm{m}$ on the master side. To do so, we introduce $\mathbf{\Pi}_l^{*;\mathrm{m}} := (\Pi_l^{*;\mathrm{m}})^d$ as the dual mortar projection $\Pi_l^{*;\mathrm{m}} : M \to M_l^\mathrm{m}$ with respect to the master side,

$$\int_{\Gamma_\mathrm{C}} \Pi_l^{*;\mathrm{m}} \mu v_l \,\mathrm{d}s = \langle \mu, v_l \rangle_{\Gamma_\mathrm{C}}, \quad v_l \in W_l^\mathrm{m}. \tag{6.2}$$

Keeping in mind that M_l^m and W_l^m reproduce constants and have a locally defined basis, a straightforward Bramble–Hilbert argument implies the approximation properties

$$\|\mu - \Pi_l^{*;\mathrm{m}} \mu\|_{-\frac{1}{2};\Gamma_\mathrm{C}}^2 \leq \sum_{f\in\mathcal{F}_l^\mathrm{m}} h_f \|\mu - \Pi_l^{*;\mathrm{m}} \mu\|_{0;f}^2, \quad \mu \in L^2(\Gamma_\mathrm{C}), \tag{6.3}$$

where $\mathcal{F}_l^{\mathrm{m}}$ stands for the set of all contact faces of the master subdomain.

In terms of (6.2), we now define the discrete contact forces of the slave and master sides by

$$\mathbf{f}_{\mathrm{C}} := \begin{cases} \mathbf{f}_{\mathrm{C}}^{\mathrm{s}} := -\boldsymbol{\lambda}_l & \text{on } \Gamma_{\mathrm{C}}^{\mathrm{s}}, \\ \mathbf{f}_{\mathrm{C}}^{\mathrm{m}} := \boldsymbol{\Pi}_l^{*;\mathrm{m}} \boldsymbol{\lambda}_l & \text{on } \Gamma_{\mathrm{C}}^{\mathrm{m}}. \end{cases} \tag{6.4}$$

Provided that the Lagrange multiplier $\boldsymbol{\lambda}_l$ on the slave side is known, we can rewrite the first line of (3.9). Recalling the definition of $\boldsymbol{\Pi}_l^{*;\mathrm{m}}$, we obtain a standard variational problem for $\mathbf{u}_l^k$ on each subdomain Ω^k, $k \in \{\mathrm{m}, \mathrm{s}\}$. Find $\mathbf{u}_l^k \in \mathbf{V}_{l;\mathrm{D}}^k$ such that

$$a_k(\mathbf{u}_l^k, \mathbf{v}_l) = f_k(\mathbf{v}_l) + \int_{\Gamma_{\mathrm{C}}^k} \mathbf{f}_{\mathrm{C}}^k \mathbf{v}_l \, \mathrm{d}s, \quad \mathbf{v}_l \in \mathbf{V}_l^k. \tag{6.5}$$

Then (6.5) shows that $\mathbf{u}_l^{\mathrm{s}}$ and $\mathbf{u}_l^{\mathrm{m}}$ are conforming finite element approximations of a linear elasticity problem on Ω^{s} and Ω^{m}, respectively. Here the unknown contact stresses on $\Gamma_{\mathrm{C}}^{\mathrm{s}}$ and $\Gamma_{\mathrm{C}}^{\mathrm{m}}$ are replaced by the numerical approximation $\mathbf{f}_{\mathrm{C}}$ as defined by (6.4). Thus the contact zone Γ_{C}^k, $k \in \{\mathrm{m}, \mathrm{s}\}$, can be regarded as a Neumann boundary part where, additionally, the error in the Lagrange multiplier has to be taken into account. Unfortunately, in contrast to given Neumann data, this error cannot be estimated *a priori* and has to be controlled by the error indicator.

There is a huge variety of different types of error estimators. One of the most simple approaches is based on the residual equation. A more recent and quite attractive alternative construction is related to local lifting techniques in combination with equilibrated fluxes. These element-wise conservative fluxes have a long tradition in structural mechanics and go back to the early papers by Brink and Stein (1998), Kelly (1984), Kelly and Isles (1989), Ladevèze and Leguillon (1983), Ladevèze and Maunder (1996), Ladevèze and Rougeot (1997), Prager and Synge (1947) and Stein and Ohnimus (1997, 1999). We refer to the monograph by Repin (2008) and to Luce and Wohlmuth (2004), where such techniques have been applied successfully and constant-free upper bounds have been established. Recently these ideas have been generalized to many situations and are widely applied: see, *e.g.*, Braess, Hoppe and Schöberl (2008), Braess, Pillwein and Schöberl (2009*b*), Cheddadi, Fučík, Prieto and Vohralík (2008, 2009), Ern and Vohralík (2009), Nicaise, Witowski and Wohlmuth (2008) and Vohralík (2008).

6.1. Construction of the equilibrated error indicator

The construction of such type of indicators is done in two steps. Firstly, equilibrated fluxes on the faces are defined locally and secondly a local volume lifting is performed.

For low-order finite elements the equilibrated fluxes $\mathbf{g}$ are defined on the set of all faces $\mathcal{F}_l$ and for each simplicial face f in $P_1(f)^d$. A unit face

normal $\mathbf{n}_f$ is fixed for each face f. If f is a boundary face of the domain Ω^k, then we set $\mathbf{n}_f$ to be the outer unit normal on $\partial\Omega^k$. Then the global problem reads as follows. Find $\mathbf{g} := (\mathbf{g}_f)_{f\in\mathcal{F}_l} \in \prod_{f\in\mathcal{F}_l} P_1(f)^d$ such that, for all elements $T \in \mathcal{T}_l$ and all $\mathbf{v} \in (P_1(T))^d$,

$$\int_T \boldsymbol{\sigma}(\mathbf{u}_l) : \boldsymbol{\epsilon}(\mathbf{v})\,\mathrm{d}x = \int_T \mathbf{f}\mathbf{v}\,\mathrm{d}x + \sum_{f\subset\partial T} \int_f (\mathbf{n}_T\mathbf{n}_f)\mathbf{g}_f\mathbf{v}\,\mathrm{d}s, \tag{6.6}$$

where $\mathbf{n}_T$ stands for the outer unit normal on ∂T. Moreover, for all Neumann and contact faces, the fluxes have to satisfy

$$\int_f \mathbf{g}_f\mathbf{v}\,\mathrm{d}s = \int_f \mathbf{f}_\mathrm{N}\mathbf{v}\,\mathrm{d}s, \quad f \in \mathcal{F}_l^\mathrm{N}, \quad \mathbf{v} \in (P_1(f))^d, \tag{6.7a}$$

$$\int_f \mathbf{g}_f\mathbf{v}\,\mathrm{d}s = \int_f \mathbf{f}_\mathrm{C}\mathbf{v}\,\mathrm{d}s, \quad f \in \mathcal{F}_l^\mathrm{C}, \quad \mathbf{v} \in (P_1(f))^d, \tag{6.7b}$$

where $\mathcal{F}_l^k$ is the set of faces on Γ_k^s and on Γ_k^m, $k \in \{\mathrm{N}, \mathrm{C}\}$. We note that formally (6.7a) and (6.7b) have the same structure but in contrast to $\mathbf{f}_\mathrm{N}$, $\mathbf{f}_\mathrm{C}$ is not *a priori* known but depends on the dual variable $\boldsymbol{\lambda}_l$ given by (5.8). A simple counting argument shows that in (6.6) and (6.7), we have to satisfy $(d+1)^d N_T$ and $d^d(N_f^\mathrm{N} + N_f^\mathrm{C})$ equations, respectively. Here N_T stands for the number of elements in $\mathcal{T}_l$, and N_f^N and N_f^C denote the number of faces on the Neumann and contact boundary part, respectively.

Remark 6.1. We note that from the point of view of approximation properties, there is no need to work with $\mathbf{g}_f \in P_1(f)^d$. A face-wise constant approximation in combination with $\mathbf{v} \in (P_0(T))^d$ in (6.6) and $\mathbf{v} \in (P_0(f))^d$ in (6.7) would be good enough. However, then the system cannot be decoupled easily and a global system has to be solved. This is not very attractive from the computational point of view.

It is well known (see the monograph by Ainsworth and Oden (2000)) that a possible solution can be constructed locally by introducing the moments of the fluxes $\mathbf{g}_f$. An abstract framework for the vertex-based patch-wise computation of the moments can be found in Ainsworth and Oden (1993). In particular, the size of the local system depends on the shape-regularity of the mesh but not on the mesh size. Depending on the type of the vertex, *i.e.*, Neumann, or interior, Dirichlet, the system has a unique solution or the system matrix is singular but solvability is guaranteed. Then the solution is fixed by imposing an additional constraint resulting from a local minimization problem for the moments. Here, we briefly recall the main steps and provide the structure of the vertex-based patch system in 2D. Figure 6.1 illustrates the notation for an interior vertex patch.

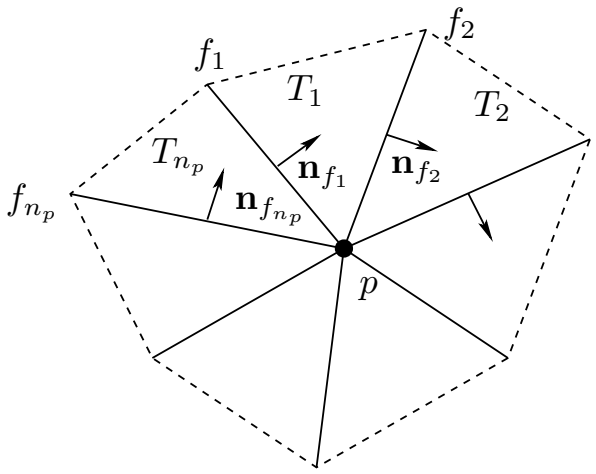

Figure 6.1. Enumeration of the elements and faces sharing a vertex in 2D.

The moments $\boldsymbol{\mu}_f^p \in \mathbb{R}^d$ are given for each face f and vertex p by

$$\boldsymbol{\mu}_f^p := \int_f \mathbf{g}_f \phi_p \, \mathrm{d}s$$

and uniquely define the fluxes $\mathbf{g}_f$ by $\mathbf{g}_f = \sum_{p \in \mathcal{P}_f} \boldsymbol{\mu}_f^p \varphi_p$, where φ_p is the normalized linear dual basis with respect to ϕ_p on the face f, *i.e.*, $\int_f \phi_p \varphi_q \, \mathrm{d}s = \delta_{pq}$. Here $\mathcal{P}_f$ stands for all vertices of f.

Here, we only work out the details for an interior vertex p in 2D and refer to Ainsworth and Oden (2000) for a discussion of the local system in the case of boundary vertices. Using $\phi_p|_{T_i}\mathbf{e}_j$, $j = 1, 2$, $i = 1, \ldots, n_p$, where n_p stands for the number of elements sharing the vertex p, as a test function in (6.6), in 2D we get the linear system

$$\begin{pmatrix} -\mathrm{Id} & \mathrm{Id} & & & & \\ & -\mathrm{Id} & \mathrm{Id} & & & \\ & & \ddots & \ddots & & \\ & & & -\mathrm{Id} & \mathrm{Id} & \\ \mathrm{Id} & & & & -\mathrm{Id} & \end{pmatrix} \begin{pmatrix} \boldsymbol{\mu}_1^p \\ \boldsymbol{\mu}_2^p \\ \vdots \\ \boldsymbol{\mu}_{n_p-1}^p \\ \boldsymbol{\mu}_{n_p}^p \end{pmatrix} = \begin{pmatrix} \mathbf{r}_1^p \\ \mathbf{r}_2^p \\ \vdots \\ \mathbf{r}_{n_p}^p \\ \mathbf{r}_{n_p-1}^p \end{pmatrix} =: \mathbf{r}^p, \tag{6.8}$$

where $(\mathbf{r}_i^p)_j := \int_{T_i} \mathbf{f}\phi_p \mathbf{e}_j \, \mathrm{d}x - \int_{T_i} \boldsymbol{\sigma}(\mathbf{u}_l) : \boldsymbol{\epsilon}(\phi_p \mathbf{e}_j) \, \mathrm{d}x$, $j = 1, 2$, $i = 1, \ldots, n_p$, and $\boldsymbol{\mu}_i^p := \boldsymbol{\mu}_{f_i}^p$, $i = 1, \ldots, n_p$. It is easy to see that this system is singular, and the dimension of its kernel is independent of n_p and equal to two. The two eigenvectors $\mathbf{v}_1$ and $\mathbf{v}_2$ associated with the eigenvalue zero are given by $\mathbf{v}_1 = (1, 0, 1, 0, \ldots, 1, 0)^\top$ and $\mathbf{v}_2 = (0, 1, 0, 1, \ldots, 0, 1)^\top$. Since $\mathbf{v}_j \mathbf{r}^p = f(\phi_p \mathbf{e}_j) - a(\mathbf{u}_l, \phi_p \mathbf{e}_j) = 0$, $j = 1, 2$, the solvability of (6.8) is granted.

We note that, in the linear setting, each solution of (6.8) will provide an upper bound for the discretization error but will, in general, not be suitable for getting lower bounds. Thus the solution of (6.8) has to be selected carefully. The flux $\mathbf{g}_f$ will enter directly into the definition of the error estimator, and discrete norm equivalences show that the error estimator depends on $\mathbf{g}_f - \{\boldsymbol{\sigma}(\mathbf{u}_l)\mathbf{n}_f\}$, where $\{\cdot\}$ stands for the average face contribution. This

observation motivates us to obtain $\boldsymbol{\mu}^p := (\boldsymbol{\mu}_1^p, \boldsymbol{\mu}_2^p, \ldots, \boldsymbol{\mu}_{n_p}^p)^\top$ as the unique solution of a local constrained minimization problem. We identify the index $i = n_p + 1$ with $i = 1$ and introduce the quadratic functional

$$J_p(\boldsymbol{\mu}^p) := \sum_{i=1}^{n_p} \sum_{j=i}^{i+1} \frac{|T_i|}{2\mu_i \big(\int_{f_j} \phi_p \,\mathrm{d}s\big)^2} \|\boldsymbol{\mu}_i^p - \boldsymbol{\tau}_{i;j}^p\|^2, \tag{6.9}$$

where μ_i is the shear modulus of the element T_i, $|T_i|$ stands for the element volume and $\boldsymbol{\tau}_{i;j}^p := \int_{f_j} \boldsymbol{\sigma}(\mathbf{u}_l)|_{T_i} \mathbf{n}_{f_j} \phi_p \,\mathrm{d}s$. Based on $J_p(\cdot)$, we impose an additional constraint for each vertex p. Find $\boldsymbol{\mu}^p$ such that $\boldsymbol{\mu}^p$ is a solution of (6.8) and satisfies

$$J_p(\boldsymbol{\mu}^p) = \min_{\boldsymbol{\eta}^p \text{ solves } (6.8)} J_p(\boldsymbol{\eta}^p).$$

We point out that in our setting the factor $2\mu_i$ in the weight of (6.9) is constant on each vertex patch and thus can be removed without influencing the result. Moreover, for meshes with no anisotropy, the weight itself can be replaced by one.

Remark 6.2. We note that the difference $\boldsymbol{\mu}_i^p - \boldsymbol{\tau}_{i;j}^p$ can also be used to define error estimators (see the monograph by Ainsworth and Oden (2000)), but then the upper bound is, in general, not constant-free.

The second step, in the construction of our error indicator, is to map the surface fluxes in terms of local lifting techniques to volume $H(\mathrm{div})$-conforming fluxes. In many cases, up to higher-order data oscillation terms, upper bounds for the discretization error with constant one can then be obtained. Thus these equilibration techniques form a flexible and an attractive class of error estimators and are of special interest if a reliable stopping criterion is required.

For scalar elliptic equations it is quite easy to construct this type of estimator. Basically two types of approach exist. The first one works on a dual mesh and uses a sub-mesh for the recovery in terms of standard mixed finite elements, *e.g.*, Raviart–Thomas (RT) or Brezzi–Douglas–Marini (BDM) elements: see Brezzi and Fortin (1991). Here the vertex patches are non-overlapping, and the fluxes are simply given by the discrete finite element flux which is well-defined in the interior of each element: see, *e.g.*, Luce and Wohlmuth (2004). Alternatively one can use the standard overlapping vertex patches and the face flux moments from the equilibrated approach as described above; see, *e.g.*, Vohralík (2008).

The situation is more involved in the case of linear elasticity. Firstly, the dual mesh approach cannot be applied in the linear elasticity setting due to the local rotations, which act as rigid body mode. Secondly, classical mixed finite elements for each row of the stress tensor cannot be used

because they violate the symmetry. Thus special mixed finite elements for symmetric tensor approximations have to be applied. This can be done by selecting Arnold–Winther-type mixed finite elements (Arnold, Falk and Winther 2006, Arnold and Winther 2002). Here, we only work with the two-dimensional setting, but these types of elements do also exist in 3D (Arnold, Awanou and Winther 2008, Arnold and Winther 2003), and on hexahedral meshes (Arnold and Awanou 2005). Using the equilibrated fluxes and an $H(\mathrm{div})$-conforming lifting, as in Nicaise *et al.* (2008) for a linear elasticity problem, we define a globally $H(\mathrm{div})$-conforming approximation $\boldsymbol{\sigma}_l$ of the stress $\boldsymbol{\sigma}(\mathbf{u})$. Then the error indicator is defined by

$$\eta_{\mathrm{L}}^2 := \sum_{k\in\{m,s\}} \sum_{T\in\mathcal{T}_l^k} \eta_{\mathrm{L};T}^2, \quad \eta_{\mathrm{L};T}^2 := \|\mathcal{C}^{-1/2}(\boldsymbol{\sigma}_l - \boldsymbol{\sigma}(\mathbf{u}_l))\|_{0;T}^2. \tag{6.10}$$

We note that once $\boldsymbol{\sigma}_l$ is known, $\eta_{\mathrm{L};T}^2$ can be easily evaluated by

$$\eta_{\mathrm{L};T}^2 = \frac{1}{2\mu}\left(\|\boldsymbol{\sigma}_l - \boldsymbol{\sigma}(\mathbf{u}_l)\|_{0;T}^2 - \frac{\lambda}{2\mu + d\lambda}\|\mathrm{tr}(\boldsymbol{\sigma}_l - \boldsymbol{\sigma}(\mathbf{u}_l))\|_{0;T}^2\right).$$

Before we specify $\boldsymbol{\sigma}_l$, we recall the basic properties of the Arnold–Winther elements in 2D. The element space $\mathbf{X}_T$ for a simplicial $T \in \mathcal{T}_l$ is given by

$$\mathbf{X}_T := \left\{\boldsymbol{\tau} \in (P_3(T))^{2\times 2},\ \boldsymbol{\tau}_{12} = \boldsymbol{\tau}_{21},\ \mathrm{div}\,\boldsymbol{\tau} \in (P_1(T))^2\right\}$$

and has dimension 24. Based on this, we can define the global space by $\mathbf{X}_l := \mathbf{X}_l^{\mathrm{m}} \times \mathbf{X}_l^{\mathrm{s}}$, where

$$\mathbf{X}_l^k := \{\boldsymbol{\tau}_l \in H(\mathrm{div};\Omega^k) \,|\, \boldsymbol{\tau}_l|_T \in \mathbf{X}_T, T \in \mathcal{T}_l^k\}, \quad k \in \{\mathrm{m},\mathrm{s}\}.$$

By definition $\mathbf{X}_l^k$ is $H(\mathrm{div})$-conforming on each subdomain Ω^k, and the degrees of freedom are given by (see Arnold and Winther (2002)):

- the nodal values (3 dof) at each vertex p,
- the zero- and first-order moments of $\boldsymbol{\tau}_l\mathbf{n}_f$ (4 dof) on each face f,
- the mean value (3 dof) on each element T.

We define our stress approximation $\boldsymbol{\sigma}_l$ of $\boldsymbol{\sigma}(\mathbf{u})$ by setting

$$\int_T \boldsymbol{\sigma}_l : \boldsymbol{\epsilon}(\mathbf{v})\,\mathrm{d}x := \int_T \boldsymbol{\sigma}(\mathbf{u}_l) : \boldsymbol{\epsilon}(\mathbf{v})\,\mathrm{d}x, \qquad \mathbf{v} \in (P_1(T))^2, \tag{6.11a}$$

$$\int_f (\boldsymbol{\sigma}_l\mathbf{n}_f)\mathbf{v}\,\mathrm{d}s := \int_f \mathbf{g}_f\mathbf{v}\,\mathrm{d}s, \qquad \mathbf{v} \in (P_1(f))^2, \tag{6.11b}$$

$$\boldsymbol{\sigma}_l(p) := \frac{1}{n_p}\sum_{i=1}^{n_p} \boldsymbol{\sigma}(\mathbf{u}_l)_{|_{T_i}}(p) + \boldsymbol{\alpha}_p. \tag{6.11c}$$

In contrast to Nicaise *et al.* (2008), where only homogeneous Dirichlet boundary conditions have been considered, we have to include a suitable

$\boldsymbol{\alpha}_p$ in (6.11c). For each node p not on $\overline{\Gamma}_{\mathrm{N}} \cup \overline{\Gamma}_{\mathrm{C}}$, we set $\boldsymbol{\alpha}_p := \mathbf{0}$. Otherwise, it is a symmetric 2×2 matrix with minimal Euclidean norm under the constraint

$$\boldsymbol{\alpha}_p \mathbf{n} := \begin{cases} \mathbf{f}_{\mathrm{N}} - \frac{1}{n_p} \sum_{i=1}^{n_p} \boldsymbol{\sigma}(\mathbf{u}_l)_{|T_i}(p)\mathbf{n} & p \in \overline{\Gamma}_{\mathrm{N}}, \\ \mathbf{f}_{\mathrm{C}} - \frac{1}{n_p} \sum_{i=1}^{n_p} \boldsymbol{\sigma}(\mathbf{u}_l)_{|T_i}(p)\mathbf{n} & p \in \overline{\Gamma}_{\mathrm{C}}, \end{cases} \tag{6.12}$$

where, for corner-points p, (6.12) has to be satisfied for both normal vectors. Our assumptions on the given data, the actual contact zone and our choice for $\mathbf{M}_l$ guarantee that $\boldsymbol{\alpha}_p$ is well-defined. Moreover, due to the symmetry of $\boldsymbol{\sigma}_l$, (6.11a) reduces to three independent conditions on each element. This definition has already been applied to contact problems in Wohlmuth (2007) and Weiss and Wohlmuth (2009).

Lemma 6.3. The subdomain-wise $H(\mathrm{div})$-conforming Arnold–Winther element $\boldsymbol{\sigma}_l$ is well-defined and satisfies

$$-\operatorname{div} \boldsymbol{\sigma}_l = \boldsymbol{\Pi}_1 \mathbf{f}, \quad \text{on } \Omega,$$
$$\boldsymbol{\sigma}_l \mathbf{n} = \begin{cases} \mathbf{f}_{\mathrm{N}} & \text{on } \Gamma_{\mathrm{N}}, \\ \mathbf{f}_{\mathrm{C}} & \text{on } \Gamma_{\mathrm{C}}, \end{cases}$$

where $\boldsymbol{\Pi}_j$ stands for the L^2-projection on piecewise polynomials of degree at most $j \in \mathbf{N}_0$.

Proof. By definition of $\mathbf{X}_l$, $\operatorname{div} \boldsymbol{\sigma}_l$ is element-wise in $(P_1(T))^2$. Integration by parts and the symmetry of $\boldsymbol{\sigma}_l$ shows that, for all $\mathbf{v} \in (P_1(T))^2$,

$$\int_T \operatorname{div} \boldsymbol{\sigma}_l \mathbf{v} \, \mathrm{d}x = -\int_T \boldsymbol{\sigma}_l : \boldsymbol{\epsilon}(\mathbf{v}) \, \mathrm{d}x + \int_{\partial T} (\boldsymbol{\sigma}_l \mathbf{n}_T) \mathbf{v} \, \mathrm{d}s.$$

Now we can use the definition (6.6) of the fluxes $\mathbf{g}_f$ and the definitions (6.11a) and (6.11b) for the Arnold–Winther element $\boldsymbol{\sigma}_l$, and we obtain

$$\begin{aligned} \int_T \operatorname{div} \boldsymbol{\sigma}_l \mathbf{v} \, \mathrm{d}x &= -\int_T \boldsymbol{\sigma}(\mathbf{u}_l) : \boldsymbol{\epsilon}(\mathbf{v}) \, \mathrm{d}x + \sum_{f \subset \partial T} \int_f (\mathbf{n}_f \mathbf{n}_T) \mathbf{g}_f \mathbf{v} \, \mathrm{d}s \\ &= -\int_T \mathbf{f} \mathbf{v} \, \mathrm{d}x. \end{aligned}$$

The stress $\boldsymbol{\sigma}_l$ is in $\mathbf{X}_l$, and thus $\boldsymbol{\sigma}_l \mathbf{n}$ restricted to each face f is in $(P_3(f))^2$. Let p_1 and p_2 be the two endpoints of f; then (6.11c) and (6.12) show that we have $\boldsymbol{\sigma}_l \mathbf{n}(p_i) = \mathbf{f}_{\mathrm{C}}(p_i)$ and $\boldsymbol{\sigma}_l \mathbf{n}(p_i) = \mathbf{f}_{\mathrm{N}}(p_i)$ for $f \subset \Gamma_{\mathrm{C}}$ and $f \subset \Gamma_{\mathrm{N}}$, $i = 1, 2$, respectively. Moreover, by assumption on the data $\mathbf{f}_{\mathrm{N}}$ and by choice of $\mathbf{M}_l$, $\boldsymbol{\sigma}_l \mathbf{n} - \mathbf{f}_k$, $k \in \{\mathrm{C}, \mathrm{N}\}$, is cubic with zero value at the endpoints. Then (6.7) in combination with (6.11c) shows that the zero- and first-order moments

of $\boldsymbol{\sigma}_l\mathbf{n} - \mathbf{f}_k$ vanish, from which we can conclude that $\boldsymbol{\sigma}_l\mathbf{n} - \mathbf{f}_k = \mathbf{0}$ on each Neumann or contact boundary face. □

Remark 6.4. We note that Lemma 6.3 does not hold for other choices of biorthogonal Lagrange multiplier basis functions such as, *e.g.*, the piecewise affine but discontinuous one.

The error indicator η_{L}, defined by (6.10), is motivated by the observation that the discrete Lagrange multiplier $\boldsymbol{\lambda}_l$ acts as a Neumann boundary condition on the contact part. It takes into account neither the inequality constraints resulting from the non-penetration nor the friction law. To have the equality $\boldsymbol{\sigma}_l\mathbf{n} = \mathbf{f}_{\mathrm{C}}$ on the contact zone, it is crucial that $\boldsymbol{\lambda}_l$ is mapped by $\boldsymbol{\Pi}_l^{*;\mathrm{m}}$ onto $\mathbf{M}_l^{\mathrm{m}}$. In the case of matching meshes we have $\boldsymbol{\lambda}_l - \boldsymbol{\Pi}_l^{*;\mathrm{m}}\boldsymbol{\lambda}_l = \mathbf{0}$, but in a more general situation this difference is non-zero and has to be estimated and controlled within the adaptive refinement process. To do so, we introduce an extra term, which is restricted to the master side of the contact zone,

$$\eta_{\mathrm{S}} := \sum_{f\in\mathcal{F}_l^{\mathrm{m}}} \eta_{\mathrm{S};f}^2, \quad \eta_{\mathrm{S};f}^2 := \frac{h_f}{2\mu^{\mathrm{m}}}\|\boldsymbol{\lambda}_l - \boldsymbol{\Pi}_l^{*;\mathrm{m}}\boldsymbol{\lambda}_l\|_{0;f}^2, \tag{6.14}$$

where μ^{m} is the Lamé parameter associated with the master body.

We now provide a first preliminary result, which is the starting point for our *a posteriori* analysis. The error in the displacement will be estimated in the energy norm $|||\cdot|||$, which is defined by

$$|||\mathbf{v}|||^2 := a(\mathbf{v},\mathbf{v}), \quad \mathbf{v}\in\mathbf{V}.$$

Lemma 6.5. The upper bound for the error in the energy norm satisfies

$$|||\mathbf{u}-\mathbf{u}_l|||^2 \le (\eta_{\mathrm{L}} + C\eta_{\mathrm{S}} + C\xi_1)|||\mathbf{u}-\mathbf{u}_l||| + \langle\boldsymbol{\lambda}_l - \boldsymbol{\lambda}, [\mathbf{u}] - [\mathbf{u}_l]\rangle_{\Gamma_{\mathrm{C}}}.$$

Proof. We start with the definition of the energy norm and apply integration by parts. The assumptions on the Dirichlet and Neumann boundary conditions yield that $\mathbf{u}-\mathbf{u}_l = \mathbf{0}$ on Γ_{D} and that $(\boldsymbol{\sigma}_l - \boldsymbol{\sigma}(\mathbf{u}))\mathbf{n} = \mathbf{0}$ on Γ_{N}. We then obtain in terms of Lemma 6.3 and (6.3) for $\mathbf{e}_l := (\mathbf{e}_l^{\mathrm{m}}, \mathbf{e}_l^{\mathrm{s}}) := (\mathbf{u}^{\mathrm{m}} - \mathbf{u}_l^{\mathrm{m}}, \mathbf{u}^{\mathrm{s}} - \mathbf{u}_l^{\mathrm{s}})$

$$\begin{aligned}
|||\mathbf{e}_l|||^2 &= \int_\Omega (\boldsymbol{\sigma}(\mathbf{u}) - \boldsymbol{\sigma}(\mathbf{u}_l)) : \boldsymbol{\epsilon}(\mathbf{e}_l)\,\mathrm{d}x \\
&\le \eta_{\mathrm{L}}|||\mathbf{e}_l||| + \int_\Omega (\boldsymbol{\sigma}(\mathbf{u}) - \boldsymbol{\sigma}_l) : \boldsymbol{\epsilon}(\mathbf{e}_l)\,\mathrm{d}x \\
&= \eta_{\mathrm{L}}|||\mathbf{e}_l||| + \int_\Omega (\mathbf{f} - \boldsymbol{\Pi}_1\mathbf{f})\mathbf{e}_l\,\mathrm{d}x \\
&\quad + \int_{\partial\Omega^{\mathrm{s}}} (\boldsymbol{\sigma}(\mathbf{u}) - \boldsymbol{\sigma}_l)\mathbf{n}^{\mathrm{s}}\mathbf{e}_l\,\mathrm{d}s + \int_{\partial\Omega^{\mathrm{m}}} (\boldsymbol{\sigma}(\mathbf{u}) - \boldsymbol{\sigma}_l)\mathbf{n}^{\mathrm{m}}\mathbf{e}_l\,\mathrm{d}s
\end{aligned}$$

$$
\begin{aligned}
&\leq (\eta_{\mathrm{L}} + C\xi_1)|||\mathbf{e}_l||| + \langle \boldsymbol{\lambda}_l - \boldsymbol{\lambda}, \mathbf{e}_l^{\mathrm{s}} \rangle_{\Gamma_{\mathrm{C}}} - \langle \boldsymbol{\Pi}_l^{*;\mathrm{m}} \boldsymbol{\lambda}_l - \boldsymbol{\lambda}, \mathbf{e}_l^{\mathrm{m}} \rangle_{\Gamma_{\mathrm{C}}} \\
&= (\eta_{\mathrm{L}} + C\xi_1)|||\mathbf{e}_l||| + \langle \boldsymbol{\lambda}_l - \boldsymbol{\lambda}, [\mathbf{e}_l] \rangle_{\Gamma_{\mathrm{C}}} - \langle \boldsymbol{\Pi}_l^{*;\mathrm{m}} \boldsymbol{\lambda}_l - \boldsymbol{\lambda}_l, \mathbf{e}_l^{\mathrm{m}} \rangle_{\Gamma_{\mathrm{C}}} \\
&= (\eta_{\mathrm{L}} + C\eta_{\mathrm{S}} + C\xi_1)|||\mathbf{e}_l||| + \langle \boldsymbol{\lambda}_l - \boldsymbol{\lambda}, [\mathbf{e}_l] \rangle_{\Gamma_{\mathrm{C}}}. \qquad \square
\end{aligned}
$$

Remark 6.6. We note that η_{S} is equal to zero in the case of a one-sided contact problem or for matching meshes. We refer to Section 6.7 for more comments on non-matching meshes.

In the following subsection, we introduce two extra terms which allow for the variational inequality. Although we restrict our analyses to very simple two-dimensional settings and to matching meshes, the definitions are given for the more general case, including non-matching meshes, a non-zero gap, and $d = 3$. As our numerical results will show, the error indicator can also be applied to such more general settings.

6.2. Influence of the contact constraints

To bound the variational crime resulting from the non-penetration condition and the friction law, we introduce two additional terms η_{C} and η_{F}. Both terms are restricted to the slave side of the contact zone and are associated with the faces

$$
\eta_j := \sum_{f \in \mathcal{F}_l^{\mathrm{s}}} \eta_{j;f}^2, \quad j \in \{\mathrm{C}, \mathrm{F}\}. \tag{6.15}
$$

Here $\mathcal{F}_l^{\mathrm{s}}$ stands for the set of all faces f on $\Gamma_{\mathrm{C}}^{\mathrm{s}}$ of the actual mesh. The term η_{C} measures the violation of the physical condition of a positive contact pressure and is associated with $\lambda_l^{\mathrm{C}} := \lambda_l^n \in M_l^+$. The term $\eta_{\mathrm{F};f}$ measures the violation of the friction law and is associated with the scalar-valued tangential part λ_l^{F}. For a Coulomb law, we set

$$
\lambda_l^{\mathrm{F}} := \sum_{p \in \mathcal{P}_{\mathrm{C};l}^{\mathrm{s}}} (\nu \gamma_p^n - \|\boldsymbol{\gamma}_p^t\|) \psi_p =: \sum_{p \in \mathcal{P}_{\mathrm{C};l}^{\mathrm{s}}} \gamma_p^{\mathrm{f}} \psi_p, \tag{6.16a}
$$

and for a Tresca law, we set

$$
\lambda_l^{\mathrm{F}} := \sum_{p \in \mathcal{P}_{\mathrm{C};l}^{\mathrm{s}}} (\mathcal{F} - \|\boldsymbol{\gamma}_p^t\|) \psi_p =: \sum_{p \in \mathcal{P}_{\mathrm{C};l}^{\mathrm{s}}} \gamma_p^{\mathrm{f}} \psi_p. \tag{6.16b}
$$

The local face contribution $\eta_{j;f}$ is then defined in terms of a non-linear operator P_l^j and uses a correctly weighted L^2-norm,

$$
\eta_{j;f} := \frac{h_f \delta_f}{2 \min(\mu^{\mathrm{s}}, \mu^{\mathrm{m}})} \|\lambda_l^j - P_l^j \lambda_l^j\|_{0;f}^2, \quad j \in \{\mathrm{C}, \mathrm{F}\}, \tag{6.17}
$$

where μ^{s} and μ^{m} are the Lamé parameters associated with the slave and master body, respectively. Here h_f stands for the face diameter and $\delta_f \in$

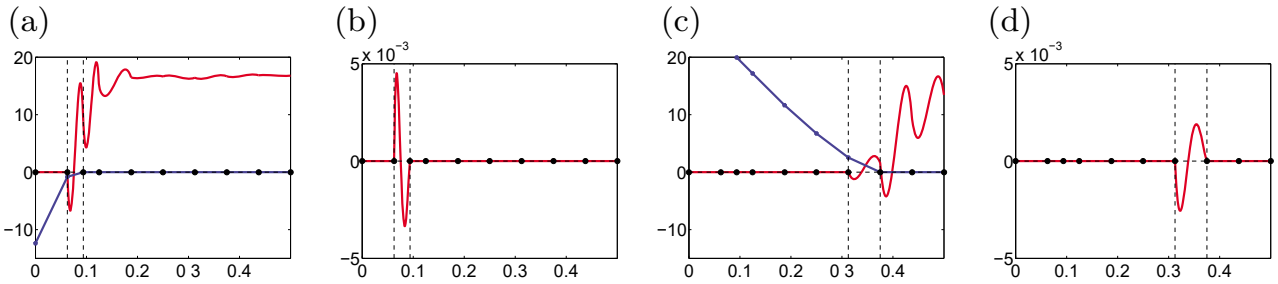

Figure 6.2. (a) Scaled λ_3^{C}, u_3^{C}, (b) the product $\lambda_3^{\mathrm{C}} u_3^{\mathrm{C}}$, (c) scaled u_3^{F}, λ_3^{F}, (d) the product $\lambda_3^{\mathrm{F}} u_3^{\mathrm{F}}$.

$\{1, 1/h_f\}$. The choice of δ_f and the definition of P_l^j will be specified in (6.20) and (6.19), respectively, and depend on the mesh and actual discrete contact zone.

Although both λ_l^{C} and λ_l^{F} are, by definition of $\mathbf{M}_l(\lambda_l^n)$ and $\mathbf{M}_l(\mathcal{F})$, in M_l^+, they are not in M^+ for non-trivial cases. As the *a priori* analysis has already shown, we have to face terms coupling the discrete Lagrange multiplier with the continuous relative displacement. We associate two scalar-valued relative displacements with the discrete Lagrange multipliers λ_l^{C} and λ_l^{F}

$$u_l^{\mathrm{C}} := \Pi_l([u_l^n] - g) = \sum_{p \in \mathcal{P}_{\mathrm{C};l}^{\mathrm{s}}} (\alpha_p^n - g_p)\phi_p, \tag{6.18a}$$

$$u_l^{\mathrm{F}} := \|\mathbf{\Pi}_l[\mathbf{u}_l^t]\|_l := \sum_{p \in \mathcal{P}_{\mathrm{C};l}^{\mathrm{s}}} \|\boldsymbol{\alpha}_p^t\|\phi_p. \tag{6.18b}$$

We recall that $\gamma_p^n(\alpha_p^n - g_p) = 0$ and $\|\boldsymbol{\alpha}_p^t\|\gamma_p^{\mathrm{f}} = 0$, but that $\lambda_l^{\mathrm{C}} u_l^{\mathrm{C}}$ and $\lambda_l^{\mathrm{F}} u_l^{\mathrm{F}}$ are, in general, non-zero. Figure 6.2 shows for a numerical example λ_3^{C}, u_3^{C} and λ_3^{F}, u_3^{F} as functions and the product $\lambda_3^{\mathrm{C}} u_3^{\mathrm{C}}$ and $\lambda_3^{\mathrm{F}} u_3^{\mathrm{F}}$. For symmetry reasons, we plot only the left half of $\Gamma_{\mathrm{C}}^{\mathrm{s}}$. We note that both products are only non-zero on two faces of $\Gamma_{\mathrm{C}}^{\mathrm{s}}$.

To get a better understanding, we illustrate the situation for $d = 3$ in Figure 6.3. The possible support of λ_l^{F} and u_l^{F} is sketched in Figure 6.3(a,b). Then $\lambda_l^{\mathrm{F}} u_l^{\mathrm{F}}$ does not vanish on the grey-shaded ring depicted in Figure 6.3(c). Starting with λ_l^{F}, we construct a $P_l^{\mathrm{F}} \lambda_l^{\mathrm{F}}$ such that the support of it is given as the grey-shaded region of Figure 6.3(d). Then it is obvious that $P_l^{\mathrm{F}} \lambda_l^{\mathrm{F}} u_l^{\mathrm{F}} = 0$. Moreover, we will require that $P_l^{\mathrm{F}} \lambda_l^{\mathrm{F}} \in M^+$.

To measure the non-conformity of λ_l^{C} and λ_l^{F}, we introduce mapped functions $P_l^{\mathrm{C}} \lambda_l^{\mathrm{C}}, P_l^{\mathrm{F}} \lambda_l^{\mathrm{F}} \in M^+$. The construction is based on a decomposition of $\Gamma_{\mathrm{C}}^{\mathrm{s}}$ into disjoint simply connected macro-faces $\overline{F} := \cup_{f \subset F} \overline{f}$, where f is an element of $\mathcal{F}_l^{\mathrm{s}}$. The set $\mathcal{F}_{l;j}$, $j \in \{\mathrm{C}, \mathrm{F}\}$, of macro-faces forms a partition of $\Gamma_{\mathrm{C}}^{\mathrm{s}}$, *i.e.*, $\overline{\Gamma_{\mathrm{C}}^{\mathrm{s}}} = \cup_{F \in \mathcal{F}_{l;j}} \overline{F}$. Moreover, we require that the macro-faces satisfy $h_F := \mathrm{diam} F \leq C \min_{f \subset F} h_f$ for all $F \in \mathcal{F}_{l;j}$ and $F = f$ if $F \subset \mathrm{supp}\, u_l^j \setminus \mathrm{supp}\, \lambda_l^j$. The following assumption plays a crucial role in the proper scaling of the additional contact terms.

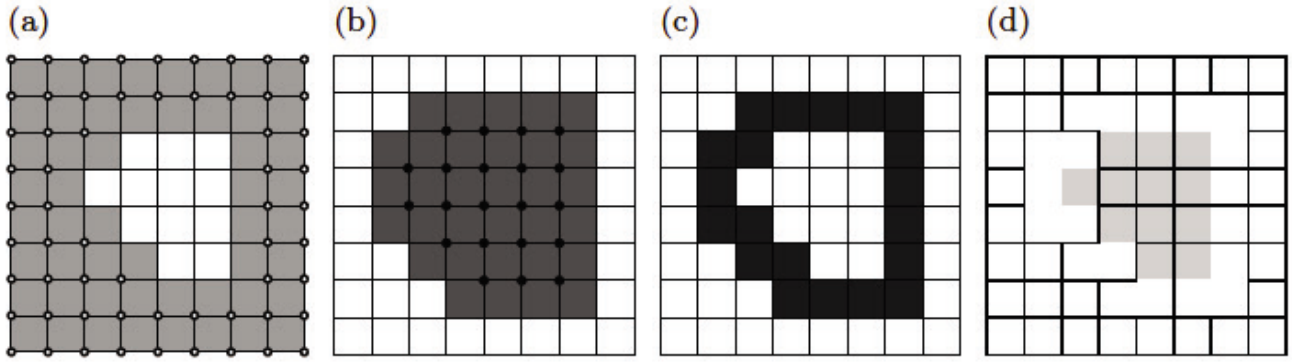

Figure 6.3. (a) $\operatorname{supp} u_l^{\mathrm{F}}$, (b) $\operatorname{supp} \lambda_l^{\mathrm{F}}$, (c) $\operatorname{supp} u_l^{\mathrm{F}} \cap \operatorname{supp} \lambda_l^{\mathrm{F}}$, (d) $\operatorname{supp} P_{\mathrm{F}} \lambda_l^{\mathrm{F}}$ and macro-faces $F \in \mathcal{F}_{l;\mathrm{F}}$.

Assumption 6.7. We assume that for $j \in \{\mathrm{C}, \mathrm{F}\}$ there exists a macro-face decomposition in the above sense such that, for $F \in \mathcal{F}_{l;j}$ with $F \neq f$ there exists at least one $f_0 \subset \Gamma_{\mathrm{C}}^{\mathrm{s}} \setminus \operatorname{supp} u_l^j$ with $f_0 \subset F$.

We note that the decomposition into macro-faces is not unique, and the macro-faces should be as small as possible. Moreover, each $f \in \mathcal{F}_l^{\mathrm{s}}$ belongs to exactly one macro-face in $\mathcal{F}_{l;j}$ denoted by F_f^j. In Figure 6.3(d), we show a possible macro-face decomposition.

Remark 6.8. This assumption can easily be violated on coarse meshes but will hold asymptotically provided that the solution satisfies

$$\{[\mathbf{u}_t] = \mathbf{0}\} = \overline{\mathcal{O}(\{[\mathbf{u}_t] = \mathbf{0}\})},$$

where $\mathcal{O}(\cdot)$ denotes the open set of its argument. In 2D this corresponds to the assumption that $[\mathbf{u}_t]$ cannot change its sign by passing through zero at a single point of $\Gamma_{\mathrm{C}}^{\mathrm{s}}$. Equivalently, we can require that in the case of a Coulomb law $\boldsymbol{\lambda}_t$ does not jump from $+\nu\lambda_n$ to $-\nu\lambda_n$. In the case of a Tresca law, we assume that $\boldsymbol{\lambda}_t$ does not jump from $+\mathcal{F}$ to $-\mathcal{F}$. For a more detailed discussion, we refer to Eck *et al.* (2005), Hild and Renard (2007) and Renard (2006). In 2D, it is automatically guaranteed that the support of λ_n does not contain isolated points, and thus we can always assume the existence of such a macro-face decomposition for $j = \mathrm{C}$ provided the mesh is fine enough.

In terms of these preliminary settings, we define the operator P_l^j which is used in (6.17). It is face-wise given for the faces $f \in \mathcal{F}_l^{\mathrm{s}}$ of the original mesh by:

$$P_l^j \lambda_l^j := \begin{cases} 0 & f \subset \operatorname{supp} u_l^j, \\ \dfrac{\int_{F_f^j} \lambda_l^j \, \mathrm{d}s}{|F_f^j \cap (\Gamma_{\mathrm{C}}^{\mathrm{s}} \setminus \operatorname{supp} u_l^j)|} & f \subset \Gamma_{\mathrm{C}}^{\mathrm{s}} \setminus \operatorname{supp} u_l^j, F_f^j \not\subset \Gamma_{\mathrm{C}}^{\mathrm{s}} \setminus \operatorname{supp} u_l^j, \\ \lambda_l^j & f \subset F_f^j \subset \Gamma_{\mathrm{C}}^{\mathrm{s}} \setminus \operatorname{supp} u_l^j, \text{ and } \lambda_l^j \geq 0, \\ Z_l^* \lambda_l^j & \text{otherwise,} \end{cases} \tag{6.19}$$

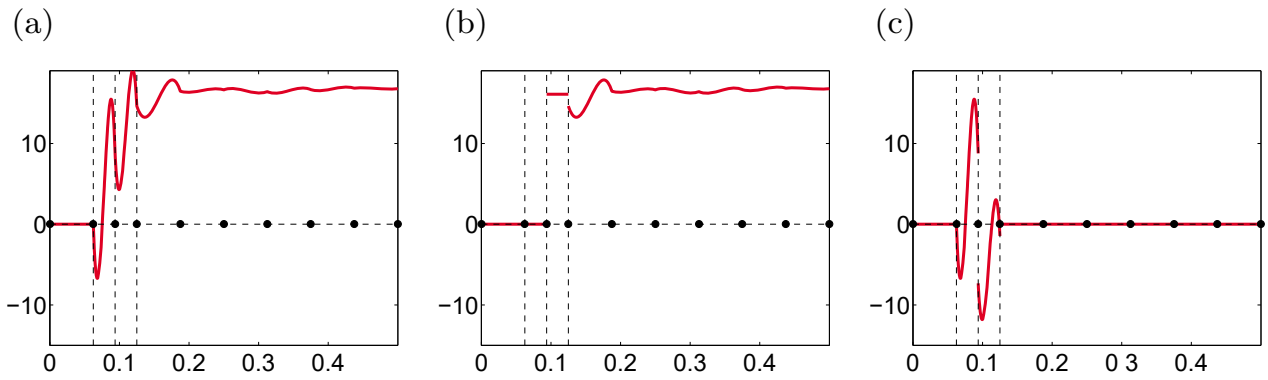

Figure 6.4. (a) λ_3^{C}, (b) $P_3^{\mathrm{C}}\lambda_3^{\mathrm{C}}$, (c) $\lambda_3^{\mathrm{C}} - P_3^{\mathrm{C}}\lambda_3^{\mathrm{C}}$.

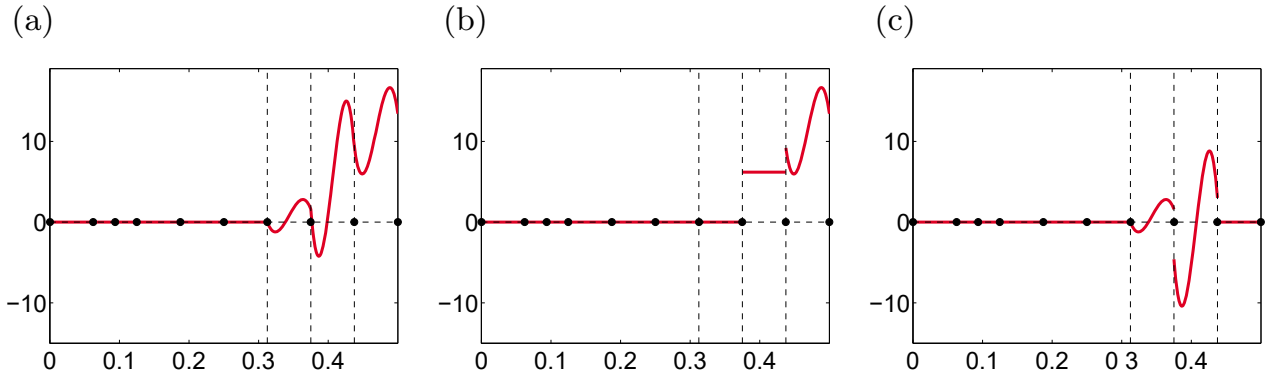

Figure 6.5. (a) λ_3^{F}, (b) $P_3^{\mathrm{F}}\lambda_3^{\mathrm{F}}$, (c) $\lambda_3^{\mathrm{F}} - P_3^{\mathrm{F}}\lambda_3^{\mathrm{F}}$.

where $|\cdot|$ stands for the $(d-1)$-dimensional area of its argument. Recalling the definition (4.7) of Z_l^*, it is easy to see that Z_l^* maps M_l^+ onto W_l^+. We note that $P_l^j\lambda_l^j$, $j \in \{\mathrm{C},\mathrm{F}\}$ is always well-defined. However, Assumption 6.7 guarantees that $P_l^j\lambda_l^j \neq 0$ if $\lambda_l^j \neq 0$.

Figures 6.4 and 6.5 show λ_3^j, $P_3^j\lambda_3^j$ and $\lambda_3^j - P_3^j\lambda_3^j$, $j \in \{\mathrm{C},\mathrm{F}\}$, for the first example discussed in Section 6.8 and $\nu = 0.8$. We note that $\lambda_3^j - P_3^j\lambda_3^j \neq 0$ only on four faces of $\Gamma_{\mathrm{C}}^{\mathrm{s}}$. For this example this also holds true for all refinement levels $l \geq 1$. Our numerical results show that for all our examples Assumption 6.7 is asymptotically satisfied.

Now, we specify our choice for δ_f in (6.17):

$$\delta_f := \begin{cases} 1 & \text{if } f \subset F_f^j \text{ such that } \int_{F_f^j} P_l^j\lambda_l^j \,\mathrm{d}s = \int_{F_f^j} \lambda_l^j \,\mathrm{d}s, \\ \frac{1}{h_f} & \text{otherwise.} \end{cases} \tag{6.20}$$

Lemma 6.9. Under Assumption 6.7, the following properties hold for $P_l^j\lambda_l^j$, $j \in \{\mathrm{C},\mathrm{F}\}$:

(i) $P_l^j\lambda_l^j\, u_l^j = 0$,
(ii) $P_l^j\lambda_l^j \geq 0$,
(iii) $\int_F P_l^j\lambda_l^j \,\mathrm{d}s = \int_F \lambda_l^j \,\mathrm{d}s$ for all $F \in \mathcal{F}_{l;j}$,
(iv) $\|\lambda_l^j - P_l^j\lambda_l^j\|^2_{-\frac{1}{2};\Gamma_{\mathrm{C}}} \leq C \sum_{f\in\mathcal{F}_l^{\mathrm{s}}} h_f \|\lambda_l^j - P_l^j\lambda_l^j\|^2_{0;h_f}$.

Proof. Property (i) follows directly from the first line in the definition (6.19) of $P_l^j \lambda_l^j$. Recalling that $\lambda_l^j \in M_l^+$ and thus $Z_l^* \lambda_l^j \geq 0$ and $\int_f \lambda_l^j \, \mathrm{d}s \geq 0$ for all faces f, we find property (ii). For $F \subset \Gamma_{\mathrm{C}}^{\mathrm{s}} \setminus \operatorname{supp} u_l^j$, the required equality follows from $\int_f \lambda_l^j \, \mathrm{d}s = \int_f Z_l^* \lambda_l^j \, \mathrm{d}s$. For $F = f \subset \operatorname{supp} u_l^j \setminus \operatorname{supp} \lambda_l^j$, we have $P_l^j \lambda_l^j = \lambda_l^j = 0$. The only non-trivial case yields

$$\begin{aligned}\int_F P_l^j \lambda_l^j \, \mathrm{d}s &= \sum_{f \subset F} \int_f P_l^j \lambda_l^j \, \mathrm{d}s = \sum_{f \subset F \setminus \operatorname{supp} u_l^j} \int_f P_l^j \lambda_l^j \, \mathrm{d}s \\ &= \frac{\int_F \lambda_l^j \, \mathrm{d}s}{|F \cap (\Gamma_{\mathrm{C}}^{\mathrm{s}} \setminus \operatorname{supp} u_l^j)|} \sum_{f \subset F \setminus \operatorname{supp} u_l^j} |f| = \int_F \lambda_l^j \, \mathrm{d}s.\end{aligned}$$

Here we have used the fact that, by Assumption 6.7, the sum is not empty. To show property (iv), we use (iii). For $v \in H^{1/2}(\Gamma_{\mathrm{C}})$, we find

$$\begin{aligned}\int_{\Gamma_{\mathrm{C}}^{\mathrm{s}}} (\lambda_l^j - P_l^j \lambda_l^j) v \, \mathrm{d}s &= \sum_{F \in \mathcal{F}_{l;j}} \int_F (\lambda_l^j - P_l^j \lambda_l^j)(v - \Pi_0 v) \, \mathrm{d}s \\ &\leq C \sum_{F \in \mathcal{F}_{l;j}} \sqrt{h_F} \|\lambda_l^j - P_l^j \lambda_l^j\|_{0;F} \|v\|_{\frac{1}{2};F},\end{aligned}$$

where Π_0 is the L^2-projection onto macro-elementwise constants. □

Property (iii) in Lemma 6.9 yields that $\delta_f = 1$ for all faces. We note that the properties specified in Lemma 6.9 are also satisfied by more sophisticated operators. As in the case of dual basis functions, we can start from the existing choice and add suitable functions. By adding a quadratic function, we can make the result continuous. In Figure 6.6, we show two different alternatives for $d = 2$. Figure 6.6(a–c) illustrates a part of the contact zone and λ_3^{C} and $P_3^{\mathrm{C}} \lambda_3^{\mathrm{C}}$. In (a,d), the operator defined by (6.19) is given. In (b,e) and (c,f), we depict an alternative definition using a piecewise affine and quadratic modification, respectively. By using polynomials of higher order in the definition (6.19), we can guarantee that $\lambda_l^j - P_l^j \lambda_l^j$ is continuous, and that $P_l^j \lambda_l^j$ also satisfies the properties of Lemma 6.9.

Although the piecewise quadratic modification results in a continuous $\lambda_3^{\mathrm{C}} - P_3^{\mathrm{C}} \lambda_3^{\mathrm{C}}$, the implementation of it in 3D is technically more involved and does not bring any qualitative benefit. Thus, from now on we only use the definition given by (6.19).

Having introduced P_j^{C} and P_j^{F}, we can improve the upper bound for $|||\mathbf{u} - \mathbf{u}_l|||$ for the special situation of a contact problem in 2D with matching meshes. However, an additional assumption is required.

Assumption 6.10. We assume that for $d = 2$, there exists a $\chi \in W_\infty^1(\Gamma_{\mathrm{C}})$ such that $|[u_t]| = \chi [u_t]$ and moreover $|[u_l^t]| = \chi [u_l^t]$.

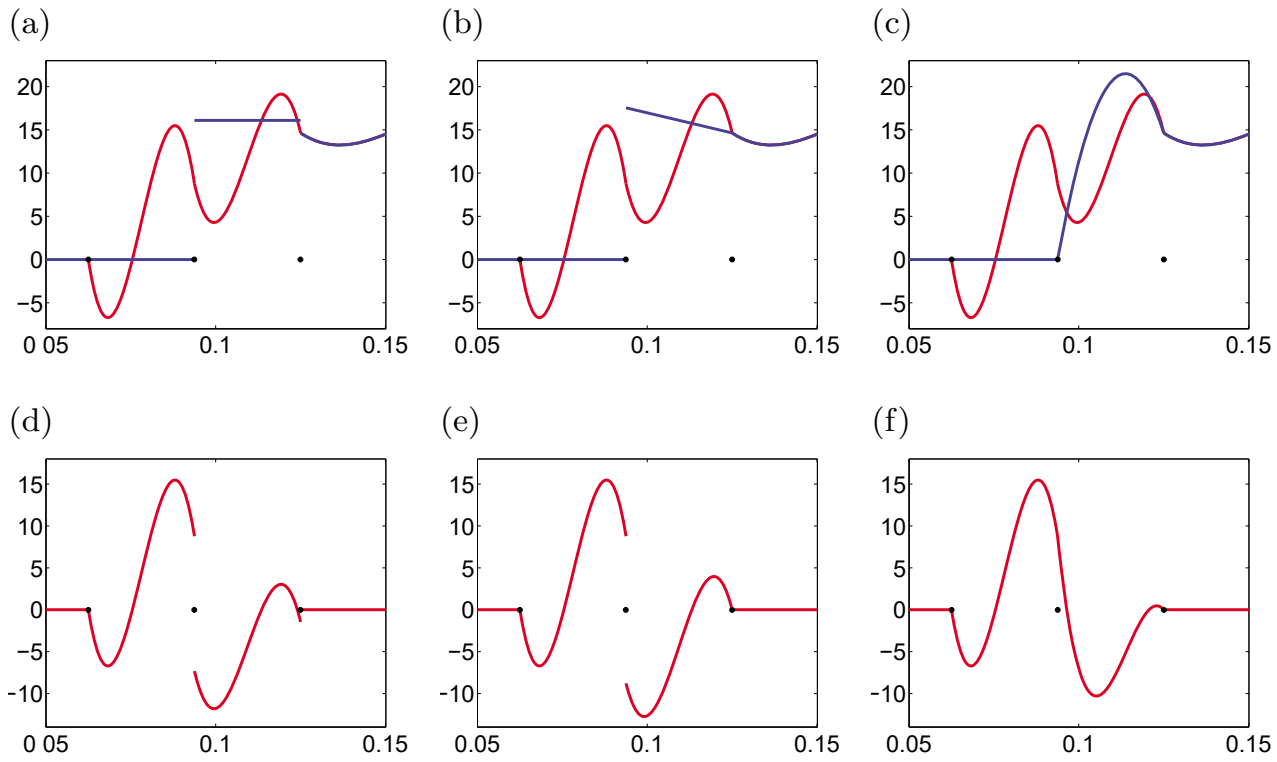

Figure 6.6. (a,d) Piecewise constant, (b,e) linear, (c,f) quadratic modification; (a–c) λ_3^{C} and $P_3^{\mathrm{C}}\lambda_3^{\mathrm{C}}$; (d–f) $\lambda_3^{\mathrm{C}} - P_3^{\mathrm{C}}\lambda_3^{\mathrm{C}}$.

Let us briefly comment on this assumption. The first part is closely related to Assumption 4.7 and is also reasonable to make in 3D. In both assumptions, the case that $[u_t]$ changes its sign by passing through zero at a single point of Γ_{C} is ruled out. The second part of the assumption is only reasonable in 2D. In fact, it follows from the first part and the *a priori* estimates for $s > 1$ for $h_l < H_0$. But there is no possibility of estimating H_0. A direct consequence of Assumption 6.10 is the estimate

$$\| |[u_t]| - |[u_l^t]| \|_{\frac{1}{2};\Gamma_{\mathrm{C}}} = \| [u_t - u_l^t]\chi \|_{\frac{1}{2};\Gamma_{\mathrm{C}}} \leq C \| [u_t] - [u_l^t] \|_{\frac{1}{2};\Gamma_{\mathrm{C}}}.$$

Lemma 6.11. Under Assumptions 6.10 and 6.7, we obtain the following upper bound in 2D, for the error in the energy norm for matching meshes, and a zero gap

$$\begin{aligned} |||\mathbf{u} - \mathbf{u}_l|||^2 \leq & (\eta_{\mathrm{L}} + C(\eta_{\mathrm{C}} + \eta_{\mathrm{F}} + \xi_1)) |||\mathbf{u} - \mathbf{u}_l||| \\ & + C\nu \| \lambda_l^n - \lambda_n \|_{-\frac{1}{2};\Gamma_{\mathrm{C}}} \| [u_l^n] - [u_n] \|_{\frac{1}{2};\Gamma_{\mathrm{C}}}, \end{aligned}$$

where we formally set $\nu = 0$ for a Tresca friction problem.

Proof. We decompose the surface stress into a normal and a tangential part and recall that $\langle \lambda_n, [u_n] \rangle_{\Gamma_{\mathrm{C}}} = 0 = \langle P_l^{\mathrm{C}} \lambda_l^n, u_l^{\mathrm{C}} \rangle_{\Gamma_{\mathrm{C}}}$ and that $\langle P_l^{\mathrm{C}} \lambda_l^n, [u_n] \rangle_{\Gamma_{\mathrm{C}}} \leq 0$. Furthermore, on matching meshes, (6.18a) states that $u_l^{\mathrm{C}} = [u_l^n]$ and thus $[u_l^n] \leq 0$. In terms of Lemma 6.9, the normal part in Lemma 6.5 can

then be bounded by

$$\begin{aligned}\langle \lambda_l^n - \lambda_n, [u_n] - [u_l^n] \rangle_{\Gamma_C} &\leq \langle \lambda_l^n, [u_n] - [u_l^n] \rangle_{\Gamma_C} \\ &\leq \langle \lambda_l^n - P_l^C \lambda_l^n, [u_n] - [u_l^n] \rangle_{\Gamma_C} \leq C \eta_C |||\mathbf{u} - \mathbf{u}_l|||.\end{aligned}$$

For the tangential part, we have in 2D

$$\langle \boldsymbol{\lambda}_l^t - \boldsymbol{\lambda}_t, [\mathbf{u}_t] - \boldsymbol{\Pi}_l [\mathbf{u}_l^t] \rangle_{\Gamma_C} = \langle \lambda_l^t - \lambda_t, [u_t] - \Pi_l [u_l^t] \rangle_{\Gamma_C}.$$

Assumption 6.10 and the fact that we are working with matching meshes guarantee that $\|\boldsymbol{\Pi}_l [\mathbf{u}_l^t]\|_l = \|\boldsymbol{\Pi}_l [\mathbf{u}_l^t]\| = |\Pi_l [u_l^t]| = |[u_l^t]|$ and that u_l^F defined by (6.18b) is equal to χu_l^t.

In a first step, we consider the case of Tresca friction. We then find that, since $\boldsymbol{\lambda} \in \mathbf{M}(\mathcal{F})$,

$$\langle \lambda_l^t - \lambda_t, -\Pi_l [u_l^t] \rangle_{\Gamma_C} \leq -\langle \mathcal{F}, |[u_l^t]| \rangle_{\Gamma_C} + \langle |\lambda_t|, |[u_l^t]| \rangle_{\Gamma_C} \leq 0.$$

Using Assumption 6.10 in combination with Lemma 6.9 and the definition of λ_l^F given by (6.16b), we finally obtain

$$\begin{aligned}\langle \lambda_l^t - \lambda_t, [u_t] \rangle_{\Gamma_C} &= \langle \lambda_l^t, \chi |[u_t]| \rangle_{\Gamma_C} - \langle \mathcal{F}, |[u_t]| \rangle_{\Gamma_C} = \langle -\lambda_l^F, |[u_t]| \rangle_{\Gamma_C} \\ &= \langle P_l^F \lambda_l^F - \lambda_l^F, |[u_t]| \rangle_{\Gamma_C} - \langle P_l^F \lambda_l^F, |[u_t]| \rangle_{\Gamma_C} \\ &\leq \langle P_l^F \lambda_l^F - \lambda_l^F, |[u_t]| \rangle_{\Gamma_C} \\ &= \langle P_l^F \lambda_l^F - \lambda_l^F, |[u_t]| - |[u_l^t]| \rangle_{\Gamma_C} = \langle P_l^F \lambda_l^F - \lambda_l^F, ([u_t] - [u_l^t]) \chi \rangle_{\Gamma_C} \\ &\leq C \|P_l^F \lambda_l^F - \lambda_l^F\|_{-\frac{1}{2};\Gamma_C} \|([u_t] - [u_l^t]) \chi\|_{\frac{1}{2};\Gamma_C} \\ &\leq C \|P_l^F \lambda_l^F - \lambda_l^F\|_{-\frac{1}{2};\Gamma_C} \|[u_t] - [u_l^t]\|_{\frac{1}{2};\Gamma_C} \leq C \eta_F |||\mathbf{u} - \mathbf{u}_l|||.\end{aligned}$$

In a second step, we consider the case of Coulomb friction. We observe that our assumptions guarantee

$$\langle \lambda_l^t, [u_t] \rangle_{\Gamma_C} = \langle \lambda_l^t, \chi^2 [u_t] \rangle_{\Gamma_C} = \langle \nu \lambda_l^n - \lambda_l^F, |[u_t]| \rangle_{\Gamma_C}.$$

Using definition (6.16a) and applying the same techniques as before, we get

$$\begin{aligned}\langle \lambda_l^t - \lambda_t, [u_t] - [u_l^t] \rangle_{\Gamma_C} &\leq \langle -\lambda_l^F, |[u_t]| \rangle_{\Gamma_C} + \nu \langle \lambda_l^n - \lambda_n, |[u_t]| - |[u_l^t]| \rangle_{\Gamma_C} \\ &\leq C \big(\eta_F |||\mathbf{u} - \mathbf{u}_l||| + \nu \|\lambda_l^n - \lambda_n\|_{-\frac{1}{2};\Gamma_C} \|[u_t] - [u_l^t]\|_{\frac{1}{2};\Gamma_C} \big). \qquad \square\end{aligned}$$

We note that Lemma 6.11 also holds true in 3D if we consider a contact problem on non-matching meshes and without friction.

6.3. Error bound for the Lagrange multiplier

We now consider the error in the Lagrange multiplier. From the abstract theory of saddle-point problems, it is well known that the discretization error in the Lagrange multiplier can be bounded in terms of its best approximation error and the discretization error in the primal variable. Unfortunately, the

best approximation error is not computable and thus cannot be directly controlled within the adaptive refinement process. Therefore, we provide an estimate where the best approximation is replaced by the error indicator η_{L}. Of crucial importance for the stability of a saddle-point problem is the inf-sup constant. The bilinear form $b(\cdot,\cdot)$ reflects the $H^{1/2}$-duality pairing. This observation motivates the use of a parameter-dependent norm for the Lagrange multiplier, which is equivalent to the $H^{1/2}$-dual norm

$$|||\boldsymbol{\mu}||| := \sup_{\mathbf{v}=(\mathbf{0},\mathbf{v}^{\mathrm{s}}),\mathbf{v}^{\mathrm{s}}\in\mathbf{V}_0^{\mathrm{s}}} \frac{b(\boldsymbol{\mu},\mathbf{v})}{\sqrt{a(\mathbf{v},\mathbf{v})}}. \tag{6.21}$$

We note that the norm of the Lagrange multiplier only depends on the Lamé parameters of the slave side but not on the master side. Alternatively, a different scaling can be used.

Lemma 6.12. The error in the Lagrange multiplier is bounded by

$$|||\boldsymbol{\lambda}-\boldsymbol{\lambda}_l||| \le |||\mathbf{u}-\mathbf{u}_l||| + \eta_L + C\xi_1,$$

where ξ_1 is the data oscillation term defined by (6.1).

Proof. We start with the observation that $b(\cdot,\mathbf{v})$ restricted to $\mathbf{v}\in\mathbf{0}\times\mathbf{V}_0^{\mathrm{s}}$ is equal to $\langle\cdot,\mathbf{v}^{\mathrm{s}}\rangle_{\Gamma_{\mathrm{C}}}$ and recall that $(\mathbf{u},\boldsymbol{\lambda})$ satisfies the equilibrium (2.15) and that $\Gamma_{\mathrm{C}}=\Gamma_{\mathrm{C}}^{\mathrm{s}}$. Using the definition (6.21), Lemma 6.3 and the symmetry of $\boldsymbol{\sigma}_l$, we find

$$\begin{aligned}\langle\boldsymbol{\lambda}-\boldsymbol{\lambda}_l,\mathbf{v}^{\mathrm{s}}\rangle_{\Gamma_{\mathrm{C}}} &= f_{\mathrm{s}}(\mathbf{v}^{\mathrm{s}}) - a_{\mathrm{s}}(\mathbf{u}^{\mathrm{s}},\mathbf{v}^{\mathrm{s}}) + \int_{\Gamma_{\mathrm{C}}^{\mathrm{s}}} \boldsymbol{\sigma}_l\mathbf{n}\mathbf{v}^{\mathrm{s}}\,\mathrm{d}s \\ &= \int_{\Omega^{\mathrm{s}}} (\boldsymbol{\sigma}_l - \mathcal{C}\boldsymbol{\epsilon}(\mathbf{u}^{\mathrm{s}})) : \epsilon(\mathbf{v}^{\mathrm{s}})\,\mathrm{d}x + \int_{\Omega^{\mathrm{s}}} (\mathbf{f}-\Pi_1\mathbf{f})\mathbf{v}^{\mathrm{s}}\,\mathrm{d}s.\end{aligned}$$

Here, we have used the fact that, by assumption, the Arnold–Winther space can exactly resolve the given Neumann data. Otherwise, an additional data oscillation term on the Neumann boundary has to be taken into account. Inserting the primal finite element approximation on the slave side, we get

$$\langle\boldsymbol{\lambda}-\boldsymbol{\lambda}_l,\mathbf{v}^{\mathrm{s}}\rangle_{\Gamma_{\mathrm{C}}^{\mathrm{s}}} \le \Big(\sqrt{a_{\mathrm{s}}(\mathbf{u}_l^{\mathrm{s}}-\mathbf{u}^{\mathrm{s}},\mathbf{u}_l^{\mathrm{s}}-\mathbf{u}^{\mathrm{s}})} + \eta_{\mathrm{L}} + C\xi_1\Big)\sqrt{a_{\mathrm{s}}(\mathbf{v}^{\mathrm{s}},\mathbf{v}^{\mathrm{s}})}. \qquad \square$$

Thus if η_L is an error estimator for the primal discretization error, it also provides an upper bound for the discretization error in the dual variable.

6.4. Upper bounds for the friction and contact terms

In this subsection, we provide upper bounds for the terms η_{C} and η_{F} defined by (6.15) and (6.17). We recall that λ_l^j is a numerical approximation of a non-negative functional, and $\lambda_l^j - P_l^j\lambda_l^j$ measures the variational crime of the approximation λ_l^j, $j\in\{\mathrm{C},\mathrm{F}\}$. Due to our assumption that we work with

simplicial meshes, $\boldsymbol{\sigma}(\mathbf{u}_l)\mathbf{n}^{\mathrm{s}}$ is constant on each face. In general, this does not hold for quadrilateral/hexahedral meshes. In that case, the estimates are technically more involved.

Lemma 6.13. Under Assumption 6.7, we have for Tresca and Coulomb friction

$$\eta_{\mathrm{C}} + \eta_{\mathrm{F}} \leq C\eta_{\mathrm{L}}.$$

Proof. We recall $\lambda_l^{\mathrm{C}} = \lambda_l^n$ and start with the normal contact term η_{C}. This term is naturally associated with the normal stress. For each face $f \in \mathcal{F}_l^{\mathrm{s}}$ and its associated macro-face F_f^{C}, we then obtain, in terms of Lemma 6.3 and Lemma 6.9,

$$\begin{aligned}
\|\lambda_l^{\mathrm{C}} - P_l^{\mathrm{C}}\lambda_l^{\mathrm{C}}\|_{0;f}^2 &\leq \|\lambda_l^{\mathrm{C}} - P_l^{\mathrm{C}}\lambda_l^{\mathrm{C}}\|_{0;F_f^{\mathrm{C}}}^2 \leq Ch_{F_f^{\mathrm{C}}}^2 |\lambda_l^n|_{1;F_f^{\mathrm{C}}}^2 \\
&\leq C\sum_{\tilde{f}\subset F_f^{\mathrm{C}}} h_{\tilde{f}}^2 |\mathbf{n}(\boldsymbol{\sigma}_l - \boldsymbol{\sigma}(\mathbf{u}_l^{\mathrm{s}}))\mathbf{n}|_{1;\tilde{f}}^2 \\
&\leq C\sum_{\tilde{f}\subset F_f^{\mathrm{C}}} \|\mathbf{n}(\boldsymbol{\sigma}_l - \boldsymbol{\sigma}(\mathbf{u}_l^{\mathrm{s}}))\mathbf{n}\|_{0;\tilde{f}}^2 \\
&\leq C\sum_{\tilde{f}\subset F_f^{\mathrm{C}}} \|(\boldsymbol{\sigma}_l - \boldsymbol{\sigma}(\mathbf{u}_l^{\mathrm{s}}))\mathbf{n}\|_{0;\tilde{f}}^2 \leq C\frac{1}{h_f}\|\boldsymbol{\sigma}_l - \boldsymbol{\sigma}(\mathbf{u}_l^{\mathrm{s}})\|_{0;\tilde{\omega}_f}^2.
\end{aligned}$$

In the last step, we have used the properties of the macro-faces and a scaled inverse-type inequality for polynomials. Here $\tilde{\omega}_f$ stands for the union of all elements $T \in \mathcal{T}_l^{\mathrm{s}}$ such that $\partial T \cap F_f^{\mathrm{C}}$ is non-trivial. Using the weighting of $\|\lambda_l^{\mathrm{C}} - P_l^{\mathrm{C}}\lambda_l^{\mathrm{C}}\|_{0;f}^2$ in the definition (6.17) of $\eta_{\mathrm{C};f}$, and (6.20) in combination with Assumption 6.7, we get $\eta_{\mathrm{C};f}^2 \leq C\sum_{T\subset\tilde{\omega}_f}\eta_{\mathrm{L};T}^2$. Summing over all faces, and noting that each element T is contained in at most a bounded number of $\tilde{\omega}_f$, we have $\eta_{\mathrm{C}} \leq C\eta_{\mathrm{L}}$.

Now, we focus on the term η_{F}, which is associated with the friction law and thus involves the tangential stress component. We can follow the lines of the proof for $\eta_{\mathrm{C};f}$ directly. Using the definition (6.16) for λ_l^{F}, and formally setting $\nu = 0$ in the case of a Tresca friction, both definitions (6.16a) and (6.16b) guarantee that

$$\|\lambda_l^{\mathrm{F}} - P_l^{\mathrm{F}}\lambda_l^{\mathrm{F}}\|_{0;f}^2 \leq C\sum_{\tilde{f}\subset F_f^{\mathrm{F}}} h_{\tilde{f}}^2 |\lambda_l^{\mathrm{F}}|_{1;\tilde{f}}^2 \leq C\sum_{\tilde{f}\subset F_f^{\mathrm{F}}} h_{\tilde{f}}^2\big(\nu|\lambda_l^n|_{1;\tilde{f}}^2 + |\tilde{\lambda}_l^t|_{1;\tilde{f}}^2\big)$$

with $\tilde{\lambda}_l^t := \sum_{p\in\mathcal{P}_{\mathrm{C};l}^{\mathrm{s}}}\|\gamma_p^t\|\psi_p$. The first term on the right-hand side has already been discussed, and we only have to consider the second term in more detail.

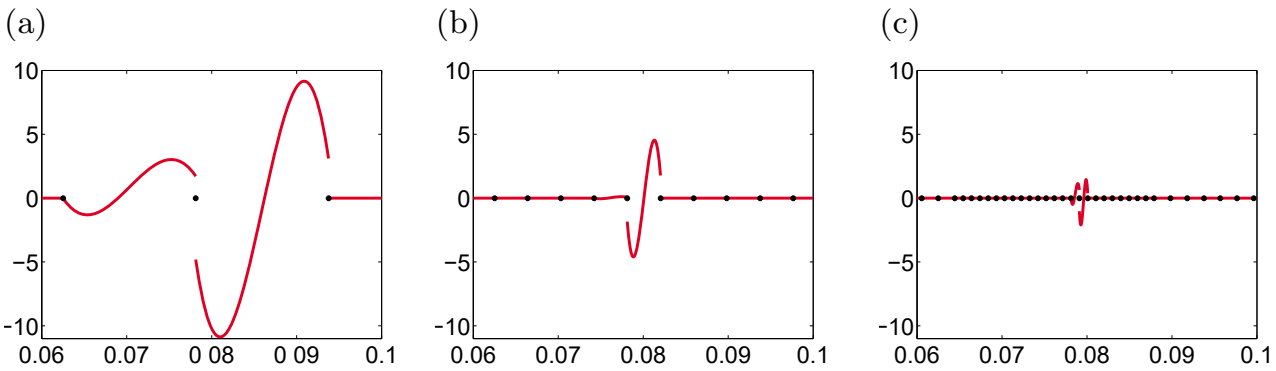

Figure 6.7. $\lambda_l^{\mathrm{C}} - P_{\mathrm{C}}\lambda_l^{\mathrm{C}}$, $l = 5$ (a), $l = 8$ (b), $l = 11$ (c).

Using a discrete norm equivalence and noting that $|\|\boldsymbol{\gamma}_p^t\| - \|\boldsymbol{\gamma}_q^t\|| \leq \|\boldsymbol{\gamma}_p^t - \boldsymbol{\gamma}_q^t\|$, we find that

$$|\tilde{\lambda}_l^t|_{1;\tilde{f}} \leq C|\boldsymbol{\lambda}_l^t|_{1;\tilde{f}} \leq C|\boldsymbol{\lambda}_l|_{1;\tilde{f}} \leq C|(\boldsymbol{\sigma}_l - \boldsymbol{\sigma}(\mathbf{u}_l^{\mathrm{s}}))\mathbf{n}|_{1;\tilde{f}}$$

and the same arguments as before apply. □

Remark 6.14. We note that if Assumption 6.7 is violated, the different scaling factor δ_f results in a mesh-dependent upper bound.

Although we obtain $\eta_{\mathrm{C}} + \eta_{\mathrm{F}} \leq C\eta_{\mathrm{L}}$ theoretically, we observe for all our numerical tests that $\eta_{\mathrm{C}} + \eta_{\mathrm{F}}$ decreases more rapidly than η_{L}. To get a better feeling for the role of η_{C} and η_{F}, we illustrate the decrease in the value of $\lambda_l^{\mathrm{C}} - P_{\mathrm{C}}\lambda_l^{\mathrm{C}}$ for different refinement levels in Figure 6.7. It can be observed that only two neighbouring faces have a non-trivial contribution on the left part of the contact zone. Due to the scaling by $\sqrt{h_f}$ of the L^2-norm of $\lambda_l^{\mathrm{C}} - P_{\mathrm{C}}\lambda_l^{\mathrm{C}}$ in the definition of η_{C}, this contribution decreases rapidly within the adaptive refinement process. In particular, in this test example, η_{C} is equivalent to $h_l^{\min}\|\lambda_l^{\mathrm{C}} - P_{\mathrm{C}}\lambda_l^{\mathrm{C}}\|_\infty$, where $\|\cdot\|_\infty$ is the L^∞-norm on $\Gamma_{\mathrm{C}}^{\mathrm{s}}$ and $h_l^{\min} := \min_{T \in \mathcal{T}_l^{\mathrm{s}}} h_T$. Due to the decrease of $\|\lambda_l^{\mathrm{C}} - P_{\mathrm{C}}\lambda_l^{\mathrm{C}}\|_\infty$ with respect to the refinement level l, we expect that η_{C} can be asymptotically neglected compared to η_{L}.

Theorem 6.15. Under Assumptions 6.7 and 6.10, for matching meshes and in 2D or in 3D with no friction, we obtain the upper bound

$$|\|\mathbf{u} - \mathbf{u}_l\|| \leq C(\eta_{\mathrm{L}} + \xi_1)$$

for a Tresca or Coulomb friction problem provided that ν is small enough.

Proof. The result follows by Lemmas 6.11 and 6.13, the application of Young's inequality and Lemma 6.12 in the case of a Coulomb problem. □

We note that Assumption 6.10 is quite strong and cannot be verified within the adaptive refinement process. However, for all our numerical test

examples it is satisfied. We refer to Hild and Lleras (2009) for an alternative approach. However, additional terms then enter into the definition of the error estimator, which cannot be bounded with optimal lower constants. This is not the case for the approach we propose.

6.5. Lower bound for the discretization error

In this subsection, we provide a local upper bound for our error estimator. For a one-sided contact problem without friction this result can be found in Weiss and Wohlmuth (2009); see Nicaise *et al.* (2008) for the linear elasticity setting. Here, we generalize it to Tresca and Coulomb friction problems in 2D and also to non-matching meshes. We restrict ourselves to $d = 2$, but the same type of argumentation can be applied to $d = 3$.

We start with a preliminary result which bounds, in the discrete setting, the jump of the stress across a face by the jump of its surface traction.

Lemma 6.16. For each face $f \in \mathcal{F}_l$, we have

$$\|[\boldsymbol{\sigma}(\mathbf{u}_l)]\|_{0;f} \leq C\|[\boldsymbol{\sigma}(\mathbf{u}_l)\mathbf{n}_f]\|_{0;f}.$$

Proof. The proof is based on the observation that $[\nabla \mathbf{u}_l \mathbf{t}_f] = \mathbf{0}$ on each face. Here $\mathbf{t}_f$ is a normalized fixed orthogonal vector to $\mathbf{n}_f$. For each face f, the set $\{\mathbf{n}_f \otimes \mathbf{n}_f, \mathbf{n}_f \otimes \mathbf{t}_f, \mathbf{t}_f \otimes \mathbf{n}_f, \mathbf{t}_f \otimes \mathbf{t}_f\}$ forms an orthonormal basis for the space of 2×2 constant tensors. Then, due to the symmetry of $\boldsymbol{\sigma}(\mathbf{u}_l)$, we have $(\boldsymbol{\sigma}(\mathbf{u}_l)\mathbf{t}_f)\mathbf{n}_f = (\boldsymbol{\sigma}(\mathbf{u}_l)\mathbf{n}_f)\mathbf{t}_f$, and thus

$$\begin{aligned}\|[\boldsymbol{\sigma}(\mathbf{u}_l)]\|_{0;f}^2 &= \|[\boldsymbol{\sigma}(\mathbf{u}_l)\mathbf{n}_f]\|_{0;f}^2 + \|[\boldsymbol{\sigma}(\mathbf{u}_l)\mathbf{t}_f]\|_{0;f}^2 \\ &= \|[\boldsymbol{\sigma}(\mathbf{u}_l)\mathbf{n}_f]\|_{0;f}^2 + \|[(\boldsymbol{\sigma}(\mathbf{u}_l)\mathbf{t}_f)\mathbf{t}_f]\|_{0;f}^2 + \|[(\boldsymbol{\sigma}(\mathbf{u}_l)\mathbf{n}_f)\mathbf{t}_f]\|_{0;f}^2.\end{aligned}$$

Recalling (2.2) and that we have constant Lamé parameters on each body, we have

$$\begin{aligned}[(\boldsymbol{\sigma}(\mathbf{u}_l)\mathbf{t}_f)\mathbf{t}_f] &= 2\mu[(\boldsymbol{\epsilon}(\mathbf{u}_l)\mathbf{t}_f)\mathbf{t}_f] + \lambda[\text{tr } \boldsymbol{\epsilon}(\mathbf{u}_l)] = 2\mu[(\nabla \mathbf{u}_l \mathbf{t}_f)\mathbf{t}_f] + \lambda[\text{tr } \boldsymbol{\epsilon}(\mathbf{u}_l)] \\ &= \lambda[\text{tr } \boldsymbol{\epsilon}(\mathbf{u}_l)] = \lambda[\text{div } \mathbf{u}_l] = \lambda[(\nabla \mathbf{u}_l \mathbf{n}_f)\mathbf{n}_f].\end{aligned}$$

For the normal contribution $[(\boldsymbol{\sigma}(\mathbf{u}_l)\mathbf{n}_f)\mathbf{n}_f]$, we can proceed in an analogous way. Using $[(\boldsymbol{\epsilon}(\mathbf{u}_l)\mathbf{n}_f)\mathbf{n}_f] = [(\nabla \mathbf{u}_l \mathbf{n}_f)\mathbf{n}_f]$, we get $[(\boldsymbol{\sigma}(\mathbf{u}_l)\mathbf{n}_f)\mathbf{n}_f] = (2\mu + \lambda)[(\nabla \mathbf{u}_l \mathbf{n}_f)\mathbf{n}_f]$ and thus the jump of the discrete stress across a face is bounded by the jump of its surface traction,

$$\begin{aligned}\|[\boldsymbol{\sigma}(\mathbf{u}_l)]\|_{0;f}^2 &= \|[\boldsymbol{\sigma}(\mathbf{u}_l)\mathbf{n}_f]\|_{0;f}^2 + \|[(\boldsymbol{\sigma}(\mathbf{u}_l)\mathbf{n}_f)\mathbf{t}_f]\|_{0;f}^2 \\ &\quad + \left(\frac{\lambda}{2\mu + \lambda}\right)^2 \|[(\boldsymbol{\sigma}(\mathbf{u}_l)\mathbf{n}_f)\mathbf{n}_f]\|_{0;f}^2 \leq 2\|[\boldsymbol{\sigma}(\mathbf{u}_l)\mathbf{n}_f]\|_{0;f}^2. \quad \square\end{aligned}$$

In our proof for the lower bound, we start with an estimate for the contact term.

Lemma 6.17. There exists a constant independent of the mesh size such that for all contact faces $f \in \mathcal{F}_l^k$, $k \in \{\mathrm{s},\mathrm{m}\}$, we have

$$\|(\boldsymbol{\sigma}_l - \boldsymbol{\sigma}(\mathbf{u}_l))\mathbf{n}_f\|_{0;f} \leq C\left(\sqrt{h_f}\|\boldsymbol{\Pi}_1\mathbf{f}\|_{0;\omega_f} + \sum_{F\in\mathcal{F}_f^{\mathrm{i}}} \|[\boldsymbol{\sigma}(\mathbf{u}_l)\mathbf{n}_F]\|_{0;F}\right),$$

where $\mathcal{F}_f^{\mathrm{i}}$ stands for the set of all interior and Neumann faces in Ω^k and on Γ_{N}^k such that $F \in \mathcal{F}_f^{\mathrm{i}}$ shares a vertex with $f \in \mathcal{F}_l^k$ and $\overline{\omega}_f := \cup_{T\in\mathcal{T}_f^k}\overline{T}$, with $\mathcal{T}_f^k$ being the set of all elements in $\mathcal{T}_l^k$ sharing a vertex with f.

Proof. To bound $\|(\boldsymbol{\sigma}_l - \boldsymbol{\sigma}(\mathbf{u}_l))\mathbf{n}_f\|_{0;f}$ for $f \in \mathcal{F}_l^k$, $k \in \{\mathrm{m},\mathrm{s}\}$, we insert the dual mortar projection $\boldsymbol{\Pi}_l^{*;k}$ with $\boldsymbol{\Pi}_l^{*;\mathrm{s}} := \boldsymbol{\Pi}_l^*$ (see the definitions (3.10b) and (6.2)), and get

$$\|(\boldsymbol{\sigma}_l - \boldsymbol{\sigma}(\mathbf{u}_l))\mathbf{n}\|_{0;f} \leq \|(\boldsymbol{\Pi}_l^{*;k} - \mathrm{Id})\boldsymbol{\sigma}(\mathbf{u}_l)\mathbf{n}\|_{0;f} + \|\boldsymbol{\sigma}_l\mathbf{n} - \boldsymbol{\Pi}_l^{*;k}\boldsymbol{\sigma}(\mathbf{u}_l)\mathbf{n}\|_{0;f}. \tag{6.22}$$

The first term in (6.22) can be bounded by using the properties of the dual mortar projection. We recall that $\boldsymbol{\Pi}_l^{*;k}$ reproduces constants and that $\boldsymbol{\Pi}_l^{*;k}\boldsymbol{\sigma}(\mathbf{u}_l)\mathbf{n}$ restricted to f depends only on the values of $\boldsymbol{\sigma}(\mathbf{u}_l)\mathbf{n}$ on f and its two adjacent faces. Let $\mathcal{F}_f^k$ be the set of all faces in $\mathcal{F}_l^k$ such that its elements share at least one endpoint with f; see Figure 6.8(a). Here the two elements in $\mathcal{F}_f^k$ not equal to f are marked with a dashed line.

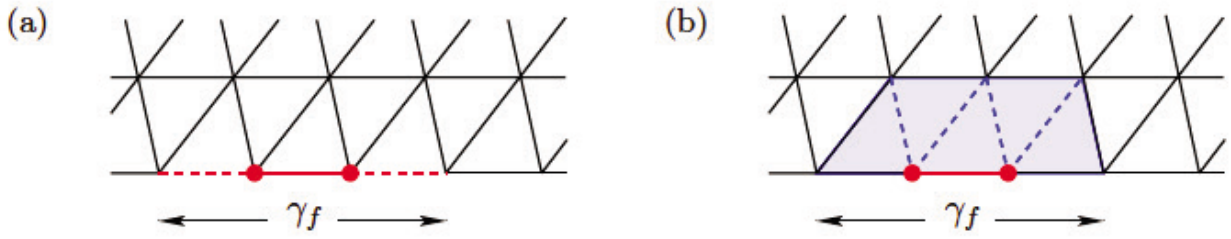

Figure 6.8. Definition of γ_f (a) and $\mathcal{F}_f^{\mathrm{i}}$ (b).

Setting $\overline{\gamma}_f := \cup_{F\in\mathcal{F}_f^k}\overline{F}$, we obtain, by using the local L^2-stability of $\Pi_l^{*;k}$,

$$\begin{aligned}\|(\boldsymbol{\Pi}_l^{*;k} - \mathrm{Id})\boldsymbol{\sigma}(\mathbf{u}_l)\mathbf{n}\|_{0;f} &= \|(\boldsymbol{\Pi}_l^{*;k} - \mathrm{Id})(\boldsymbol{\sigma}(\mathbf{u}_l)\mathbf{n} - (\boldsymbol{\sigma}(\mathbf{u}_l)\mathbf{n})|_f)\|_{0;f}\\ &\leq C\|\boldsymbol{\sigma}(\mathbf{u}_l)\mathbf{n} - (\boldsymbol{\sigma}(\mathbf{u}_l)\mathbf{n})|_f\|_{0;\gamma_f}.\end{aligned}$$

Due to the fact that $\boldsymbol{\sigma}(\mathbf{u}_l)$ restricted to each element is constant and that γ_f contains at most three faces, we find

$$\|\boldsymbol{\sigma}(\mathbf{u}_l)\mathbf{n} - (\boldsymbol{\sigma}(\mathbf{u}_l)\mathbf{n})|_f\|_{0;\gamma_f}^2 \leq Ch_f \sum_{F\in\mathcal{F}_f^k, F\neq f} \|(\boldsymbol{\sigma}(\mathbf{u}_l)_{|T_f}(p_F) - \boldsymbol{\sigma}(\mathbf{u}_l)_{|T_F}(p_F))\|^2.$$

Here p_F, $F \in \mathcal{F}_f^k$, $F \neq f$ is the vertex shared between f and F, and T_F,

$F \in \mathcal{F}_f^k$, stands for the element in $\mathcal{T}_l^k$ such that $F \subset \partial T$. Keeping in mind that all involved quantities are element-wise defined and constant on each element, the jump at the vertices can be bounded by the jump across the faces. Lemma 6.16 then gives

$$\|(\boldsymbol{\sigma}(\mathbf{u}_l)_{|T_f}(p_F) - \boldsymbol{\sigma}(\mathbf{u}_l)_{|T_F}(p_F))\| \le \sum_{\hat{f} \in \mathcal{F}_{p_F}^k} \|[\boldsymbol{\sigma}(\mathbf{u}_l)]|_{\hat{f}}\| \le \sum_{\hat{f} \in \mathcal{F}_{p_F}^k} \|[\boldsymbol{\sigma}(\mathbf{u}_l)\mathbf{n}_{\hat{f}}]|_{\hat{f}}\|.$$

Here $\mathcal{F}_{p_F}^k$ stands for the set of all interior faces in Ω^k sharing the node p_F. Moreover, we introduce $\mathcal{F}_f^{\mathrm{i}}$ as the union of sets $\mathcal{F}_{p_F}^k$ where p_F is an endpoint of f; see Figure 6.8(b). The two endpoints of f are marked with a bullet.

To bound the second term on the right-hand side of (6.22), we use the fact that the local norm of an element in $\mathbf{M}_l^k$ can be bounded by testing it with an element of $\mathbf{W}_l^k = \operatorname{tr} \mathbf{V}_l^k|_{\Gamma_{\mathrm{C}}}$ with local support. Keeping in mind that $\boldsymbol{\sigma}_l\mathbf{n} - \boldsymbol{\Pi}^{*;k}\boldsymbol{\sigma}(\mathbf{u}_l)\mathbf{n} \in \mathbf{M}_l^k$, we can then write it as $\boldsymbol{\alpha}_1\psi_{p_1^f} + \boldsymbol{\alpha}_2\psi_{p_2^f}$ on f, where p_i^f, $i = 1, 2$, are the two endpoints of f. We now set $\mathbf{v}_h = \hat{\boldsymbol{\alpha}}_1\phi_{p_1^f} + \hat{\boldsymbol{\alpha}}_2\phi_{p_2^f}$, where $\|\hat{\boldsymbol{\alpha}}_i\| = 1$ and $\hat{\boldsymbol{\alpha}}_i\boldsymbol{\alpha}_i = \|\boldsymbol{\alpha}_i\|$, $i = 1, 2$. Using the biorthogonality of ϕ_p and ψ_q, a simple calculation shows

$$\begin{aligned}\|\boldsymbol{\sigma}_l\mathbf{n} - \boldsymbol{\Pi}_l^{*;k}\boldsymbol{\sigma}(\mathbf{u}_l)\mathbf{n}\|_{0;f} &\le \frac{C}{\sqrt{h_f}} \int_{\Gamma_{\mathrm{C}}^k} (\boldsymbol{\sigma}_l\mathbf{n}^k - \boldsymbol{\Pi}_l^{*;k}\boldsymbol{\sigma}(\mathbf{u}_l^k)\mathbf{n}^k)\mathbf{v}_l \,\mathrm{d}s \\ &= \frac{C}{\sqrt{h_f}} \int_{\Gamma_{\mathrm{C}}^k} (\mathbf{f}_{\mathrm{C}}^k - \boldsymbol{\sigma}(\mathbf{u}_l^k)\mathbf{n}^k)\mathbf{v}_l \,\mathrm{d}s.\end{aligned}$$

We note that the definition of $\mathbf{v}_l$ yields that its support is in $\overline{\omega}_f$ and that its L^2-norm on Ω^k is bounded by Ch_f and its L^2-norm on $F \in \mathcal{F}_f^{\mathrm{i}}$ is bounded by $\sqrt{h_f}$. We now apply Green's formula on each element and find, in terms of (6.5),

$$\begin{aligned}\int_{\Gamma_{\mathrm{C}}^k} (\mathbf{f}_{\mathrm{C}}^k - \boldsymbol{\sigma}(\mathbf{u}_l^k)\mathbf{n}^k)\mathbf{v}_l \,\mathrm{d}s &= a_k(\mathbf{u}_l^k, \mathbf{v}_l) - f_k(\mathbf{v}_l) - \int_{\Gamma_{\mathrm{C}}^k} \boldsymbol{\sigma}(\mathbf{u}_l^k)\mathbf{n}^k\mathbf{v}_l \,\mathrm{d}s \\ &= \int_{\Omega^k} \mathbf{f}\mathbf{v}_l \,\mathrm{d}x - \sum_{F \in \mathcal{F}_f^{\mathrm{i}}} \int_F [\boldsymbol{\sigma}(\mathbf{u}_l)\mathbf{n}_F]\mathbf{v}_l \,\mathrm{d}s \\ &\le C\left(h_f\|\boldsymbol{\Pi}_1\mathbf{f}\|_{0;\omega_f} + \sqrt{h_f} \sum_{F \in \mathcal{F}_f^{\mathrm{i}}} \|[\boldsymbol{\sigma}(\mathbf{u}_l)\mathbf{n}_F]\|_{0;F} \right). \quad \square\end{aligned}$$

To obtain an upper bound for $\eta_{L;T}$, a discrete norm equivalence for Arnold–Winther elements is of crucial importance. For $\boldsymbol{\tau} \in \mathbf{X}_T$, we have

$$c\|\boldsymbol{\tau}\|_{0;T}^2 \le m_{0;T}(\boldsymbol{\tau}) + m_{1;T}(\boldsymbol{\tau}) + m_{2;T}(\boldsymbol{\tau}) \le C\|\boldsymbol{\tau}\|_{0;T}^2. \tag{6.23}$$

Here $m_{0;T}(\cdot)$, $m_{1;T}(\cdot)$ and $m_{2;T}(\cdot)$ are given by

$$
\begin{aligned}
m_{0;T}(\boldsymbol{\tau}) &:= |T| \sum_{p \in \mathcal{P}_T} \|\boldsymbol{\tau}(p)\|^2 , \\
m_{1;T}(\boldsymbol{\tau}) &:= \sum_{f \in \mathcal{F}_T} \left\| \int_f \boldsymbol{\tau} \mathbf{n}_f \, \mathrm{d}s \right\|^2 + \left\| \int_f \boldsymbol{\tau} \mathbf{n}_f (\phi_1^f - \phi_2^f) \, \mathrm{d}s \right\|^2 , \\
m_{2;T}(\boldsymbol{\tau}) &:= \frac{1}{|T|} \left\| \int_T \boldsymbol{\tau} \, \mathrm{d}x \right\|^2 ,
\end{aligned}
$$

in terms of the degrees of freedom. The set $\mathcal{P}_T$ stands for all vertices of T, $\mathcal{F}_T$ is the set of all faces of T, and ϕ_i^f, $i = 1, 2$, are the two nodal Lagrange basis functions associated with the two endpoints of f. Basically the proof is reduced to a scaling argument, the use of the matrix valued Piola transformation and the fact that in finite-dimensional spaces all norms are equivalent; see Arnold and Winther (2002) for details.

Observing that $\boldsymbol{\sigma}(\mathbf{u}_l)|_T \in \mathbf{X}_T$, we can use (6.23) to bound the local contribution $\eta_{\mathrm{L};T}$. We do so by considering the three parts separately. Using (6.11), we get

$$
\begin{aligned}
m_{2;T}(\boldsymbol{\sigma}_l - \boldsymbol{\sigma}(\mathbf{u}_l)) &= 0, \\
m_{1;T}(\boldsymbol{\sigma}_l - \boldsymbol{\sigma}(\mathbf{u}_l)) &\le C \sum_{f \in \mathcal{F}_T} h_f \|\mathbf{g}_f(\mathbf{n}_T \mathbf{n}_f) - \boldsymbol{\sigma}(\mathbf{u}_l)\mathbf{n}_T\|_{0;f}^2, \\
m_{0;T}(\boldsymbol{\sigma}_l - \boldsymbol{\sigma}(\mathbf{u}_l)) &\le C \sum_{p \in \mathcal{P}_T} \sum_{f \in \mathcal{F}_p} h_f \|[\boldsymbol{\sigma}(\mathbf{u}_l)]\|_{0;f}^2,
\end{aligned}
$$

where $\mathcal{F}_p$ is the set of all faces sharing the vertex p. For interior faces, $[\boldsymbol{\sigma}(\mathbf{u}_l)\mathbf{n}_f]$ is the jump across the face, for Dirichlet boundary faces we define $[\boldsymbol{\sigma}(\mathbf{u}_l)\mathbf{n}_f] := \mathbf{0}$, for Neumann faces we set $[\boldsymbol{\sigma}(\mathbf{u}_l)\mathbf{n}_f] := \boldsymbol{\sigma}(\mathbf{u}_l)\mathbf{n}_T - \mathbf{f}_{\mathrm{N}}$, and for contact faces $[\boldsymbol{\sigma}(\mathbf{u}_l)\mathbf{n}_f] := \boldsymbol{\sigma}(\mathbf{u}_l)\mathbf{n}_T - \mathbf{f}_{\mathrm{C}}$. We note that the constant in the bound of $m_{0;T}(\boldsymbol{\sigma}_l - \boldsymbol{\sigma}(\mathbf{u}_l))$ depends on the maximum number of elements sharing a vertex but not on the mesh size.

Let us briefly comment on the given bounds for $m_{i;T}(\boldsymbol{\sigma}_l - \boldsymbol{\sigma}(\mathbf{u}_l))$, $i = 0, 1$. Recalling that the equilibrated fluxes are consistent for each face, we find the upper bound

$$
\|\mathbf{g}_f(\mathbf{n}_T \mathbf{n}_f) - \boldsymbol{\sigma}(\mathbf{u}_l)\mathbf{n}_T\|_{0;f} \le \|\mathbf{g}_f - \{\boldsymbol{\sigma}(\mathbf{u}_l)\mathbf{n}_f\}\|_{0;f} + \frac{1}{2}\|[\boldsymbol{\sigma}(\mathbf{u}_l)\mathbf{n}_f]\|_{0;f},
$$

and thus the bound for $m_{1;T}(\boldsymbol{\sigma}_l - \boldsymbol{\sigma}(\mathbf{u}_l))$ has the same structure as in the linear setting.

The terms on the right are known from residual and equilibrated error estimators. In the linear setting (see Ainsworth and Oden (2000), Babuška and Strouboulis (2001) and Verfürth (1994)), they can be bounded by the element and face residuals, and thus by the local discretization error and by

local higher-order data oscillation terms. We recall that the proof involves cubic element and quadratic edge bubbles. More precisely, it is based firstly on the observation that on a finite-dimensional polynomial space the L^2-norm $\|\cdot\|_{0;\omega}$ and the weighted L^2-norm $\|b_\omega^{1/2}\cdot\|_{0;\omega}$ are equivalent, where $b_\omega^{1/2}$ is a suitably scaled bubble function. Secondly, integration by parts can be applied. Due to the local patch-wise construction of the error estimator, there is no difference compared to the linear setting, and as long as no contact face is involved the same techniques can be used.

These preliminary observations and Lemma 6.16 can be used to bound $m_{0;T}(\boldsymbol{\sigma}_l - \boldsymbol{\sigma}(\mathbf{u}_l))$ by the jump of the surface traction:

$$m_{0;T}(\boldsymbol{\sigma}_l - \boldsymbol{\sigma}(\mathbf{u}_l)) \le C \sum_{p\in\mathcal{P}_T} \sum_{f\in\mathcal{F}_p} h_f \|[\boldsymbol{\sigma}(\mathbf{u}_l)\mathbf{n}_f]\|_{0;f}^2.$$

Using the norm equivalence (6.23) and the bounds for the terms $m_{i;T}(\boldsymbol{\sigma}_l - \boldsymbol{\sigma}(\mathbf{u}_l))$, $0 \le i \le 2$, we now obtain

$$\begin{aligned}\eta_{\mathrm{L};T}^2 \le C &\sum_{f\in\mathcal{F}_T^{\mathrm{i}}} h_f\big(\|\mathbf{g}_f - \{\boldsymbol{\sigma}(\mathbf{u}_l)\mathbf{n}_f\}\|_{0;f}^2 + \|[\boldsymbol{\sigma}(\mathbf{u}_l)\mathbf{n}_f]\|_{0;f}^2\big) \\ &+ \sum_{f\in\mathcal{F}_T^{\mathrm{b}}} h_f\|(\boldsymbol{\sigma}_l - \boldsymbol{\sigma}(\mathbf{u}_l))\mathbf{n}_f\|_{0;f}^2.\end{aligned} \tag{6.24}$$

Here $\mathcal{F}_T^{\mathrm{i}}$ stands for the set of all faces not on $\Gamma_{\mathrm{C}}\cup\Gamma_{\mathrm{N}}$ and sharing a vertex with the element T, and $\mathcal{F}_T^{\mathrm{b}}$ is the set of all faces on $\Gamma_{\mathrm{C}}\cup\Gamma_{\mathrm{N}}$ and sharing a vertex with the element T. Figure 6.9 illustrates for a given T the two sets: the elements in $\mathcal{F}_T^{\mathrm{b}}$ are marked with dashed lines and the elements in $\mathcal{F}_T^{\mathrm{i}}$ with bold solid lines.

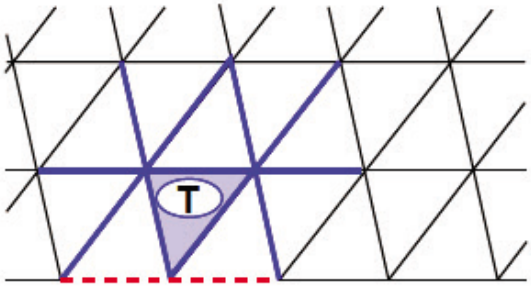

Figure 6.9. Definition of $\mathcal{F}_T^{\mathrm{i}}$ and $\mathcal{F}_T^{\mathrm{b}}$.

Combining (6.24) and Lemma 6.17, we get the following lower bound for the discretization error.

Theorem 6.18. The element contribution $\eta_{L;T}$ of the error estimator can be bounded by the error on a local neighbourhood and some local oscillation terms

$$\eta_{L;T}^2 \le C \sum_{\hat{T}\in\mathcal{T}_T} \big(|||\mathbf{u} - \mathbf{u}_l|||_{\hat{T}}^2 + \xi_{\hat{T}}^2\big),$$

where $\mathcal{T}_T$ is the set of all elements sharing a vertex with T.

We note that the number of elements in $\mathcal{T}_T$ does not depend on the mesh size but only on the shape-regularity of the triangulation.

Remark 6.19. As the construction of $\eta_{\mathrm{L};T}$ is not restricted to 2D, and since all the proofs in this subsection also work out in 3D, Theorem 6.18 can also be shown to hold true in 3D. Moreover, in contrast to many other results, for the proof it does not make any difference if friction or no friction is applied. And as the proof shows, the results are also valid in the case of non-matching meshes.

6.6. Residual-type error estimator

Lemma 6.13 and Theorem 6.18 justify that it is sufficient to take a standard estimator for linear elasticity problems and use $\boldsymbol{\lambda}_l$ as the Neumann condition on the possible contact boundary in the case of matching meshes or a one-sided contact problem. These considerations show that η_{L} can be replaced by any other error estimator suitable for the Lamé equation. Of special interest is a residual-type indicator η_{R}. Following the definition of the classical residual-based error estimator for the Laplace operator, we set

$$\eta_{\mathrm{R};T}^2 := \frac{h_T^2}{2\mu}\|\mathbf{f} + \operatorname{div}\boldsymbol{\sigma}(\mathbf{u}_l)\|_{0;T}^2 + \frac{1}{2}\sum_{f\subset\Gamma_T^{\mathrm{int}}}\frac{h_f}{2\mu}\|[\boldsymbol{\sigma}(\mathbf{u}_l)\mathbf{n}_f]\|_{0;f}^2 + \sum_{f\subset\Gamma_T^{\mathrm{ext}}}\frac{h_f}{2\mu}r_f^2, \tag{6.25}$$

where h_T and h_f stand for the element and face diameter, respectively, $\mathbf{n}_f$ denotes a unit face normal, and $\Gamma_T^{\mathrm{int}} := \{f \subset \partial T, f \subset \Omega\}$, $\Gamma_T^{\mathrm{ext}} := \partial T \setminus \Gamma_T^{\mathrm{int}}$. The term r_f^2 depends on the type of the boundary part,

$$r_f^2 := \begin{cases} 0 & f \subset \Gamma_{\mathrm{D}}, \\ \|\boldsymbol{\sigma}(\mathbf{u}_l)\mathbf{n} - \mathbf{f}_{\mathrm{N}}\|_{0;f}^2 & f \subset \Gamma_{\mathrm{N}}, \\ \|\boldsymbol{\sigma}(\mathbf{u}_l^{\mathrm{s}})\mathbf{n}^{\mathrm{s}} + \boldsymbol{\lambda}_l\|_{0;f}^2 & f \subset \Gamma_{\mathrm{C}}^{\mathrm{s}}, \\ \|\boldsymbol{\sigma}(\mathbf{u}_l^{\mathrm{m}})\mathbf{n}^{\mathrm{m}} - \boldsymbol{\Pi}_l^{*;\mathrm{m}}\boldsymbol{\lambda}_l\|_{0;f}^2 & f \subset \Gamma_{\mathrm{C}}^{\mathrm{m}}. \end{cases}$$

The case $f \subset \Gamma_{\mathrm{D}} \cup \Gamma_{\mathrm{N}}$ is standard. For $f \in \Gamma_{\mathrm{C}}$, we apply the interpretation of $\boldsymbol{\lambda}_l$ as Neumann boundary data.

It is possible to show that both error indicators η_{R} defined by (6.25) and η_{L} given in (6.10) are up to higher-order data oscillations locally equivalent. To do so, it is sufficient to consider the case of linear elasticity and given $\boldsymbol{\lambda}_l$. Using the discrete norm equivalence (6.23) for Arnold–Winther-type elements, it is easy to see that $\eta_{\mathrm{L};T}$ is equivalent to the sum of patch-wise contributions of $\eta_{\mathrm{R};\tilde{T}}$ and the face contributions of the difference between the equilibrated and the discrete fluxes. This difference satisfies a local system with a system matrix independent of the mesh size (see also (6.8)),

and the right-hand side is defined in terms of local face and element residual contributions. Then an algebraic argument and a correct scaling yield the equivalence.

Remark 6.20. We point out that a numerical study shows that the ratio between η_{C}, η_{F} and η_{L} tends asymptotically to zero. As a result the terms η_{C} and η_{F} do not contribute significantly to the total estimated error and can thus often be neglected in the stopping criteria. The situation may be different if we only consider the local influence of $\eta_{\mathrm{C};f}$ and $\eta_{\mathrm{F};f}$ on the adaptive refinement process. Then these terms help the estimator to resolve, already on quite coarse meshes, the transfer between contact and no contact and the sliding and sticky part.

6.7. Non-matching meshes

Let us briefly comment on the more general case of non-matching meshes. Then Lemma 6.5 still holds and shows that we also have to consider η_{S} defined by (6.14). Following the lines of *a posteriori* error estimates for a linear mortar setting (see, *e.g.*, Belhachmi (2003, 2004), Bergam, Bernardi, Hecht and Mghazli (2003), Bernardi and Hecht (2002), Wheeler and Yotov (2005), Pousin and Sassi (2005) and Wohlmuth (1999*a*, 1999*b*)), suitable upper bounds can be shown for η_{S}. We note that in the case of non-matching meshes, mesh-independent upper and lower bounds always rely on some assumptions on the ratio of the coefficients and mesh sizes from master and slave side. In the case of globally constant Lamé parameters, we can bound η_{S} by η_{L} if the local ratio between the mesh size on the master and the slave side is bounded, *i.e.*,

$$\max_{f^{\mathrm{m}} \in \mathcal{F}_l^{\mathrm{m}}} \frac{h_{f^{\mathrm{m}}}}{\min_{f^{\mathrm{s}} \in \mathcal{F}_l^{\mathrm{s}}; f^{\mathrm{m}} \cap f^{\mathrm{s}} \neq \emptyset} h_{f^{\mathrm{s}}}} < C.$$

The proof follows the lines of Section 6.4.

However, Lemma 6.11 no longer holds. A more detailed look into the proof reveals, that then the term $[\mathbf{u}_l] - \mathbf{\Pi}_l[\mathbf{u}_l]$ enters into the estimate. This term is zero if the mesh on the slave side of the contact is a refinement of the one on the master side, but on general non-matching meshes this term does not vanish. To obtain an upper bound for the error in the energy norm, an additional term of the form

$$\hat{\eta}_{\mathrm{D}}^2 := \sum_{f \in \mathcal{F}_l^{\mathrm{s}}} \frac{2\mu^{\mathrm{s}}}{h_f} \| [\mathbf{u}_l] - \mathbf{\Pi}_l[\mathbf{u}_l] \|_{0;f}^2$$

is a possibility. But then, the lower bound is tricky and will not work out. This can be explained by the difference in the structure of the exact solution. In the linear mortar setting, we can exploit the fact that the jump of the exact solution vanishes across the interfaces and $\mathbf{\Pi}_l[\mathbf{u}_l] = \mathbf{0}$. This no longer holds for contact problems. The jump in the normal direction is only zero

on the actual contact zone and in the tangential direction only on the sticky part but, in general, not on all of $\Gamma_{\rm C}$. A more careful analysis shows that one has to bound $\langle P_l^{\rm C}\lambda_l^{\rm C} - \lambda_n, \Pi_l[u_l^n] - [u_l^n]\rangle_{\Gamma_{\rm C}}$ for the normal contribution. We refer to Coorevits, Hild and Pelle (2000) and Wohlmuth (2007) for some results on contact problems with non-matching meshes. However, we note that none of those is fully satisfying from the theoretical point of view. In particular, certain 'higher-order' terms depend on the unknown solution and are not accessible during the refinement process. Alternatively one can include in the indicator terms depending on

$$\eta_{\rm D}^2 := \sum_{f\in\mathcal{F}_l^{\rm s}} \frac{2\mu^{\rm s}}{h_f} \| \max(0, [u_l^n])\|_{0;f}^2, \tag{6.26}$$

to take into account the possible discrete penetration. But then the ratio between upper and lower bound will be not independent of the mesh size. We refer to Bernardi and Hecht (2002), Pousin and Sassi (2005) and Wohlmuth (1999*a*, 1999*b*) for error indicators and estimators in the case of non-matching meshes.

One of the problems with non-matching meshes is that standard inverse estimates for finite elements do not necessarily apply for $[\mathbf{v}_l]$ on $\Gamma_{\rm C}$, $\mathbf{v}_l \in \mathbf{V}_l$. *A priori* error estimates use the best approximation property of the spaces and the stability of mortar projections, while *a posteriori* error estimates work with duality and the residual. In the linear elasticity setting of a glueing problem, the jump $[\mathbf{u}_l]$ across the interfaces characterizes the non-conformity of the approach. The natural norm to associate with is the $H^{1/2}$-norm. Unfortunately, in the case of non-matching meshes no inverse inequality holds. To get a better understanding of the influence of non-matching meshes, we consider a simplified setting. Let $I := (-1, 1)$; then we introduce two different globally quasi-uniform partitions given by the nodes $p_1 := -1$, $p_2 := 0$ and $p_3 := 1$ and $q_1 := -1$, $q_2 := t \in [-1/2; 1/2]$ and $q_3 := 1$. Associated with these nodes are two finite element functions $v_p := \sum_{i=1}^3 \alpha_i \phi_i^p$ and $v_q := \sum_{i=1}^3 \beta_i \phi_i^q$, where ϕ_i^p and ϕ_i^q are the standard hat functions associated with the nodes p_i, and q_i, $1 \le i \le 3$, respectively. Then the standard inverse estimates applied to this very special situation gives $\|w\|_{s;I} \le C\|w\|_{0;I}$ for $s \in [0, 1]$ and $w = v_p$ or $w = v_q$. Here the constant does not depend on s, or on the coefficient, or on $t \in [-1/2; 1/2]$. The situation is drastically different if we consider $w = v_p - v_q$. Figure 6.10 shows $\phi_2^p - \phi_2^q$ for different values of $t \in \{-1/2, -2/3, -1/6, 0\}$.

Lemma 6.21. For $t \in [-1/2; 1/2]$ and $t \neq 0$, we obtain

$$\|\phi_2^p - \phi_2^q\|_{s;I} \le \begin{cases} C\|\phi_2^p - \phi_2^q\|_{0;I} & s \in [0; \frac{1}{2}), \\ C\sqrt{-\log|t|}\|\phi_2^p - \phi_2^q\|_{0;I} & s = \frac{1}{2}, \\ \frac{C}{|t|^{s-\frac{1}{2}}}\|\phi_2^p - \phi_2^q\|_{0;I} & s \in (\frac{1}{2}, 1]. \end{cases}$$

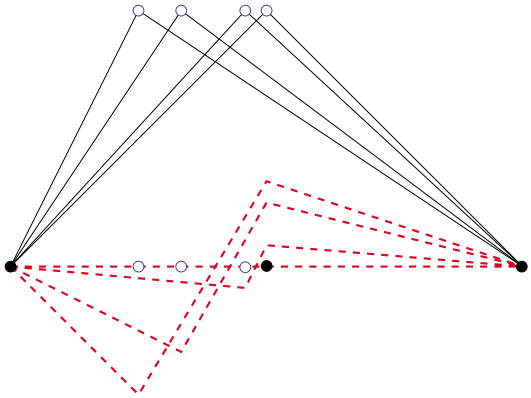

Figure 6.10. Influence of the node q_2 on the basis function ϕ_2^q and $\phi_2^p - \phi_2^q$.

Proof. Due to symmetry arguments, it is sufficient to consider the case $t \in [-1/2, 0)$. A straightforward computation then shows that $\Delta\phi_2 := \phi_2^p - \phi_2^q$ is given by

$$\Delta\phi_2(x) = \begin{cases} \frac{t}{t+1}(x+1) & -1 \le x \le t, \\ x + \frac{1}{1-t}(x-t) & t < x < 0, \\ \frac{t}{1-t}(x-1) & 0 \le x \le 1, \end{cases}$$

and that $\|\Delta\phi_2\|_{0;I}^2 = \mathcal{O}(t^2)$ whereas $\|\Delta\phi_2\|_{1;I}^2 = \mathcal{O}(|t|)$. For $0 < s < 1$, we use the standard definition of the Aronstein–Slobodeckij norm in 1D; see, *e.g.*, Adams (1975). Introducing $I_1 := (-1, t)$, $I_2 := (t, 0)$ and $I_3 := (0, 1)$, we get

$$|\Delta\phi_2|_{s;I}^2 = \sum_{i,j=1}^{3} \int_{I_i} \int_{I_j} \frac{(\Delta\phi_2(x) - \Delta\phi_2(y))^2}{(x-y)^{2s+1}} \,\mathrm{d}x \,\mathrm{d}y.$$

Using that $\Delta\phi_2$ is piecewise affine, we find by a simple interpolation argument that

$$\sum_{i=1}^{3} \int_{I_i} \int_{I_i} \frac{(\Delta\phi_2(x) - \Delta\phi_2(y))^2}{(x-y)^{2s+1}} \,\mathrm{d}x \,\mathrm{d}y \;= \mathcal{O}(|t|^2 + |t|^{3-2s}).$$

Integration of the remaining terms yields for $s \in (0, 1)$

$$\sum_{i,j=1, j\neq i}^{3} \int_{I_i} \int_{I_j} \frac{(\Delta\phi_2(x) - \Delta\phi_2(y))^2}{(x-y)^{2s+1}} \,\mathrm{d}x \,\mathrm{d}y \;= \begin{cases} \mathcal{O}(|t|^{3-2s}) & s \neq \frac{1}{2}, \\ \mathcal{O}(-|t|^2 \log(|t|)) & s = \frac{1}{2}. \end{cases}$$

□

Figure 6.11 illustrates the inverse inequality for different parameters $s \in \{0.1, 0.25, 0.5, 0.51, 0.75, 0.95\}$. The straight line is $\|\phi_2^p - \phi_2^q\|_{s;I}$ evaluated analytically, and the markers indicate qualitatively the upper bound. For $s = 0.1$ and $s = 0.25$, the upper bound in the inverse inequality is bounded independently of t. For $s = 0.5$ logarithmic growth can be observed, and for $s > 0.5$ the singularity is the more dominant the closer s is to 1.

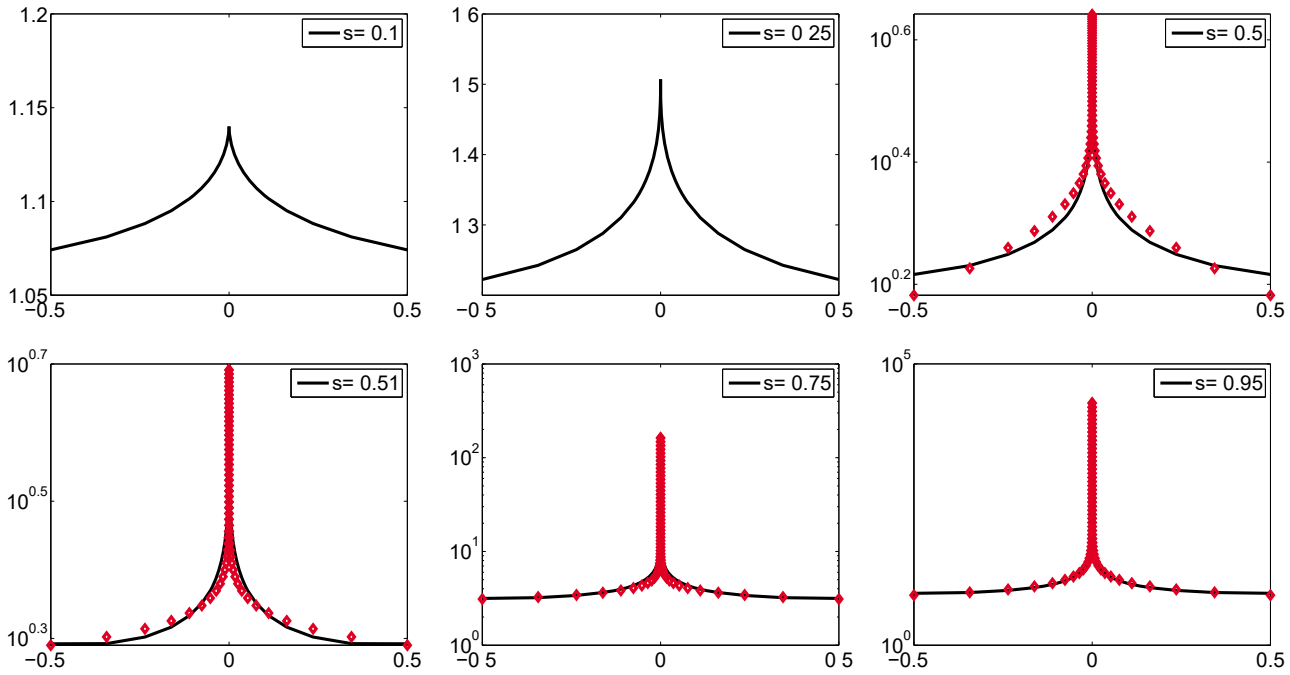

Figure 6.11. Influence of the parameter s on the inverse inequality for $t \in [-0.5, 0.5]$, $t \neq 0$.

This lemma shows that on non-matching meshes we cannot simply apply inverse estimates to go from one norm to another. As a possible remedy, one first has to apply approximation properties and secondly inverse estimates for the faces on the interface between master and slave side. But then the ratio between the mesh sizes on master and slave side must be considered.

Although we do not give a rigorous mathematical analysis of the terms associated with the influence of non-matching meshes, we provide some numerical results. We consider the same numerical example as illustrated in the paragraph on different materials of Section 6.8 and set $i = 3$. The normal contact pressure has a mild singularity at the left endpoint of the contact interface.

Figure 6.12 illustrates the normal displacement and the normal contact stress at the contact zone of the slave and the master body for Levels 3, 5 and 7.

As can be seen from Figure 6.12, there is almost no penetration, although we do work on non-matching meshes. Thus we can expect η_{D} defined by (6.26) to be very small compared to η_{L}. The situation is different for the contact stress. Due to the choice of a biorthogonal set of basis functions, the visualization of λ_l^n as a function shows oscillations. Figure 6.12(d–f) illustrates how the difference $\lambda_l^n - \Pi_l^{*;\mathrm{m}} \lambda_l^n$ decays with respect to the refinement level.

Figure 6.13(a) shows the error decay of the different contributions. From the very beginning the term η_{D} is much smaller than η_{L} and can thus be neglected. We note, however, that it has the same convergence order as η_{L}. For the term η_{S} defined by (6.14), we observe that it is quantitatively

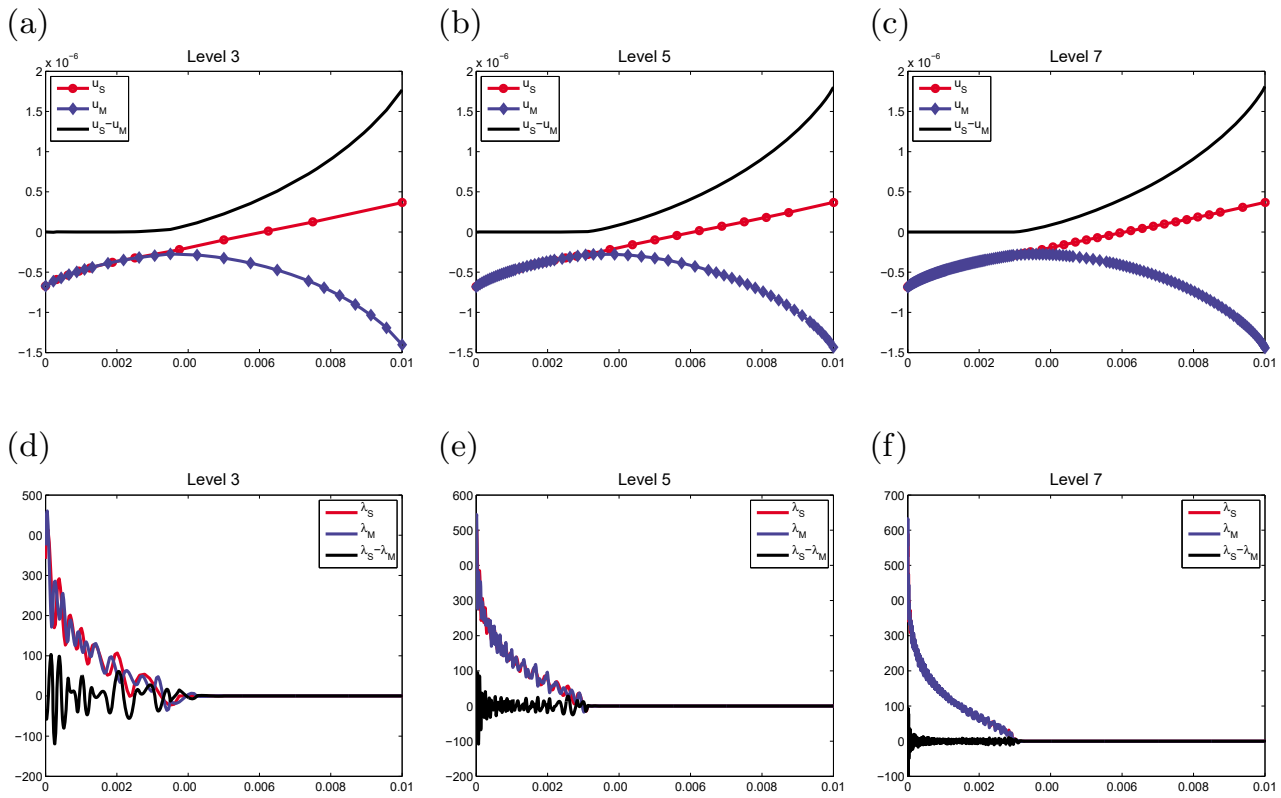

Figure 6.12. Normal displacement (a–c) and normal contact stress (d–f) for different refinement levels.

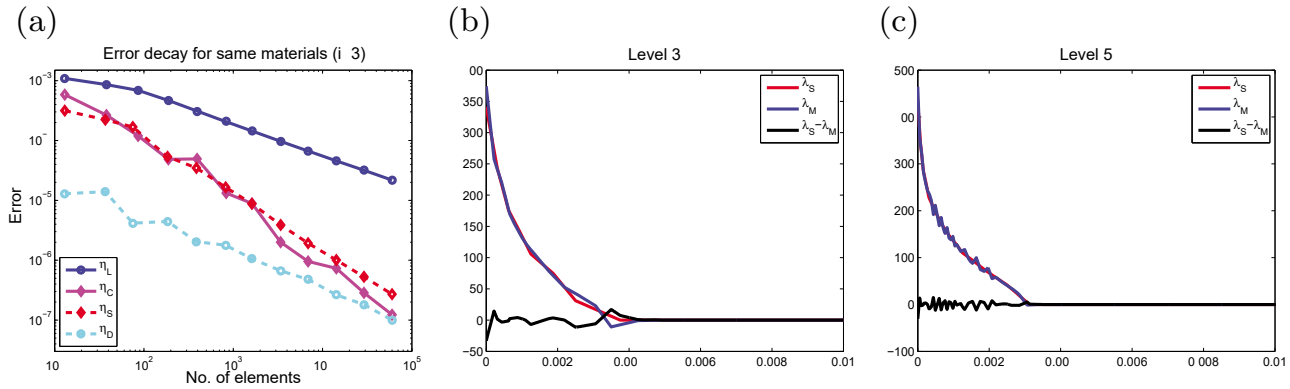

Figure 6.13. Normal contact stress for different refinement levels.

and qualitatively of the same order as η_{C}. This might be surprising since only a few faces contribute to η_{C}, whereas all contact faces contribute to η_{S}. We note, however, that closer to the singularities the face diameter h_f, which enters as weight into the definition of η_{S}, is much smaller than at the end of the actual zone of contact. Figures 6.13(b) and 6.13(c) show $Z_l^* \lambda_l^n$, $Z_l^{*;\mathrm{m}} \Pi_l^{*;\mathrm{m}} \lambda_l^n$ and the difference $Z_l^* \lambda_l^n - Z_l^{*;\mathrm{m}} \Pi_l^{*;\mathrm{m}} \lambda_l^n$. Here, the operator $Z_l^{*;\mathrm{m}}$ is defined similarly to (4.7) but with respect to the master side. As can be clearly observed, much smaller values for the difference are obtained and the plotted functions exhibit fewer oscillations. Thus, using these values to define η_{S} would result in a smaller value, but then the equilibrium (6.5) is no longer satisfied, and our proof does not apply.

Remark 6.22. The term η_S measures how well the mesh on the master side can resolve the discrete surface traction provided by the Lagrange multiplier on the slave side. The weight corresponds to the case of a Neumann boundary. Correspondingly, the term $\hat{\eta}_D$ reflects the consistency error of a linear mortar approach and quantifies the difference in the discrete solution on master and slave sides. It has the standard weight of a Dirichlet boundary term. We recall that for contact problems, the principle of equilibrium of forces holds and thus η_S is also appropriate. This is not the case for $\hat{\eta}_D$. Here one should use the modified definition η_D given in (6.26), which takes into account the contact constraints.

6.8. Numerical results for adaptive mesh refinement

We consider a series of different test examples. A detailed discussion and the specific problem settings can be found in Hüeber and Wohlmuth (2010), Weiss and Wohlmuth (2009) and Wohlmuth (2007). We start with one-sided contact problems where η_L is a mathematically sound error estimator.

One-sided two-dimensional Coulomb problem

In a first test, we consider a one-sided Coulomb friction problem in 2D with the friction coefficient given by $\nu = 0$, $\nu = 0.3$ and $\nu = 0.8$. Using η_L and a mean value strategy to define the adaptively refined meshes, we compute η_R, η_L, η_C and η_F on each refinement level and show the decay with respect to the number of elements in Figure 6.14. The normal and tangential stress for $\nu = 0.3$ and $\nu = 0.8$ is given in Figure 4.7. For $\nu = 0.0$, the term η_F is equal to zero.

For all three settings, we observe that we recover an optimal decay of the residual and equilibrated error estimator. As expected, the two additional terms η_C and η_F can be neglected asymptotically compared to η_L and η_R. These numerical results show that η_L yields a reliable stopping criteria. For $\nu = 0.8$, we observe, from the very beginning, that both terms η_C and

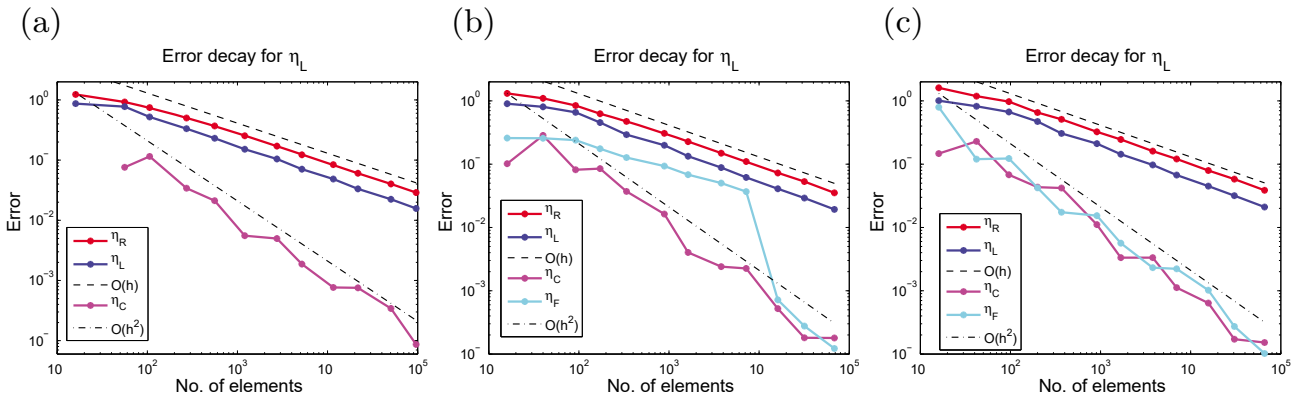

Figure 6.14. Error decay for adaptive refinement using η_L for $\nu = 0.0$ (a), $\nu = 0.3$ (b), $\nu = 0.8$ (c).

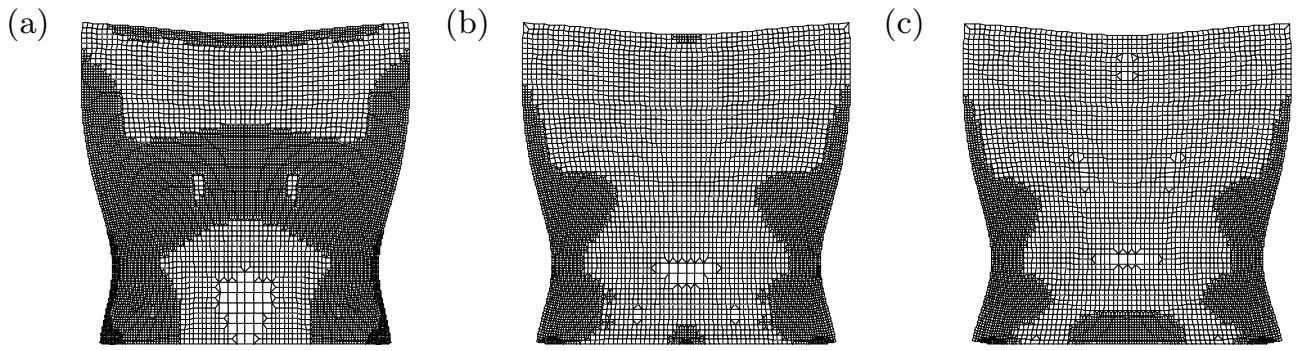

Figure 6.15. Distorted meshes after 8 adaptive refinement steps for different values of the coefficient of friction $\nu = 0.0$ (a), $\nu = 0.3$ (b), $\nu = 0.8$ (c).

η_{F} tend with h_l^2 to zero where we set $h_l := (\#\mathcal{T}_l)^{1/d}$. The situation is different for $\nu = 0.3$. Here we observe, during the first refinement steps, a reduced decay order of η_{F} compared to η_{C}. This effect can be explained by Figure 4.7(b). For $\nu = 0.3$, we have a very small sticky zone, and thus on coarse meshes Assumption 6.7 is violated, and we have only one vertex p with $|\gamma_p^t| - \nu\gamma_p^n \neq 0$. Then $P_l^{\mathrm{F}}\lambda_l^{\mathrm{F}} = 0$ and $\delta_f = 1/h_f$ on the two boundary faces sharing the vertex p. As soon as the sticky part is resolved, the friction term η_{F} drops down.

The meshes obtained from the error indicator η_{L} after 8 refinement steps are shown in Figure 6.15. We remark that the interior of the contact boundary $\Gamma_{\mathrm{C}}^{\mathrm{s}}$ will be refined considerably more at the sticky part of the boundary. This effect arises from the high gradient of the tangential component of the Lagrange multiplier. Furthermore, the boundary region of the contact boundary actually in contact is detected and thus refined by the error indicator.

In the next test series, we illustrate the influence of the choice of error indicator on the adaptive refinement process for $\nu = 0.3$. We compare η_{L}, $\eta_{\mathrm{L}} + \eta_{\mathrm{C}} + \eta_{\mathrm{F}}$ and η_{R}. Figure 6.16(a) shows a zoom of the very small sticky zone with the normal and the tangential components of the Lagrange multiplier as well as the friction bound $\nu\lambda_n$ and the difference $\nu\lambda_n - \|\lambda_t\|$. The last expression is positive at all sticky nodes; for the sliding nodes it vanishes. Figure 6.16(b) shows that there is no significant difference in η_{L} and that the adaptive refinement process is not sensitive to the selected error indicator. In particular, a standard residual-based error indicator provides very good results, and no additional terms resulting from the contact situation with Coulomb friction are required. The only difference can be observed in η_{F}. In this example, the sticky zone is very small, and thus it cannot be well resolved on lower refinement levels. Using $\eta_{\mathrm{L}} + \eta_{\mathrm{C}} + \eta_{\mathrm{F}}$ as the indicator for the adaptive marking gives quite large element contributions for elements having both sticky and sliding vertices. Thus, these elements are within the pre-asymptotic range and all elements with $\delta_f \neq 1$ are selected to be refined in the next step. As a consequence, the sticky contact zone can be resolved

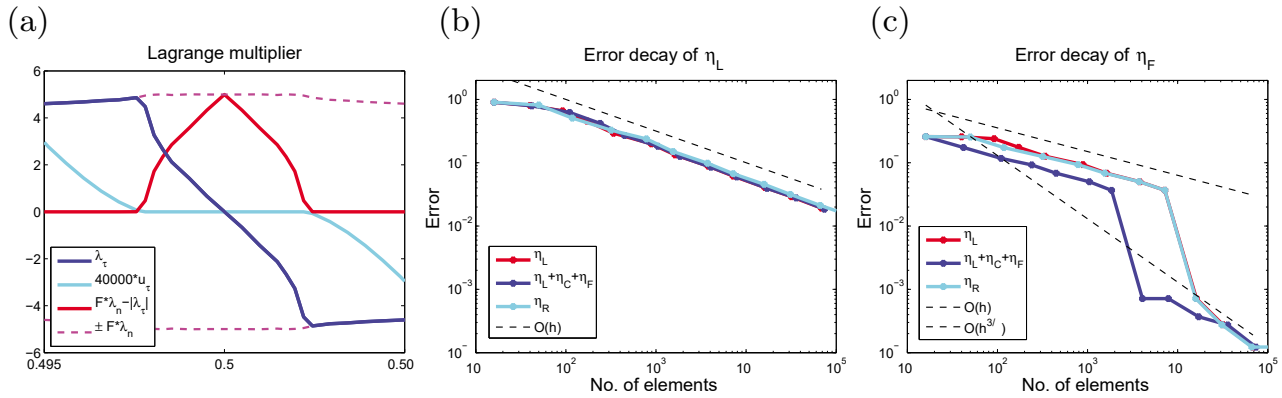

Figure 6.16. Zoom of Lagrange multiplier (a), estimated error η_{L} (b) and η_{F} (c) for different refinement strategies for $\nu = 0.3$.

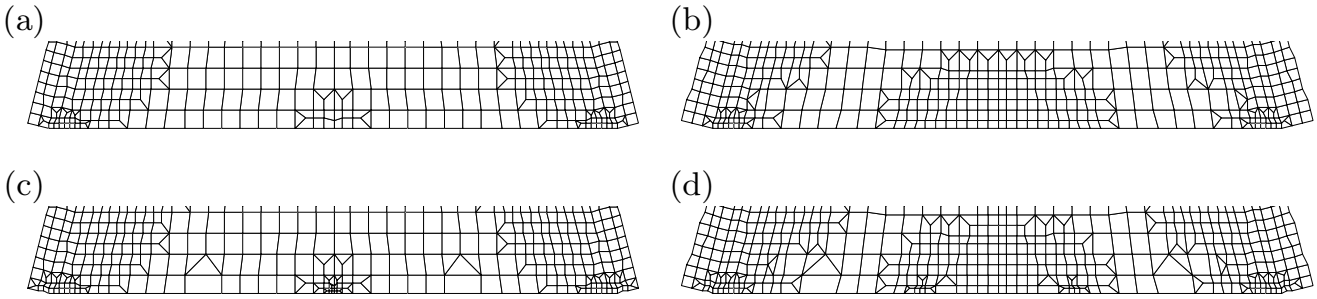

Figure 6.17. Distorted meshes at contact boundary after 6 adaptive refinement steps for η_{L} (a,b) and $\eta_{\mathrm{L}} + \eta_{\mathrm{C}} + \eta_{\mathrm{F}}$ (c,d) refinement for the coefficients of friction $\nu = 0.3$ (a,c) and $\nu = 0.8$ (b,d).

for a smaller refinement level compared to the case where the refinement is only controlled by η_{L} or η_{R}. However, this influence is quite small on the global estimated error, as can be seen in Figure 6.16(b). For all three series of adaptively refined meshes, we observe qualitatively and quantitatively the same results.

To show the effect of η_{F} in more detail, we consider in Figure 6.17 a zoom of the meshes at the contact boundary for η_{L} and $\eta_{\mathrm{L}} + \eta_{\mathrm{C}} + \eta_{\mathrm{F}}$ used as the marking indicator for the two cases of $\nu = 0.3$ and $\nu = 0.8$. In both cases, we observe that the intersection between the sticky and the sliding zone as well as the intersection between contact and no contact is well resolved by the error indicator. The first one is resolved more accurately when the term η_{F} is used in the refinement strategy.

Influence of the regularity of the solution

To test the influence of the regularity of the solution on the adaptive refinement, we consider a parameter-dependent one-sided contact problem with no friction. The unit square is pushed onto a triangle with different opening angles α at the contact vertex. In our tests, we use $\alpha = 2/3\pi$, $\alpha = \pi/2$ and $\alpha = \pi/3$. Due to the decreasing regularity of the solution for decreasing α, we observe that for $\alpha = \pi/3$, the mesh is much more locally refined compared to $\alpha = 2\pi/3$.

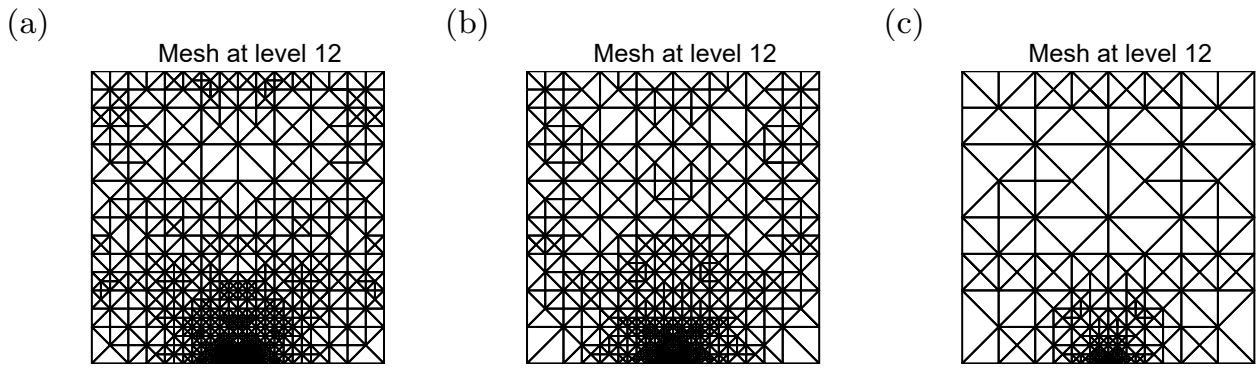

Figure 6.18. Square on triangle: mesh on level 12 for $\alpha = 2\pi/3$ (a), $\alpha = \pi/2$ (b), $\alpha = \pi/3$ (c).

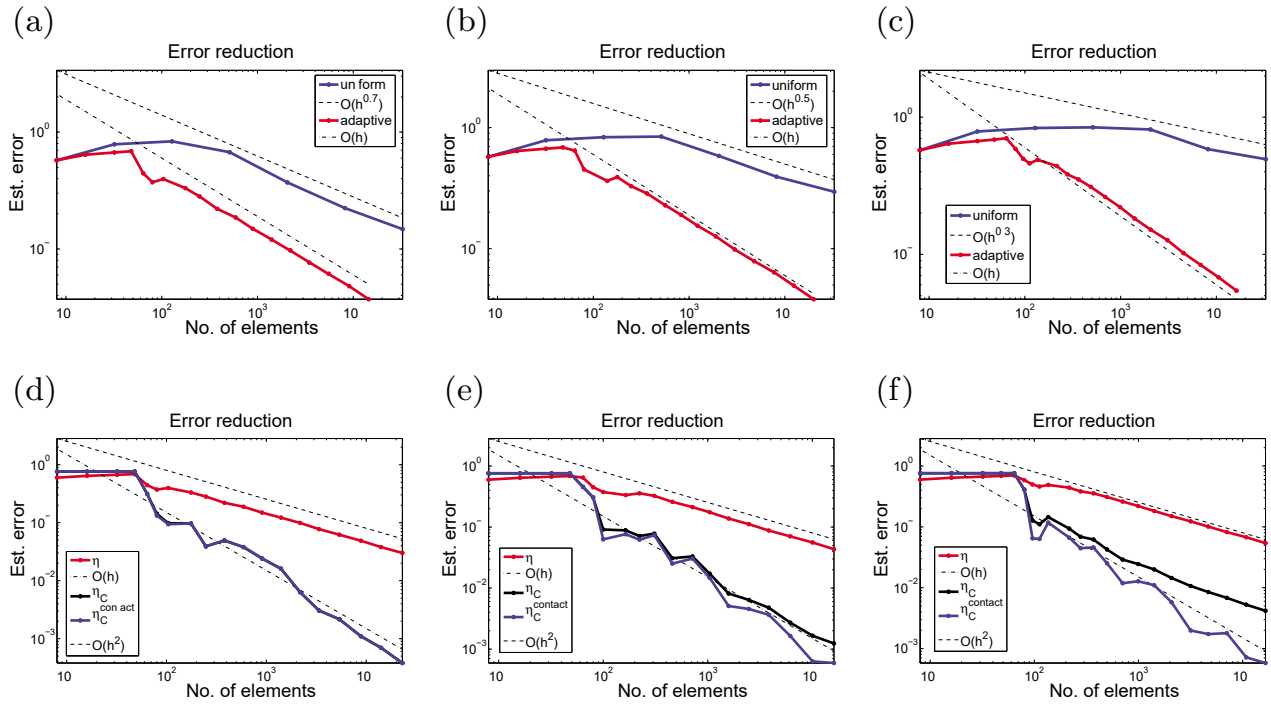

Figure 6.19. Square on triangle $\alpha = 2\pi/3, \pi/2, \pi/3$: Estimated error η_{L} for adaptive and uniform refinement (a–c) and comparison of η_{L}, η_{C} and $\eta_{\mathrm{C}}^{\mathrm{contact}}$ (d–f).

The regularity of the solution is known and our numerical convergence rates for uniform refinement are in good agreement with the theory: see Figure 6.19. The slope in the estimated error decay is approximatively 0.7 for $\alpha = 2\pi/3$, 0.5 for $\alpha = \pi/2$ and 0.3 for $\alpha = \pi/3$. Thus, with respect to the total degrees of freedom, we have only a sub-optimal convergence. The situation is drastically improved if adaptive mesh refinement techniques are applied. We then observe $\mathcal{O}(h_l)$ behaviour for all three cases.

As in the first example, we observe for all α that the error contribution η_{C} decreases much faster compared to η_{L}. However, for low regularity, we

do not observe that η_{C} is of order $\mathcal{O}(h_l^2)$. To get a better understanding of the situation, we define

$$\eta_{\mathrm{C}}^{\mathrm{contact}} := \left(\sum_{f \in \mathcal{F}_l^{\mathrm{s;b}}} \eta_{\mathrm{C};f}^2 \right)^{1/2} \leq \eta_{\mathrm{C}},$$

where $\mathcal{F}_l^{\mathrm{s;b}} \subset \mathcal{F}_l^{\mathrm{s}}$ is the set of all faces being separated from $\mathrm{supp}(\Pi_l[u_l^n] - g_l)$ by at most m faces, where $m \in \mathbb{N}$ is a small and fixed number. If the singularity in λ_n is weak enough, we find asymptotically $\eta_{\mathrm{C}}^{\mathrm{contact}} = \eta_{\mathrm{C}}$. However, for strong singularities, there are non-trivial contributions of $P_l^{\mathrm{C}}\lambda_l^{\mathrm{C}} - \lambda_l^{\mathrm{C}}$, whereas $(P_l^{\mathrm{C}}\lambda_l^{\mathrm{C}} - \lambda_l^{\mathrm{C}})([u_n] - g) = 0$ in a neighbourhood of the singularity: see, *e.g.*, the case $\alpha = \pi/3$ in Figure 6.19(f).

Two-sided contact problem with a corner singularity

We use a geometry such that there is a zero gap between the two bodies and set $\nu = 0$. Figure 6.20(c) shows how the error decays for uniform and adaptive refinement. Asymptotically we find better convergence rates for the adaptive setting. This results from the presence of the singularities which can be found at the two endpoints of the contact boundary. Due to the singularities at $(-0.5, 0)$ and $(0.5, 0)$, we observe strong local refinement at these points.

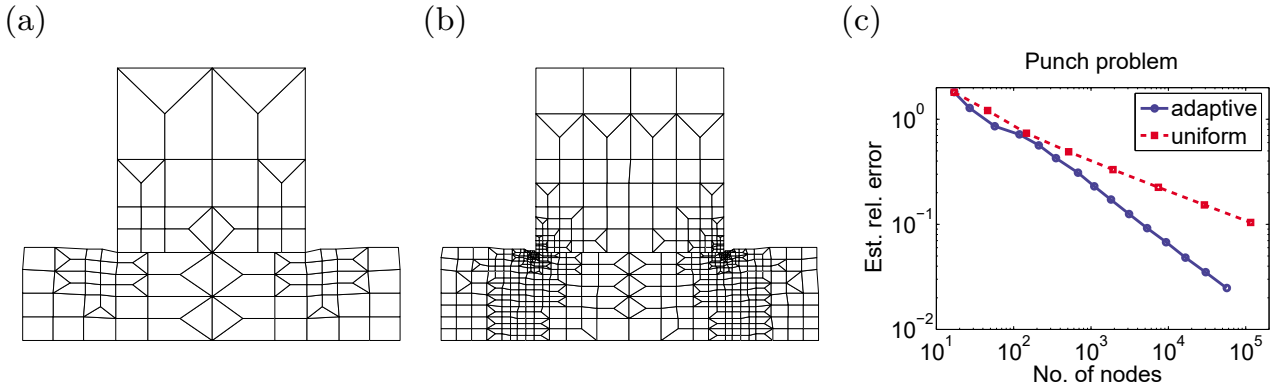

Figure 6.20. Deformed meshes after 3 and 6 adaptive refinement steps (a,b) and error decay (c).

Two-sided contact problem with different materials

In this test setting we consider the influence of the material parameters on the adaptive refinement process. Two unit squares in contact are considered. Our initial mesh on the upper body consists of 9 uniform quadrilaterals, and on the lower body we have 4 uniform quadrilateral elements. Thus, we have non-conforming meshes at the contact boundary. In this example, we study the influence of the material parameters on the error indicator. We consider five different situations ($i = 1, \ldots, 5$) for the material parameters. For the

upper subdomain, we select Young's modulus as

$$E_1^{\text{up}} = E_2^{\text{up}} = E_3^{\text{up}} = 2 \times 10^5, \quad E_4^{\text{up}} = 2 \times 10^6, \quad E_5^{\text{up}} = 2 \times 10^9,$$

and for the lower body we define

$$E_1^{\text{low}} = 2 \times 10^9, \quad E_2^{\text{low}} = 2 \times 10^6, \quad E_3^{\text{low}} = E_4^{\text{low}} = E_5^{\text{low}} = 2 \times 10^5.$$

We remark that for $i = 3$, both subdomains have the same material parameters, whereas for $i = 1, 2$ the upper subdomain is softer and for $i = 4, 5$ the lower subdomain is softer. For $i = 1, 2, 3$ the upper subdomain plays the role of the slave side, and for $i = 4, 5$ the lower subdomain is the slave side.

Figure 6.21 shows the adaptively refined meshes after 8 refinement steps using η_{L} as error indicator. As expected, the adaptive refinement strongly depends on the material parameters. The softer the domain, the more it is refined. Having the same material parameters on both sides, we get the same level of mesh refinement on both sides; see Figure 6.21(c).

In addition, we compare the estimated error decay between uniform and adaptive refinement using η_{L} as the error indicator. The decay of η_{L} and η_{C} for both approaches are shown in Figure 6.22 for $i = 1, 3, 5$. In all three situations, we observe that the error decay for the adaptive refinement shows the expected order. The different orders in the error decay of uniform and adaptive refinement can also be observed in the contact term η_{C}.

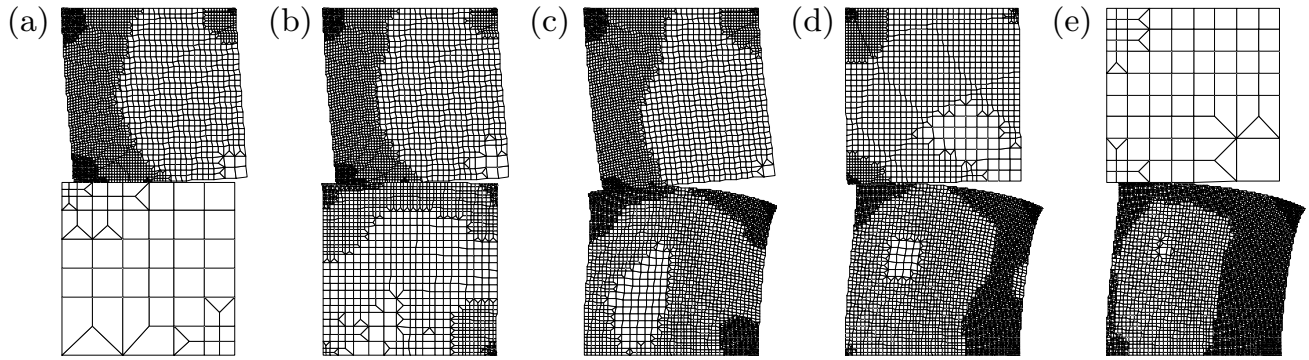

Figure 6.21. Influence of the material parameter on the adaptive refinement, $1 \leq i \leq 5$ (left to right).

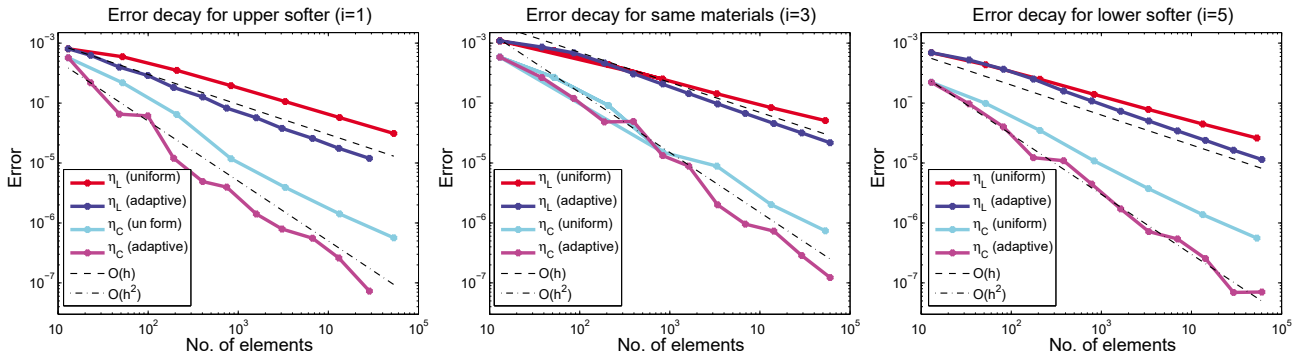

Figure 6.22. Error decay for uniform and adaptive refinement.

In the rest of this section, we show that the error indicator can also be applied to more general situations such as non-matching meshes in 3D and large deformation.

Dynamical contact problem
We now apply our error indicator to a dynamic contact problem with Coulomb friction and use a refinement and coarsening strategy. We use a modified mid-point rule and a stabilized active set strategy as the time-integration scheme and non-linear solver. In the case of a mesh which is constant in time, the total energy including contact work is preserved within each time step. As the initial condition, we have zero displacements and a constant velocity. The resulting adaptively refined meshes at different time steps are depicted in Figure 6.23. Here, a co-rotational formulation for the contact has been used (see Hauret, Salomon, Weiss and Wohlmuth (2008) and Salomon, Weiss and Wohlmuth (2008)), and the displacement is decomposed in each time step into a rotation and a small displacement which can be handled within the theory of linearized elasticity.

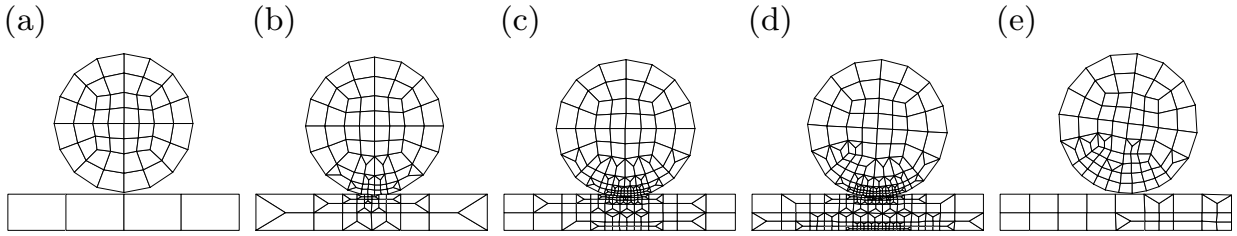

Figure 6.23. Adaptive grid at time step t_k: $k = 0$ (a), $k = 20$ (b), $k = 40$ (c), $k = 80$ (d), $k = 120$ (e).

Three-dimensional contact problem
We consider the situation of a torus between two rectangular plates. The plates are considered as the slave sides defining the mesh for the Lagrange multiplier $\boldsymbol{\lambda}$. We apply Coulomb's law with $\nu = 0.8$ and assume the plates to be softer. Figures 6.24(a) and 6.24(b) show the refined meshes with the effective von Mises stress. As can be observed, a local adaptive refinement occurs at the contact zone, resulting in highly non-matching meshes.

Contact problem with large deformation
In our last numerical example, we consider a contact problem without friction but with finite deformations in the two-dimensional setting. Instead of the linearized stress tensor $\boldsymbol{\sigma}$ (see (2.2)), we use a well-known neo-Hookean material law. In the definition of the error indicator, we replace $\boldsymbol{\sigma}$ by the first Piola–Kirchhoff stress tensor given by

$$\mathbf{P} = \frac{\lambda}{2}\big(J^2 - 1\big)\mathbf{F}^{-\top} + \mu\big(\mathbf{F} - \mathbf{F}^{-\top}\big),$$

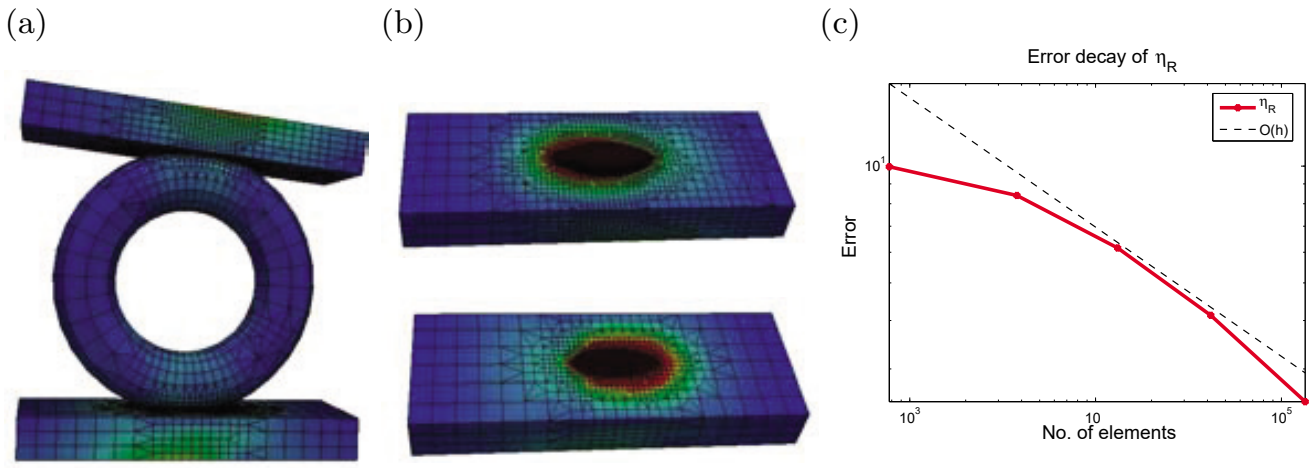

Figure 6.24. Adaptively generated mesh (a,b) and error decay (c).

with the deformation gradient $\mathbf{F} = \mathbf{Id} + \nabla\mathbf{u}$ and its determinant $J := \det(\mathbf{F})$. Due to this additional nonlinearity in the material, the first line in the discretized algebraic problem formulation (5.1) is no longer linear and the semi-smooth Newton scheme automatically takes into account the non-linear material law. Using the semi-smooth Newton method to treat nonlinear contact conditions has the main advantage that both nonlinearities, the contact conditions and the material nonlinearity, can be handled within one iteration loop.

We press a half-ring onto a bar by applying suitable Dirichlet boundary conditions. The half-ring, being the lower half-part of a full ring, is assumed to be the slave side Ω^s with inner radius $r_i = 80$ and outer radius $r_o = 100$ having its mid-point at the origin. The numerical results are presented in Figure 6.25. We adapt η_{R} to the non-linear material law and obtain an error indicator which can be easily evaluated. Figure 6.25(c) shows the estimated error decay. We also observe order-h_l convergence in that situation.

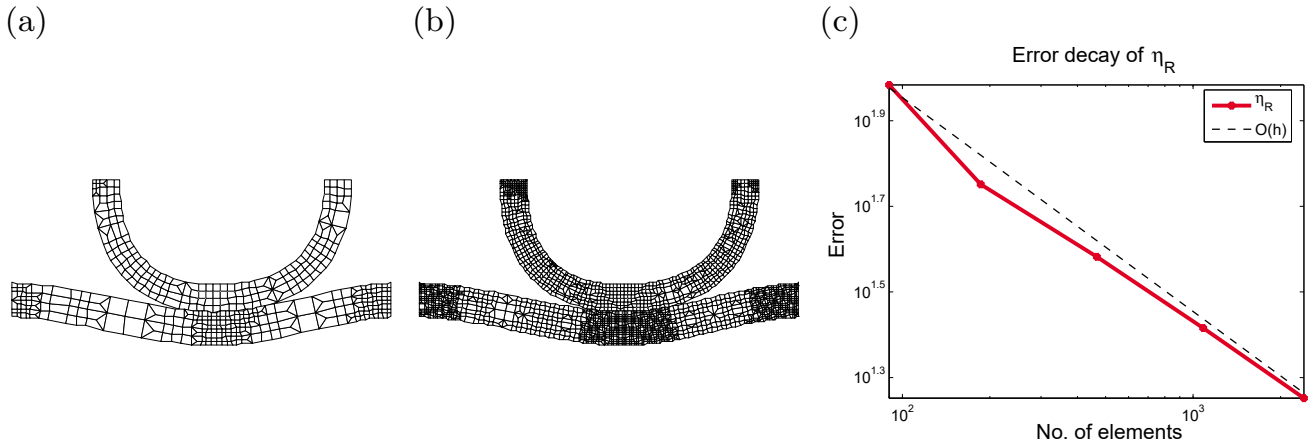

Figure 6.25. Distorted meshes after 2 and 4 adaptive refinement steps (a,b) and error decay (c).

Finally, we point out that AFEM refinement strategies can also be designed for variational inequalities such as contact- or obstacle-type problems. These refinement strategies were originally designed for conforming finite elements applied to the Laplace operator. We refer to the original work by Dörfler (1996) and the surveys of Morin, Nochetto and Siebert (2002) and Nochetto, Siebert and Veeser (2009). Nowadays these techniques have been widely generalized and successfully applied to other types of equations and elements. Special refinement rules, in combination with a control over the data oscillation terms, lead to a guaranteed error decay. Moreover, optimal convergence results, under mild regularity assumptions, have been stated in Binev, Dahmen and DeVore (2004) and Stevenson (2005, 2007); see also Cascon, Kreuzer, Nochetto and Siebert (2008). For variational inequalities, the first theoretical results can be found in Braess, Carstensen and Hoppe (2007, 2009*a*) for obstacle problems. For one-sided contact problems and no friction, a guaranteed decay in the energy can be achieved: see Weiss and Wohlmuth (2009). Here we only show some numerical results. We point out that the proof relies on the fact that the discrete solution $\mathbf{u}_l$ satisfies the non-penetration condition $[u_l^n] \leq 0$ strongly. Thus the analysis can be based on the constrained minimization problem (2.7) for contact without friction. The discrete convex cone $\mathbf{K}_l$ is then a subset of $\mathbf{K}$, and so we have

$$J(\mathbf{u}) \leq J(\mathbf{u}_l).$$

This does not hold for two-body contact problems on non-matching meshes, and there is no straightforward way to generalize the result to non-matching meshes.

The main difficulty in the application of AFEM results to variational inequalities is the loss of the Galerkin orthogonality compared to a standard conforming finite element discretization for linear problems. It is shown in Braess, Carstensen and Hoppe (2007) that a possible remedy is to consider the error in the energy $\delta_l := J(\mathbf{u}_l) - J(\mathbf{u})$ and not the error in the energy norm. For the most simple case of $\nu = 0$ and no gap, we get

$$\begin{aligned}
\delta_l - \delta_{l+1} &= J(\mathbf{u}_l) - J(\mathbf{u}_{l+1}) \\
&= \frac{1}{2}|||\mathbf{u}_l - \mathbf{u}_{l+1}|||^2 + a(\mathbf{u}_l - \mathbf{u}_{l+1}, \mathbf{u}_{l+1}) - f(\mathbf{u}_l - \mathbf{u}_{l+1}) \\
&= \frac{1}{2}|||\mathbf{u}_l - \mathbf{u}_{l+1}|||^2 - b(\boldsymbol{\lambda}_{l+1}, \mathbf{u}_l - \mathbf{u}_{l+1}) \\
&\geq \frac{1}{2}|||\mathbf{u}_l - \mathbf{u}_{l+1}|||^2.
\end{aligned}$$

Figure 6.26 shows the energy reduction for the second example in Section 6.8. The mean value of the energy decay per refinement step is between 0.7 and 0.8 for all three settings.

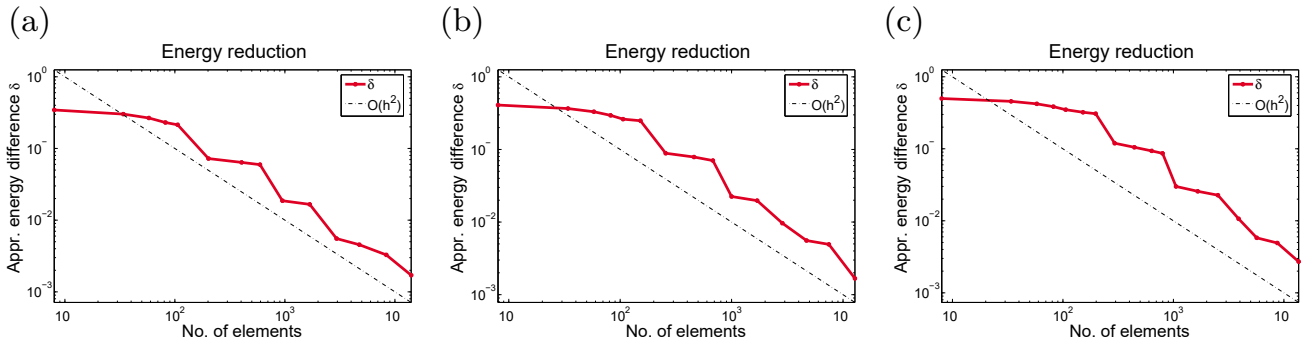

Figure 6.26. Energy reduction for $\alpha = 2\pi/3$ (a), $\alpha = \pi/2$ (b), $\alpha = \pi/3$ (c).

6.10. Conclusion

Based on the variational formulation (6.5), we have introduced an error indicator η_{L}, which is shown to be an error estimator for some simplified situations. For contact problems without friction this is true for matching meshes or one-sided contact problems with a zero gap and constant normal on the contact zone. Assumption 6.7 depends only on the discrete solution and can be checked easily for each pair $(\mathbf{u}_l, \boldsymbol{\lambda}_l)$. The situation is more challenging for friction problems with Tresca or Coulomb friction. In that case, we have to restrict ourselves to 2D and the additional Assumption 6.10 is required. Our theoretical and numerical results show that there is no need to add terms related to the variational inequality, such as η_{C} and η_{F}, to the estimator. These observations provide an interesting and attractive general construction principle of *a posteriori* error estimators for variational inequalities. In a first step, the weak variational inequality for the primal variable has to be reformulated by means of a locally defined Lagrange multiplier as a variational equality. We recall that the Lagrange multiplier acts as an additional external source term, volume or surface, on the system. Then, in a second step, we apply any type of well-known *a posteriori* error estimator. If the pairing between discrete Lagrange multiplier and discrete finite element solution is suitable, we can then recover upper and lower bounds for the discretization error in the primal but also the dual variable. This is a very strong result and also applies to obstacle-type problems. As a by-product, we find that for a linear setting with inhomogeneous Neumann data, the boundary terms in the residual error estimator can be removed, and only the data oscillation enters the bounds.

7. Energy-preserving time-integration scheme

In the previous sections, an abstract framework was provided to solve numerically a stationary contact problem efficiently in terms of Lagrange multipliers. The discretization is realized as weakly consistent and uniformly stable saddle-point formulation, and the Lagrange multiplier plays an essential role in the definition of the non-linear solver as well as in the design

of the error estimator. However, it is well known that these multipliers often show oscillations and numerical instabilities in dynamic situations: see, *e.g.*, Borri, Bottasso and Trainelli (2001), Hauret and Le Tallec (2006), Ballard, Léger and Pratt (2006), Martins, Barbarin, Raous and Pinto da Costa (1999) and Raous, Barbarin and Vola (2002). Figure 7.1 illustrates this effect if a classical Newmark scheme is applied on a saddle-point formulation for a dynamical Hertz contact problem.

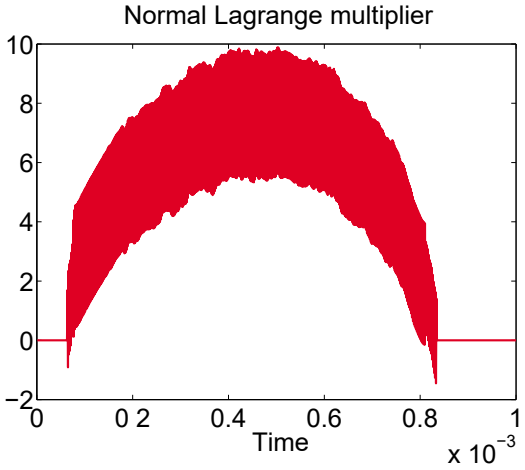

Figure 7.1. Oscillations of the Lagrange multiplier in normal direction.

Thus there is huge demand for more robust numerical schemes. Recently, different techniques have been introduced for coping with these instabilities. The most promising approaches are based on a mass redistribution and go back to the early work by Khenous, Laborde and Renard (2006*a*, 2006*b*, 2008), and alternatively on a predictor–corrector scheme (see Deuflhard, Krause and Ertel (2008), Klapproth, Deuflhard and Schiela (2009), Klapproth, Schiela and Deuflhard (2010), Kornhuber, Krause, Sander, Deuflhard and Ertel (2007), Krause and Walloth (2009)), which is motivated by well-established two-stage schemes in plasticity; see the overview by Simo (1998). Although quite different, from the initial perspective, the proposed modifications in Khenous, Laborde and Renard (2006*b*) and Kornhuber *et al.* (2007) both require an additional global L^2-type projection step. The algorithm in the latter work involves per time step a global projection which is equivalent to solving a uniformly well-conditioned constrained minimization problem, whereas the mass redistribution can be worked out in a global pre-process.

Stability is obviously of crucial importance, but in many engineering applications energy conservation is also essential. We refer to the early contributions of Armero and Petöcz (1998, 1999), Demkowicz and Bajer (2001), Laursen and Chawla (1997) and Pandolfi, Kane, Marsden and Ortiz (2002), and to the more recent work by Betsch and Hesch (2007), Gonzales, Schmidt and Ortiz (2010) and Hesch and Betsch (2009, 2010). Special emphasis on

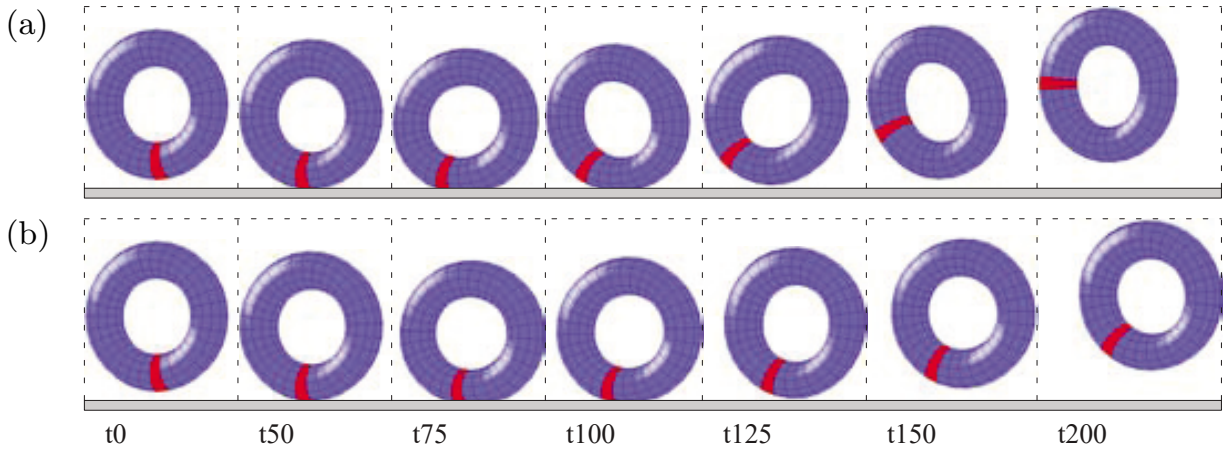

Figure 7.2. Deformation: no friction (a) and stick condition (b).

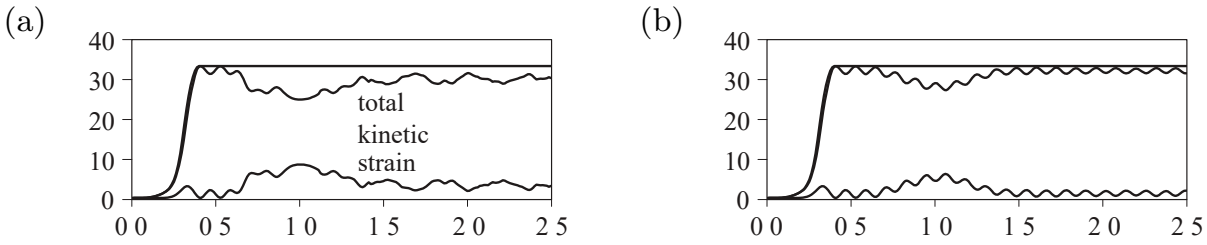

Figure 7.3. Energy: no friction (a) and stick condition (b).

the DAE aspect of mechanical systems with constraints can be found in Betsch and Steinmann (2002*a*, 2002*b*), Lunk and Simeon (2006) and Simeon (2006), and we refer to Gonzalez (2000), Hilber, Hughes and Taylor (1977) and Simo and Tarnow (1992) for time-integration schemes in non-linear elasto-dynamics.

Figure 7.2 (see Hartmann, Brunßen, Ramm and Wohlmuth (2007) for details) illustrates the application of an energy-preserving method which is a combination of a velocity update motivated by the persistency condition of Laursen and Love (2002), and the generalized energy-momentum method proposed in Kuhl and Ramm (1999).

The energy is shown in Figure 7.3(a,b). As can be seen from the two pictures, the total energy as the sum of the kinetic and strain energy is constant with respect to time.

Although these approaches are energy-conserving, no reliable numerical results for the contact stresses can be obtained without additional post-processing and stabilization. Here, we combine different techniques, a mass redistribution for its stabilization effect and the persistency condition for its role in the energy evolution.

To start with, we extend our simple quasi-static model (2.3)–(2.6) to the dynamic case and include the density of the body, and we refer to Eck *et al.* (2005), Hüeber, Matei and Wohlmuth (2007), Hüeber and Wohlmuth (2005*b*) and Kikuchi and Oden (1988). The problem under consideration

can be written in its weak form as follows. Find $\mathbf{u} \in L^\infty((0,T),\mathbf{V}_\mathrm{D})$ and $\boldsymbol{\lambda} \in L^2((0,T),\mathbf{M}(\lambda_n))$ such that

$$\dot{\mathbf{u}} \in H^{1/2}((0,T),\mathbf{V}), \quad \ddot{\mathbf{u}} \in L^2((0,T),\mathbf{V}_0')$$

and

$$\begin{aligned}
m(\ddot{\mathbf{u}},\mathbf{v}) + a(\mathbf{u},\mathbf{v}) + b(\boldsymbol{\lambda},\mathbf{v}) &= f(\mathbf{v}), && \mathbf{v} \in \mathbf{V}_0 && t \in (0,T],\\
b_n(\boldsymbol{\mu}-\boldsymbol{\lambda},\mathbf{u}) + b_t(\boldsymbol{\mu}-\boldsymbol{\lambda},\dot{\mathbf{u}}) &\le g(\boldsymbol{\mu}-\boldsymbol{\lambda}), && \boldsymbol{\mu} \in \mathbf{M}(\lambda_n), && t \in (0,T],\\
(\mathbf{u}(0,\cdot),\mathbf{v}) &= (\mathbf{u}_0,\mathbf{v}), && \mathbf{v} \in \mathbf{V}_0,\\
(\dot{\mathbf{u}}(0,\cdot),\mathbf{v}) &= (\mathbf{v}_0,\mathbf{v}), && \mathbf{v} \in \mathbf{V},
\end{aligned}$$

where the zero-order bilinear form $m(\cdot,\cdot)$ is given by $m(\mathbf{u},\mathbf{v}) := \int_\Omega \varrho \mathbf{u}\mathbf{v}\,\mathrm{d}x$, and we assume that ρ is constant on each subdomain.

Using the notation of Section 5 and the basis transformation of Section 5.2, we then obtain the following semi-discrete problem:

$$\begin{aligned}
M_l\ddot{\mathbf{u}}_l + A_l\mathbf{u}_l + B_l\boldsymbol{\lambda}_l &= \mathbf{f}_l,\\
C_p^n(\gamma_p^n, u_p^n) &= 0, \quad p \in \mathcal{P}_{\mathrm{C};l}^\mathrm{s},\\
C_p^t(\boldsymbol{\gamma}_p, \dot{\mathbf{u}}_p) &= \mathbf{0}, \quad p \in \mathcal{P}_{\mathrm{C};l}^\mathrm{s}.
\end{aligned} \tag{7.1}$$

Comparing (5.7) with (7.1), we find that both systems have a similar structure. The main difference is that in the dynamic case we have to use the already introduced splitting of the NCP function into its normal and tangential part. Formally, the semi-discrete system can be classified as a differential-algebraic equation with index three: see Brenan, Campbell and Petzold (1989) and Hairer and Wanner (1991). For this type of problem, standard time-integration schemes can result in strong oscillations; see also Figure 7.1.

We do not follow the original approach of Khenous *et al.* (2006*a*, 2006*b*) but apply a locally defined mass modification, which can be directly assembled within the standard framework of finite element technology and does not require a global projection. Introducing a combined space–time integration, we have to replace the mass matrix M_l in (7.1) by a modified one, M_l^mod. The presentation here follows the lines of Hager and Wohlmuth (2009*a*) and Hager, Hüeber and Wohlmuth (2008); see also the more recent contributions of Doyen and Ern (2009), Hager (2010) and Renard (2010).

Using an M_l^mod such that $m_{pq}^\mathrm{mod} = m_{qp}^\mathrm{mod} = 0$ for all $p \in \mathcal{P}_{\mathrm{C};l}^\mathrm{s}$ reduces the index of the DAE system (7.1) from three to one and has a stabilization and regularization effect on the modified solution. Thus such an approach seems to be very attractive provided the computational cost is of low complexity and the order of the discretization is not reduced. To recover the motion $\mathbf{r}$ of a rigid body, we have to make sure that $\mathbf{r}^\top M_l^\mathrm{mod}\mathbf{r} = \mathbf{r}^\top M_l\mathbf{r}$. Sufficient conditions are formulated in Khenous *et al.* (2006*a*) as preservation of the

total mass $\int_\Omega \varrho \, \mathrm{d}x$, of the centre of gravity $\int_\Omega \varrho \, \mathbf{x} \, \mathrm{d}x$ and of the moments of inertia $\int_\Omega \varrho \, \mathbf{x}\mathbf{x}^\top \, \mathrm{d}x$:

(M0) $\mathbf{1}^\top M_l^{\mathrm{mod}} \, \mathbf{1} = \mathbf{1}^\top M_l \, \mathbf{1}$,

(M1) $\mathbf{1}^\top M_l^{\mathrm{mod}} \, \mathbf{x}_i = \mathbf{1}^\top M_l \, \mathbf{x}_i$, $1 \le i \le d$,

(M2) $\mathbf{x}_i^\top M_l^{\mathrm{mod}} \, \mathbf{x}_j = \mathbf{x}_i^\top M_l \, \mathbf{x}_j$, $1 \le i, j \le d$.

Here we use the notation $\mathbf{1} = (1, \ldots, 1)^\top \in \mathbb{R}^{N_l}$, $N_l := \dim \mathbf{V}_l$, and $\mathbf{x}_i = ((\mathbf{x}_p^\top \mathbf{e}_i)\mathbf{e}_i)_{p \in \mathcal{P}_l} \in \mathbb{R}^{N_l}$, with $\mathbf{x}_p$ being the coordinate vector of the vertex p and $\mathbf{e}_i \in \mathbb{R}^d$ the ith unit vector.

7.1. Local construction of M_l^{mod}

As standard in the finite element context, we assume that the elements of M_l are obtained by an element-wise assembling process and by the use of quadrature formulas on each element $t \in \mathcal{T}_l$. Our definition of the modified mass matrix is based on a second triangulation which groups elements on the slave side near the contact zone into macro-elements. As a preliminary step, we introduce the strip S_l by

$$\overline{S}_l := \cup_{p \in \mathcal{P}^{\mathrm{s}}_{\mathrm{C};l}} \operatorname{supp} \phi_p \quad \text{and} \quad \overline{\Omega_{S_l}} := \overline{\Omega \setminus S_l}.$$

In the following, we assume that a fixed macro-triangulation $\mathcal{T}_H$ is associated with $\mathcal{T}_l$. By this we understand that there exists a second triangulation, possibly with hanging nodes, such that each element of $\mathcal{T}_H$ can be written as the union of elements in $\mathcal{T}_l$. Moreover $\mathcal{T}_H$ has the following properties.

- If $T \in \mathcal{T}_H$ with $T \subset \Omega_{S_l}$ then $T \in \mathcal{T}_l$.
- If $T \in \mathcal{T}_H \setminus \mathcal{T}_l$, then there exists exactly one element $t_T \in \mathcal{T}_l$ with $t_T \subset \Omega_{S_l} \cap T$ and at most M elements $t \in \mathcal{T}_l$ with $t \subset S_l \cap T$, where M is a fixed small number and not depending on l. Furthermore, all sub-elements of T can be accessed starting from t_T by crossing only faces of sub-elements of T.

We note that for a given $\mathcal{T}_l$, there exists more than one macro-triangulation. Figure 7.4 illustrates different possibilities of $\mathcal{T}_H$ for a given $\mathcal{T}_l$. The elements of the original mesh are marked with dashed lines, whereas the elements of the macro-triangulation are given by bold lines. The shaded subdomains show the different types of elements in $\mathcal{T}_H \setminus \mathcal{T}_l$ and the strips S_l, $\overline{D}_l := \cup_{T \in \mathcal{T}_H \setminus \mathcal{T}_l} \overline{T}$ and $\tilde{D}_l$, which is defined as the union of all elements t in $\mathcal{T}_l$ such that $\partial t \cap \overline{D}_l \neq \emptyset$.

Remark 7.1. If $\mathcal{T}_l$ is obtained from $\mathcal{T}_{l-1}$ by uniform refinement based on a decomposition of each element into 2^d sub-elements, then a natural construction for $\mathcal{T}_H$ is straightforward: see Figure 7.4(b).

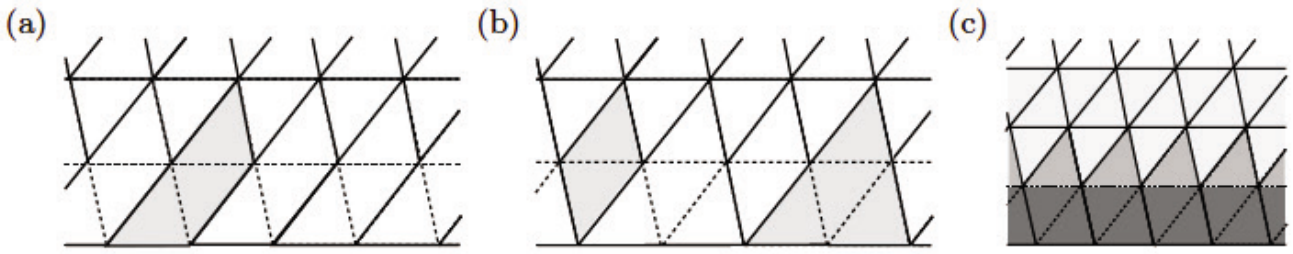

Figure 7.4. Different macro-triangulations $\mathcal{T}_H$ for a given $\mathcal{T}_l$ (a,b) and the strips S_l, D_l, $\tilde{D}_l$ (c).

In the following, we restrict ourselves to simplicial triangulations $\mathcal{T}_l$ but note that these techniques can also be applied to more general meshes. We refer to Hager *et al.* (2008) for a discussion in the case of quadrilateral meshes.

The mass matrix M_l^{mod} is associated with the modified bilinear form $m_H(\cdot,\cdot)$, which is defined in terms of a suitable quadrature formula applied to the elements of the macro-triangulation, *i.e.*,

$$m_H(\mathbf{v}_l, \mathbf{w}_l) := \sum_{T \in \mathcal{T}_H} \sum_{i=1}^{N_T} w_i^T \mathbf{v}_l(q_i^T) \mathbf{w}_l(q_i^T),$$

where N_T is the number of quadrature nodes and q_i^T and w_i^T are the quadrature nodes and weights, respectively. From now on we omit the upper index T if it is clear from the context.

On each element $t \in \mathcal{T}_H \cap \mathcal{T}_l$, we use a standard quadrature formula such that $\int_t \rho \phi_p \phi_q \, \mathrm{d}x$ is exactly evaluated by it. For each $T \in \mathcal{T}_H \setminus \mathcal{T}_l$, we select our quadrature formula in a special way. The construction of the macro-triangulation guarantees that for $T \in \mathcal{T}_H$ there exists a unique $t_T \in \mathcal{T}_l$ such that $t_T \subset T$ and $\partial t_T \cap \overline{\Gamma}_{\mathrm{C}}^{\mathrm{s}} = \emptyset$. On t_T, we use the second-order Lagrange interpolation nodes q_i, $1 \le i \le N_T$, as quadrature points. For a simplicial element t_T, we have $N_T := 6$ for $d = 2$ and $N_T := 10$ for $d = 3$. For a quadrilateral/hexahedral element, we have $N_T := 9$ for $d = 2$ and $N_T := 27$ for $d = 3$. The weights are computed as

$$w_i := \int_T \phi_{q_i}^2 \, \mathrm{d}x, \quad 1 \le i \le N_T,$$

where $\phi_{q_i}^2$, $1 \le i \le N_T$, is the second-order nodal Lagrange basis function on t_T extended as polynomial to T.

Lemma 7.2. The choice of the quadrature formula yields the following properties for the modified mass matrix M_l^{mod}.

(1) (M0)–(M2) hold.

(2) $(M_l^{\mathrm{mod}})_{pq} = (M_l^{\mathrm{mod}})_{qp} = \mathbf{0}$ if $p \in \mathcal{P}_l^{\mathrm{s}}$.

(3) The local mass matrices M_T associated with each macro-element are positive semi-definite and have rank r_T. For a simplicial element t_T, we have $r_T = d + 1$, and for a quadrilateral/hexahedral element, r_T is 2^d.

Proof. The definition of the macro-elements and the construction of the nodes and weights directly yield that globally quadratic functions are integrated exactly and thus (M0)–(M2) hold. The definition of t_T and of the quadrature nodes gives that no quadrature node is placed in the interior of S_l or on Γ_C^s. Each basis function ϕ_p associated with a vertex $p \in \mathcal{P}_l^s$ is zero on $\overline{\Omega_{S_l}}$ and thus $\phi_p(q_i^T) = 0$, for all quadrature nodes q_i^T, $1 \le i \le N_T$, and all $T \in \mathcal{T}_H$. If $T \in \mathcal{T}_H \cap \mathcal{T}_l$, it is obvious that M_T is positive definite. For $T \in \mathcal{T}_H \setminus \mathcal{T}_l$, M_T is an $n_T \times n_T$ matrix, with $n_T \ge r_T$. The kernel of M_T has dimension at least $n_T - r_T$, and M_T has a positive definite sub-matrix $M_{t_T} \in \mathbb{R}^{r_T \times r_T}$. □

In Figure 7.5, we present for $d = 2$ a suitable quadrature formula for two different macro-elements T. Here, we have selected the case when the macro-elements are associated with a coarser simplicial mesh from which $\mathcal{T}_l$ is obtained by uniform refinement. We note that in this special situation all sub-elements of a macro-element have the same volume, and the weights do not depend on the shape of t_T.

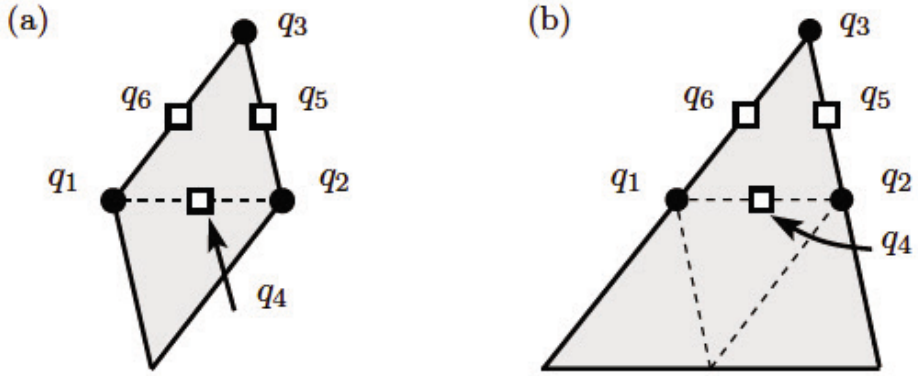

Figure 7.5. Quadrature rules for two different macro-elements.

In the situation in Figure 7.5(a) the weights are given by $w_1 = w_2 = 1/3|t_T|$, $w_3 = 2/3|t_T|$, $w_4 = 2|t_T|$, and $w_5 = w_6 = -2/3|t_T|$, and in the situation in Figure 7.5(b) the weights are $w_1 = w_2 = 8/3|t_T|$, $w_3 = 4|t_T|$, $w_4 = 16/3|t_T|$, and $w_5 = w_6 = -16/3|t_T|$. The local mass matrix M_T associated with the macro-element T in Figures 7.5(a) and 7.5(b) reads as

$$M_T = \frac{|t_T|}{3}\begin{pmatrix} 2 & \frac{3}{2} & -\frac{1}{2} & 0 \\ \frac{3}{2} & 2 & -\frac{1}{2} & 0 \\ -\frac{1}{2} & -\frac{1}{2} & 1 & 0 \\ 0 & 0 & 0 & 0 \end{pmatrix}, \quad M_T = \frac{|t_T|}{3}\begin{pmatrix} 8 & 4 & -4 & 0 & 0 & 0 \\ 4 & 8 & -4 & 0 & 0 & 0 \\ -4 & -4 & 4 & 0 & 0 & 0 \\ 0 & 0 & 0 & 0 & 0 & 0 \\ 0 & 0 & 0 & 0 & 0 & 0 \\ 0 & 0 & 0 & 0 & 0 & 0 \end{pmatrix},$$

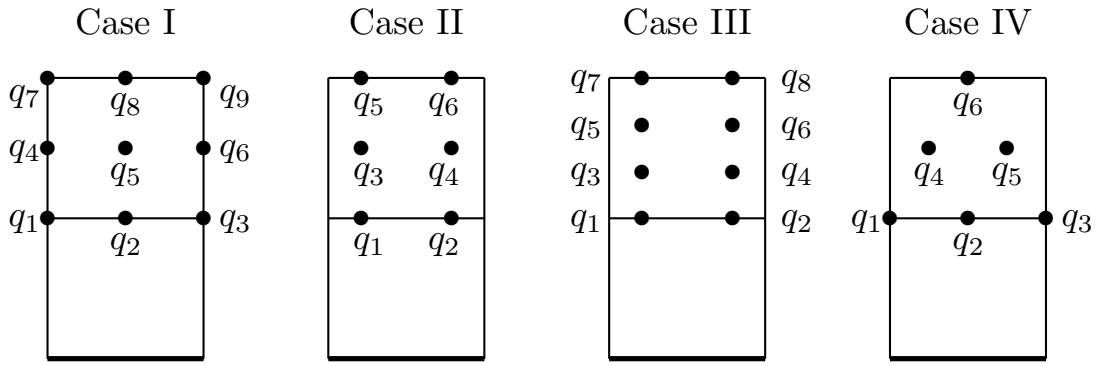

Figure 7.6. Different quadrature rules for a quadrilateral macro-element.

respectively. Both local matrices are obviously singular but have rank three and are positive semi-definite.

We briefly comment on the properties specified in Lemma 7.2 and recall that the first one guarantees that the rigid body motions are not affected by the modification. The second one reduces the index from three to one, and the third is essential to guarantee stability. For quadrilateral finite elements in 2D, we can also select different quadrature rules. The quadrature formula has to satisfy the properties (1) and (2) of Lemma 7.2. In addition, all elements in $Q_2(t_T)$ extended as polynomials onto T have to be integrated exactly. Here $Q_j(t_T) := Q_j(\hat{T}) \circ F_{t_T}^{-1}$, where F_{t_T} is the element mapping from the reference quadrilateral $\hat{T}$ onto t_T, and $Q_j(\hat{T})$ is the space of all bi-linear elements for $j = 1$ and of all bi-quadratic elements for $j = 2$. This condition is very natural and results from the fact that $Q_1(t)$, $t \in \mathcal{T}_l$, is the local low-order finite element space. We refer to Ciarlet (1998) for a rigorous mathematical analysis of the influence of quadrature errors on the quality of the finite element approach. Then property (3) of Lemma 7.2 is automatically satisfied.

Figure 7.6 shows a typical macro-element T for a quadrilateral mesh and four different quadrature formulas. All of them guarantee that quadratic functions on T are integrated exactly, but only the first three yield stable numerical results.

The quadrature nodes are given as shown in Figure 7.6. Case I follows the specified construction principle. The weights for this special macro-element are given by $w_1 = w_3 = 5/9|t_T|$, $w_2 = 20/9|t_T|$, $w_4 = w_6 = -4/9|t_T|$, $w_5 = -16/9|t_T|$, $w_7 = w_9 = 2/9|t_T|$ and $w_8 = 8/9|t_T|$ in Case I. Cases II and III are based on Gauss nodes in the tangential direction, whereas in the normal direction we use equilibrated spaced nodes. In Case II, the weights are $w_1 = w_2 = 2/3|t_T|$, $w_3 = w_4 = -4/3|t_T|$, and $w_5 = w_6 = 5/3|t_T|$. The weights for Case III are given by $w_1 = w_2 = 4|t_T|$, $w_3 = w_4 = -15/2|t_T|$, $w_5 = w_6 = 6|t_T|$ and $w_7 = w_8 = -3/2|t_T|$. Case II can only be used if the element mappings are affine. For the more general case of $\det F_{t_T}^{-1} \in Q_1(t_T)$, Case I or Case III should be used. Both cases can also be easily applied in the

Table 7.1. Energy and displacement results for Case IV.

Time	Kinetic energy	Elastic energy	Total energy	x_2-displacement
$4.0 \cdot 10^{-6}$	$9.3 \cdot 10^{-2}$	$7.3 \cdot 10^{-3}$	$1.0 \cdot 10^{-1}$	$-3.4 \cdot 10^{-2}$
$5.0 \cdot 10^{-6}$	-3.1	3.2	$1.0 \cdot 10^{-1}$	$-4.1 \cdot 10^{-2}$
$6.0 \cdot 10^{-6}$	$-1.4 \cdot 10^{5}$	$1.4 \cdot 10^{5}$	$1.0 \cdot 10^{-1}$	$1.8 \cdot 10^{-1}$
$6.5 \cdot 10^{-6}$	$-2.9 \cdot 10^{7}$	$2.9 \cdot 10^{7}$	$1.0 \cdot 10^{-1}$	-3.4
$7.0 \cdot 10^{-6}$	$-6.1 \cdot 10^{9}$	$6.1 \cdot 10^{9}$	$1.0 \cdot 10^{-1}$	$4.9 \cdot 10^{1}$

3D setting. The negative weights do not disturb the computation as long as all local mass matrices M_T for $T \in \mathcal{T}_H$ are positive semi-definite. Case IV is based on triangular-distributed second-order Lagrange interpolation nodes. The weights are defined by $w_1 = w_3 = 1/3$, $w_2 = 1$, $w_4 = w_5 - 2/3$ and $w_6 = 2/3$, and give rise to the following local mass matrix:

$$M_T = \frac{|t_T|}{24} \begin{pmatrix} 23 & 9 & -5 & -3 & 0 & 0 \\ 9 & 23 & -3 & -5 & 0 & 0 \\ -5 & -3 & 3 & 5 & 0 & 0 \\ -3 & -5 & 5 & 3 & 0 & 0 \\ 0 & 0 & 0 & 0 & 0 & 0 \\ 0 & 0 & 0 & 0 & 0 & 0 \end{pmatrix}.$$

A straightforward computation shows that M_T has rank four but has one negative eigenvalue. Moreover, a closer look reveals that the global mass matrix can also have a negative eigenvalue. Thus, even for simple contact problems a non-physical negative kinetic energy can occur: see Table 7.1. Although the total energy is preserved, the numerical results are of no use. From the very beginning the kinetic energy is negative and exponentially increasing. The vertical displacement at a selected node is highly oscillating and far too big. This effect is a result of the negative eigenvalue of the local mass matrix M_T. Thus Case IV cannot be used for numerical computations.

7.2. Analysis in terms of an interpolation operator

We do not provide a full analysis for the mass modification. In Hager and Wohlmuth (2009*a*) it has been shown that for a linear elasticity problem, one can show $\mathcal{O}(h_l + \Delta t^2)$ *a priori* estimates for the fully discretized problem in the $H^1(\Omega)$-norm in space and the discrete L^∞-norm in time for the displacement and in the $L^2(\Omega_{S_l})$-norm in space and the discrete L^∞-norm in time for the velocity. Moreover, under some additional regularity, an order $(h_l^2 + \Delta t^2)$ can be obtained in the $L^2(\Omega)$-norm in space and the discrete L^∞-norm in time for the displacement. We restrict ourselves to families of quasi-uniform shape-regular triangulations. Figure 7.7 shows a qualitative

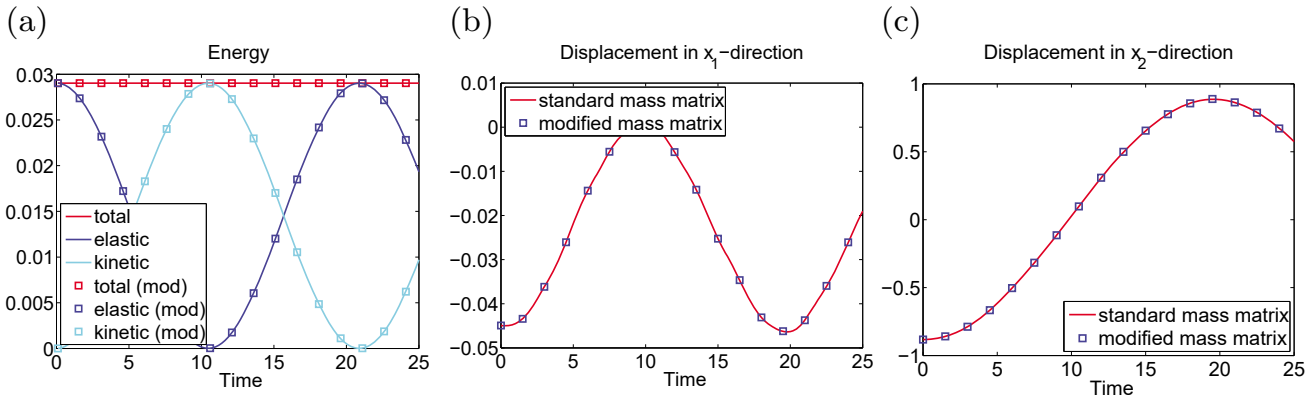

Figure 7.7. Energy (a), horizontal (b) and vertical displacement at a selected node (c).

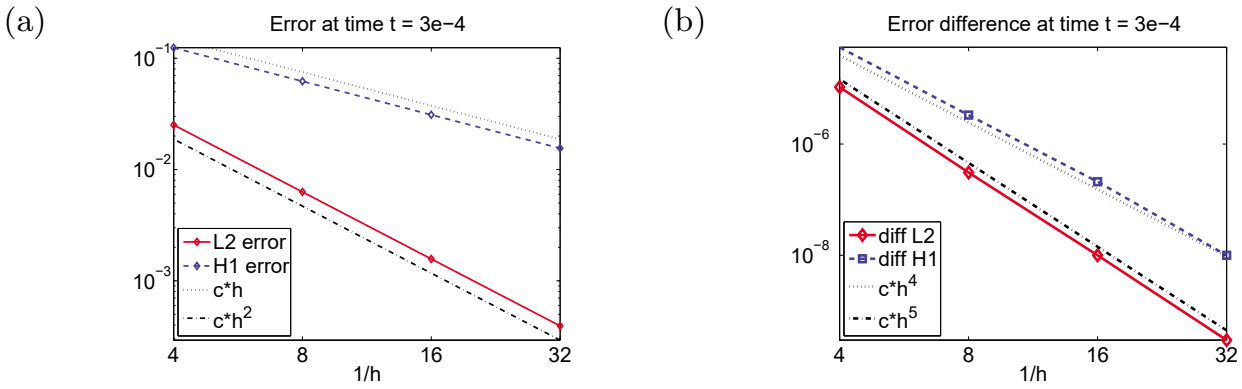

Figure 7.8. Error decay in the L^2- and H^1-norm in space (a) and decay of the difference of the two formulations (b).

comparison between the modified mass approach and the standard one for a geometrically non-linear elasticity problem without contact: see Hager *et al.* (2008) for details. As can be observed, there is no significant difference in the displacement and in both settings the energy is preserved.

The same parameter and geometry setting but for the linearized strain formulation is considered for a quantitative comparison in Figure 7.8. In Figure 7.8(b) we show that the difference between the two approaches can be asymptotically neglected and is of higher order than the discretization error. For the discretization error in space an order h_l^2 and an order h_l in the L^2- and H^1-norm can be observed, respectively, whereas the difference decreases with order h_l^5 and order h_l^4, respectively.

The analysis of the modified formulation applies ideas from the analysis of the influence of quadrature errors as well as of the influence of a standard mass lumping. Here we only provide two results that are essential to obtaining *a priori* estimates.

In the previous subsection, the modified bilinear form $m_H(\cdot,\cdot)$ was introduced in terms of a quadrature formula based on the macro-triangulation. Now, we define an interpolation operator I_H such that

$$m_H(\mathbf{v}_l, \mathbf{w}_l) = m(I_H \mathbf{v}_l, I_H \mathbf{w}_l), \quad \mathbf{w}_l, \mathbf{v}_l \in \mathbf{V}_l. \tag{7.2}$$

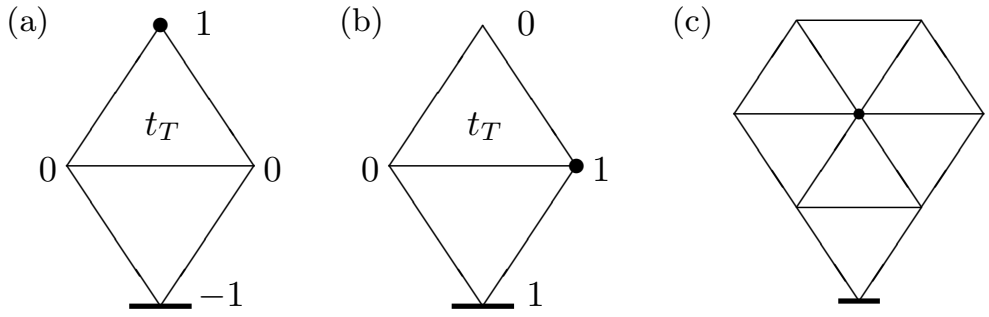

Figure 7.9. (a,b) Nodal values of two modified basis functions on the macro-element T; (c) support of (a).

To do so, we introduce a set of modified basis functions ϕ_p^{mod} which are possibly discontinuous. The new basis functions are defined for each macro-element and are associated with the vertices $p \in \mathcal{P}_l \backslash \mathcal{P}_{\mathrm{C};l}^{\mathrm{s}}$. If $T \in \mathcal{T}_H \cap \mathcal{T}_l$, then $\phi_p^{\mathrm{mod}}|_T := \phi_p|_T$ for all vertices p of T. If $T \in \mathcal{T}_H \backslash \mathcal{T}_l$, then $\phi_p^{\mathrm{mod}}|_T := E(\phi_p|_{t_T})$ for all vertices p of t_T, where E stands for the polynomial extension of $\phi_p|_{t_T}$ onto T. Figures 7.9 and 7.10 illustrate the two-dimensional case for a simplicial mesh.

In Figure 7.9 the macro-element T is the union of two elements in $\mathcal{T}_l$, whereas in Figure 7.10 the macro-element T is the union of four elements in $\mathcal{T}_l$. In both cases, only three basis functions are locally associated with the macro-element. The support of the modified basis function is still local but can be enlarged: see Figures 7.9(c) and 7.10(c).

In terms of these modified basis functions, we define our interpolation operator $I_H : \mathbf{V}_l \to \mathrm{span}\,\{\phi_p^{\mathrm{mod}} \mathbf{e}_i; 1 \le i \le d, p \in \mathcal{P}_l \setminus \mathcal{P}_{\mathrm{C};l}^{\mathrm{s}}\}$ by

$$I_H \mathbf{v}_l := \sum_{p \in \mathcal{P}_l \backslash \mathcal{P}_{\mathrm{C};l}^{\mathrm{s}}} \mathbf{v}_l(p) \phi_p^{\mathrm{mod}}.$$

The construction of the quadrature formula and the operator I_H are both based on the macro-elements such that it is easy to see that (7.2) holds. In terms of the properties of the operator I_H, the semi-discrete system (7.1) can be analysed. We refer to the recent contributions of Doyen and Ern (2009) and to Hager and Wohlmuth (2009*a*) in the case of a linear problem with given surface traction on Γ_{C}. We do not provide any details but remark that the analysis follows the lines of mass lumping techniques. We refer to Thomée (1997) for the parabolic case and to Baker and Dougalis (1976) for the second-order hyperbolic case. The main difference is that in our situation M_l^{mod} is singular and does not define a matrix that is spectrally equivalent to M_l. Thus the analysis is more technical and relies on some additional arguments. Firstly, the semi-discrete system has to be considered and Gronwall's lemma plays an important role. Secondly the fully discrete system has to be analysed and Taylor expansion with respect to time enters into the proof. Although these two steps are quite technical they are well

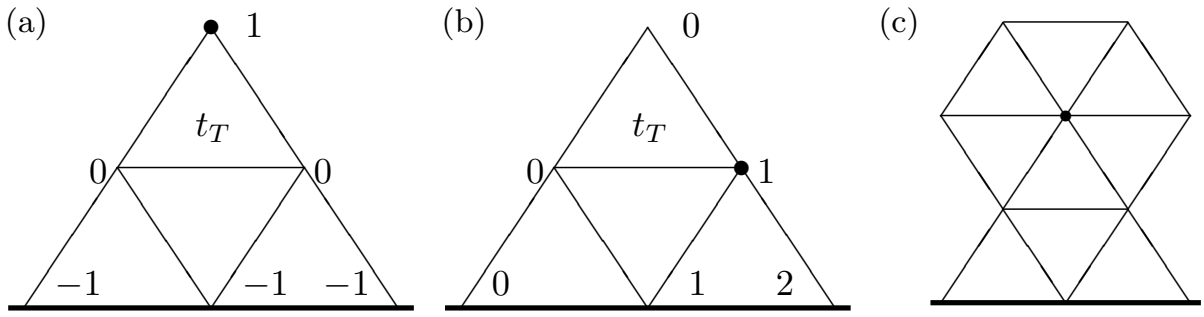

Figure 7.10. (a,b) Nodal values of two modified basis functions on the macro-element T; (c) support of (a).

established; see also Baker and Dougalis (1976), Evans (1998), Dautray and Lions (1992), Raviart and Thomas (1983) and Thomée (1997).

One crucial ingredient is the following lemma, which bounds the quadrature error introduced by the bilinear form $m_H(\cdot,\cdot)$:

$$\Delta m(\mathbf{v}_l, \mathbf{w}_l) := m_H(\mathbf{v}_l, \mathbf{w}_l) - m(\mathbf{v}_l, \mathbf{w}_l).$$

Lemma 7.3. If $\mathbf{v}_l, \mathbf{w}_l \in \mathbf{V}_l$ then

$$|\Delta m(\mathbf{v}_l, \mathbf{w}_l)| \le C h_l \big(\|\mathbf{v}_l\|_{0;D_l} \|\mathbf{w}_l\|_{1;D_l} + \|\mathbf{w}_l\|_{0;D_l} \|\mathbf{v}_l\|_{1;D_l} \big), \tag{7.3a}$$

and if $\mathbf{v}, \mathbf{w} \in \mathbf{V}$ then

$$|\Delta m(\mathbf{Z}_l \mathbf{v}, \mathbf{Z}_l \mathbf{w})| \le C h_l^2 \big(\|\mathbf{v}\|_{1;\Omega} \|\mathbf{w}\|_{2;\Omega} + \|\mathbf{w}\|_{1;\Omega} \|\mathbf{v}_l\|_{2;\Omega} \big), \tag{7.3b}$$

where $\mathbf{Z}_l$ is a locally defined Scott–Zhang-type operator (Scott and Zhang 1990).

Proof. The proof is based on the properties of the operator I_H. Using (7.2) and noting that $(I_H \mathbf{v}_l)|_{\Omega_{S_l}} = \mathbf{v}_l|_{\Omega_{S_l}}$, we find

$$\begin{aligned}
\Delta m(\mathbf{v}_l, \mathbf{w}_l) &= m(I_H \mathbf{v}_l - \mathbf{v}_l, I_H \mathbf{w}_l) + m(\mathbf{v}_l, I_H \mathbf{w}_l - \mathbf{w}_l) \\
&\le C(\|I_H \mathbf{v}_l - \mathbf{v}_l\|_{0;S_l} \|I_H \mathbf{w}_l\|_{0;S_l} + \|\mathbf{v}_l\|_{0;S_l} \|I_H \mathbf{w}_l - \mathbf{w}_l\|_{0;S_l}) \\
&\le C h_l (\|\mathbf{v}_l\|_{1;D_l} \|\mathbf{w}_l\|_{0;D_l} + \|\mathbf{v}_l\|_{0;S_l} \|\mathbf{w}_l\|_{1;D_l}).
\end{aligned}$$

To show (7.3b), we apply (7.3a), the local L^2- and H^1-stability of $\mathbf{Z}_l$, and a 1D Sobolev embedding

$$\begin{aligned}
\Delta m(\mathbf{Z}_l \mathbf{v}, \mathbf{Z}_l \mathbf{w}) &\le C h_l (\|\mathbf{Z}_l \mathbf{v}\|_{1;D_l} \|\mathbf{Z}_l \mathbf{w}\|_{0;D_l} + \|\mathbf{Z}_l \mathbf{v}\|_{0;S_l} \|\mathbf{Z}_l \mathbf{w}\|_{1;D_l}) \\
&\le C h_l (\|\mathbf{v}\|_{1;\tilde{D}_l} \|\mathbf{w}\|_{0;\tilde{D}_l} + \|\mathbf{v}\|_{0;\tilde{D}_l} \|\mathbf{w}\|_{1;\tilde{D}_l}) \\
&\le C h_l (\sqrt{h_l} \|\mathbf{v}\|_{2;\Omega} \sqrt{h_l} \|\mathbf{w}\|_{1;\Omega} + \sqrt{h_l} \|\mathbf{v}\|_{1;\Omega} \sqrt{h_l} \|\mathbf{w}\|_{2;\Omega}),
\end{aligned}$$

where $D_l \subset \tilde{D}_l$, and the diameter of the strip $\tilde{D}_l$ perpendicular to Γ_C is bounded by $C h_l$. □

Remark 7.4. The bound (7.3b) can be weakened by using Besov space norms with index 1/2 and 3/2; see, *e.g.*, Li *et al.* (2010).

Remark 7.5. In the proof of Lemma 7.3, we do not use that I_H reproduces macro-element-wise affine functions. The same arguments hold true if I_H is replaced by a locally defined operator which reproduces $\mathbf{v}_l \in \mathbf{V}_l$ on Ω_{S_l}, and on $t \subset S_l$ it reproduces $\mathbf{v}_l$ if it is constant. This observation motivates the use of a more simple quadrature formula based on the triangulation $\mathcal{T}_l$ to define the bilinear form $m_H(\cdot,\cdot)$; see also Section 7.4.

As can be easily seen, the modified bilinear form $m_H(\cdot,\cdot)$ is continuous and coercive with respect to the $L^2(\Omega_{S_l})$-norm but not coercive with respect to the $L^2(\Omega)$-norm. Thus Aubin–Nitsche-type arguments provide only *a priori* estimates in the $L^2(\Omega_{S_l})$-norm, which is a semi-norm on $L^2(\Omega)$. The following lemma shows that *a priori* estimates in the $L^2(\Omega)$-norm can also be obtained and have the same order.

Lemma 7.6. For $\mathbf{v} \in \mathbf{V}$, we have

$$\|\mathbf{v}\|_{0;\Omega} \leq C(\|\mathbf{v}\|_{0;\Omega_{S_l}} + h_l\|\mathbf{v}\|_{1;\Omega}).$$

Proof. We start with the non-overlapping decomposition of Ω into S_l and Ω_{S_l}. To bound $\|\mathbf{v}\|_{0;S_l}$, we apply element-wise a Poincaré–Friedrichs-type inequality and a scaling argument. In terms of

$$\|\mathbf{v}\|_{0;t}^2 \leq C\big(h_l^2\|\mathbf{v}\|_{1;t}^2 + h_l\|\mathbf{v}\|_{0;f}^2\big),$$
$$\|\mathbf{v}\|_{0;f}^2 \leq C\bigg(\frac{1}{h_l}\|\mathbf{v}\|_{0;t}^2 + |\mathbf{v}|_{1;t}\cdot\|\mathbf{v}\|_{0;t}\bigg),$$

where $f \subset \partial t$ is a face of the element $t \in \mathcal{T}_l$, we find

$$\|\mathbf{v}\|_{0;S_l}^2 \leq C\big(h_l^2\|\mathbf{v}\|_{1;S_l}^2 + h_l\|\mathbf{v}\|_{0;\partial S_l\cap\partial\Omega_{S_l}}^2\big) \leq C\big(h_l^2\|\mathbf{v}\|_{1;\Omega}^2 + \|\mathbf{v}\|_{0;\Omega_{S_l}}^2\big). \quad \square$$

7.3. Energy-preserving time integration

For many applications energy is one of the quantities of interest to preserve. Here, we present an energy-conserving time-integration scheme based on the standard Newmark method (Hughes 1987, Kane, Marsden, Ortiz and West 2000) in combination with a persistency condition introduced in Laursen and Chawla (1997); see also Bajer and Demkowicz (2002), Chawla and Laursen (1998), Demkowicz and Bajer (2001), Laursen and Meng (2001) and Laursen and Simo (1993*b*). The discrete displacement at time $t_k := t_0 + k\Delta t$ is given by $\mathbf{u}_l^k$ and the velocity by $\mathbf{v}_l^k$.

The Newmark scheme with $\gamma := \frac{1}{2}$ and $\beta := \frac{1}{4}$ applied to the first line of

(7.1), where we replace M_l by M_l^{mod}, then yields

$$\left(\frac{2}{(\Delta t)^2}M_l^{\mathrm{mod}} + \frac{1}{2}A_l\right)\Delta\mathbf{u}_l^{k+1} + B_l\boldsymbol{\lambda}_l^{k+\frac{1}{2}} = \mathbf{f}_l^{k+\frac{1}{2}} + \frac{2}{\Delta t}M_l^{\mathrm{mod}}\mathbf{v}_l^k - A_l\mathbf{u}_l^k, \tag{7.4a}$$

$$\mathbf{v}_l^{k+1} = \frac{2}{\Delta t}\Delta\mathbf{u}_l^{k+1} - \mathbf{v}_l^k, \tag{7.4b}$$

where the time increment $\Delta\mathbf{u}_l^{k+1}$ of the displacement is defined by $\Delta\mathbf{u}_l^{k+1} := \mathbf{u}_l^{k+1} - \mathbf{u}_l^k$, and we set $\mathbf{f}_l^{k+1/2} := \frac{1}{2}(\mathbf{f}_l^{k+1} + \mathbf{f}_l^k)$.

To obtain an energy-conserving scheme for frictionless contact problems, we have to discretize the non-penetration condition in a suitable way: see the second line in (7.1). As is well known, the complementarity condition $\lambda_n([u_n] - g) = 0$ is not suitable, but has to be replaced by the persistency condition $\lambda_n([\dot{u}_n] - \dot{g}) = 0$: see Laursen and Chawla (1997). Letting g_p^k be the space- and time-discretized gap function, we replace the non-penetration condition by

$$g_p^k > 0 \;\Rightarrow\; (\gamma_p^n)^{k+1/2} = 0,$$

$$g_p^k \le 0 \;\Rightarrow\; \begin{cases} (\gamma_p^n)^{k+1/2} \ge 0, \\ \Delta(u_p^n)^{k+1} \le g_p^k, \\ \Delta(u_p^n)^{k+1}(\gamma_p^n)^{k+1/2} = 0. \end{cases}$$

This discrete version of the persistency condition can then be rewritten in the NCP function framework, and reads as

$$C_p^n((\gamma_p^n)^{k+1/2}, \Delta(u_p^n)^{k+1}) := (\gamma_p^n)^{k+1/2} - \max\{0,\, (\gamma_p^n)^{k+1/2} + c_n\tilde{g}_p^k\} = 0, \tag{7.4c}$$

for all $p \in \mathcal{P}_{\mathrm{C};l}^{\mathrm{s}}$, where

$$\tilde{g}_p^k := \begin{cases} -\frac{(\gamma_p^n)^{k+1/2}}{c_n} - g_p^k & \text{if } g_p^k > 0, \\ \Delta(u_p^n)^{k+1} & \text{if } g_p^k \le 0. \end{cases}$$

The tangential part of the NCP function (see the third line of (7.1)) is discretized in time by

$$C_p^t\big(\boldsymbol{\gamma}_p^{k+\frac{1}{2}}, \Delta\mathbf{u}_p^k\big) = \mathbf{0}, \quad p \in \mathcal{P}_{\mathrm{C};l}^{\mathrm{s}} \tag{7.4d}$$

(see also Chawla and Laursen (1998)). Now the space- and time-discretized system of a two-body contact problem with Coulomb friction is given in each time step by the non-linear system of equations (7.4a)–(7.4d).

Introducing the discrete energy $E_l^k = (E_l^{\mathrm{kin}})^k + (E_l^{\mathrm{pot}})^k$ at time t_k as the sum of the kinematic $(E_l^{\mathrm{kin}})^k := \frac{1}{2}\mathbf{v}_l^k M_l^{\mathrm{mod}}\mathbf{v}_l^k$ and the potential energy

$(E_l^{\text{pot}})^k := \frac{1}{2}\mathbf{u}_l^k A_l \mathbf{u}_l^k$, we can show that the time-integration scheme preserves energy.

Lemma 7.7. The contact algorithm defined by (7.4a)–(7.4d) guarantees energy preservation in the sense that

$$E_l^{k+1} - E_l^k = \Delta t \mathbf{v}_l^{k+\frac{1}{2}} (\mathbf{f}_l^{k+\frac{1}{2}} - B_l (\boldsymbol{\lambda}_l^t)^{k+\frac{1}{2}}),$$

where $\mathbf{v}_l^{k+\frac{1}{2}} := \frac{1}{2}(\mathbf{v}_l^{k+1} + \mathbf{v}_l^k)$. Moreover, in the case of $\nu = 0$, we have $\mathbf{v}_l^{k+\frac{1}{2}} B_l \boldsymbol{\lambda}_l^{k+\frac{1}{2}} = 0$.

Proof. We start with the observation that (7.4b) yields for the mass contribution

$$\begin{aligned}
\mathbf{v}_l^{k+\frac{1}{2}} M_l^{\text{mod}} \left(\frac{\Delta \mathbf{u}_l^{k+1}}{\Delta t} - \mathbf{v}_l^k \right) &= \frac{1}{4}(\mathbf{v}_l^{k+1} + \mathbf{v}_l^k) M_l^{\text{mod}} (\mathbf{v}_l^{k+1} - \mathbf{v}_l^k) \\
&= \frac{1}{4}(\mathbf{v}_l^{k+1} M_l^{\text{mod}} \mathbf{v}_l^{k+1} - \mathbf{v}_l^k M_l^{\text{mod}} \mathbf{v}_l^k) \\
&= \frac{1}{2}(E_l^{\text{kin}})^{k+1} - \frac{1}{2}(E_l^{\text{kin}})^k,
\end{aligned}$$

and for the stiffness term

$$\begin{aligned}
\mathbf{v}_l^{k+\frac{1}{2}} A_l \left(\frac{1}{2} \Delta \mathbf{u}_l^{k+1} + \mathbf{u}_l^k \right) &= \frac{\mathbf{u}_l^{k+1} - \mathbf{u}_l^k}{2\Delta t} A_l (\mathbf{u}_l^{k+1} + \mathbf{u}_l^k) \\
&= \frac{1}{2\Delta t}(\mathbf{u}_l^{k+1} A_l \mathbf{u}_l^{k+1} - \mathbf{u}_l^k A_l \mathbf{u}_l^k) \\
&= \frac{1}{\Delta t}\big((E_l^{\text{pot}})^{k+1} - (E_l^{\text{pot}})^k\big).
\end{aligned}$$

Using $\mathbf{v}_l^{k+\frac{1}{2}}$ as the test function in (7.4a), we then obtain

$$E_l^{k+1} - E_l^k = \Delta t \mathbf{v}_l^{k+\frac{1}{2}} (\mathbf{f}_l^{k+\frac{1}{2}} - B_l \boldsymbol{\lambda}_l^{k+\frac{1}{2}}).$$

In the last step, we consider $\mathbf{v}_l^{k+\frac{1}{2}} B_l \boldsymbol{\lambda}_l^{k+\frac{1}{2}}$ in more detail. It can be decomposed into its normal and tangential contribution, *i.e.*,

$$\mathbf{v}_l^{k+\frac{1}{2}} B_l \boldsymbol{\lambda}_l^{k+\frac{1}{2}} = \mathbf{v}_l^{k+\frac{1}{2}} B_l \big((\boldsymbol{\lambda}_l^t)^{k+\frac{1}{2}} + (\boldsymbol{\lambda}_l^n)^{k+\frac{1}{2}} \big).$$

For the normal part, we find, in terms of the discrete persistency condition, which is realized by (7.4c), that it vanishes. In the case $\nu = 0$, (5.4) yields that $C_p^t(\gamma_p^{k+\frac{1}{2}}, \Delta \mathbf{u}_p^k) = (\boldsymbol{\gamma}_p^t)^{k+\frac{1}{2}}$ and thus (7.4d) guarantees that the tangential part is equal to zero for $\nu = 0$. □

7.4. Numerical results

In this subsection, we provide some numerical results which illustrate the performance of the applied mass modification. We refer to Hager *et al.* (2008), Hüeber (2008) and Hager and Wohlmuth (2009*a*) for the problem setting and parameter choices. These techniques can also be generalized to an overlapping two-scale domain decomposition approach: see Hager (2010) and Hager, Hauret, Le Tallec and Wohlmuth (2010*a*).

The introduction of the macro-element triangulation is motivated by theoretical and computational aspects. It allows a local assembling process while at the same time the properties (M0)–(M2) can easily be satisfied. Our theoretical considerations show however that the same order of convergence in the *a priori* estimates can be obtained with less restrictive assumptions: see Remark 7.5. Therefore, we use a second type of quadrature formula associated with the elements of the original mesh $\mathcal{T}_l$.

If $t \in \mathcal{T}_l$ is in Ω_{S_l}, we use a standard quadrature rule such that $\int_t \rho\phi_p\phi_q \,\mathrm{d}x$ is exactly evaluated by it. If $t \in \mathcal{T}_l$ is in S_l, we use a quadrature formula such that all nodes are placed on $\partial t \cap (\partial S_l \cap \Omega_{S_l})$. Moreover, we require that on each element constants are integrated exactly and that the resulting element mass matrices are positive semi-definite. Figure 7.11 illustrates the situation for simplicial elements in 2D.

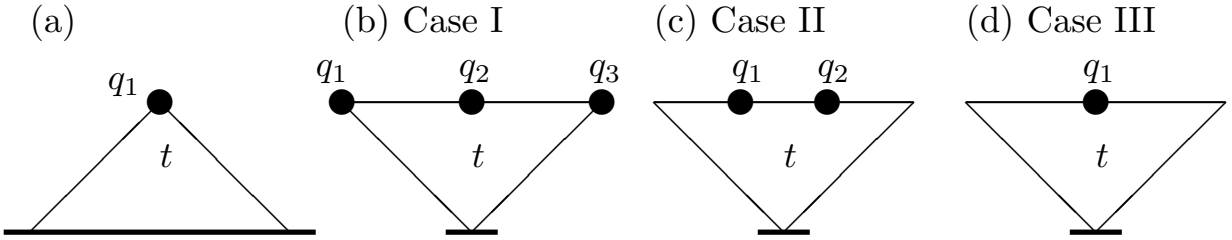

Figure 7.11. Different positions of t with respect to $\partial S_l \cap \Omega_{S_l}$.

In the situation in Figure 7.11(a), *i.e.*, the element has one face on the contact boundary, there is no other option than placing the quadrature node on the opposite vertex and setting the weight w_1 to $|t|$. If the element t shares only one vertex with $\Gamma_{\mathrm{C}}^{\mathrm{s}}$, we have several options: see Cases I–III. For Case I, we define $w_1 := w_3 := 1/12|t|$ and $w_2 := 5/6|t|$. The weights in Case II are set equal and thus are $1/2|t|$. And in Case III, we have $w_1 := |t|$. Then in all cases constant functions are integrated exactly and the local mass matrices are given by

$$M_T = \frac{|t|}{24}\begin{pmatrix} 7 & 5 & 0 \\ 5 & 7 & 0 \\ 0 & 0 & 0 \end{pmatrix}, \quad M_T = \frac{|t|}{18}\begin{pmatrix} 5 & 4 & 0 \\ 4 & 5 & 0 \\ 0 & 0 & 0 \end{pmatrix}, \quad M_T = \frac{|t|}{18}\begin{pmatrix} 1 & 1 & 0 \\ 1 & 1 & 0 \\ 0 & 0 & 0 \end{pmatrix}$$

for Case I to Case III. It is obvious that only the first two matrices have rank two and are positive semi-definite. Thus Case III is not recommended.

Associated with this type of quadrature rule, we can define an interpolation operator such that (7.2) and Lemma 7.3 hold true. As we will see in the following, this type of quadrature formula also gives rise to good numerical results and can be applied as well to obtain a stable space–time integration scheme.

Influence of the choice of the quadrature formula

In this subsection, we compare the influence of the choice of the quadrature formula on our numerical results. Figure 7.12 shows the problem setting and two different meshes. One is based on simplicial elements and the other one on quadrilaterals, which are not necessarily affine equivalent to the reference square.

Figure 7.13 shows the discrete kinetic, the potential and the total energy at time t_k. As seen in the previous subsection, the total energy is preserved for all time steps.

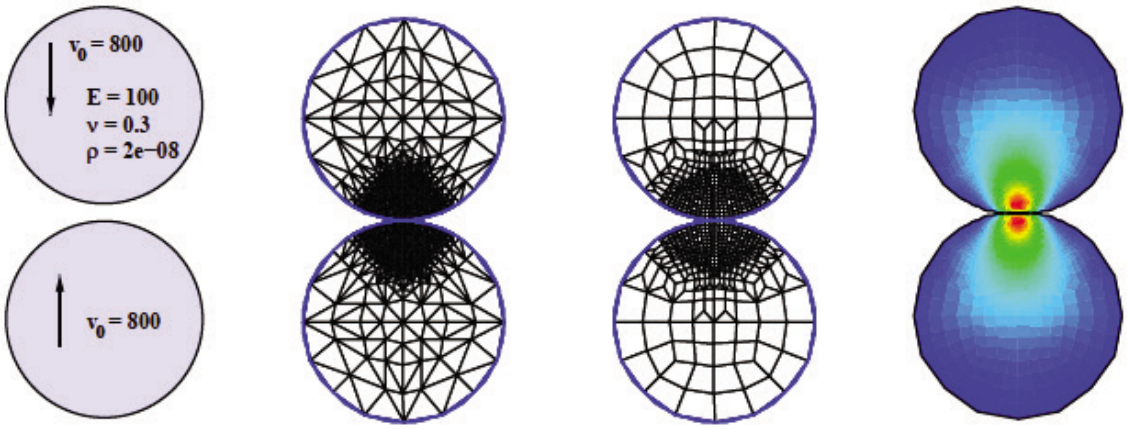

Figure 7.12. Initial grids and effective stress for a contact problem with $\nu = 0$.

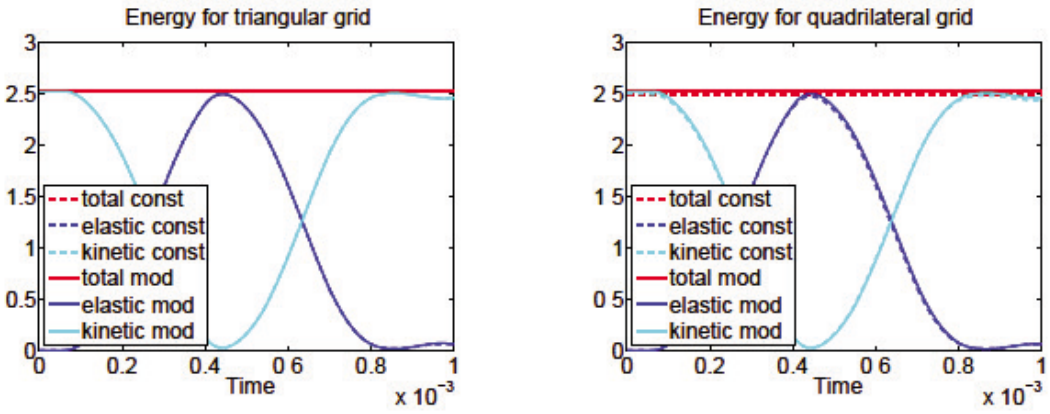

Figure 7.13. Energy results for the two-circle contact problem without friction.

As the initial conditions are given by a constant velocity and zero displacement, the total energy can be captured exactly by all our discussed quadrature rules on simplicial meshes. The situation is different for the presented quadrilateral mesh. Here, we have a non-constant Jacobian for the element mappings and thus a small difference is obtained if the simplified quadrature rule based on the original mesh is applied. However, this difference is not significant, in particular on fine meshes.

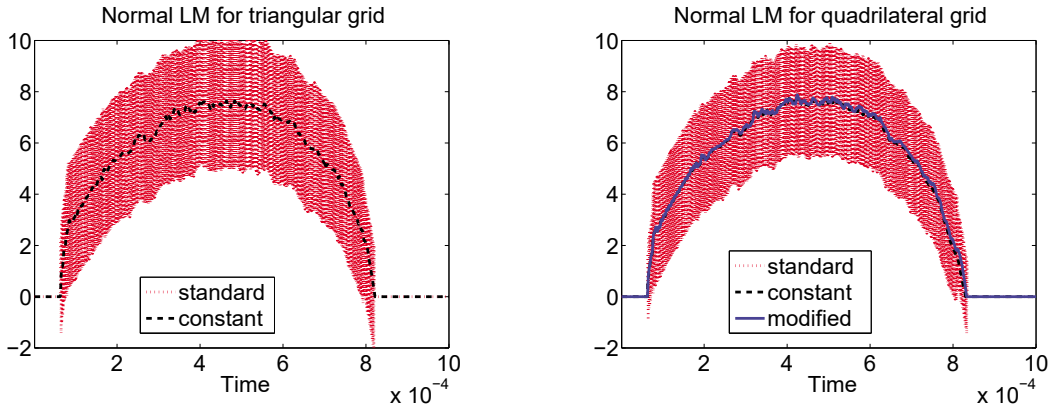

Figure 7.14. LM for simplicial and quadrilateral grid at the bottom slave node.

In Figure 7.14 we compare the results in the Lagrange multiplier. For the standard discretization with no mass modification, a highly oscillating Lagrange multiplier in the normal direction is obtained. The amplitude and frequency is rather independent of the applied mesh and is not reduced for smaller time steps. The numerical results are drastically improved if the modified mass matrix approach is applied. The numerical results do not show a significant difference between the different proposed quadrature rules.

Index reduction

In the original mass modification approach, the mass modification was only carried out with respect to the normal components. From the theoretical point of view this is sufficient to reduce the index. We recall that the algebraic constraints are given in the displacement for the non-penetration which involves the normal components. The friction law works on the tangential velocity, and these constraints result in an index-two system, which, compared to the original index-three system, has better stability properties. However, as our numerical results show, the index-two system still shows oscillations in the Lagrange multiplier.

As can be seen from Figure 7.15, only the mass modification in both directions is able to remove the oscillations from the Lagrange multiplier. However, the mass modification in the normal direction not only removes

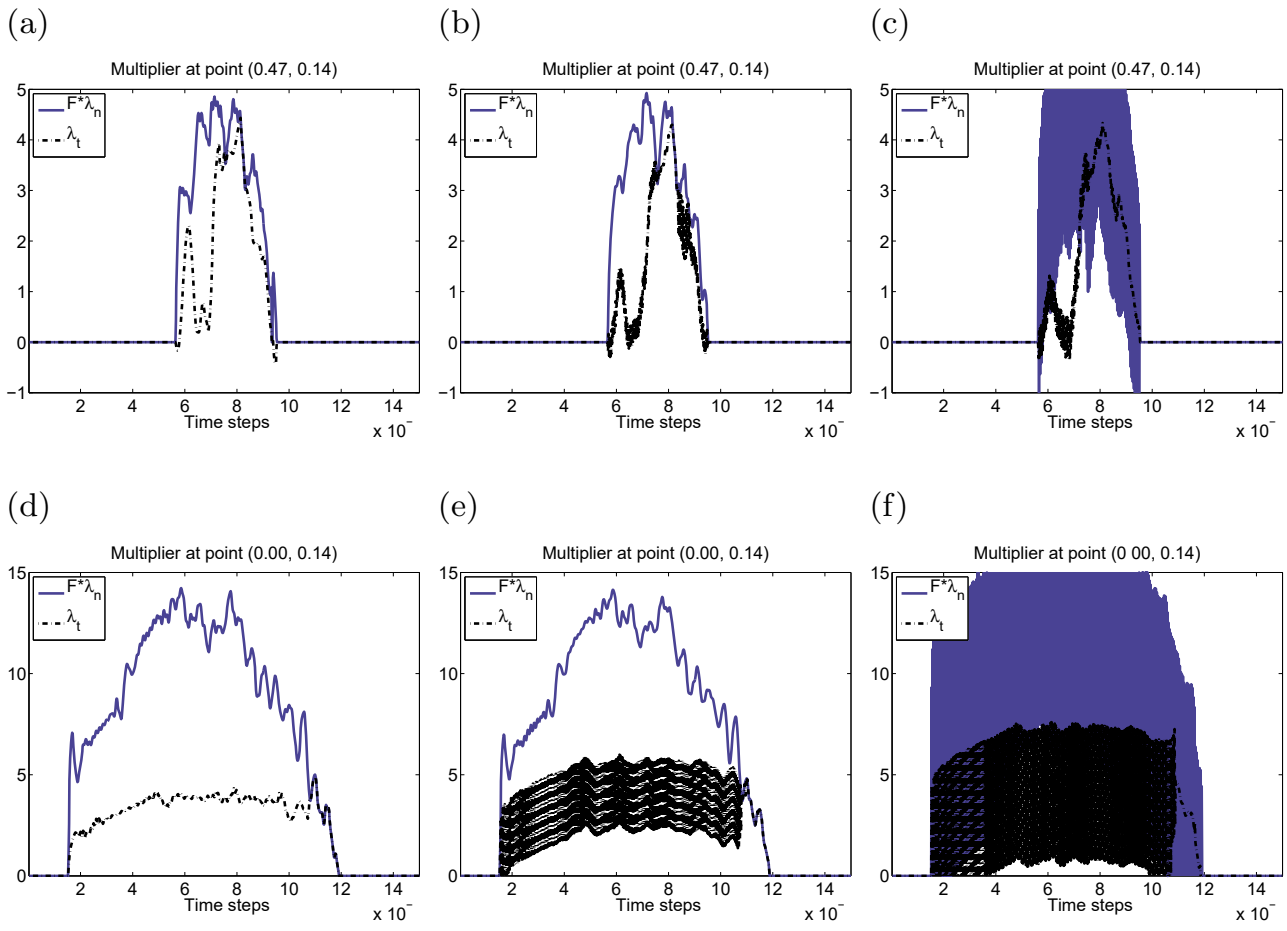

Figure 7.15. Normal and tangential Lagrange multiplier with respect to time at two different selected nodes: mass modification in both directions (a,d), in the normal direction (b,e) and no mass modification (c,f).

the oscillations in normal directions but also reduces the oscillations in the tangential direction compared to the unmodified approach.

Finite deformations

As we have seen in Section 6.8 for the adaptive refinement process, the proposed algorithms naturally generalize to finite deformations. The same holds true for the time-integration scheme. The simple Newmark method has to be replaced by a generalized scheme: see, *e.g.*, Chung and Hulbert (1993), Gonzalez (2000) and Hulbert (1992). We refer to Hesch and Betsch (2006) for a comparison between a simple node-to-node and a Lagrange multiplier-based simulation of dynamic large-deformation contact problems. Figure 7.16 shows the influence of the friction on the numerical results. We consider the two cases $\nu = 0$ and $\nu = 0.3$. In the long range the results are quite different, whereas in the short range almost no difference can be observed.

The total contact work up to time t_k is set to be equal to

$$(W_l^{\text{con}})^k := \sum_{j=0}^{k-1} \Delta t \mathbf{v}_l^{j+\frac{1}{2}} B_l(\boldsymbol{\lambda}_l^t)^{j+\frac{1}{2}}.$$

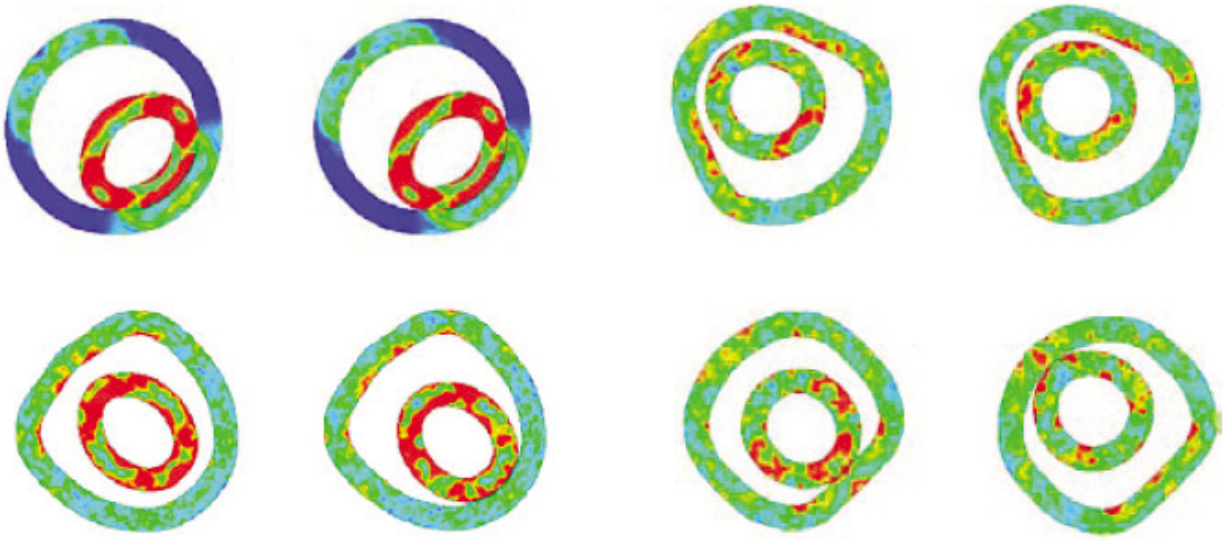

Figure 7.16. Van Mises stress at four different time steps for $\nu = 0$ and $\nu = 0.3$.

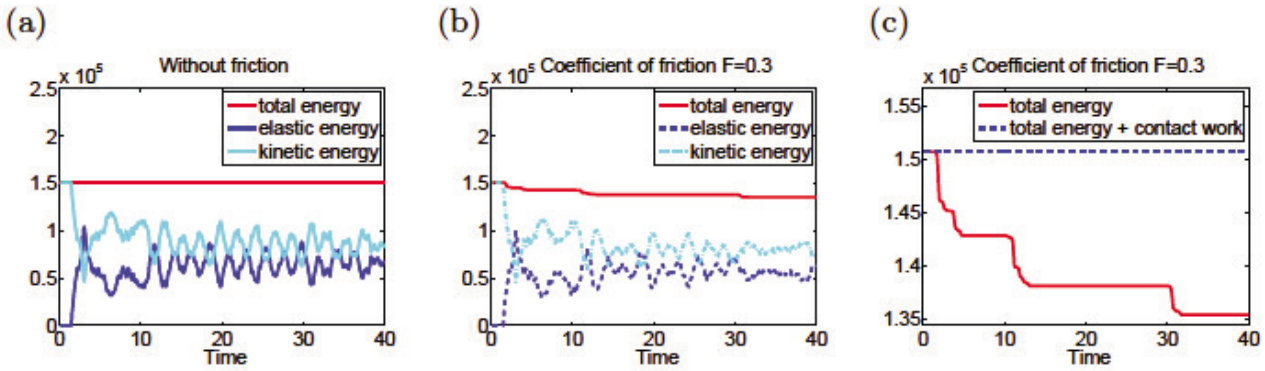

Figure 7.17. Energy $\nu = 0$ (a) and $\nu = 0.3$ (b) and contact work (c).

Then Lemma 7.7 guarantees that $E_l^k + (W_l^{\text{con}})^k$ is constant provided that there is no source term. Figure 7.17 shows the energy for the two different situations. In Figure 7.17(a), it can be seen that the total energy is constant over time. For $\nu = 0.3$, we observe that the energy is decreasing due to the loss in the friction: see Figure 7.17(b). In Figure 7.17(c), we observe that this loss is in balance with the total contact work.

Coulomb friction in the three-dimensional setting

As a final test, we consider two different three-dimensional settings and include Coulomb friction with $\nu = 0.5$. In both cases, we apply a simple quadrature formula based on the elements of the mesh $\mathcal{T}_l$, which is exact for element-wise constants and does not have nodes on $\overline{S_l} \setminus \partial\Omega_{S_l}$.

In the first setting, a ball comes in contact with a hexahedron. The evolution of the energy and the contact work is presented in Figure 7.18(a,b). Figure 7.18(c) shows the value of the Lagrange multipliers in normal direction at the lowest point of the ball over time.

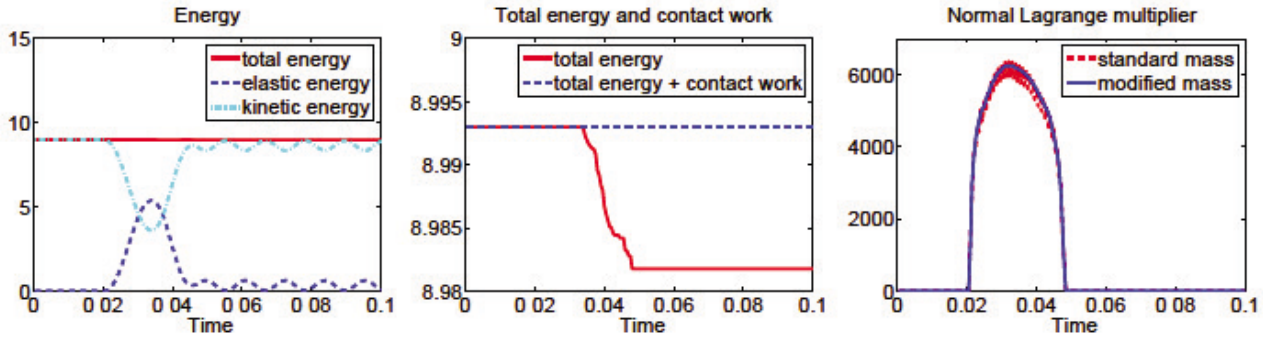

Figure 7.18. Energy (a), contact work (b) and normal Lagrange multiplier in the normal direction (c).

The last example illustrates that also for sliding geometries with many nodes in contact and a contact set which varies widely, the algorithm is numerically stable and no spurious oscillations occur.

A two-dimensional cross-section is depicted in Figure 7.19(a), and the initial condition is illustrated in Figure 7.19(b,c). Here, the outer tube is assumed to be the slave side.

In Figure 7.20 the two-dimensional cross-sections of the situations with the effective stress σ_{eff} at four different time steps are shown.

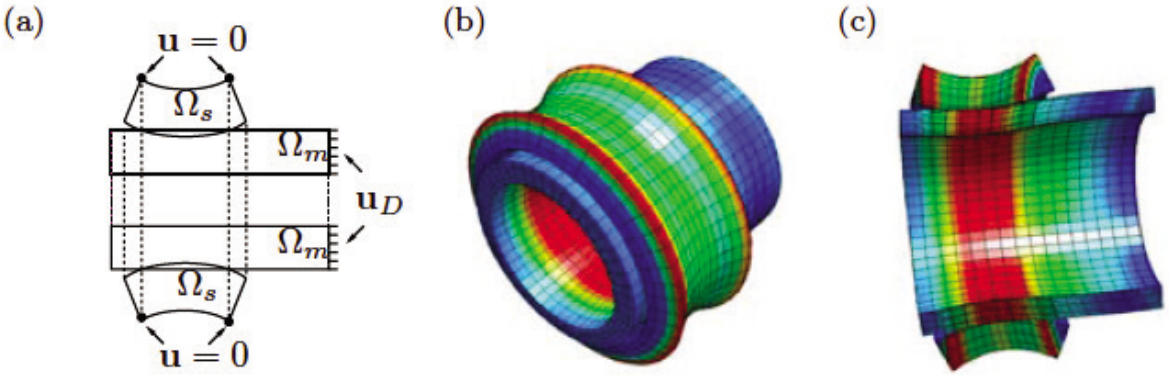

Figure 7.19. Problem definition and initial configuration $\mathbf{u}_0$ at t_0.

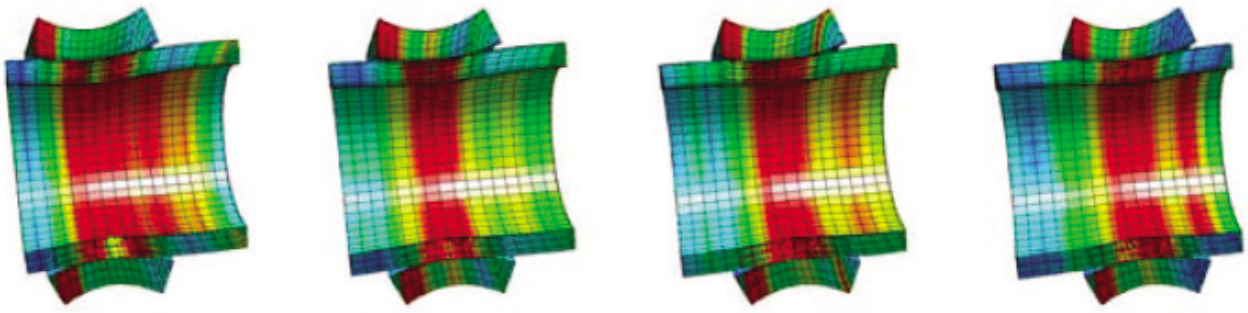

Figure 7.20. Situation at t_{15}, t_{30}, t_{45} and t_{60}.

7.5. Conclusion

Although the Lagrange multiplier-based formulation has many attractive features, it requires a careful handling of time-integration schemes. A naive application may result in high oscillation in the contact stresses and thus the non-linear solver possibly breaks down. As shown, a local modification of the mass matrix at the contact nodes in both normal and tangential directions reduces the oscillations significantly. In many applications, the quadrature rule based on the original mesh gives satisfying results and is easier to handle. On the other hand, the first- and second-order moments can only be preserved if a quadrature rule associated with a macro-triangulation is applied. We note that neither proposed mass matrix modification requires any global operator, and both fit into standard assembling procedures for finite elements. Moreover, in the case of linear elasticity problems an *a priori* analysis shows that optimal convergence can be obtained under suitable regularity, and numerical results indicate that the difference from a standard finite element scheme in space is negligible and asymptotically of higher order. The analysis follows the lines of variational crimes and standard mass lumping techniques. However, we point out that in contrast to lumping techniques, the resulting modified mass matrix is singular and thus the proof of the theoretical results is more involved and technical. From the differential-algebraic point of view the reduction of the DAE system from index three to one results in a stable algorithm.

8. Further applications from different fields

In this section, we provide some more complex applications with inequality constraints from different application areas. For each problem a brief introduction into its physical or financial interpretation is given; the details about the physical and mathematical models are, however, omitted. For each selected example, it is characteristic that the solution of a partial differential equation system has to satisfy additionally an inequality constraint. For the discretization in space we use volume- and/or surface-based Lagrange multipliers such that in space we have a variationally consistent discretization. In time, we apply a suitable finite difference scheme, possibly modified according to Section 7. As in Section 5, the fully discretized variational inequality system in terms of a pair of variables can be rewritten as a non-linear equality system. The constraints are taken nodally into account by suitable problem-dependent non-linear complementarity functions.

8.1. Mathematical finance: American options

Our first application stems from the field of financial economics. The application of a semi-smooth Newton method as a numerical solver for obstacle-

type variational inequalities obtained by the mathematical model of an American option can be found in Hager, Hüeber and Wohlmuth (2010*b*), where more numerical results are also presented, including sparse grid techniques. We refer to the monograph by Achdou and Pironneau (2005) and to Pironneau and Achdou (2009) for an introduction to mathematical models for option pricing and for a discussion of numerical and implementational issues. An American option is a contract which permits its owner to receive a certain pay-off $\psi = \psi(\mathbf{x}) \geq 0$ at any time τ between 0 and the expiry date T, depending on the value of the underlying assets $\mathbf{x}$ at time τ. In this subsection, we consider options on a set of two assets $\mathbf{x} = (x_1, x_2)$ and ask for its fair price. A simple mathematical model is based on the Black–Scholes equation (Black and Scholes 1973) and the no-arbitrage principle (Hull 2006, Wilmott, Dewynne and Howison 1997). The symmetric and positive definite volatility matrix

$$\Xi = \begin{pmatrix} \sigma_1^2 & \frac{2\varrho}{1+\varrho^2}\sigma_1\sigma_2 \\ \frac{2\varrho}{1+\varrho^2}\sigma_1\sigma_2 & \sigma_2^2 \end{pmatrix},$$

the volatilities σ_k, the correlation rate $\varrho \in (-1, 1)$, the interest rate r and the dividend rates q_k on the asset x_k, $k \in \{1, 2\}$, enter as parameters into the model. In the case of an American option, the no-arbitrage principle implies that its fair value can never be below its pay-off as the option can always be exercised. Further, a hedging argument yields that the Black–Scholes equation becomes an inequality (Hull 2006, Wilmott *et al.* 1997). Thus, the price P of an American put with pay-off function ψ satisfies the following set of conditions for $\mathbf{x} \in \mathbb{R}^2_+$, $t \in (0, T]$ with $t := T - \tau$:

$$\dot{P} - \mathcal{L}P \geq 0, \quad P - \psi \geq 0, \quad (\dot{P} - \mathcal{L}P)(P - \psi) = 0, \tag{8.1}$$

with the initial conditions $P|_{t=0} = \psi$. Here the partial differential operator $\mathcal{L}$ is given by

$$\mathcal{L} := \frac{1}{2}\sum_{k,l=1}^{2} \Xi_{k,l} x_k x_l \frac{\partial^2}{\partial x_k \partial x_l} + \sum_{k=1}^{2}(r - q_k)x_k \frac{\partial}{\partial x_k} - r. \tag{8.2}$$

To solve this problem numerically, we truncate the semi-infinite domain $\mathbb{R}^2_+$ to a bounded one $\Omega := (0, X_1) \times (0, X_2)$ and impose artificial boundary conditions on it. We refer to the monograph by Achdou and Pironneau (2005) for a discussion of possible choices for these boundary conditions depending on the pay-off function ψ. Here we apply a strategy where on the boundary a 1D variational inequality has to be solved, and the solution of it imposes appropriate Dirichlet boundary conditions at time t^i: see Hager *et al.* (2010*b*) for details.

In contrast to our contact formulations, the inequality constraints are not imposed on part of the boundary but in the domain itself. As a con-

sequence, we have to replace the surface-based Lagrange multiplier by a volume-based one, and the $H^{1/2}$-duality by the H^1-duality. However, for the numerical solution strategy, this difference does not matter. As before, we use a biorthogonal Lagrange multiplier and transform (8.1) into a non-linear equality system based on a weak variational formulation. Using low-order conforming finite elements on a family of simplicial meshes, we arrive at the discrete system in saddle-point form. Find $(\mathbf{P}_l^i, \boldsymbol{\lambda}_l^i)$,

$$\frac{1}{\Delta t} M_l(\mathbf{P}_l^i - \mathbf{P}_l^{i-1}) + \frac{1}{2} A_l(\mathbf{P}_l^i + \mathbf{P}_l^{i-1}) - D_l \boldsymbol{\lambda}_l^i = \mathbf{0}, \tag{8.3}$$

with M_l, A_l and D_l being the lumped mass, the stiffness and the diagonal duality matrix associated with the mesh on level l, respectively. Given $\mathbf{P}_l^{i-1}$, (8.3) has to be solved for $(\mathbf{P}_l^i, \boldsymbol{\lambda}_l^i)$ together with the node-wise complementarity condition

$$\boldsymbol{\lambda}_l^i - \max(0, \boldsymbol{\lambda}_l^i - c(\mathbf{P}_l^i - \boldsymbol{\psi}_l)) = \mathbf{0}, \tag{8.4}$$

where $\boldsymbol{\psi}_l$ is a finite element representation of the pay-off function on level l and c a fixed positive constant. From the algebraic point of view, there is no structural difference to a contact formulation without friction, and thus a semi-smooth Newton method can be easily applied as solver. We note that the situation here is simple. Firstly the inequality is the only source of a non-linearity, secondly the NCP function given by (8.4) is piecewise affine, and thirdly we can use the solution from the previous time step as initial guess. Thus the implementation of the solver is directly based on the equivalent primal–dual active set strategy. The adaptive refinement strategy follows the same lines as discussed in Section 6. Here two essential differences have to be taken into account. In the case of an obstacle problem, the value of the Lagrange multiplier is *a priori* known if the actual zone of contact between solution and obstacle is known. Thus this extra information can be used to redistribute element-wise the computed discrete Lagrange multiplier. Using such a post-processed Lagrange multiplier on the right side of the vertex-based equation system for the flux moments gives much better results. Details can be found in Weiss and Wohlmuth (2010).

Following the construction principle of Section 6 and applying mixed RT_0, RT_1 or BDM_1 elements will result in robust and reliable adaptive mesh refinement in the case of smooth obstacles. From the theoretical point of view, the use of RT_0 elements is sufficient. Then the divergence and the face fluxes are obtained from the right side of the PDE and the moments by the element-wise and face-wise L^2-projection onto constants, respectively. For RT_1 or BDM_1 elements, the face-wise linear moments will be exactly reproduced by the face fluxes of the mixed element. Moreover, for RT_1 elements, we obtain that the divergence is given by the element-wise L^2-projection onto polynomials of degree at most one.

However, a naive application of the proposed construction principle fails in the case of a non-smooth obstacle. To get a better understanding, we consider firstly a simple obstacle problem on the unit square where the obstacle has the form of a pyramid.

Obstacle-type problem

The obstacle is non-differentiable at the two axes. Figure 8.1(a) shows the solution and the obstacle. Ignoring the kinks in the obstacle, the definition of η_{L} results in a non-optimal estimated error decay: see Figure 8.1(b).

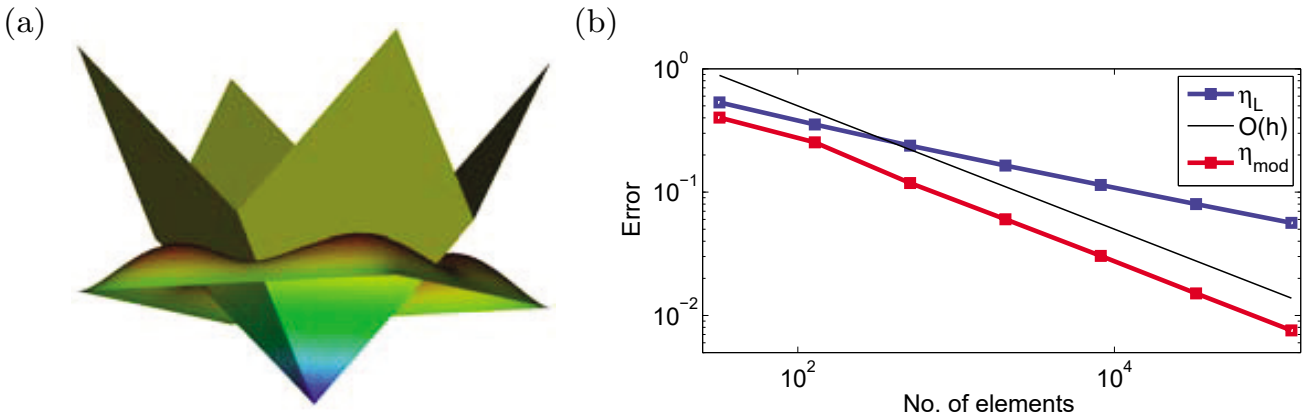

Figure 8.1. Non-smooth obstacle: obstacle and solution (a), and comparison of the unmodified and the modified estimated error (b).

To see what goes wrong, we consider additionally the adaptively refined meshes on Level 3 and Level 6. In Figure 8.2(a,b), we observe a strong over-refinement at the kinks of the obstacle, where the solution is actually in contact with the obstacle. This highly over-refined zone results from the fact that the local contribution $\eta_{\mathrm{L};T}$ measures the distance between the finite element solution and a globally $H(\mathrm{div})$-conforming mixed finite element, although the solution is not in $H(\mathrm{div};\Omega)$. Thus one cannot expect η_{L} to be efficient.

A possible remedy can be quite easily constructed. The Lagrange multiplier is additively decomposed into a volume part in $H^{-1}(\Omega)$ and an interface part in $H^{-1/2}(\gamma)$, where the obstacle ψ has kinks on γ. The interface part depends only on the obstacle and is given by the jump of its normal fluxes. Then the lifting of the fluxes is not globally $H(\mathrm{div};\Omega)$-conforming but does correctly reflect the jump. In Figure 8.2(c,d), we illustrate the positive effect of the decomposition of the Lagrange multiplier on the adaptive refinement process. In terms of the proposed modification, the estimated error in the interior of the contact zone is zero, and therefore no overestimation of the error occurs. Moreover, as can be seen in Figure 8.1(b), the obtained error decay has the correct slope.

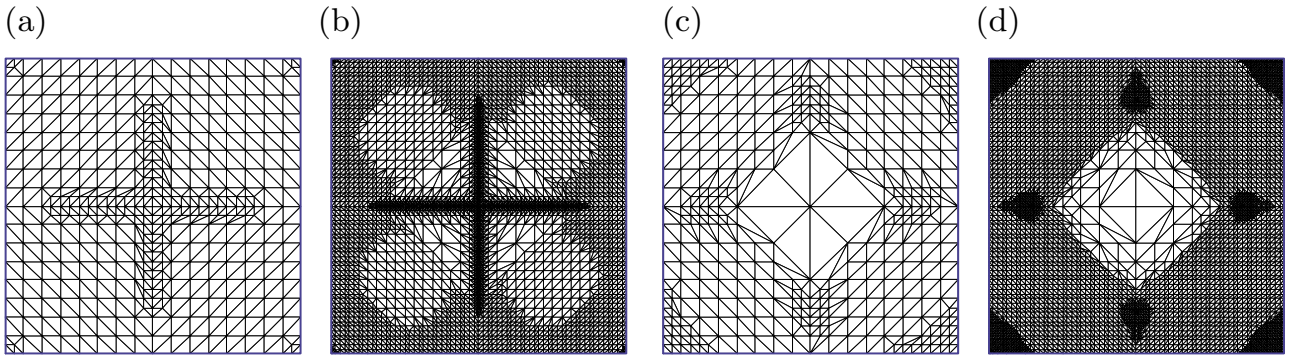

Figure 8.2. Non-smooth obstacle: refined mesh on Level 3 and Level 6, naive application of η_L (a,b) and with suitable modification (c,d).

American basket option

We are now in the setting to apply an adaptive algorithm for the numerical solution of pricing American basket options. An error estimator in space and time designed for parabolic variational inequalities with special focus on American options is introduced in Moon *et al.* (2007); see also the more recent contribution of Nochetto *et al.* (2010). As is standard for time-dependent systems, we include a coarsening strategy in the adaptive refinement process. In addition, we apply the previously discussed modification in the error indicator, because of the kinks in the pay-off function, and take note of the different structure of the PDE (8.2) compared to the Laplace operator. Two different pay-off functions are tested, $\psi_{\max} := \max(0, K - \max(x_1, x_2))$ and $\psi_{\min} := \max(0, K - \min(x_1, x_2))$, and we refer to Weiss and Wohlmuth (2010) for the problem specification.

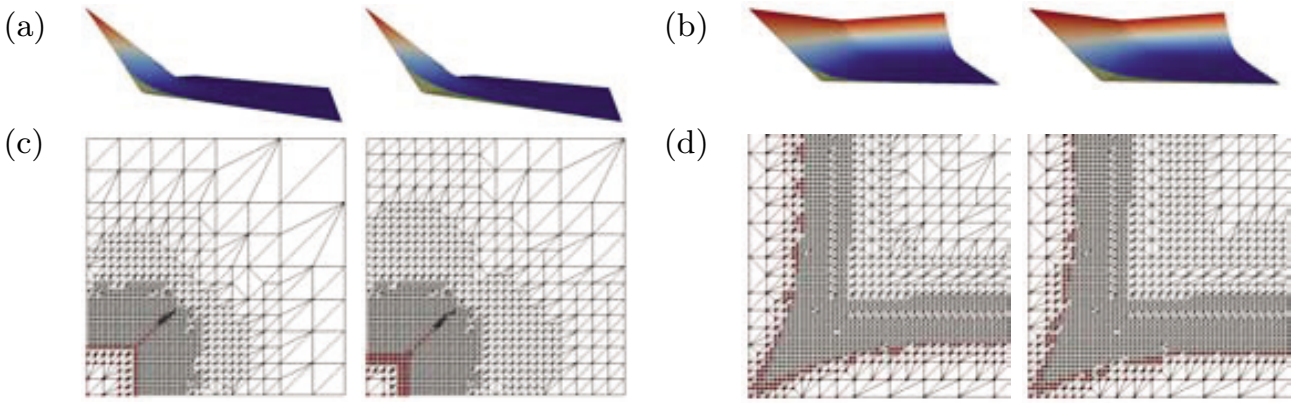

Figure 8.3. American put option: solution (a,b) and adaptive mesh (c,d) at times $t = 0.5$ and $t = 0.9$; (a,c) $\psi_{\max}$, (b,d) $\psi_{\min}$.

The adaptively refined meshes in Figure 8.3 show that the error estimator does not over-refine at the kinks of the pay-off functions and that the proposed modification also works well for much more complex situations.

8.2. Porous media: multi-phase flow problems

As second example, we consider an incompressible multi-phase flow process in porous media. Here we can identify two different sources for inequalities in the mathematical model. To simplify the notation, both of them will be described separately. The first one results from heterogeneous media and is associated with interior interfaces: see Helmig, Weiss and Wohlmuth (2009). The second one is related to a phase transition process and yields inequality constraints on the simulation domain: see Lauser, Hager, Helmig and Wohlmuth (2010).

Interface inequalities: heterogeneous media with entry pressure

The mathematical model for a two-phase one-component system we are using here lives on the macro-scale and is based on mass conservation, momentum balance and Darcy's law for each phase: see, *e.g.*, Helmig (1997). Here we consider two phases in isothermal equilibrium, the wetting phase ($\alpha = w$) and the non-wetting phase ($\alpha = n$). Originally Darcy's law was obtained for slow laminar flow of a single phase but can be easily extended to the two-phase setting by using the relative permeability (Scheidegger 1960). Then the phase velocity $\mathbf{v}_\alpha$, $\alpha \in \{w, n\}$, is given by

$$\mathbf{v}_\alpha = -\xi_\alpha(S_\alpha) K (\nabla p_\alpha - \rho_\alpha \mathbf{g}), \quad \xi_\alpha(S_\alpha) := \frac{k_{r\alpha}(S_\alpha)}{\mu_\alpha},$$

where K, $\mathbf{g}$, $k_{r\alpha}$, μ_α and ρ_α stand for the intrinsic permeability, the gravity, the relative permeability, the dynamic viscosity and the density of phase α, respectively. Moreover, p_α denotes the unknown phase pressure. Then the mass balance yields

$$\frac{\partial(\Phi \rho_\alpha S_\alpha)}{\partial t} + \operatorname{div}(\rho_\alpha \mathbf{v}_\alpha) = \rho_\alpha q_\alpha, \quad \alpha \in \{w, n\}, \tag{8.5}$$

where S_α is the unknown saturation of the phase α, Φ is the porosity, and q_α denotes the source/sink term.

To close the system, we have to add two additional relations: a capillary pressure-saturation relation, *i.e.*, $p_n - p_w = p_c(S_n)$, and a saturation balance, *i.e.*, $S_n + S_w = 1$. Here we use a non-standard dynamic capillary pressure relation including a retardation term (Hassanizadeh and Gray 1993, Hassanizadeh, Celia and Dahle 2002):

$$p_n - p_w = p_c(S_n) = p_c^{\text{stat}}(S_n) + \tau \frac{\partial S_n}{\partial t}, \quad \tau \geq 0. \tag{8.6}$$

The static capillary pressure function p_c^{stat} is assumed to be continuously differentiable, non-negative, strictly increasing and $p_c^{\text{stat}}(S_n)$ tends to p_c^{entry} for $S_n \to 0$. Typical choices for p_c^{stat} are the Brooks–Corey (Brooks and Corey 1964) or the Van Genuchten model (Van Genuchten 1980). We note

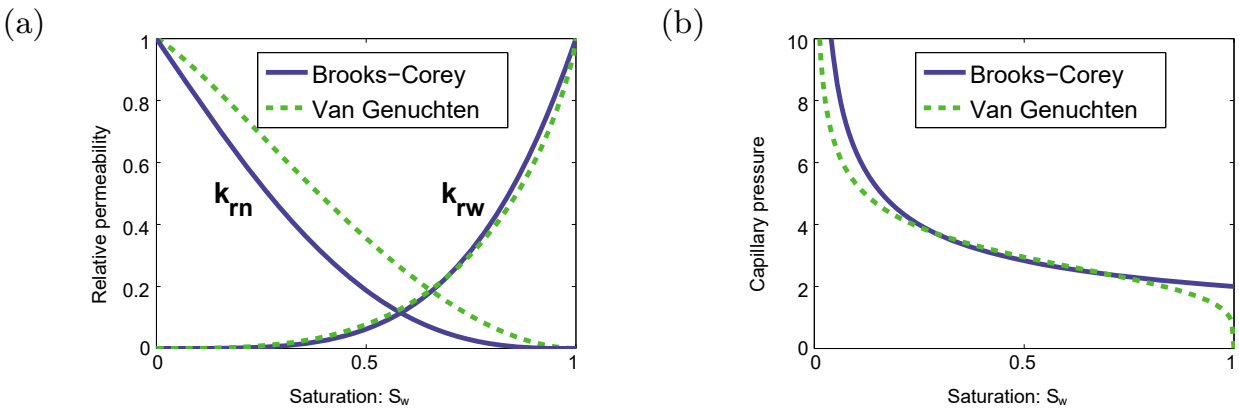

Figure 8.4. Comparison of the Van Genuchten and Brooks–Corey model: relative permeability (a) and capillary pressure (b).

that the Van Genuchten model with zero entry pressure can be regarded as a regularization of the Brooks–Corey approach (see Figure 8.4), and the parameters in both models are related (Lenhard, Parker and Mishra 1989).

Equation (8.5) for $\alpha = n$ and $\alpha = w$ yields a strongly coupled highly non-linear system. Next, we describe how the heterogeneity of the material is accounted for. For simplicity, we assume that the domain Ω is split into two subdomains Ω^{m}, Ω^{s} with the interface $\Gamma := \partial\Omega^{\mathrm{m}} \cap \partial\Omega^{\mathrm{s}}$, such that the parameters Φ and K are constant on each subdomain. Further, the domains are chosen such that the master subdomain has a lower entry pressure, *i.e.*, a higher relative permeability, than the slave domain. The flow at the interface Γ has to be modelled correctly. Here, we describe only the more interesting case when the non-wetting phase penetrates into the subdomain with the higher entry pressure. The mathematical model introduced in de Neef (2000) gives rise to the following transmission conditions at the material interface:

$$[p_c] \geq 0, \quad S_n^{\mathrm{s}} \geq 0, \quad [p_c] S_n^{\mathrm{s}} = 0, \tag{8.7}$$

where $S_n^{\mathrm{s}} = 1 - S_w^{\mathrm{s}}$ stands for the saturation of the non-wetting phase on the slave side, and $[p_c]$ denotes the jump of the capillary pressure. Then, (8.7) states that the capillary pressure at the interface is continuous if the non-wetting phase is present on the side with the higher entry pressure.

In order to solve the above problem numerically, we apply a node-centred conservative finite volume scheme in space in combination with upwind techniques: see Huber and Helmig (2000). We remark that the meshes used do not need to be matching at the interface Γ. Then, in terms of the mortar projection, we can define node-wise inequality constraints for the saturation S_n and the capillary pressure p_c on the slave side. In contrast to the previous application, the non-linearity of the system is not restricted to the inequality constraints (8.7). A popular approach to reduce the complexity is based on a fractional flow formulation. It is equivalent to the original system but can be more efficiently solved by block decoupling strategies. In the case of the

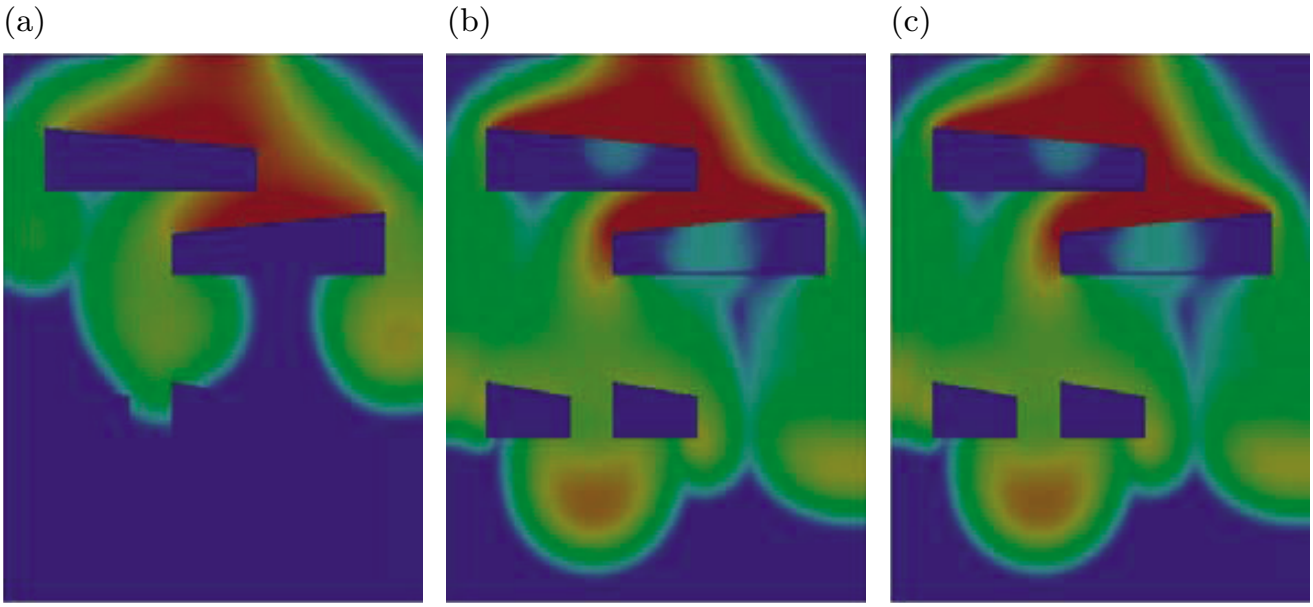

Figure 8.5. Comparison of different time-integration and decoupling schemes.

classical fractional flow formulation, the total velocity $\mathbf{v}_t$ is introduced by $\mathbf{v}_t := \mathbf{v}_w + \mathbf{v}_n$. Then a coupled but considerably simplified system with a much more moderate non-linearity is obtained for the so-called global pressure and the saturation: see, *e.g.*, Binning and Celia (1999), Chavent and Jaffré (1986), Rivière (2008) and Wooding and Morel-Seytoux (1976). Here, we cannot directly apply this approach since the interface model has no equivalence in terms of the non-physical variable of the global pressure. We work with an alternative fractional flow formulation which is based on a pressure equation for p_w and a saturation equation for S_w. The interface condition is then directly formulated in these primary variables, and we obtain, by replacing (8.7) by the equality to zero of an NCP function, a fully coupled system for (p_w, S_w) having possibly two different pressure values on the interface.

For the discretization in time, different strategies can be applied; see Figure 8.5 for a comparison of the numerical results. Here, we illustrate the algorithm for a matrix with three inclusions of lower relative permeability. In Figure 8.5(a), the wetting velocity $\mathbf{v}_w$ is not at all updated in time, resulting in a significant different solution compared to the two alternative approaches shown in Figure 8.5(b,c). This strategy is the most simple one, and we have to solve in a pre-process a linear elliptic pressure equation and then in each time step a non-linear equation for the saturation. In Figure 8.5(b), the fully non-linear and coupled system for the pressure and saturation is solved by an implicit Euler scheme. This approach is the most expensive one since in each time step a fully coupled system has to be solved, where the non-linearities result from the PDE and the inequality constraints at the interfaces. In Figure 8.5(c) a suitable decoupling strategy is applied. An explicit time integration is used for the pressure equation, whereas an im-

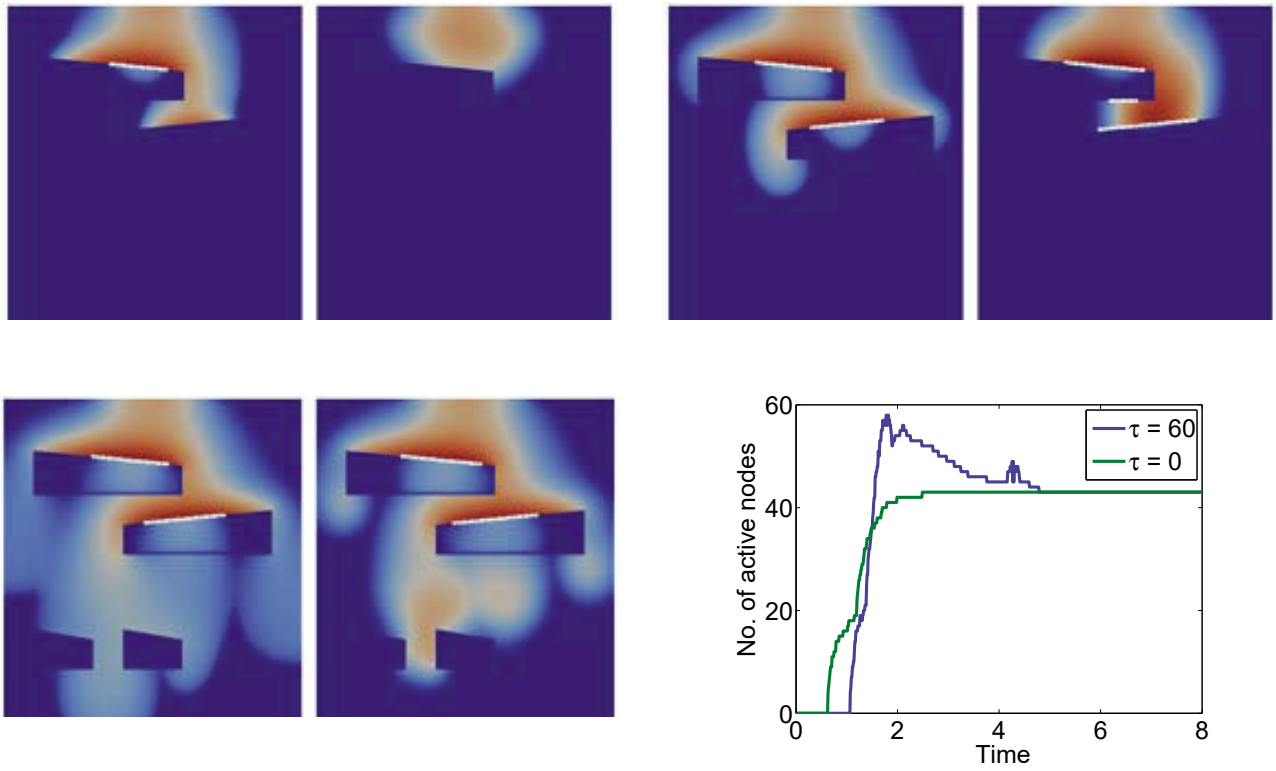

Figure 8.6. Pair of solutions for $\tau = 0$ and $\tau = 60$ at three different time steps and number of active nodes with respect to time.

plicit scheme is selected for the saturation equation. This explicit–implicit method can also be regarded as one step of a non-linear block Gauss–Seidel solver applied to the fully coupled implicit time-integration system. As can be seen, this inexact approach is quite attractive. It gives highly accurate results and is considerably less expensive than the solution of the fully coupled system. The sequential solution of a linear pressure equation and a non-linear saturation equation is required.

Figure 8.6 shows the influence of the dynamic parameter τ on the solution and on the active set. Here we denote the faces on which we have continuity of the pressure as active and mark these faces by white squares. In the short and middle time range there is a significant difference in the results. First of all, a non-zero τ has a retardation effect on the wave front. Thus the penetration of the non-wetting phase into the subdomains with lower regularity starts later, and in the short range we observe a smaller number of active faces. Secondly, due to the dynamic capillary pressure, a non-monotonous wave profile is created with a sharper wave front, resulting in a larger active set in the middle time range. In the long range, we will reach a stationary equilibrium, and thus there is no difference between $\tau = 0$ and $\tau = 60$. This is reflected by the fact that, for sufficiently large times, the number of active faces is equal.

So far we have described the mathematical model of a heterogeneous material interface resulting in a surface-based inequality. In the next step, we describe how a volume-based inequality enters into the model.

Volume inequalities: phase transition processes

We now extend the model from the simple two-phase one-component situation to an Mp–Nc system with N different components and with M different phases. In the following, we use the lower index $\alpha = 1, \ldots, M$ for the phase, ordered by their wettability, *i.e.*, $\alpha = 1$ denotes the gas phase, and the upper index $j = 1, \ldots, N$ stands for the component. Assuming that the fugacity of any component is the same in all phases, we have *a priori* $MN + 2M + N + 1$ unknowns. As before, p_α and S_α stand for the phase pressure and for the saturation of phase α, $\alpha = 1, \ldots, M$. In addition, we have for a non-isothermal system the temperature T. Related to the different components is the fugacity f^j and the mole fraction x_α^j of component j in phase α, $j \in \{1, \ldots, N\}$, $\alpha \in \{1, \ldots, M\}$. We refer to Acosta, Merten, Eigenberger, Class, Helmig, Thoben and Müller-Steinhagen (2006), Class and Helmig (2002), Class, Helmig and Bastian (2002) and Niessner and Helmig (2007) for the description of general non-isothermal multi-phase systems. For each component one mass balance equation has to hold, and for the temperature the energy balance equation has to be satisfied, resulting in a coupled highly non-linear system of $(N + 1)$ partial differential equations. In addition to the coupled PDE system, we have to observe suitable constitutive relations, such as, for the saturations,

$$\sum_{\alpha=1}^{M} S_\alpha = 1, \tag{8.8}$$

and for the phase pressures p_α,

$$p_{\alpha-1} - p_\alpha = p_{c,(\alpha-1)\alpha}, \quad 2 \leq \alpha \leq M,$$

with the capillary pressure $p_{c,(\alpha-1)\alpha} = p_{c,(\alpha-1)\alpha}(S_\alpha)$ depending on the saturation S_α of the phase with higher wettability (Niessner and Helmig 2007). As in the first example (see (8.6)), different models can be used to define $p_{c,(\alpha-1)\alpha}(\cdot)$. In addition MN constitutive relations between fugacities and mole fractions have to be provided. These relations are in general quite complex and rely on additional assumptions on the nature of the system. In many applications from these relations, we can completely eliminate f^j and obtain the mole fractions x_α^j, $1 \leq j \leq N$ and $2 \leq \alpha \leq M$ explicitly in terms of p_1, x_1^j, $1 \leq j \leq N$, T, *i.e.*,

$$x_\alpha^j = g_\alpha^j(p_1, x_1^1, \ldots, x_1^N, T), \quad 1 \leq j \leq N,\ 2 \leq \alpha \leq M \tag{8.9}$$

with some given functions $g(\cdot)$ depending on the law of Henry and Raoult (Class 2001).

In terms of the constitutive equations, the number of unknowns can then be reduced from $MN + 2M + N + 1$ to $M + N + 1$. One possibility is to set the pressure of the gas phase, its mole fractions with respect to the N

components, $M-1$ saturations and the temperature as primary variables $\mathbf{X}$:

$$\mathbf{X} := \big(p_1, x_1^1, \ldots, x_1^N, S_2, \ldots, S_M, T\big). \tag{8.10}$$

To close the $(N+1)$-dimensional PDE system, we have to include compatibility conditions for the different phases. The component sum of the mole fractions x_α^j is equal to one if the phase α is actually present, *i.e.*, $S_\alpha > 0$. This observation yields the following complementarity conditions:

$$1 - \sum_{j=1}^{N} x_\alpha^j \geq 0, \quad S_\alpha \geq 0, \quad S_\alpha \left(1 - \sum_{j=1}^{N} x_\alpha^j\right) = 0, \quad 1 \leq \alpha \leq M, \tag{8.11}$$

where we have included the physical condition of a non-negative saturation. Replacing the inequality constraints (8.11) by the equivalent form

$$\hat{C}_\alpha(S_\alpha, x_\alpha^1, \ldots, x_\alpha^N) := S_\alpha - \max\left(0, S_\alpha - c_\alpha\left(1 - \sum_{j=1}^{N} x_\alpha^j\right)\right) = 0 \tag{8.12}$$

with a fixed positive constant $c_\alpha > 0$, we obtain a highly non-linear system. Although at first glance the derivatives of the non-complementarity function seem to be as easy to calculate as those in the case of the normal contact conditions of Section 5, there is an essential difference. We note that in (8.12), the NCP functions $\hat{C}_\alpha$, $1 \leq \alpha \leq M$, depend on all variables and not only on the primary variable $\mathbf{X}$. All unknowns that are not a primary variable (see (8.10)) have to be replaced by (8.8) and (8.9) before the Newton scheme is applied, and thus the partial derivatives of $g_\alpha^j(\cdot)$ appear. In the primary variable $\mathbf{X}$, we thus define the NCP function

$$C(\mathbf{X}) := \begin{pmatrix} (1 - \sum_{j=1}^{N} x_1^j) \\ (S_\alpha)_{\alpha=2}^{M} \end{pmatrix}$$

for $\mathbf{X}$ such that $S_\alpha - c_\alpha(1 - \sum_{j=1}^{N} g_\alpha^j(\mathbf{X})) \leq 0$ for $2 \leq \alpha \leq M$, and otherwise we set

$$C(\mathbf{X}) := \begin{pmatrix} 1 - \sum_{\alpha=2}^{M} S_\alpha - \max(0, 1 - \sum_{\alpha=2}^{M} S_\alpha - c_1(1 - \sum_{j=1}^{N} x_1^j)) \\ (S_\alpha - \max(0, S_\alpha - c_\alpha(1 - \sum_{j=1}^{N} g_\alpha^j(\mathbf{X}))))_{\alpha=2}^{M} \end{pmatrix}.$$

Let us consider now the more simple case of a two-phase two-component system, where the phase index $\alpha = 1$ stands for the non-wetting phase and $\alpha = 2$ denotes the wetting phase. Moreover, we assume that component $j = 1$ is air and $j = 2$ is water. In this simplified setting, we have three PDEs to satisfy, two NCP functions have to be zero, and the primary variables are $\mathbf{X} = (p_1, x_1^1, x_1^2, S_2, T)$. Assuming the gas phase behaves as an ideal gas, the fugacities are given by

$$f^1 = x_1^1 p_1, \quad f^2 = x_1^2 p_1.$$

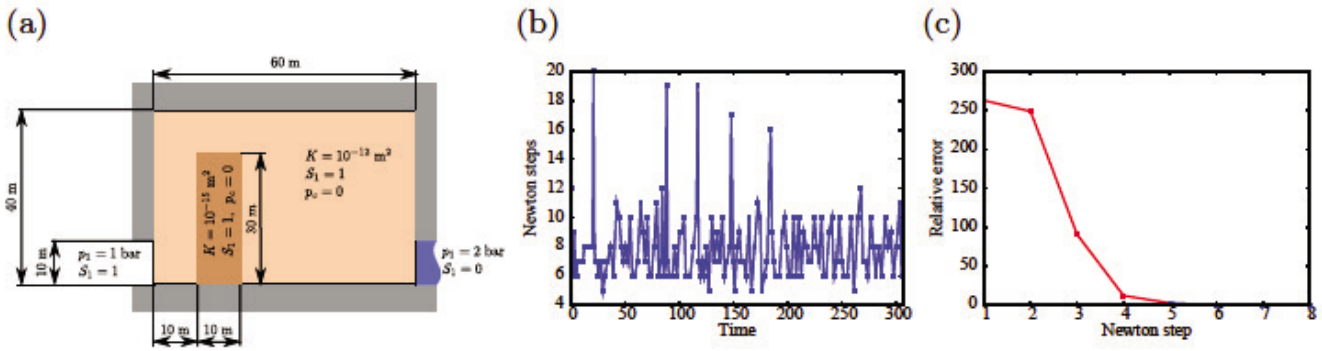

Figure 8.7. (a) Problem setting, (b) Newton iterations with respect to time and (c) error decay within one time step.

In terms of Raoult's law we get, by assuming that x_2^2 is close to one,

$$f^2 = p_{\text{vap}}^2 x_2^2 \quad \text{and thus} \quad x_2^2 = \frac{f^2}{p_{\text{vap}}^2} = \frac{p_1}{p_{\text{vap}}^2} x_1^2. \tag{8.13}$$

Here $p_{\text{vap}}^2 = p_{\text{vap}}^2(T)$ stands for the vapour pressure of water. To obtain x_2^1, we use Henry's law with the Henry coefficient $H_2^1 = H_2^1(T)$:

$$f^1 = H_2^1 x_2^1 \quad \text{and thus} \quad x_2^1 = \frac{f^1}{H_2^1} = \frac{p_1}{H_2^1} x_1^1. \tag{8.14}$$

Using (8.13) and (8.14), we obtain the explicit form for $g_2^1(\cdot)$ and $g_2^2(\cdot)$:

$$g_2^1(p_1, x_1^1, x_1^2, S_2, T) = \frac{p_1 x_1^1}{H_2^1(T)}, \quad g_2^2(p_1, x_1^1, x_1^2, S_2, T) = \frac{p_1 x_1^2}{p_{\text{vap}}^2(T)}.$$

Furthermore, we consider the simplified model of a constant temperature, *i.e.*, the Henry coefficient and the vapour pressure are constant. In the kth Newton step, we then have to consider the following three cases.

- If $\mathbf{X}^{k-1}$ such that

$$I_2^{k-1} := S_2^{k-1} - c_2 \left(1 - \frac{p_1^{k-1} (x_1^1)^{k-1}}{H_2^1} - \frac{p_1^{k-1} (x_1^2)^{k-1}}{p_{\text{vap}}^2} \right) \leq 0,$$

  then

$$\begin{pmatrix} (x_1^1)^k + (x_1^2)^k & = & 1 \\ S_2^k & = & 0 \end{pmatrix}.$$

- If $\mathbf{X}^{k-1}$ such that $I_2^{k-1} > 0$ and

$$I_1^{k-1} := 1 - S_2^{k-1} - c_1 (1 - (x_1^1)^{k-1} - (x_1^2)^{k-1}) \leq 0,$$

  then

$$\begin{pmatrix} S_2^k & = & 1 \\ \frac{p_1^{k-1} (x_1^1)^k}{H_2^1} + \frac{p_1^{k-1} (x_1^2)^k}{p_{\text{vap}}^2} & = & 1 - \left(\frac{(x_1^1)^{k-1}}{H_2^1} + \frac{(x_1^2)^{k-1}}{p_{\text{vap}}^2} \right) (p_1^k - p_1^{k-1}) \end{pmatrix}.$$

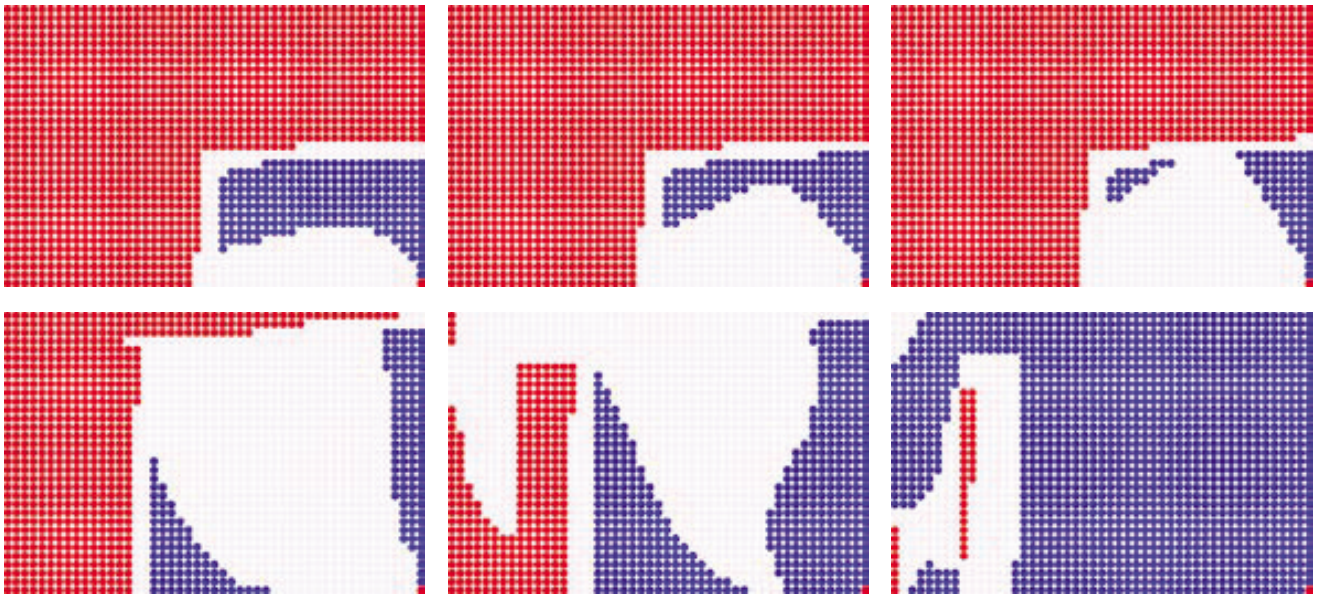

Figure 8.8. Evolution of the different 'active' zones.

- If $\mathbf{X}^{k-1}$ such that $I_2^{k-1} > 0$ and $I_1^{k-1} > 0$, then

$$\begin{pmatrix} (x_1^1)^k + (x_1^2)^k & = & 1 \\ \frac{p_1^{k-1}(x_1^1)^k}{H_2^1} + \frac{p_1^{k-1}(x_1^2)^k}{p_{\text{vap}}^2} & = & 1 - \left(\frac{(x_1^1)^{k-1}}{H_2^1} + \frac{(x_1^2)^{k-1}}{p_{\text{vap}}^2} \right) (p_1^k - p_1^{k-1}) \end{pmatrix}.$$

Figure 8.7 shows the geometry of the problem considered and the performance of the semi-smooth Newton applied to the fully coupled non-linear PDE system enriched by the algebraic NCP functions. Here, a polynomial capillary pressure function has been used: see Leverett (1941).

In Figure 8.8, we plot the three possible cases for different time steps. The light grey circles mark the region where both phases are present. The dark grey ones show the region where only the water phase is present, and the grey ones mark the region where only the gas phase is present. During the simulation the gas phase is more and more displaced by the water phase.

For a similar example in 2D and a more realistic three-phase seven-component example in 3D simulating the injection of CO_2 into the soil and the subsequent extraction of methane, we refer to Lauser *et al.* (2010).

8.3. Structural mechanics: frictional contact of elasto-plastic bodies

Our final example is the modelling of frictional contact between several elasto-plastic bodies (Hager and Wohlmuth 2009*b*). This application includes several pairs of complementarity conditions, a volume-based one describing the plastification process, and a surface-based one for the contact. We restrict ourselves to infinitesimal associative plasticity and linear hardening and point out that the framework is much more general and can be extended to non-linear material or hardening laws (Han and Reddy 1995, Han and Reddy 1999, Simo and Hughes 1998). We refer to Wieners and Wohlmuth (2011) for an application of a semi-smooth Newton

solver to non-local gradient plasticity. In contrast to linear elasticity, the stress is now decomposed additively into an elastic and plastic part

$$\boldsymbol{\sigma} := \mathcal{C}\boldsymbol{\varepsilon}^{\mathrm{el}} := \mathcal{C}(\boldsymbol{\varepsilon}(\mathbf{u}) - \boldsymbol{\varepsilon}^{\mathrm{pl}}),$$

where $\boldsymbol{\varepsilon}^{\mathrm{pl}}$ is assumed to be symmetric and trace-free. Now both contact and plasticity can be formulated within the same abstract framework. Here we use a combination of Tresca and Coulomb law with the friction bound given by $\mathcal{F} + \nu\lambda_n$ and apply the rules for linear isotropic or kinematic hardening, respectively. To see the structure, we recall on the left the contact and on the right we introduce the plasticity setting:

$$\boldsymbol{\lambda} := -\boldsymbol{\sigma}\mathbf{n}, \qquad \boldsymbol{\eta} := \operatorname{dev}\boldsymbol{\sigma} - a_0^{-2} K\boldsymbol{\varepsilon}^{\mathrm{pl}}, \tag{8.15a}$$

$$\begin{aligned} Y^{\mathrm{co}}(\lambda_n) &:= \mathcal{F} + \nu\lambda_n, & Y^{\mathrm{pl}}(\alpha) &:= a_0^{-1}(\sigma_0 + H\alpha), \\ f^{\mathrm{co}}(\lambda_n, \boldsymbol{\lambda}_t) &:= \|\boldsymbol{\lambda}_t\| - Y^{\mathrm{co}}(\lambda_n), & f^{\mathrm{pl}}(\alpha, \boldsymbol{\eta}) &:= \|\boldsymbol{\eta}\| - Y^{\mathrm{pl}}(\alpha), \end{aligned} \tag{8.15b}$$

$$\dot{\mathbf{u}}_t\|\boldsymbol{\lambda}_t\| = \gamma^{\mathrm{co}}\boldsymbol{\lambda}_t, \qquad \dot{\boldsymbol{\varepsilon}}^{\mathrm{pl}}\|\boldsymbol{\eta}\| = \gamma^{\mathrm{pl}}\boldsymbol{\eta}, \tag{8.15c}$$

$$\begin{aligned} \gamma^{\mathrm{co}} &\geq 0, & \gamma^{\mathrm{pl}} &\geq 0, \\ -f^{\mathrm{co}}(\lambda_n, \boldsymbol{\lambda}_t) &\geq 0, & -f^{\mathrm{pl}}(\alpha, \boldsymbol{\eta}) &\geq 0, \\ \gamma^{\mathrm{co}} f^{\mathrm{co}}(\lambda_n, \boldsymbol{\lambda}_t) &= 0, & \gamma^{\mathrm{pl}} f^{\mathrm{pl}}(\alpha, \boldsymbol{\eta}) &= 0, \end{aligned} \tag{8.15d}$$

$$\begin{aligned} \lambda_n &\geq 0, \\ g(\mathbf{u}) := g_n - u_n &\geq 0, \\ \lambda_n g(\mathbf{u}) &= 0, \end{aligned} \qquad \dot{\alpha} = a_0^{-1}\gamma^{\mathrm{pl}}. \tag{8.15e}$$

Comparing the contact relations with the rules of plasticity, many parallels can be seen. In (8.15a), the dual variable $\boldsymbol{\lambda}$ for the contact and the inner variable $\boldsymbol{\eta}$ for the plasticity is given. The yield functions defined in (8.15b) have the same structure, and depend on the friction parameters $\mathcal{F}$ and ν and the hardening parameter H and the yield stress σ_0, respectively. The flow rule specified in (8.15c) imposes in each case a condition on the direction. Furthermore, the yield function f^{pl} and the consistency parameter γ^{pl} satisfy the same complementarity conditions (8.15d) as f^{co} and γ^{co}. The constant scaling factor $a_0^2 := \frac{d}{d-1}$ is used in order to have a consistent notation for both the two- and three-dimensional case.

One of the main differences between the conditions for contact and plasticity is the evolution law (8.15e), which causes the plasticity law to be associative, in contrast to the complementarity conditions for the normal contact.

The discrete version of the system is derived similarly to the previous examples. The plastic inner variables $(\alpha, \boldsymbol{\varepsilon}^{\mathrm{pl}})$ are approximated by the discrete space $\mathbf{Q}_h^{\mathrm{pl}}$, spanned by the piecewise constant indicator functions χ_T, $T \in \mathcal{T}_l$. Hence we have one degree of freedom per element, which is a special case of the widely used approach associating the plastic variables with

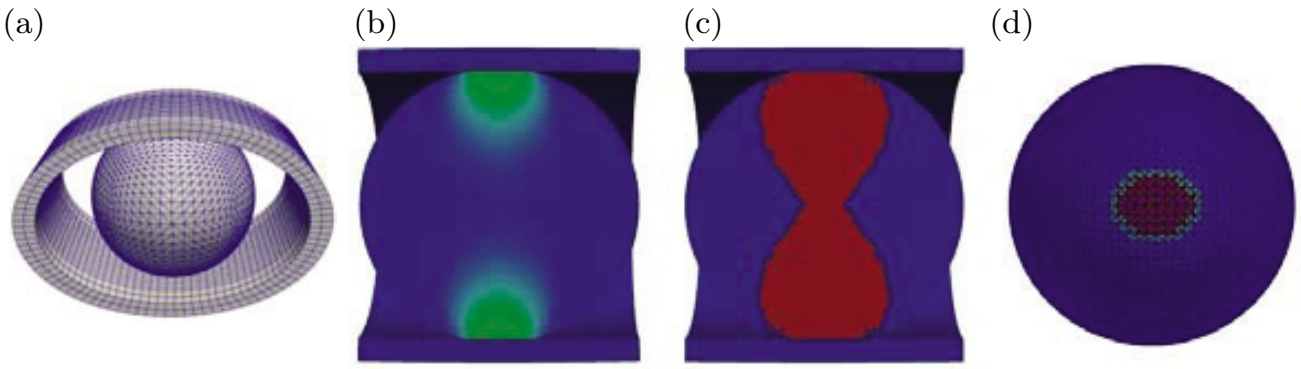

Figure 8.9. (a) Geometry, (b) inner variable, (c,d) active sets.

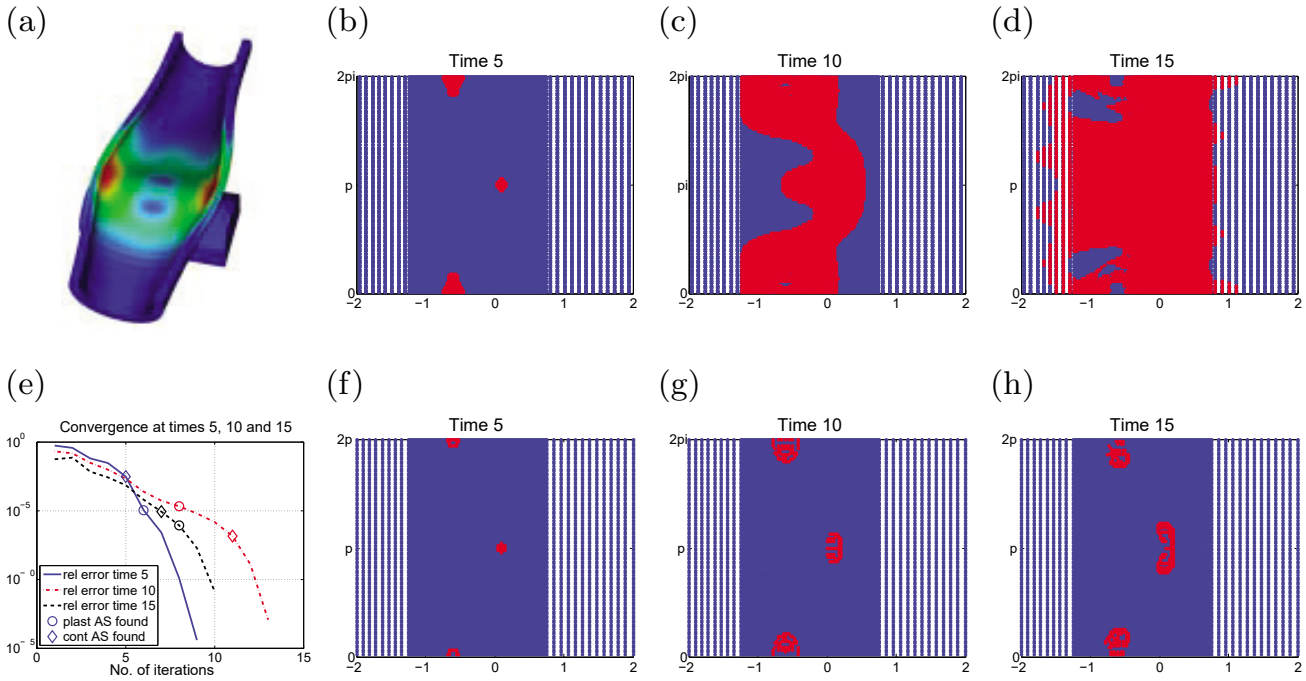

Figure 8.10. (a) Section view of the geometry; (b–d) active sets for plasticity; (e) convergence history; (f–h) active sets for contact.

Gauss integration points (Simo and Hughes 1998, Wieners 2007). We refer to Alberty, Carstensen and Zarrabi (1999) for the convergence analysis of a similar discretization. This leads to the discrete inner variables

$$\alpha_l = \sum_{T\in\mathcal{T}_l} \chi_T \alpha_T, \quad \boldsymbol{\varepsilon}_l^{\mathrm{pl}} = \sum_{T\in\mathcal{T}_l} \chi_T \boldsymbol{\varepsilon}_T^{\mathrm{pl}}, \quad \operatorname{dev} \boldsymbol{\sigma}_l = 2\mu \sum_{T\in\mathcal{T}_l} \chi_T \operatorname{dev} (\boldsymbol{\Pi}_0 \boldsymbol{\varepsilon}(\mathbf{u}_l)_T),$$

on which the definition of the NCP function is based. Because of the similar structure of contact and plasticity, all results of Section 5 can be applied.

We apply these discretization techniques to two examples in the three-dimensional setting. In Figure 8.9, the stress and the active sets are illustrated. Here we have the plastification as well as the contact zone. The geometry of the setting is shown in Figure 8.9(a). Figure 8.9(d) illustrates the contact zone whereas in Figure 8.9(c) the region with plastification is depicted.

In Figure 8.10, we apply an exponential hardening law, and thus an extra source of non-linearity appears. Figure 8.10(b–d) shows the nodes where plastification occurs for three different time steps. The volume nodes are projected onto the surface. In Figure 8.10(f–h), we show the actual contact nodes. Here we provide the results for t_5, t_{10} and t_{15}; the results for t_3, t_6 and t_9 are given in Hager and Wohlmuth (2010), where details on the problem specification can also be found.

In Figure 8.10(e), we show the convergence history of the semi-smooth Newton method. The iteration in which the correct active sets are detected for the first time are marked by a circle for plasticity and by a diamond for contact. We point out that it depends on the time step which set is found first. For all time steps a super-linear convergence rate can be observed.

8.4. Conclusion

In this section, we have illustrated that variationally consistent Lagrange multiplier formulations for PDE systems with algebraic constraints provide a flexible and powerful discretization technique. Of special interest are applications where both types of constraint, surface- and volume-based, enter into the setting. Both types can be handled within the same abstract framework of generalized saddle-point-type problems. The use of NCP functions allows a consistent linearization of the inequality constraints and is thus of special interest in combination with Newton-type solvers. Global convergence can only be guaranteed in special situations; however, for most problems local super-linear convergence is obtained. Rescaling of the NCP function and regularization of the Jacobian might significantly improve the robustness of non-linear solvers in the pre-asymptotic range.

REFERENCES

Y. Achdou and O. Pironneau (2005), *Computational Methods for Option Pricing*, SIAM.

M. Acosta, C. Merten, G. Eigenberger, H. Class, R. Helmig, B. Thoben and H. Müller-Steinhagen (2006), 'Modeling non-isothermal two-phase multicomponent flow in the cathode of PEM fuel cells', *J. Power Sour.* **159**, 1123–1141.

R. Adams (1975), *Sobolev Spaces*, Academic Press.

J. Ahrens, B. Geveci and C. Law (2005), ParaView: An end-user tool for large data visualization. In *The Visualization Handbook* (C. D. Hansen and C. R. Johnson, eds), Elsevier, pp. 717–732. Available at: www.paraview.org.

M. Ainsworth and J. Oden (1993), '*A posteriori* error estimators for 2nd order elliptic systems II: An optimal order process for calculating self-equilibrated fluxes', *Comput. Math. Appl.* **26**, 75–87.

M. Ainsworth and J. Oden (2000), *A Posteriori Error Estimation in Finite Element Analysis*, Wiley.

M. Ainsworth, J. Oden and C. Lee (1993), 'Local *a posteriori* error estimators for variational inequalities', *Numer. Methods Partial Diff. Equations* **9**, 23–33.

P. Alart and A. Curnier (1991), 'A mixed formulation for frictional contact problems prone to Newton like solution methods', *Comput. Methods Appl. Mech. Engrg* **92**, 353–375.

J. Alberty, C. Carstensen and D. Zarrabi (1999), 'Adaptive numerical analysis in primal elastoplasticity with hardening', *Comput. Methods Appl. Mech. Engrg* **171**, 175–204.

K. Andersen, E. Christiansen, A. Conn and M. Overton (2000), 'An efficient primal–dual interior point method for minimizing a sum of Euclidean norms', *SIAM J. Sci. Comput.* **22**, 243–262.

F. Armero and E. Petöcz (1998), 'A new class of conserving algorithms for dynamic contact problems.', *Comput. Methods Appl. Mech. Engrg* **158**, 269–300.

F. Armero and E. Petöcz (1999), 'A new dissipative time-stepping algorithm for frictional contact problems: Formulation and analysis', *Comput. Methods Appl. Mech. Engrg* **179**, 151–178.

D. Arnold and G. Awanou (2005), 'Rectangular mixed finite elements for elasticity', *Math. Models Meth. Appl. Sci.* **15**, 1417–1429.

D. Arnold and R. Winther (2002), 'Mixed finite element methods for elasticity', *Numer. Math.* **92**, 401–419.

D. Arnold and R. Winther (2003), Mixed finite elements for elasticity in the stress-displacement formulation. In *Current Trends in Scientific Computing* (Z. Chen, R. Glowinski and K. Li, eds), Vol. 329 of *Contemporary Mathematics*, AMS, pp. 33–42.

D. Arnold, G. Awanou and R. Winther (2008), 'Finite elements for symmetric tensors in three dimensions', *Math. Comput.* **77**, 1229–1251.

D. Arnold, R. Falk and R. Winther (2006), Differential complexes and stability of finite element methods II: The elasticity complex. In *Compatible Spatial Discretizations* (D. N. Arnold *et al.*, eds), Vol. 142 of *The IMA Volumes in Mathematics and its Applications*, Springer, pp. 47–67.

I. Babuška and T. Strouboulis (2001), *The Finite Element Method and its Reliability.*, Clarendon.

A. Bajer and L. Demkowicz (2002), 'Dynamic contact/impact problems, energy conservation, and planetary gear trains', *Comput. Methods Appl. Mech. Engng* **191**, 4159–4191.

G. Baker and V. Dougalis (1976), 'The effect of quadrature errors on finite element approximations for second order hyperbolic equations', *SIAM J. Numer. Anal.* **13**, 577–598.

P. Ballard (1999), 'A counter-example to uniqueness in quasi-static elastic contact problems with small friction', *Internat. J. Engrg Sci.* **37**, 163–178.

P. Ballard and S. Basseville (2005), 'Existence and uniqueness for dynamical unilateral contact with Coulomb friction: A model problem', *M2AN: Math. Model. Numer. Anal.* **39**, 59–77.

P. Ballard, A. Léger and E. Pratt (2006), Stability of discrete systems involving shocks and friction. In *Analysis and Simulation of Contact Problems* (P. Wriggers and U. Nackenhorst, eds), Vol. 27 of *Lecture Notes in Applied and Computational Mechanics*, Springer, pp. 343–350.

P. Bastian, K. Birken, K. Johannsen, S. Lang, N. Neuß, H. Rentz-Reichert and C. Wieners (1997), 'UG: A flexible software toolbox for solving partial differential equations', *Comput. Vis. Sci.* **1**, 27–40.

P. Bastian, M. Blatt, A. Dedner, C. Engwer, R. Klöfkorn, R. Kornhuber, M. Ohlberger and O. Sander (2008), 'A generic grid interface for parallel and adaptive scientific computing II: Implementation and tests in DUNE', *Computing* **82**, 121–138.

G. Bayada, J. Sabil and T. Sassi (2002), 'Neumann–Dirichlet algorithm for unilateral contact problems: Convergence results', *CR Math. Acad. Sci. Paris* **335**, 381–386.

G. Bayada, J. Sabil and T. Sassi (2008), 'Convergence of a Neumann–Dirichlet algorithm for tow-body contact problems with nonlocal Coulomb's friction law', *ESAIM: Math. Model. Numer. Anal.* **42**, 243–262.

Z. Belhachmi (2003), '*A posteriori* error estimates for the 3D stabilized mortar finite element method applied to the Laplace equation', *Math. Model. Numer. Anal.* **37**, 991–1011.

Z. Belhachmi (2004), 'Residual *a posteriori* error estimates for a 3D mortar finite-element method: The Stokes system', *IMA J. Numer. Anal.* **24**, 521–546.

Z. Belhachmi and F. Ben Belgacem (2000), 'Finite elements of order two for Signorini's variational inequality', *CR Acad. Sci. Paris, Sér. I: Math.* **331**, 727–732.

F. Ben Belgacem (2000), 'Numerical simulation of some variational inequalities arisen from unilateral contact problems by the finite element methods', *SIAM J. Numer. Anal.* **37**, 1198–1216.

F. Ben Belgacem and Y. Maday (1997), 'The mortar element method for three dimensional finite elements', *M2AN: Math. Model. Numer. Anal.* **31**, 289–302.

F. Ben Belgacem and Y. Renard (2003), 'Hybrid finite element methods for the Signorini problem', *Math. Comp.* **72**, 1117–1145.

F. Ben Belgacem, P. Hild and P. Laborde (1997), 'Approximation of the unilateral contact problem by the mortar finite element method', *CR Acad. Sci. Paris, Sér. I* **324**, 123–127.

F. Ben Belgacem, P. Hild and P. Laborde (1998), 'The mortar finite element method for contact problems', *Math. Comput. Modelling* **28**, 263–271.

F. Ben Belgacem, P. Hild and P. Laborde (1999), 'Extension of the mortar finite element method to a variational inequality modeling unilateral contact', *Math. Models Methods Appl. Sci.* **9**, 287–303.

A. Bergam, C. Bernardi, F. Hecht and Z. Mghazli (2003), 'Error indicators for the mortar finite element discretization of a parabolic problem', *Numer. Algorithms* **34**, 187–201.

C. Bernardi and F. Hecht (2002), 'Error indicators for the mortar finite element discretization of the Laplace equation', *Math. Comput.* **71**, 1371–1403.

C. Bernardi, Y. Maday and A. Patera (1993), Domain decomposition by the mortar element method. In *Asymptotic and Numerical Methods for Partial Differential Equations With Critical Parameters* (H. Kaper *et al.*, eds), Reidel, pp. 269–286.

C. Bernardi, Y. Maday and A. Patera (1994), A new nonconforming approach to domain decomposition: The mortar element method. In *Nonlinear Partial Differential Equations and their Applications* (H. Brezis and J.-L. Lions, eds), Vol. XI of *Collège de France Seminar*, Pitman, pp. 13–51.

P. Betsch and C. Hesch (2007), Energy-momentum conserving schemes for frictionless contact problem I: NTS method. In *Computational Methods in Contact Mechanics*, Vol. 3 of *IUTAM*, Springer, pp. 77–96.

P. Betsch and P. Steinmann (2002*a*), 'Conservation properties of a time FE method III: Mechanical systems with holonomic constraints', *Internat. J. Numer. Methods Engrg* **53**, 2271–2304.

P. Betsch and P. Steinmann (2002*b*), 'A DAE approach to flexible multibody dynamics', *Multibody Syst. Dyn.* **8**, 367–391.

M. Bildhauer, M. Fuchs and S. Repin (2008), 'Duality based *a posteriori* error estimates for higher order variational inequalities with power growth functionals', *Ann. Acad. Sci. Fenn., Math.* **33**, 475–490.

P. Binev, W. Dahmen and R. DeVore (2004), 'Adaptive finite element methods with convergence rates', *Numer. Math.* **97**, 219–268.

P. Binning and M. Celia (1999), 'Practical implementation of the fractional flow approach to multi-phase flow simulation', *Adv. Water Resour.* **22**, 461–478.

F. Black and M. Scholes (1973), 'The pricing of options and corporate liabilities', *J. Pol. Econ.* **81**, 637–659.

H. Blum and F. Suttmeier (2000), 'An adaptive finite element discretisation for a simplified Signorini problem', *Calcolo* **37**, 65–77.

P. Boieri, F. Gastaldi and D. Kinderlehrer (1987), 'Existence, uniqueness, and regularity results for the two-body contact problem', *Appl. Math. Optim.* **15**, 251–277.

M. Borri, C. Bottasso and L. Trainelli (2001), 'Integration of elastic multibody systems by invariant conserving/dissipating algorithms II: Numerical schemes and applications', *Comput. Methods Appl. Mech. Engrg* **190**, 3701–3733.

V. Bostan and W. Han (2006), '*A posteriori* error analysis for finite element solutions of a frictional contact problem', *Comput. Methods Appl. Mech. Engrg* **195**, 1252–1274.

V. Bostan, W. Han and B. Reddy (2005), '*A posteriori* error estimation and adaptive solution of elliptic variational inequalities of the second kind', *Appl. Numer. Math.* **52**, 13–38.

D. Braess (2005), '*A posteriori* error estimators for obstacle problems: Another look', *Numer. Math.* **101**, 523–549.

D. Braess and W. Dahmen (1998), 'Stability estimates of the mortar finite element method for 3-dimensional problems', *East–West J. Numer. Math.* **6**, 249–263.

D. Braess and W. Dahmen (2002), The mortar element method revisited: What are the right norms? In *Domain Decomposition Methods in Science and Engineering: Thirteenth International Conference on Domain Decomposition Methods* (N. Debit *et al.*, eds), CIMNE, pp. 27–40.

D. Braess, C. Carstensen and R. Hoppe (2007), 'Convergence analysis of a conforming adaptive finite element method for an obstacle problem', *Numer. Math.* **107**, 455–471.

D. Braess, C. Carstensen and R. Hoppe (2009*a*), 'Error reduction in adaptive finite element approximations of elliptic obstacle problems', *J. Comput. Math.* **27**, 148–169.

D. Braess, C. Carstensen and B. Reddy (2004), 'Uniform convergence and *a posteriori* error estimators for the enhanced strain finite element method', *Numer. Math.* **96**, 461–479.

D. Braess, R. Hoppe and J. Schöberl (2008), '*A posteriori* estimators for obstacle problems by the hypercircle method', *Comput. Visual. Sci.* **11**, 351–362.

D. Braess, V. Pillwein and J. Schöberl (2009*b*), 'Equilibrated residual error estimates are *p*-robust', *Comput. Methods Appl. Mech. Engrg* **198**, 1189–1197.

A. Brandt and C. Cryer (1983), 'Multigrid algorithms for the solution of linear complementarity problems arising from free boundary problems', *SIAM J. Sci. Statist. Comput.* **4**, 655–684.

K. Brenan, S. Campbell and L. Petzold (1989), *Numerical Solution of Initial-Value Problems in Differential-Algebraic Equations*, North-Holland.

H. Brezis (1971), 'Problèmes unilatéraux', *J. Math. Pures Appl.* **9**, 1–168.

F. Brezzi and M. Fortin (1991), *Mixed and Hybrid Finite Element Methods*, Springer.

F. Brezzi and D. Marini (2001), 'Error estimates for the three-field formulation with bubble stabilization', *Math. Comput.* **70**, 911–934.

F. Brezzi, W. Hager and P. Raviart (1977), 'Error estimates for the finite element solution of variational inequalities', *Numer. Math.* **28**, 431–443.

U. Brink and E. Stein (1998), '*A posteriori* error estimation in large-strain elasticity using equilibrated local Neumann problems', *Comput. Methods Appl. Mech. Engrg* **161**, 77–101.

R. Brooks and A. Corey (1964), 'Hydraulic properties of porous media', *Colorado State University, Fort Collins, Hydrology Paper* **3**, 22–27.

S. Brunßen and B. Wohlmuth (2009), 'An overlapping domain decomposition method for the simulation of elastoplastic incremental forming processes', *Internat. J. Numer. Methods Engrg* **77**, 1224–1246.

S. Brunßen, C. Hager, B. Wohlmuth and F. Schmid (2008), Simulation of elastoplastic forming processes using overlapping domain decomposition and inexact Newton methods. In *IUTAM Symposium on Theoretical, Computational and Modelling Aspects of Inelastic Media* (B. D. Reddy, ed.), Springer Science and Business media, pp. 155–164.

G. Buscaglia, R. Duran, E. Fancello, R. Feijoo and C. Padra (2001), 'An adaptive finite element approach for frictionless contact problems', *Internat. J. Numer. Methods Engrg* **50**, 394–418.

C. Carstensen, O. Scherf and P. Wriggers (1999), 'Adaptive finite elements for elastic bodies in contact', *SIAM J. Sci. Comput.* **20**, 1605–1626.

M. Cascon, C. Kreuzer, R. Nochetto and K. Siebert (2008), 'Quasi-optimal convergence rate for an adaptive finite element method', *SIAM J. Numer. Anal.* **46**, 2524–2550.

T. Chan, G. Golub and P. Mulet (1999), 'A nonlinear primal–dual method for total variation-based image restoration', *SIAM J. Sci. Comput.* **20**, 1964–1977.
D. Chapelle and K. Bathe (1993), 'The inf-sup test', *Comput. Struct.* **47**, 537–545.
G. Chavent and J. Jaffré (1986), *Mathematical Models and Finite Elements for Reservoir Simulation*, North-Holland.
V. Chawla and T. Laursen (1998), 'Energy consistent algorithms for frictional contact problems', *Internat. J. Numer. Methods Engrg* **42**, 799–827.
I. Cheddadi, R. Fučík, M. Prieto and M. Vohralík (2008), 'Computable *a posteriori* error estimates in the finite element method based on its local conservativity: Improvements using local minimization', *ESAIM: Proc.* **24**, 77–96.
I. Cheddadi, R. Fučík, M. Prieto and M. Vohralík (2009), 'Guaranteed and robust *a posteriori* error estimates for singularly perturbed reaction–diffusion problems', *ESAIM: Math. Model. Numer. Anal.* **43**, 867–888.
B. Chen, X. Chen and C. Kanzow (2000), 'A penalized Fischer–Burmeister NCP-function', *Math. Program., Ser. A* **88**, 211–216.
J. Chen (2007), 'On some NCP-functions based on the generalized Fischer–Burmeister function', *Asia–Pac. J. Oper. Res.* **24**, 401–420.
Z. Chen and R. Nochetto (2000), 'Residual type *a posteriori* error estimates for elliptic obstacle problems', *Numer. Math.* **84**, 527–548.
A. Chernov, S. Geyn, M. Maischak and E. Stephan (2006), Finite element/boundary element coupling for two-body elastoplastic contact problems with friction. In *Analysis and Simulation of Contact Problems* (P. Wriggers and U. Nackenhorst, eds), Vol. 27 of *Lecture Notes in Applied and Computational Mechanics*, Springer, pp. 171–178.
A. Chernov, M. Maischak and E. Stephan (2008), 'hp-mortar boundary element method for two-body contact problems with friction', *Math. Meth. Appl. Sci.* **31**, 2029–2054.
P. Christensen (2002*a*), 'A nonsmooth Newton method for elastoplastic problems', *Comput. Methods Appl. Mech. Engrg* **191**, 1189–1219.
P. Christensen (2002*b*), 'A semi-smooth Newton method for elasto-plastic contact problems', *Internat. J. Solids Structures* **39**, 2323–2341.
P. Christensen and J. Pang (1999), Frictional contact algorithms based on semismooth Newton methods. In *Reformulation: Nonsmooth, Piecewise Smooth, Semismooth and Smoothing Methods* (M. Fukushima and L. Qi, eds), Kluwer, pp. 81–116.
P. Christensen, A. Klarbring, J. Pang and N. Strömberg (1998), 'Formulation and comparison of algorithms for frictional contact problems', *Internat. J. Numer. Methods Engrg* **42**, 145–173.
J. Chung and G. Hulbert (1993), 'A time integration algorithm for structural dynamics with improved numerical dissipation: The generalized α-method', *J. Appl. Mech.* **60**, 371–375.
P. Ciarlet (1991), Basic error estimates for elliptic problems. In *Finite Element Methods, Part 1* (P. Ciarlet and J. Lions, eds), Vol. 2 of *Handbook of Numerical Analysis*, North-Holland, pp. 19–351.
P. Ciarlet (1998), *Mathematical Elasticity*, Vol. I, North-Holland.
H. Class (2001), Theorie und numerische Modellierung nichtisothermer Mehrphasenprozesse in NAPL-kontaminierten porösen Medien. PhD thesis, Institut für Wasserbau, Universität Stuttgart.

H. Class and R. Helmig (2002), 'Numerical simulation of non-isothermal multiphase multicomponent processes in porous media 2: Applications for the injection of steam and air', *Adv. Water Resour.* **25**, 551–564.

H. Class, R. Helmig and P. Bastian (2002), 'Numerical simulation of non-isothermal multiphase multicomponent processes in porous media 1: An efficient solution technique', *Adv. Water Resour.* **25**, 533–550.

P. Coorevits, P. Hild and J. Pelle (2000), '*A posteriori* error estimation for unilateral contact with matching and non-matching meshes', *Comput. Methods Appl. Mech. Engrg* **186**, 65–83.

P. Coorevits, P. Hild, K. Lhalouani and T. Sassi (2001), 'Mixed finite element methods for unilateral problems: Convergence analysis and numerical studies', *Math. Comp.* **71**, 1–25.

R. Dautray and J. Lions (1992), *Mathematical Analysis and Numerical Methods for Science and Technology: Evolution Problems*, Vol. 5, Springer.

M. de Neef (2000), Modelling capillary effects in heterogeneous porous media. PhD thesis, University of Delft, Netherlands.

G. De Saxcé and Z. Feng (1991), 'New inequality and functional for contact with friction: The implicit standard material approach', *Mech. Based Des. Struct. Mach.* **19**, 301–325.

R. Dembo, S. Eisenstat and T. Steinhaug (1982), 'Inexact Newton methods', *SIAM J. Numer. Anal.* **19**, 400–408.

L. Demkowicz (1982), 'On some results concerning the reciprocal formulation for the Signorini's problem', *Comput. Math. Appl.* **8**, 57–74.

L. Demkowicz and A. Bajer (2001), 'Conservative discretization of contact/impact problems for nearly rigid bodies', *Comput. Methods Appl. Mech. Engng* **190**, 1903–1924.

L. Demkowicz and T. Oden (1982), 'On some existence and uniqueness results in contact problems with nonlocal friction', *Nonlinear Anal.: Theory Methods Appl.* **6**, 1075–1093.

P. Deuflhard (2004), *Newton Methods for Nonlinear Problems: Affine Invariance and Adaptive Algorithms*, Springer.

P. Deuflhard, R. Krause and S. Ertel (2008), 'A contact-stabilized Newmark method for dynamical contact problems', *Internat. J. Numer. Methods Engrg* **73**, 1274–1290.

T. Dickopf and R. Krause (2009*a*), 'Efficient simulation of multi-body contact problems on complex geometries: A flexible decomposition approach using constrained minimization', *Internat. J. Numer. Methods Engrg* **77**, 1834–1862.

T. Dickopf and R. Krause (2009*b*), 'Weak information transfer between non-matching warped interfaces.', Bercovier, Michel (ed.) *et al.*, Domain decomposition methods in science and engineering XVIII. Selected papers based on the presentations at the 18th international conference of domain decomposition methods, Jerusalem, Israel, January 12–17, 2008. Berlin: Springer. Lecture Notes in Computational Science and Engineering 70, 283-290 (2009).

C. Dohrmann, S. Key and M. Heinstein (2000), 'A method for connecting dissimilar finite element meshes in two dimensions', *Internat. J. Numer. Methods Engrg* **48**, 655–678.

W. Dörfler (1996), 'A convergent adaptive algorithm for Poisson's equation', *SIAM J. Numer. Anal.* **33**, 1106–1124.
P. Dörsek and J. Melenk (2010), 'Adaptive hp-FEM for the contact problem with Tresca friction in linear elasticity: The primal–dual formulation and *a posteriori* error estimation', *Appl. Numer. Math.* **60**, 689–704.
Z. Dostál (2009), *Optimal Quadratic Programming Algorithms, with Applications to Variational Inequalities*, Vol. 23 of *Springer Optimization and its Applications*, Springer.
Z. Dostál and D. Horák (2003), 'Scalability and FETI based algorithm for large discretized variational inequalities', *Math. Comput. Simul.* **61**, 347–357.
Z. Dostál, A. Friedlander and S. Santos (1998), 'Solution of coercive and semicoercive contact problems by FETI domain decomposition', *Contemp. Math.* **218**, 82–93.
Z. Dostál, F. Gomes Neto and S. Santos (2000), 'Solution of contact problems by FETI domain decomposition with natural coarse space projections', *Comput. Methods Appl. Mech. Engrg* **190**, 1611–1627.
Z. Dostál, D. Horák and D. Stefanica (2007), 'A scalable FETI-DP algorithm for a semi-coercive variational inequality', *Comput. Methods Appl. Mech. Engrg* **196**, 1369–1379.
Z. Dostál, D. Horák and D. Stefanica (2009), 'A scalable FETI-DP algorithm with non-penetration mortar conditions on contact interface', *J. Comput. Appl. Math.* **231**, 577–591.
Z. Dostál, D. Horák, R. Kučera, V. Vondrák, J. Haslinger, J. Dobiaš and S. Pták (2005), 'FETI based algorithms for contact problems: Scalability, large displacements and 3D Coulomb friction', *Comput. Methods Appl. Mech. Engrg* **194**, 395–409.
D. Doyen and A. Ern (2009), 'Convergence of a space semi-discrete modified mass method for the dynamic Signorini problem', *Commun. Math. Sci.* **7**, 1063–1072.
G. Duvaut and J. Lions (1976), *Inequalities in Mechanics and Physics*, Springer. Translation by C. W. John.
C. Eck (2002), 'Existence of solutions to a thermo-viscoelastic contact problem with Coulomb friction', *Math. Models Methods Appl. Sci.* **12**, 1491–1511.
C. Eck and J. Jarušek (1998), 'Existence results for the static contact problem with Coulomb friction', *Math. Models Methods Appl. Sci.* **8**, 445–468.
C. Eck and J. Jarušek (2001), 'On the thermal aspect of dynamic contact problems', *Math. Bohem.* **126**, 337–352.
C. Eck and J. Jarušek (2003), 'Existence of solutions for the dynamic frictional contact problem of isotropic viscoelastic bodies', *Nonlinear Anal., Theory Methods Appl.* **53**, 157–181.
C. Eck and W. Wendland (2003), 'A residual-based error estimator for BEM discretizations of contact problems', *Numer. Math.* **95**, 253–282.
C. Eck and B. Wohlmuth (2003), 'Convergence of a contact-Neumann iteration for the solution of two-body contact problems', *Math. Models Methods Appl. Sci.* **13**, 1103–1118.
C. Eck, J. Jarušek and M. Krbec (2005), *Unilateral Contact Problems: Variational Methods and Existence Theorems*, CRC Press.

S. Eisenstat and H. Walker (1996), 'Choosing the forcing terms in an inexact Newton method', *SIAM J. Sci. Comput.* **17**, 16–32.

B. Erdmann, M. Frei, R. Hoppe, R. Kornhuber and U. Wiest (1993), 'Adaptive finite element methods for variational inequalities', *East–West J. Numer. Math.* **1**, 165–197.

A. Ern and M. Vohralík (2009), 'Flux reconstruction and *a posteriori* error estimation for discontinuous Galerkin methods on general nonmatching grids', *CR Math. Acad. Sci. Paris* **347**, 441–444.

L. Evans (1998), *Partial Differential Equations*, AMS.

F. Facchinei and J. Pang (2003*a*), *Finite-Dimensional Variational Inequalities and Complementary Problems*, Vol. I, Springer Series in Operations Research.

F. Facchinei and J. Pang (2003*b*), *Finite-Dimensional Variational Inequalities and Complementary Problems*, Vol. II, Springer Series in Operations Research.

R. Falk (1974), 'Error estimates for the approximation of a class of variational inequalities', *Math. Comp.* **28**, 963–971.

C. Felippa (2000), 'On the original publication of the general canonical functional of linear elasticity', *J. Appl. Mech.* **67**, 217–219.

G. Fichera (1964), 'Problemi elastostatici con vincoli unilaterali: Il problema di Signorini con ambigue condizioni al contorno', *Mem. Accad. Naz. Lincei* **8**, 91–140.

A. Fischer (1992), 'A special Newton-type optimization method', *Optimization* **24**, 269–284.

A. Fischer-Cripps (2000), *Introduction to Contact Mechanics*, Springer Mechanical Engineering Series.

K. Fischer and P. Wriggers (2006), 'Mortar based frictional contact formulation for higher order interpolations using the moving friction cone', *Comput. Methods Appl. Mech. Engrg* **195**, 5020–5036.

B. Flemisch, J. Fritz, R. Helmig, J. Niessner and B. Wohlmuth (2007), DUMUX: A multi-scale multi-physics toolbox for flow and transport processes in porous media. In *ECCOMAS Thematic Conference on Multi-Scale Computational Methods for Solids and Fluids* (A. Ibrahimbegovic and F. Dias, eds), Cachan, France, pp. 82–87.

B. Flemisch, J. Melenk and B. Wohlmuth (2005*a*), 'Mortar methods with curved interfaces', *Appl. Numer. Math.* **54**, 339–361.

B. Flemisch, M. Puso and B. Wohlmuth (2005*b*), 'A new dual mortar method for curved interfaces: 2D elasticity', *Internat. J. Numer. Methods Engrg* **63**, 813–832.

S. Fluegge, ed. (1972), *Handbuch der Physik*, Vol. VIa, chapter on Linear Thermoelasticity, Springer, pp. 297–346.

D. French, S. Larsson and R. Nochetto (2001), 'Pointwise *a posteriori* error analysis for an adaptive penalty finite element method for the obstacle problem', *Comput. Methods Appl. Math.* **1**, 18–38.

M. Fuchs and S. Repin (2010), 'Estimates of the deviations from the exact solutions for variational inequalities describing the stationary flow of certain viscous incompressible fluids', *Math. Methods Appl. Sci.* **33**, 1136–1147.

C. Geiger and C. Kanzow (2002), *Theorie und Numerik Restringierter Optimierungsaufgaben*, Springer.

M. Gitterle, A. Popp, M. Gee and W. Wall (2010), 'Finite deformation frictional mortar contact using a semi-smooth Newton method with consistent linearization', *Internat. J. Numer. Methods Engrg* **84**, 543–571.

R. Glowinski (1984), *Numerical Methods for Nonlinear Variational Problems*, Springer.

R. Glowinski and P. Le Tallec (1989), *Augmented Lagrangian and Operator Splitting Methods in Nonlinear Mechanics*, Vol. 9 of *SIAM Studies in Applied Mathematics*.

R. Glowinski, J. Lions and R. Trémolières (1981), *Numerical Analysis of Variational Inequalities*, North-Holland.

M. Gonzales, B. Schmidt and M. Ortiz (2010), 'Energy-stepping integrators in Lagrangian mechanics', *Internat. J. Numer. Methods Engrg* **82**, 205–241.

O. Gonzalez (2000), 'Exact energy and momentum conserving algorithms for general models in nonlinear elasticity', *Comput. Methods Appl. Mech. Engrg* **190**, 1763–1783.

W. Gordon and C. Hall (1973*a*), 'Construction of curvilinear co-ordinate systems and applications to mesh generation', *Internat. J. Numer. Methods Engng* **7**, 461–477.

W. Gordon and C. Hall (1973*b*), 'Transfinite element methods: Blending-function interpolation over arbitrary curved element domains', *Numer. Math.* **21**, 109–129.

J. Gwinner (2009), 'On the p-version approximation in the boundary element method for a variational inequality of the second kind modelling unilateral contact and given friction', *Appl. Numer. Math.* **59**, 2774–2784.

W. Hackbusch (1985), *Multi-Grid Methods and Applications*, Springer.

W. Hackbusch and H. Mittelmann (1983), 'On multi-grid methods for variational inequalities', *Numer. Math.* **42**, 65–76.

C. Hager (2010), Robust numerical algorithms for dynamic frictional contact problems with different time and space scales. PhD thesis, IANS, Universität Stuttgart.

C. Hager and B. Wohlmuth (2009*a*), 'Analysis of a space-time discretization for dynamic elasticity problems based on mass-free surface elements', *SIAM J. Numer. Anal.* **47**, 1863–1885.

C. Hager and B. Wohlmuth (2009*b*), 'Nonlinear complementarity functions for plasticity problems with frictional contact', *Comput. Methods Appl. Mech. Engrg* **198**, 3411–3427.

C. Hager and B. Wohlmuth (2010), 'Semismooth Newton methods for variational problems with inequality constraints', *GAMM–Mitt.* **33**, 8–24.

C. Hager, P. Hauret, P. Le Tallec and B. Wohlmuth (2010*a*), Overlapping domain decomposition for multiscale dynamic contact problems. Technical report IANS Preprint 2010/007, Universität Stuttgart.

C. Hager, S. Hüeber and B. Wohlmuth (2008), 'A stable energy conserving approach for frictional contact problems based on quadrature formulas', *Internat. J. Numer. Methods Engrg* **73**, 205–225.

C. Hager, S. Hüeber and B. Wohlmuth (2010*b*), 'Numerical techniques for the valuation of basket options and its Greeks', *J. Comput. Fin.* **13**, 1–31.

E. Hairer and G. Wanner (1991), *Solving Ordinary Differential Equations II: Stiff and Differential-Algebraic Problems*, Springer.

W. Han (2005), *A Posteriori Error Analysis via Duality Theory: With Applications in Modeling and Numerical Approximations*, Springer.

W. Han and B. Reddy (1995), 'Computational plasticity: The variational basis and numerical analysis', *Comput. Mech. Advances* **2**, 283–400.

W. Han and B. Reddy (1999), *Plasticity: Mathematical Theory and Numerical Analysis*, Springer.

W. Han and M. Sofonea (2000), 'Numerical analysis of a frictionless contact problem for elastic-viscoplastic materials', *Comput. Methods Appl. Mech. Engrg* **190**, 179–191.

W. Han and M. Sofonea (2002), *Quasistatic Contact Problems in Viscoelasticity and Viscoplasticity*, Studies in Advanced Mathematics, AMS, International Press.

P. Harker and J. Pang (1990), 'Finite-dimensional variational inequality and nonlinear complementarity problems: A survey of theory, algorithms and applications', *Math. Progr.* **48**, 161–220.

S. Hartmann, S. Brunßen, E. Ramm and B. Wohlmuth (2007), 'Unilateral nonlinear dynamic contact of thin-walled structures using a primal–dual active set strategy', *Internat. J. Numer. Meth. Engrg* **70**, 883–912.

J. Haslinger and I. Hlaváček (1981), 'Contact between two elastic bodies II: Finite element analysis', *Aplikace Mathematiky* **26**, 263–290.

J. Haslinger, I. Hlaváček and J. Nečas (1996), Numerical methods for unilateral problems in solid mechanics. In *Handbook of Numerical Analysis* (P. Ciarlet and J.-L. Lions, eds), Vol. IV, North-Holland, pp. 313–485.

J. Haslinger, I. Hlaváček, J. Nečas and J. Lovíšek (1988), *Solution of Variational Inequalities in Mechanics*, Springer.

S. Hassanizadeh and W. Gray (1993), 'Thermodynamic basis of capillary pressure in porous media', *Water Resour. Research* **29**, 3389–3405.

S. Hassanizadeh, M. Celia and H. Dahle (2002), 'Experimental measurements of saturation overshoot on infiltration', *Vadose Zone J.* **1**, 38–57.

P. Hauret and P. Le Tallec (2006), 'Energy-controlling time integration methods for nonlinear elastodynamics and low-velocity impact', *Comput. Methods Appl. Mech. Engrg* **195**, 4890–4916.

P. Hauret and P. Le Tallec (2007), 'A discontinuous stabilized mortar method for general 3D elastic problems', *Comput. Methods Appl. Mech. Engng* **196**, 4881–4900.

P. Hauret, J. Salomon, A. Weiss and B. Wohlmuth (2008), 'Energy consistent corotational schemes for frictional contact problems', *SIAM J. Sci. Comput.* **30**, 2488–2511.

R. Helmig (1997), *Multiphase Flow and Transport Processes in the Subsurface*, Springer.

R. Helmig, A. Weiss and B. Wohlmuth (2009), 'Variational inequalities for modeling flow in heterogeneous porous media with entry pressure', *Comput. Geosci.* **13**, 373–390.

H. Hertz (1882), 'Über die Berührung fester elastischer Körper', *J. Reine Angew. Math.* **92**, 156–171.

C. Hesch and P. Betsch (2006), 'A comparison of computational methods for large deformation contact problems of flexible bodies', *ZAMM: Z. Angew. Math. Mech.* **86**, 818–827.

C. Hesch and P. Betsch (2009), 'A mortar method for energy-momentum conserving schemes in frictionless dynamic contact problems', *Internat. J. Numer. Methods Engrg* **77**, 1468–1500.

C. Hesch and P. Betsch (2010), 'Transient three-dimensional domain decomposition problems: Frame-indifferent mortar constraints and conserving integration', *Internat. J. Numer. Methods Engrg* **82**, 329–358.

H. Hilber, T. Hughes and R. Taylor (1977), 'Improved numerical dissipation for time integration algorithms in structural dynamics', *Earthquake Engrg Struct. Dyn.* **5**, 283–292.

P. Hild (2000), 'Numerical implementation of two nonconforming finite element methods for unilateral contact', *Comput. Methods Appl. Mech. Engrg* **184**, 99–123.

P. Hild (2003), 'An example of nonuniqueness for the continuous static unilateral contact model with Coulomb friction', *CR Math. Acad. Sci. Paris* **337**, 685–688.

P. Hild (2004), 'Non-unique slipping in the Coulomb friction model in two-dimensional linear elasticity', *Q. J. Mech. Appl. Math.* **57**, 225–235.

P. Hild and P. Laborde (2002), 'Quadratic finite element methods for unilateral contact problems', *Appl. Numer. Math.* **41**, 410–421.

P. Hild and V. Lleras (2009), 'Residual error estimators for Coulomb friction', *SIAM J. Numer. Anal.* **47**, 3550–3583.

P. Hild and S. Nicaise (2005), '*A posteriori* error estimations of residual type for Signorini's problem', *Numer. Math.* **101**, 523–549.

P. Hild and S. Nicaise (2007), 'Residual *a posteriori* error estimators for contact problems in elasticity', *Math. Model. Numer. Anal.* **41**, 897–923.

P. Hild and Y. Renard (2006), Local uniqueness results for the discrete friction problem. In *Analysis and Simulation of Contact Problems* (P. Wriggers and U. Nackenhorst, eds), Vol. 27 of *Lecture Notes in Applied and Computational Mechanics*, Springer, pp. 129–136.

P. Hild and Y. Renard (2007), 'An error estimate for the Signorini problem with Coulomb friction approximated by finite elements', *SIAM J. Numer. Anal.* **45**, 2012–2031.

P. Hild and Y. Renard (2010), 'A stabilized Lagrange multiplier method for the finite element approximation of contact problems in elastostatics', *Numer. Math.* **115**, 101–129.

M. Hintermüller and G. Stadler (2006), 'An infeasible primal–dual algorithm for total variation-based inf-convolution-type image restoration', *SIAM J. Sci. Comput.* **28**, 1–23.

M. Hintermüller, K. Ito and K. Kunisch (2002), 'The primal–dual active set strategy as a semi–smooth Newton method', *SIAM J. Optim.* **13**, 865–888.

M. Hintermüller, V. Kovtunenko and K. Kunisch (2004), 'Semismooth Newton methods for a class of unilaterally constrained variational problems', *Adv. Math. Sci. Appl.* **14**, 513–535.

R. Hoppe (1987), 'Multigrid algorithms for variational inequalities', *SIAM J. Numer. Anal.* **24**, 1046–1065.

R. Hoppe and R. Kornhuber (1994), 'Adaptive multilevel methods for obstacle problems', *SIAM J. Numer. Anal.* **31**, 301–323.

H. Hu (1955), 'On some variational principles in the theory of elasticity and the theory of plasticity', *Scientia Sinica* **4**, 33–54.

S. Hu, Z. Huang and J. Chen (2009), 'Properties of a family of generalized NCP-functions and a derivative free algorithm for complementarity problems', *J. Comput. Appl. Math.* **230**, 69–82.

R. Huber and R. Helmig (2000), 'Node-centered finite volume discretizations for the numerical simulation of multiphase flow in heterogeneous porous media', *Comput. Geosci.* **4**, 141–164.

S. Hüeber (2008), Discretization techniques and efficient algorithms for contact problems. PhD thesis, IANS, Universität Stuttgart.

S. Hüeber and B. Wohlmuth (2005*a*), 'An optimal *a priori* error estimate for nonlinear multibody contact problems', *SIAM J. Numer. Anal.* **43**, 157–173.

S. Hüeber and B. Wohlmuth (2005*b*), 'A primal–dual active set strategy for nonlinear multibody contact problems', *Comput. Methods Appl. Mech. Engrg* **194**, 3147–3166.

S. Hüeber and B. Wohlmuth (2009), 'Thermo-mechanical contact problem on non-matching meshes', *Comput. Methods Appl. Mech. Engrg* **198**, 1338–1350.

S. Hüeber and B. Wohlmuth (2010), Equilibration techniques for solving contact problems with Coulomb friction. *Comput. Methods Appl. Mech. Engrg* doi:10.1016/j.cma.2010.12.021.

S. Hüeber, M. Mair and B. Wohlmuth (2005*a*), '*A priori* error estimates and an inexact primal–dual active set strategy for linear and quadratic finite elements applied to multibody contact problems', *Appl. Numer. Math.* **54**, 555–576.

S. Hüeber, A. Matei and B. Wohlmuth (2005*b*), 'A mixed variational formulation and an optimal *a priori* error estimate for a frictional contact problem in elasto-piezoelectricity', *Bull. Math. Soc. Sci. Math. Roumanie* **48**, 209–232.

S. Hüeber, A. Matei and B. Wohlmuth (2007), 'Efficient algorithms for problems with friction', *SIAM J. Sci. Comput.* **29**, 70–92.

S. Hüeber, G. Stadler and B. Wohlmuth (2008), 'A primal–dual active set algorithm for three-dimensional contact problems with Coulomb friction', *SIAM J. Sci. Comput.* **30**, 572–596.

T. Hughes (1987), *The Finite Element Method: Linear, Static and Dynamic Finite Element Analysis*, Prentice-Hall.

G. Hulbert (1992), 'Time finite element methods for structural dynamics', *Internat. J. Numer. Methods Engrg* **33**, 307–331.

J. Hull (2006), *Options, Futures, and Other Derivatives*, sixth edition, Prentice-Hall.

K. Ito and K. Kunisch (2003), 'Semi-smooth Newton methods for variational inequalities of the first kind', *M2AN: Math. Model. Numer. Anal.* **37**, 41–62.

K. Ito and K. Kunisch (2004), 'The primal–dual active set method for nonlinear optimal control problems with bilateral constraints', *SIAM J. Control. Optim.* **43**, 357–376.

K. Ito and K. Kunisch (2008*a*), *Lagrange Multiplier Approach to Variational Problems and Applications*, SIAM.

K. Ito and K. Kunisch (2008*b*), 'On a semi-smooth Newton method for the Signorini problem', *Appl. Math.* **53**, 455–468.

J. Jarušek (1983), 'Contact problems with bounded friction: Coercive case', *Czech. Math. J.* **33**, 237–261.

C. Johnson (1992), 'Adaptive finite element methods for the obstacle problem', *Math. Models Methods Appl. Sci.* **2**, 483–487.

K. Johnson (1985), *Contact Mechanics*, Cambridge University Press.

C. Kane, J. Marsden, M. Ortiz and M. West (2000), 'Variational integrators and the Newmark algorithm for conservative and dissipative mechanical systems', *Internat. J. Numer. Methods Engrg* **49**, 1295–1325.

C. Kanzow, N. Yamashita and M. Fukushima (1997), 'New NCP-functions and their properties', *J. Optimization Theory Appl.* **94**, 115–135.

G. Karypis and V. Kumar (1998), 'A fast and high quality multilevel scheme for partitioning irregular graphs', *SIAM J. Sci. Comput.* **20**, 359–392.

E. Kasper and R. Taylor (2000*a*), 'A mixed-enhanced strain method I: Geometrically linear problems', *Computers and Structures* **75**, 237–250.

E. Kasper and R. Taylor (2000*b*), 'A mixed-enhanced strain method II: Geometrically nonlinear problems', *Computers and Structures* **75**, 251–260.

D. Kelly (1984), 'The self-equilibration of residuals and complementary *a posteriori* error estimates in the finite element method', *Internat. J. Numer. Methods Engrg* **20**, 1491–1506.

D. Kelly and J. Isles (1989), 'Procedures for residual equilibration and local error estimation in the finite element method', *Commun. Appl. Numer. Methods* **5**, 497–505.

H. Khenous, P. Laborde and Y. Renard (2006*a*), 'Comparison of two approaches for the discretization of elastodynamic contact problems', *CR Math. Acad. Sci. Paris* **342**, 791–796.

H. Khenous, P. Laborde and Y. Renard (2006*b*), On the discretization of contact problems in elastodynamics. In *Analysis and Simulation of Contact Problems* (P. Wriggers and U. Nackenhorst, eds), Vol. 27 of *Lecture Notes in Applied and Computational Mechanics*, Springer, pp. 31–38.

H. Khenous, P. Laborde and Y. Renard (2008), 'Mass redistribution method for finite element contact problems in elastodynamics', *Eur. J. Mech., A, Solids* **27**, 918–932.

N. Kikuchi and J. Oden (1988), *Contact Problems in Elasticity: A Study of Variational Inequalities and Finite Element Methods*, Vol. 8 of *SIAM Studies in Applied Mathematics*.

D. Kinderlehrer and G. Stampacchia (2000), *An Introduction to Variational Inequalities and their Applications*, SIAM.

C. Klapproth, P. Deuflhard and A. Schiela (2009), 'A perturbation result for dynamical contact problems', *Numer. Math., Theory Methods Appl.* **2**, 237–257.

C. Klapproth, A. Schiela and P. Deuflhard (2010), 'Consistency results on Newmark methods for dynamical contact problems', *Numer. Math.* **116**, 65–94.

R. Kornhuber (1994), 'Monotone multigrid methods for elliptic variational inequalities I', *Numer. Math.* **69**, 167–184.

R. Kornhuber (1996), 'Monotone multigrid methods for elliptic variational inequalities II', *Numer. Math.* **72**, 481–499.

R. Kornhuber (1997), *Adaptive Monotone Multigrid Methods for Nonlinear Variational Problems*, Teubner.

R. Kornhuber and R. Krause (2001), 'Adaptive multigrid methods for Signorini's problem in linear elasticity', *Comput. Vis. Sci.* **4**, 9–20.

R. Kornhuber and Q. Zou (2011), 'Efficient and reliable hierarchical error estimates for the discretization error of elliptic obstacle problems', *Math. Comp.* **80**, 69–88.

R. Kornhuber, R. Krause, O. Sander, P. Deuflhard and S. Ertel (2007), 'A monotone multigrid solver for two body contact problems in biomechanics', *Comput. Vis. Sci.* **11**, 3–15.

T. Koziara and N. Bicanic (2008), 'Semismooth Newton method for frictional contact between pseudo-rigid bodies', *Comput. Methods Appl. Mech. Engrg* **197**, 2763–2777.

R. Krause (2008), On the multiscale solution of constrained minimization problems. In *Domain Decomposition Methods in Science and Engineering XVII* (U. Langer *et al.* eds), Vol. 60 of *Lecture Notes in Computational Science and Engineering*, Springer, pp. 93–104.

R. Krause (2009), 'A nonsmooth multiscale method for solving frictional two-body contact problems in 2D and 3D with multigrid efficiency', *SIAM J. Sci. Comput.* **31**, 1399–1423.

R. Krause and C. Mohr (2011), 'Level set based multi-scale methods for large deformation contact problems', *Appl. Numer. Math.* **61**, 428–442.

R. Krause and M. Walloth (2009), 'A time discretization scheme based on Rothe's method for dynamical contact problems with friction', *Comput. Methods Appl. Mech. Engrg* **199**, 1–19.

R. Krause and B. Wohlmuth (2002), 'A Dirichlet–Neumann type algorithm for contact problems with friction', *Comput. Vis. Sci.* **5**, 139–148.

M. Kuczma and L. Demkowicz (1992), 'An adaptive algorithm for unilateral viscoelastic contact problems for beams and plates', *Comput. Methods Appl. Mech. Engng* **101**, 183–196.

D. Kuhl and E. Ramm (1999), 'Generalized energy-momentum method for nonlinear adaptive shell dynamics', *Comput. Methods Appl. Mech. Engrg* pp. 343–366.

C. Lacour and F. Ben Belgacem (2011), *The Mortar Finite Element Method: Basics, Theory and Implementation*, Chapman & Hall/CRC Press. To appear.

P. Ladevèze and D. Leguillon (1983), 'Error estimate procedure in the finite element method and applications', *SIAM J. Numer. Anal.* **20**, 485–509.

P. Ladevèze and E. Maunder (1996), 'A general method for recovering equilibrating element tractions', *Comput. Methods Appl. Mech. Engrg* **137**, 111–151.

P. Ladevèze and P. Rougeot (1997), 'New advances on *a posteriori* error on constitutive relation in f.e. analysis', *Comput. Methods Appl. Mech. Engrg* **150**, 239–249.

B. Lamichhane and B. Wohlmuth (2007), 'Biorthogonal bases with local support and approximation properties', *Math. Comp.* **76**, 233–249.

B. Lamichhane, B. Reddy and B. Wohlmuth (2006), 'Convergence in the incompressible limit of finite element approximations based on the Hu–Washizu formulation', *Numer. Math.* **104**, 151–175.

T. Laursen (2002), *Computational Contact and Impact Mechanics*, Springer.

T. Laursen and V. Chawla (1997), 'Design of energy conserving algorithms for frictionless dynamic contact problems', *Internat. J. Numer. Methods Engrg* **40**, 836–886.

T. Laursen and G. Love (2002), 'Improved implicit integrators for transient impact problems: Geometric admissibility within the conserving framework', *Internat. J. Numer. Methods Engrg* **53**, 245–274.

T. Laursen and X. Meng (2001), 'A new solution procedure for application of energy-conserving algorithms to general constitutive models in nonlinear elastodynamics', *Comput. Methods Appl. Mech. Engrg* **190**, 6309–6322.

T. Laursen and J. Simo (1993*a*), 'A continuum-based finite element formulation for the implicit solution of multibody, large deformation frictional contact problems', *Internat. J. Numer. Methods Engrg* **36**, 3451–3485.

T. Laursen and J. Simo (1993*b*), 'Algorithmic symmetrization of Coulomb frictional problems using augmented Lagrangians', *Comput. Methods Appl. Mech. Engng* **108**, 133–146.

A. Lauser, C. Hager, R. Helmig and B. Wohlmuth (2010), A new approach for phase transitions in miscible multi-phase flow in porous media. SimTech-Preprint 2010-34, Universität Stuttgart. To appear in *Adv. Water Resour.*

C. Lee and J. Oden (1994), '*A posteriori* error estimation of *h-p* finite element approximations of frictional contact problems.', *Comput. Methods Appl. Mech. Engrg* **113**, 11–45.

R. Lenhard, J. Parker and S. Mishra (1989), 'On the correspondence between Brooks–Corey and Van Genuchten models', *J. Irrig. and Drain. Engrg* **115**, 744–751.

M. Leverett (1941), 'Capillary behavior in porous solids', *AIME Petroleum Transactions* **142**, 152–169.

K. Lhalouani and T. Sassi (1999), 'Nonconforming mixed variational inequalities and domain decomposition for unilateral problems', *East–West J. Numer. Math.* **7**, 23–30.

J. Li, J. Melenk, B. Wohlmuth and J. Zou (2010), 'Optimal *a priori* estimates for higher order finite elements for elliptic interface problems', *Appl. Numer. Math.* **60**, 19–37.

J. Lions and G. Stampacchia (1967), 'Variational inequalities', *Comm. Pure Appl. Math.* **XX**, 493–519.

W. Liu and N. Yan (2000), '*A posteriori* error estimators for a class of variational inequalities', *J. Sci. Comput.* **15**, 361–393.

R. Luce and B. Wohlmuth (2004), 'A local *a posteriori* error estimator based on equilibrated fluxes', *SIAM J. Numer. Anal.* **42**, 1394–1414.

C. Lunk and B. Simeon (2006), 'Solving constrained mechanical systems by the family of Newmark and α-methods', *Z. Angew. Math. Mech.* **86**, 772–784.

M. Maischak and E. Stephan (2005), 'Adaptive *hp*-versions of BEM for Signorini problems', *Appl. Numer. Math.* **54**, 425–449.

M. Maischak and E. Stephan (2007), 'Adaptive *hp*-versions of boundary element methods for elastic contact problems', *Comput. Mech.* **39**, 597–607.

J. Martins, S. Barbarin, M. Raous and A. Pinto da Costa (1999), 'Dynamic stability of finite dimensional linearly elastic systems with unilateral contact and Coulomb friction', *Comput. Methods Appl. Mech. Engrg* **177**, 289–328.

M. Melenk and B. Wohlmuth (2011), On the convergence of surface based Lagrange multipliers in finite element methods. In preparation.

K. Moon, R. Nochetto, T. von Petersdorff and C. Zhang (2007), '*A posteriori* error analysis for parabolic variational inequalities', *ESAIM: Math. Model. Numer. Anal.* **41**, 485–511.

J. Moreau (1977), 'Evolution problem associated with a moving convex set in a Hilbert space', *J. Differential Equations* **26**, 347–374.

P. Morin, R. Nochetto and K. Siebert (2002), 'Convergence of adaptive finite element methods', *SIAM Rev.* **44**, 631–658.

J. Nečas, J. Jarušek and J. Haslinger (1980), 'On the solution of the variational inequality to the Signorini problem with small friction', *Boll. Unione Mat. Ital., V. Ser., B* **17**, 796–811.

S. Nicaise, K. Witowski and B. Wohlmuth (2008), 'An *a posteriori* error estimator for the Lame equation based on H(div)-conforming stress approximations', *IMA J. Numer. Anal.* **28**, 331–353.

R. Nicolaides (1982), 'Existence, uniqueness and approximation for generalized saddle point problems', *SIAM J. Numer. Anal.* **19**, 349–357.

J. Niessner and R. Helmig (2007), 'Multi-scale modeling of three-phase-three-component processes in heterogeneous porous media', *Adv. Water Resour.* **30**, 2309–2325.

R. Nochetto and L. Wahlbin (2002), 'Positivity preserving finite element approximation', *Math. Comput.* **71**, 1405–1419.

R. Nochetto, T. von Petersdorff and C. Zhang (2010), '*A posteriori* error analysis for a class of integral equations and variational inequalities', *Numer. Math.* **116**, 519–552.

R. Nochetto, K. Siebert and A. Veeser (2003), 'Pointwise *a posteriori* error control for elliptic obstacle problems', *Numer. Math.* **95**, 163–195.

R. Nochetto, K. Siebert and A. Veeser (2005), 'Fully localized *a posteriori* error estimators and barrier sets for contact problems', *SIAM J. Numer. Anal.* **42**, 2118–2135.

R. Nochetto, K. Siebert and A. Veeser (2009), Theory of adaptive finite element methods: An introduction. In *Multiscale, Nonlinear and Adaptive Approximation: Dedicated to Wolfgang Dahmen on the Occasion of his 60th Birthday* (R. DeVore *et al.*, eds), Springer, pp. 409–542.

T. Oden, E. Becker, T. Lin and L. Demkowicz (1985), Formulation and finite element analysis of a general class of rolling contact problems with finite elastic deformations. In *The Mathematics of Finite Elements and Applications V: MAFELAP 1984*, pp. 505–532.

A. Pandolfi, C. Kane, J. Marsden and M. Ortiz (2002), 'Time-discretized variational formulation of non-smooth frictional contact', *Internat. J. Numer. Methods Engrg* **53**, 1801–1829.

J. Pang (1990), 'Newton's method for B-differentiable equations', *Math. Oper. Res.* **15**, 311–341.

J. Pang and S. Gabriel (1993), 'NE/SQP: A robust algorithm for the nonlinear complementarity problem', *Math. Progr.* **60**, 295–337.

J. Pang and L. Qi (1993), 'Nonsmooth equations: Motivation and algorithms', *SIAM J. Optim.* **3**, 443–465.

O. Pironneau and Y. Achdou (2009), Partial differential equations for option pricing. In *Handbook of Numerical Analysis*, Vol XV: *Mathematical Modeling and Numerical Methods in Finance* (A. Bensoussan *et al*, eds), Elsevier/North-Holland, pp. 369–495.

A. Popp, M. Gee and W. Wall (2009), 'A finite deformation mortar contact formulation using a primal–dual active set strategy', *Internat. J. Numer. Methods Engrg* **79**, 1354–1391.

A. Popp, M. Gitterle, M. Gee and W. Wall (2010), 'A dual mortar approach for 3D finite deformation contact with consistent linearization', *Internat. J. Numer. Methods Engrg* **83**, 1428–1465.

J. Pousin and T. Sassi (2005), '*A posteriori* error estimates and domain decomposition with nonmatching grids', *Adv. Comput. Math.* **23**, 241–263.

W. Prager and J. Synge (1947), 'Approximations in elasticity based on concepts of function spaces', *Quart. Appl. Math.* **5**, 241–269.

M. Puso (2004), 'A 3D mortar method for solid mechanics', *Internat. J. Numer. Methods Engrg* **59**, 315–336.

M. Puso and T. Laursen (2004*a*), 'A mortar segment-to-segment contact method for large deformation solid mechanics', *Comput. Methods Appl. Mech. Engrg* **193**, 601–629.

M. Puso and T. Laursen (2004*b*), 'A mortar segment-to-segment frictional contact method for large deformations', *Comput. Methods Appl. Mech. Engrg* **193**, 4891–4913.

M. Puso, T. Laursen and J. Solberg (2008), 'A segment-to-segment mortar contact method for quadratic elements and large deformations', *Comput. Methods Appl. Mech. Engrg* **197**, 555–566.

M. Raous, S. Barbarin and D. Vola (2002), Numerical characterization and computation of dynamic instabilities for frictional contact problems. In *Friction and Instabilities* (J. A. C. Martinis *et al.*, ed.), Vol. 457 of *CISM Courses Lect.*, Springer, pp. 233-291.

P. Raviart and J. Thomas (1983), *Introduction à l'Analyse Numérique des Équations aux Dérivées Partielles*, Collection Mathématiques Appliquées pour la Maîtrise, Masson.

Y. Renard (2006), 'A uniqueness criterion for the Signorini problem with Coulomb friction', *SIAM J. Math. Anal.* **38**, 452–467.

Y. Renard (2010), 'The singular dynamic method for constrained second order hyperbolic equations: Application to dynamic contact problems', *J. Comput. Appl. Math.* **234**, 906–923.

S. Repin (2008), *A Posteriori Estimates for Partial Differential Equations*, Radon Series on Computational and Applied Mathematics, de Gruyter.

S. Repin, S. Sauter and A. Smolianski (2003), '*A posteriori* error estimation for the Dirichlet problem with account of the error in the approximation of boundary conditions', *Computing* **70**, 205–233.

B. Rivière (2008), *Discontinuous Galerkin Methods for Solving Elliptic and Parabolic Equations*, SIAM.

J. Salomon, A. Weiss and B. Wohlmuth (2008), 'Energy conserving algorithms for a corotational formulation', *SIAM J. Numer. Anal.* **46**, 1842–1866.

A. Scheidegger (1960), *The Physics of Flow through Porous Media*, University of Toronto Press.

O. Schenk and K. Gärtner (2004), 'Solving unsymmetric sparse systems of linear equations with PARDISO', *J. Future Generation Computer Systems* **20**, 475–487.

O. Schenk and K. Gärtner (2006), 'On fast factorization pivoting methods for symmetric indefinite systems', *Elec. Trans. Numer. Anal.* **23**, 158–179.

J. Schöberl (1997), 'An advancing front 2D/3D-mesh generator based on abstract rules', *Comput. Visual. Sci.* **1**, 41–52.

J. Schöberl (1998), 'Solving the Signorini problem on the basis of domain decomposition techniques', *Computing* **60**, 323–344.

L. Scott and S. Zhang (1990), 'Finite element interpolation of nonsmooth functions satisfying boundary conditions', *Math. Comp.* **54**, 483–493.

B. Simeon (2006), 'On Lagrange multipliers in flexible multibody dynamics', *Comput. Methods Appl. Mech. Engrg* **195**, 6993–7005.

J. Simo (1998), Local behavior in finite element methods. In *Numerical Methods for Solids, Part 3* and *Numerical Methods for Fluids, Part 1* (P. Ciarlet and J. Lions, eds), Vol. VI of *Handbook of Numerical Analysis*, North-Holland, pp. 183–499.

J. Simo and F. Armero (1992), 'Geometrically nonlinear enhanced strain mixed methods and the method of incompatible modes', *Internat. J. Numer. Methods Engrg* **33**, 1413–1449.

J. Simo and T. Hughes (1998), *Computational Inelasticity*, Springer.

J. Simo and T. Laursen (1992), 'Augmented Lagrangian treatment of contact problems involving friction', *Comput. Struct.* **42**, 97–116.

J. Simo and M. Rifai (1990), 'A class of assumed strain methods and the method of incompatible modes', *Internat. J. Numer. Methods Engrg* **29**, 1595–1638.

J. Simo and N. Tarnow (1992), 'The discrete energy-momentum method: Conserving algorithms for nonlinear elastodynamics', *Z. Angew. Math. Phys.* **43**, 757–792.

J. Simo, F. Armero and R. Taylor (1993), 'Improved versions of assumed enhanced tri-linear elements for 3D finite deformation problems', *Comput. Methods Appl. Mech. Engrg* **110**, 359–386.

E. Stein and S. Ohnimus (1997), 'Equilibrium method for postprocessing and error estimation in the finite element method', *Comput. Assist. Mech. Engrg Sci.* **4**, 645–666.

E. Stein and S. Ohnimus (1999), 'Anisotropic discretization- and model-error estimation in solid mechanics by local Neumann problems', *Comput. Methods Appl. Mech. Engrg* **176**, 363–385.

R. Stevenson (2005), 'An optimal adaptive finite element method', *SIAM J. Numer. Anal.* **42**, 2188–2217.
R. Stevenson (2007), 'Optimality of a standard adaptive finite element method', *Found. Comput. Math.* **7**, 245–269.
D. Sun and L. Qi (1999), 'On NCP-functions', *Comput. Optim. Appl.* **13**, 201–220.
F. Suttmeier (2005), 'On a direct approach to adaptive FE-discretisations for elliptic variational inequalities', *J. Numer. Math.* **13**, 73–80.
V. Thomée (1997), *Galerkin Finite Element Methods for Parabolic Problems*, Springer.
A. Toselli and O. Widlund (2005), *Domain Decomposition Methods: Algorithms and Theory*, Springer.
M. Van Genuchten (1980), 'A closed-form equation for predicting the hydraulic conductivity of unsaturated soils', *Soil Sci. Soc. Am. J.* **44**, 892–898.
A. Veeser (2001), On *a posteriori* error estimation for constant obstacle problems. In *Numerical Methods for Viscosity Solutions and Applications* (M. Falcone and C. Makridakis, eds), Vol. 59 of *Advances in Mathematics for Applied Sciences*, World Scientific, pp. 221–234.
R. Verfürth (1994), '*A posteriori* error estimation and adaptive mesh-refinement techniques', *J. Comput. Appl. Math.* **50**, 67–83.
R. Verfürth (1996), *A Review of A Posteriori Error Estimation and Adaptive Mesh-Refinement Techniques*, Advances in Numerical Mathematics, Wiley–Teubner.
M. Vohralík (2008), '*A posteriori* error estimation in the conforming finite element method based on its local conservativity and using local minimization', *CR Math. Acad. Sci. Paris* **346**, 687–690.
K. Washizu (1955), On the variational principles of elasticity and plasticity. Report 25-18, Massachusetts Institute of Technology.
A. Weiss and B. Wohlmuth (2009), '*A posteriori* error estimator and error control for contact problems', *Math. Comp.* **78**, 1237–1267.
A. Weiss and B. Wohlmuth (2010), '*A posteriori* error estimator for obstacle problems', *SIAM J. Sci. Comput.* **32**, 2627–2658.
M. Wheeler and I. Yotov (2005), '*A posteriori* error estimates for the mortar mixed finite element method', *SIAM J. Numer. Anal.* **43**, 1021–1042.
C. Wieners (2007), 'Nonlinear solution methods for infinitesimal perfect plasticity', *Z. Angew. Math. Mech.* **87**, 643–660.
C. Wieners and B. Wohlmuth (2011), 'A primal–dual finite element approximation for a nonlocal model in plasticity', *SIAM J. Sci. Comput.* **49**, 692–710.
K. Willner (2003), *Kontinuums- und Kontaktmechanik*, Springer.
P. Wilmott, J. Dewynne and S. Howison (1997), *Option Pricing: Mathematical Models and Computation*, Oxford Financial Press.
B. Wohlmuth (1999*a*), 'Hierarchical *a posteriori* error estimators for mortar finite element methods with Lagrange multipliers', *SIAM J. Numer. Anal.* **36**, 1636–1658.
B. Wohlmuth (1999*b*), 'A residual based error-estimator for mortar finite element discretizations', *Numer. Math.* **84**, 143–171.
B. Wohlmuth (2000), 'A mortar finite element method using dual spaces for the Lagrange multiplier', *SIAM J. Numer. Anal.* **38**, 989–1012.

B. Wohlmuth (2001), *Discretization Methods and Iterative Solvers Based on Domain Decomposition*, Springer.

B. Wohlmuth (2005), 'A $\mathcal{V}$-cycle multigrid approach for mortar finite elements', *SIAM J. Numer. Anal.* **42**, 2476–2495.

B. Wohlmuth (2007), 'An *a posteriori* error estimator for two-body contact problems on non-matching meshes', *J. Sci. Comput.* **33**, 25–45.

B. Wohlmuth and R. Krause (2001), 'Multigrid methods based on the unconstrained product space for mortar finite element discretizations', *SIAM J. Numer. Anal.* **39**, 192–213.

B. Wohlmuth and R. Krause (2003), 'Monotone multigrid methods on nonmatching grids for nonlinear multibody contact problems', *SIAM J. Sci. Comput.* **25**, 324–347.

R. Wooding and H. Morel-Seytoux (1976), 'Multiphase fluid flow through porous media', *Annu. Rev. Fluid Mech.* **8**, 233–274.

P. Wriggers (2006), *Computational Contact Mechanics*, second edition, Springer.

P. Wriggers and U. Nackenhorst, eds (2007), *Computational Methods in Contact Mechanics*, Vol. 3 of *IUTAM Bookseries*, Springer.

P. Wriggers and O. Scherf (1998), 'Different *a posteriori* error estimators and indicators for contact problems', *Math. Comput. Modelling* **28**, 437–447.

S. Wright (1997), *Primal–Dual Interior Point Methods*, SIAM.

B. Yang and T. Laursen (2008*a*), 'A contact searching algorithm including bounding volume trees applied to finite sliding mortar formulations', *Comput. Mech.* **41**, 189–205.

B. Yang and T. Laursen (2008*b*), 'A large deformation mortar formulation of self contact with finite sliding', *Comput. Methods Appl. Mech. Engrg* **197**, 756–772.

B. Yang, T. Laursen and X. Meng (2005), 'Two dimensional mortar contact methods for large deformation frictional sliding', *Internat. J. Numer. Methods Engrg* **62**, 1183–1225.